



University of
Nottingham
UK | CHINA | MALAYSIA

Fabrication of Polyurethane Composites via Reactive Binder Jetting (RBJ) using a Dual-Ink Binding System

by

Arielle Torres, MEng

Thesis submitted to the University of Nottingham
for the degree of Doctor of Philosophy

March 2024

Abstract

The high processing temperatures traditionally required for Additive Manufacturing (AM) often degrade polymer powders, limiting part performance and recyclability. Reactive Binder Jetting (RBJ), a novel AM process, addresses these challenges by utilizing a dual-ink binding system that facilitates powder consolidation at ambient temperatures. This eliminates the need for energy-intensive equipment, such as lasers or heaters, enabling sustainable manufacturing of complex, functional parts.

This research focuses on the fabrication of polyurethane (PU) components using RBJ. PU is highly versatile due to its tunable co-polymer structure, making it a valuable material for applications ranging from insulation foams to biomedical implants. RBJ challenges addressed in thesis include reliable ink jetting, maintaining stoichiometry and achieving optimal saturation levels for part consolidation. To address these challenges, all materials were characterised, inkjet printing parameters were optimised, and fully consolidated, three-dimensional (3D) 'green' part tested.

The findings demonstrate RBJ printing is capable of forming robust polymer 'green' parts, introducing potential applications within the biomedical or sports industries. Through characterisation of reactive inks, control of droplet deposition strategies, and validation via mechanical testing, this work establishes RBJ as a sustainable alternative for polymer AM. The research highlights opportunities for future innovations, such as expanding the range of printable materials, including sustainable inks and reactive powders, improving RBJ printing process scalability, and developing multifunctional components with gradient properties.

Acknowledgements

I would like to take the opportunity to express my gratitude for the contributions made by the following individuals:

Partner

Alexander Douglas

Supervisors

Christopher Tuck

Richard Hague

Yinfeng He

Colleagues

Simon Attwood

Ali Sohaib

Christopher Strong

Negar Galini

Shreeja Basak

Salomé Sanchez

Andrea Alice Konta

Giuseppe Del Guercio

Technicians

Mark East

Mark Hardy

Adam Whitbread

Publications

Conferences

33rd Annual International Solid Freeform Fabrication Symposium (SFF Symp 2022), Austin, Texas, USA, 25 - 27 July 2022. Oral Presentation: *Functional Polyurethane Composites via Reactive Binder Jetting (RBJ) of a Dual-Ink Binding System*; Authors: Arielle Torres, Yinfeng He, Richard Hague and Chris Tuck; Programme: Special Session on Binder Jet AM II - Binder-Powder Interaction.

American Chemistry Society (ACS) Spring 2022, San Diego, California, USA, 20 - 24 March 2022. Virtual Poster Presentation: *Additive manufacturing (AM) of functional composite structures via Reactive Binder Jetting (RBJ) using a highly reactive two-part binding system*; Authors: Arielle Torres, Yinfeng He, Richard Hague and Chris Tuck; Programme: Division of Polymeric Materials Science and Engineering (PMSE).

Showcases

Engineering Research Showcase, University of Nottingham, 28 April 2022. Three Minute Thesis (3MT) Presentation: *Functional Polyurethane Composites via Reactive Binder Jetting (RBJ) of a Dual-Ink Binding System*.

Engineering Research Showcase, University of Nottingham, 5 May 2021. Poster Presentation: *Particle Fusion via Reactive Material Jetting: Fabricating Functional Net-Shape Polymeric Structures with Varying Mechanical Properties*.

Engineering Research Showcase, University of Nottingham, 6 May 2020. Pitch Perfect Presentation: *High Speed Reactive Inkjet Powder Bed Fusion*.

Table of Contents

Abstract	i
Acknowledgements	ii
Publications	iv
Table of Contents	xii
List of Figures	xix
List of Tables	xxi
List of Abbreviations	xxii
1 Introduction	1
1.1 Project Background	1
1.2 Novelty of Research	3
1.3 Aims and Objectives	4
1.4 Thesis Structure	5
2 Literature Review	6

2.1	Inkjet Printing Technology	6
2.1.1	Early Developments	6
2.1.1.1	Printhead Technology	7
2.1.2	Ink Rheology	9
2.1.2.1	Viscosity Behaviours	9
2.1.2.2	Impact of Surface Tension of Inks	10
2.1.2.3	Dimensionless Parameters	11
2.1.3	Droplet Formation	13
2.2	Ink-Based Powder Additive Manufacturing (AM)	15
2.2.1	Powder Recoating	16
2.2.1.1	Spreading Mechanisms	17
2.2.1.2	Packing Density of Powder Bed	17
2.2.1.3	Effect of Particle Sizes	18
2.2.2	Powder Consolidation Mechanisms	18
2.2.2.1	Energy-Absorbing Inks	19
2.2.2.2	Binder Inks	22
2.2.2.3	'Green' Part Sintering	23
2.2.3	Ink Infiltration Mechanics	24
2.2.3.1	Ink Spreading on Powder Substrate	25
2.2.3.2	Ink Saturation of Powder	26
2.2.3.3	Recyclability of Processed Powder	28

2.3	Polyurethane	29
2.3.1	Chemistry of Polyurethane	29
2.3.1.1	Molecular Structure of Polyurethanes	30
2.3.1.2	Impact of Polyurethane (PU) Components on Part Prop- erties	31
2.3.1.3	Applications and Properties	32
2.3.1.4	Sustainable Alternatives	34
2.3.2	Polyurethane Manufacturing Techniques	35
2.3.2.1	Conventional Methods	35
2.3.2.2	Additive Manufacturing (AM) Methods	35
2.3.2.3	Reactive Inkjet Printing	37
2.4	Research Gaps and Opportunities for Innovation	38
3	Materials and Methods	40
3.1	Materials	40
3.1.1	Reactants	41
3.1.1.1	Isocyanates	41
3.1.1.2	Alcohols	42
3.1.1.3	Catalysts	44
3.1.1.4	Dyes	45
3.1.2	Polyurethane Powders	45
3.1.3	Printheads	46

3.2	Methods	47
3.2.1	Overview	47
3.2.2	Ink Preparation	48
3.2.2.1	Diol Inks	48
3.2.2.2	Isocyanate Inks	50
3.2.3	Characterisation Methods	50
3.2.3.1	Rheological Behaviours of RBJ Materials	51
3.2.3.2	Composition of RBJ Materials	51
3.2.3.3	Morphological Characterisation of RBJ Printed Parts	53
3.2.4	Inkjet Printing of Reactive Inks	54
3.2.4.1	Printer Set Up	54
3.2.4.2	Controlling Stoichiometry of Reactive Dual-Ink Binder System	57
4	Development of Reactive Dual-Ink Binder System for Inkjet Printing	60
4.1	Evaluation of Reactive Inks	62
4.1.1	Miscibility	63
4.1.2	Viscosity	65
4.1.2.1	Increasing Shear Rate	65
4.1.2.2	Increasing Temperature	69
4.1.3	Reactivity of Dual-Ink Binder System	72
4.1.3.1	Compositional Changes during Reaction Time	72

4.1.4	Selection of Suitable Reactive Inks for Reactive Binder Jetting (RBJ)	76
4.2	Inkjet Printing Optimisation for Reactive Inks	80
4.2.1	Droplet Generation	80
4.2.1.1	Impact of Jetting Temperature	81
4.2.1.2	Impact of Jetting Voltage	81
4.2.1.3	Impact of Waveform Profile	82
4.2.2	Molar Ratio of Dual-Ink Binder System	83
4.2.2.1	Number of Moles per Droplet	84
4.2.2.2	Stoichiometry Calibration of Dual-Ink Binders	88
4.3	Validation of Reactive Inks on Non-Porous Substrate	91
4.3.1	Initial Quality Checks	92
4.3.2	Mixing Behaviour	95
4.3.3	Degree of Polymerisation	96
4.4	Summary	98
5	Performance and Printing Optimisation of Single Powder Layer (SPL)	
	Parts	100
5.1	Suitability of Commercial Thermoplastic Polyurethane (TPU) Powders for Reactive Binder Jetting (RBJ)	100
5.1.1	Flowability for Powder Recoating	101
5.1.2	Particle Size Distribution	103
5.1.3	Morphological Characterisation of Commercial Powders	105

5.2	Single Powder Layer (SPL) Printing	107
5.2.1	Experimental Set Up for Single Powder Layer (SPL) Printing . .	108
5.2.1.1	Ink Visibility and Jetting Feedback	108
5.2.1.2	Custom Powder Bed Samples	109
5.2.1.3	Summary	110
5.2.2	Initial Printing via Sample Frames	111
5.2.2.1	Deposition Sequence	111
5.2.2.2	Single Powder Layer (SPL) Validation	113
5.2.2.3	Critical Parameters to Adjust for Powder Substrate . .	114
5.2.3	Impact of Droplet Spacing (DS)	115
5.2.3.1	Printed Powder Comparison	115
5.2.3.2	Droplet Spacing (DS) Comparison	117
5.2.3.3	Compositional Analysis via TGA and FTIR	118
5.2.4	Impact of Increasing Reactive Ink Layers (RILs)	124
5.2.4.1	Visual Analyses of Reactive Ink Layer (RIL) Samples .	126
5.2.4.2	SEM Images of Reactive Ink Layer (RIL) Samples . . .	128
5.2.4.3	Cross-Sectional Sample Density Profiling	130
5.2.5	Summary	135
6	Validation of Reactive Binder Jetting (RBJ) via Multiple Powder Layer (MPL) Printing	137
6.1	Printer Set Up for Reactive Binder Jetting (RBJ)	138

6.1.1	Jetting Adjustments via LP50 (Software Modifications)	138
6.1.1.1	Waveform Conversions	138
6.1.1.2	Droplet Spacing	138
6.1.1.3	Pixel Density and Image Sizing	139
6.1.2	Powder Recoating via LP50 (Hardware Modifications)	140
6.1.2.1	Powder Bed Platform	140
6.1.2.2	Powder Recoating Blade	141
6.1.2.3	Dual-Printhead Assembly Holder	142
6.1.3	Printing Parameter Calibrations for Reactive Binder Jetting (RBJ)	142
6.1.3.1	Parameter Selection	143
6.1.3.2	Offset Print Testing	144
6.2	Three-Dimensional (3D) Printing Optimisation	145
6.2.1	Powder Recoating Parameters	145
6.2.1.1	Delamination	145
6.2.1.2	Maximising Saturation	147
6.2.2	Print Stability on Build Platform	150
6.2.2.1	Print Layer Displacement	152
6.2.2.2	Printed Raft Stabilisation	153
6.3	Part Quality and Performance	154
6.3.1	Geometrical Analyses of Multiple Powder Layer (MPL) Printed Parts	155
6.3.1.1	Uniform Shapes	155

6.3.1.2	Non-Uniform Shapes	156
6.3.2	Mechanical Analyses of Multiple Powder Layer (MPL) Printed Parts	157
6.3.2.1	Tensile Testing of Multiple Powder Layer (MPL) Printed Parts	157
6.3.2.2	Compression Testing of Multiple Powder Layer (MPL) Printed Parts	158
6.4	Summary	160
7	Discussion	161
7.1	Reactive Inks	161
7.2	Printer Parameters	163
7.3	Saturation Level	166
7.4	Unexpected Challenges	172
8	Conclusions and Future Work	174
8.1	Conclusions	174
8.2	Future Work	176
8.2.1	Widening Printable Ink Range	176
8.2.2	Exploring Alternative Powders	177
8.2.3	Higher-Volume Deposition Printheads	178
	References	180

List of Figures

1.1	Branched diagram of the seven additive manufacturing technologies and their respective subdivision.	1
1.2	Two droplets of reactive ink selectively penetrate and consolidate the powder to form a three-dimensional part.	3
2.1	Classification of inkjet printing technology within the additive manufacturing industry.	7
2.2	Configurations for piezoelectric drop-on-demand printhead in (a) squeeze, (b) bend, (c) push and (d) shear modes.	8
2.3	Example of a voltage waveform with four distinguishable voltage segments.	8
2.4	Droplet shapes for materials with contact angles less than and greater than 90°	10
2.5	Representation of the printable region $1 \leq Z \leq 10$ where fluid properties are optimal for droplet formation.	12
2.6	Droplet formation for experimental results.	14
2.7	Satellite droplet formation.	14
2.8	Spreading mechanics for the (a) counter-rotating roller and (b) doctor blade.	17
2.9	Four distinct classifications of powder binding mechanisms.	19

2.10	Schematics for two sintering processes including (a) High Speed Sintering (HSS) and (b) Selective Mask Sintering (SMS).	20
2.11	Step-by-step printing process for the HP Multi Jet Fusion printer.	21
2.12	Droplet impact outcomes for powder bed substrates at increasing drop velocities.	24
2.13	Relationship between ink droplet diameter before impact with the substrate and maximum droplet spreading diameter after impact.	25
2.14	Warping in 'green' parts at powder layer thicknesses between 0.1 - 0.2 mm.	26
2.15	Geometric accuracies of BJ printed parts for heated and unheated powder beds.	27
2.16	SEM image of (a) virgin and (b) aged polyamide 12 (PA12) powders used for Selective Laser Sintering (SLS) processes.	28
2.17	Chemical reaction between di-isocyanate and hydroxyl to form urethane repeat unit(s).	30
2.18	PU Market categorised into five application segments.	33
2.19	Mechanical properties of TPU materials manufactured via conventional and AM processes.	36
2.20	In situ reaction kinetics of polyurethane conversions for reactants containing catalyst concentrations between 0.1 - 2.0 wt%.	38
3.1	Chemical structure for (a) HDI and (b) PHDI.	42
3.2	Chemical structure for ethylene glycol (EG).	42
3.3	Chemical structure for poly(ethylene glycol) (PEG).	43
3.4	Chemical structure for 1,4-butanediol (BD).	43
3.5	Chemical structure for dibutyltin dilaurate (DBTL).	44

3.6	Chemical structure for stannous octoate (SO).	44
3.7	Chemical structure for dimethylethanolamine (DMEA).	45
3.8	Fuljifilm printheads (a) DMC-11610 and (b) DMC-Samba.	46
3.9	Method for optimising reactive ink formulations and obtaining the moles per droplet to calibrate the molar ratio within a dual-ink binder system.	48
3.10	Example TGA plot profiling the thermal decomposition of commercial TPU powders - Ultrasint™ and UNEX - at 20 °C min ⁻¹ .	53
3.11	Full Dimatix Inkjet Printer setup in glove box with antechamber (top) with internal part labels (bottom).	55
3.12	PiXDRO LP50 inkjet printer modified with a dual-printhead, vacuum, and powder bed system.	56
3.13	Example of a multi-set jetting waveform with three repeating droplet generation segments.	59
4.1	Ink B formulations containing 2.0 wt % (a) stannous octoate (SO), (b) dibutyltin dilaurate (DBTL), and (c) dimethylethanolamine (DMEA).	63
4.2	Shear viscosities for reactive inks (a) A, (b) B and (c) B1 at increasing shear rates from 10 - 1000 s ⁻¹ at 50 °C, 60 °C, and 70 °C.	66
4.3	Shear viscosity of reactive inks (a) A, (b) B, and (c) B1 at increasing temperatures (25 – 70 °C).	70
4.4	Reduction in shear viscosity for all reactive ink formulations.	71
4.5	Time lapse of transmission peak intensities for reactive inks A03 and B01 at different catalyst concentration.	73
4.6	Time lapse of transmission peak intensities for reactive inks A03 and B at different catalyst concentration.	74

4.7	Change in intensity of transmission peak minima for reactive ink combinations ink A-B and A-B1.	75
4.8	Colour mapping of print performance across range of available voltages.	82
4.9	Example of a single waveform pattern with labelled segments.	83
4.10	Droplet mass with error bars for reactive inks at suitable print voltages.	84
4.11	Example of a multiple-pattern waveform (MPW) with segment labels. .	86
4.12	Images of droplet generation via a triple multiple-pattern waveform (MPW).	87
4.13	Measured droplet volumes for reactive inks at 1x, 2x, and 3x waveforms.	88
4.14	Moles per droplet measurements at all suitable printhead temperatures for selected reactive inks.	88
4.15	Moles per droplet measurements at suitable print voltages for selected reactive inks.	89
4.16	Plot of moles per drop for reactive inks associated with reliable jetting. .	90
4.17	Print pattern and layout for assessing nozzle functionality.	92
4.18	Print signatures for reactive inks (a) A01 and (b) B102_2.0.	93
4.19	Images of single-ink layers at 1x, 2x, 3x, and 10x for ink A and ink B1. .	94
4.20	Image of a 1x dual-ink layer with a dysfunctional nozzle.	95
4.21	Images of a dual-ink square print at an offset to show ink behaviours. . .	96
4.22	FTIR transmission scans of a printed PU film.	97
5.1	PSD for commercial TPU powders - Ultrasint™ (δ) and UNEX (\circ) . . .	104
5.2	SEM images of commercial powders (a) Ultrasint™ (HP) at 400x magnification, and (b) UNEX (UX) at 200x magnification.. . . .	106

5.3	Visual representation of dyed reactive inks.	109
5.4	Demonstration of custom powder holders for single-powder layer printing.	110
5.5	Deposition sequencing for ISO and DIOL reactive inks.	112
5.6	Comparison between Sequence 1 (ISO ink 1st) and Sequence 2 (DOIL ink 2nd)	112
5.7	Image array of a fully consolidated single powder layer (SPL) samples. .	113
5.8	SPL samples printed using DS of 6 μm and 10 μm for UX and HP powders.	116
5.9	SEM images of SPL samples printed using a range of droplet spacings at 200x magnification.	117
5.10	TGA of CPU prints heated from 50 - 800 $^{\circ}\text{C}$	120
5.11	Transmission peak intensities between 1800 - 1600 cm^{-1} for samples UX01-UX03 and HP01-HP03.	122
5.12	Composition of a single RIL.	125
5.13	Composition of multiple RILs.	125
5.14	SPL prints jetted with 1x, 2x and 3x RILs.	126
5.15	Geometry of 1x and 2x RIL printed samples	128
5.16	SEM images at 100x of SPL samples printed with 1x, 2x and 3x RILs. .	129
5.17	3D XCT image of 1x RIL sample composed of UX powder.	130
5.18	Array of cross-sectional XCT images of SPL print sample	131
5.19	SEM images of cross-sectioned SPL prints for 2x and 3x RILs.	132
5.20	Cross-sectional profile of void percentage for 2x and 3x RIL samples. . .	134

6.1	Graphical FPL defined by a single powder layer and one or more Reactive Ink Layers (RILs).	138
6.2	Print layer image for different droplet spacings.	140
6.3	Custom powder bed for LP50 printer with part labels.	141
6.4	Custom LP50 recoater mechanism with part labels.	141
6.5	Custom dual printhead assembly holder for LP50 printer with part labels.	142
6.6	Overview of powder recoating process with key settings labelled.	144
6.7	Visual summary of a horizontal offset print for ISO (red) and DIOL (blue) inks.	144
6.8	Example of delamination occurring in Reactive Binder Jetting (RBJ) printed dog bone.	146
6.9	SPL samples S1-S5 printed at 10 μm DS with increasing RILs.	147
6.10	SPL samples T1-T5 printed at 20 μm DS with increasing RILs.	149
6.11	Summary of the recoating process.	151
6.12	Four 10 mm square print layers in locations L1-L4 on powder bed.	152
6.13	Print layer offset following RBJ printing of 18x RILs.	153
6.14	Rectangular 3D RBJ part built with a supportive raft	154
6.15	Images of 3D RBJ printed samples composed of the dual-ink binder system and UX powder.	155
6.16	Overview of target dimensions and settings for printing and recoating for each sample.	156
6.17	Close up images of two irregular RBJ parts.	157
6.18	Close up images of two rectangular RBJ parts.	157

6.19	Tensile testing setup for an RBJ printed parts with stress-strain plot. . .	158
6.20	Compression testing setup for an RBJ printed parts with stress-strain plot.	159

List of Tables

2.1	Common polyurethane (PU) components and their respective influences.	31
2.2	Common applications for polyurethane (PU) foams including their inherent properties.	33
3.1	Key properties of constituent materials used in dual-ink binder systems.	40
3.2	Key differences between two types of Dimatix Material Cartridges (DMCs) used in this project.	47
3.3	Characteristic frequencies of bonds present in isocyanates, alcohols and polyurethane.	52
4.1	Summary of composition of all reactive ink formulations investigated. . .	61
4.2	Selection criteria for reactive inks suitable for Reactive Binder Jetting (RBJ).	62
4.3	Viscosities and percentage increases for all ink formulations.	67
4.4	Estimated molecular weights for reactive inks A, B, and B1.	68
4.5	Percentage difference in peak transmission from 0 - 60 minutes.	76
4.6	Weighted matrices (a) 'Miscibility', (b) 'Viscosity', and (c) 'Reactivity' for reactive ink A, B and B1.	77
4.7	Summary of constituent materials properties for selected reactive inks. .	85

4.8	Summary of molar masses and densities for selected reactive inks.	86
4.9	Colour mapping of all suitable reactive ink pairings with key.	91
5.1	Powder flow measurements for commercial polyurethane powders - Ultrasint™ and UNEX.	102
5.2	Summary of the PSD, skewness and specific SA for Ultrasint™ and UNEX powders.	104
5.3	Summary of mean particle sizing and deviations for Ultrasint™ and UNEX powders.	107
5.4	Summary of single powder layer (SPL) samples investigated.	108
5.5	Range of wavenumbers for relevant peak transmissions between 1800-1600 cm^{-1}	124

List of Abbreviations

3D	Three-Dimensional
A%	Elongation at break
AM	Additive Manufacturing
ATR	Attenuated Total Reflectance
BD	1,4-butanediol
BFE	Basic Flowability Energy
BJ	Binder Jetting
BSI	British Standards Institution
CAD	Computer Aided Design
CIJ	Continuous Inkjet
CNC	Computer Numerical Control
DBTL	Dibutyltin dilaurate
DIOL	Diol-based Reactive Ink
DMC	Dimatix Materials Cartridge
DMEA	Dimethylethylamine
DMP	Dimatix Materials Printer
DSA	Drop Shape Analyser
DSC	Differential Scanning Calorimetry
DOD	Drop-on-Demand
EG	Ethylene glycol
FDM	Fused Deposition Modelling
FTIR	Fourier-Transform Infrared
FPL	Full Print Layer
GUI	Graphic User Interface
HDI	1,6-hexamethylene diisocyanate
HIP	Hot Isostatic Pressing
HP	Hewlett-Packard
HSS	High Speed Sintering
IBM	International Business Machines
IM	Injection moulding
IPA	Isopropanol
IPDI	Isophorone diisocyanate

IR	Infrared
ISFO	International Organization for Standardization
ISO	Isocyanate-based Reactive Ink
MDI	Methylene diphenyl diisocyanate
MJF	Multi-Jet Fusion
MPW	Multiple-Pattern Waveform
MPL	Multiple Powder Layer
NMR	Nuclear Magnetic Resonance
NIPU	Non-isocyanate polyurethane
PEEK	Polyether ether ketone
PA12	Polyamide 12
PEG	Poly(ethylene glycol)
PHDI	Poly(hexamethylene diisocyanate)
PMMA	polymethyl methacrylate
PBF	Powder Bed Fusion
PLT	Powder Layer Thickness
PDOD	Piezoelectric Drop-on-Demand
PET	Poly(ethylene terephthalate)
PTFE	Poly(tetrafluoroethylene)
PhD	Doctor of Philosophy
PU	Polyurethane
PVP	Polyvinylpyrrolidone
RAM	Radiation Absorbing Material
RBJ	Reactive Binder Jetting
RIJP	Reactive Inkjet Printing
RIL	Reactive Ink Layer
RH	Relative humidity
SEM	Scanning Electron Microscope
SMP	Shape Memory Polymer
SLS	Selective Laser Sintering
SO	Stannous octoate
SMS	Selective Mask Sintering
SPL	Single Powder Layer
TDI	Toluene diisocyanate
TGA	Thermogravimetric Analysis
TPU	Thermoplastic Polyurethane
USP	Unique selling point
UTS	Ultimate tensile strength

1 | Introduction

1.1 Project Background

Additive Manufacturing (AM), also referred to as three-dimensional (3D) printing, encompasses a range of advanced processes which selectively build material in a layer-by-layer fashion to achieve functional, three-dimension (3D) parts. According to the British Standards Institution (BSI), AM is formally defined as the "process of joining materials to make parts from 3D model data, usually layer upon layer".¹

Figure 1.1 outlines the seven families of AM methods developed to date, including established subsidiary processes associated with each.² Processable materials include an array of metals, ceramics and polymers in either a composite, alloyed or pure state.

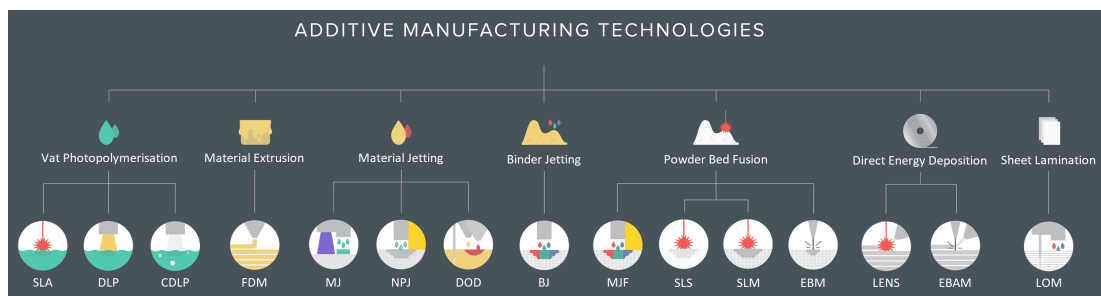


Figure 1.1: Branched diagram of the seven additive manufacturing technologies and their respective subdivision (adapted from Redwood²).

Unlike traditional subtractive methods such as computer numerical controlled (CNC) machining, AM minimises material waste and unlocks unprecedented design freedoms. Thus, a major advantage to using AM is the cost-effective fabrication of complex, net-shape parts that would otherwise require expensive tooling, hours of machining or not be manufacturable in any other way.³

Multiple-part assemblies have been manufactured as a single pre-assembled part using AM techniques, demonstrating how fasteners and assembly times can be eliminated. AM technologies have become a desirable manufacturing alternatives in industries that manufacture complex parts or assemblies using expensive materials, such as platinum, tantalum or polyether ether ketone (PEEK). Therefore, further work is justified in widen the range of suitable materials and improving manufacturing reliability for a range of applications.

However, due to the additive approach, AM parts are inherently more likely to form defects, especially at boundaries between previously processed and newly added material.^{3,4} The presence of voids or cracks are typically considered undesirable properties, however porous AM parts can be advantageous within the biomedical and pharmaceutical industries.⁵

Polyurethane (PU), a versatile polymer characterised by its alternating 'hard' and 'soft' segment structure, has emerged as a promising material for AM. Tunable mechanical properties makes PU suitable for diverse applications, from insulation foams to biomedical implants to durable sports equipment. In 2016, PU was ranked 6th among all polymers with a global production of 18 tonnes and global market valuation of €53 bn.⁶ Therefore, further research into processable materials and novel manufacturing techniques capable of producing high quality, functional PU parts is justified by the large, growing PU market.

Binder Jetting (BJ) is a powder-based AM technique which selectively deposits a liquid binder onto a powder bed to form three-dimensional (3D) structures layer by layer. However, BJ printed parts often require significant post-processing to debind loose, unconsolidated powder and strength via furnace sintering. Common challenges include unreliable ink deposition, undesirable ink spreading, and part damage during powder layer recoating.

This research focuses on the development of a novel ink-based powder AM process called Reactive Binder Jetting (RBJ). This process was developed at the University of Nottingham and successfully patented in 2018 by Tuck *et al.*⁷. RBJ is a ink-based powder AM process that selectively deposits pico-litre droplets of two or more reactive

inks onto a powder bed substrate. As demonstrated in Figure 1.2, the two reactive inks will react upon contact to form a consolidated part. Related to BJ printing, RBJ utilising inkjet printing technology to deposit a reactive dual-ink binder system which chemically binds powder together to form a binder-powder composite.

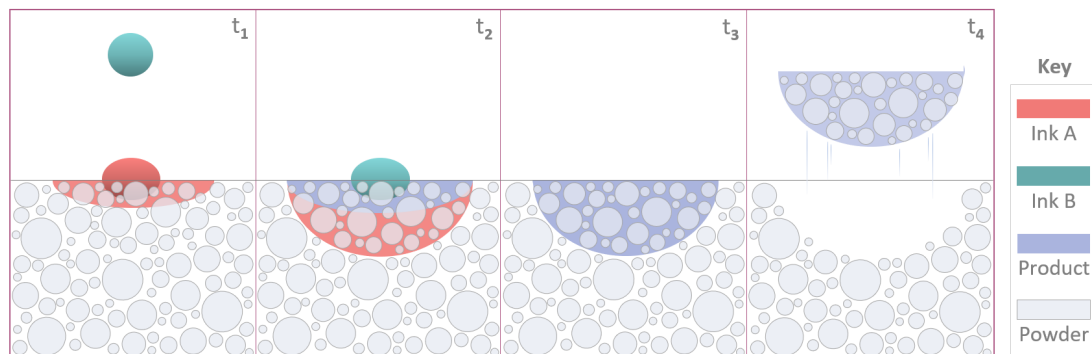


Figure 1.2: Two droplets of reactive ink selectively penetrate and consolidate the powder to form a three-dimensional part.

Clever formulation design and application enables in-situ polymerisation to occur between the powder particles and print layers without the need for thermal processing. Therefore, eliminating the need to use energy-intensive equipment, such as furnaces, CO₂ lasers or infrared (IR) lamps. RBJ has potential to become a sustainable, cost-effective alternative capable of manufacturing thermally-sensitive materials, such as drugs for biodegradable implant applications.^{8,9}

The primary challenges identified with RBJ printing include reliable jetting of inks, maintaining a desired stoichiometry and achieving optimal saturation levels for consolidation. The purpose of this research was to validate RBJ printing as a viable, low-temperature AM process for PU manufacturing, thus paving the way for new innovations in polymer-based AM.

1.2 Novelty of Research

The work contained within this document demonstrates the viability of using RBJ printing to successful manufacture fully consolidated 3D parts, capable of undergoing chemical and mechanical characterisation techniques. Overall, your research significantly advances the state of knowledge in RBJ printing by providing valuable insights into ink characterisation, printer parameter optimisation, part evaluation, and future

directions for research and development. Thus, these contributions have the potential to further advance manufacturing innovation and facilitate the adoption of RBJ printing across various industrial sectors as a low-temperature AM technique . This research introduces several areas of novelty including:

- i **Development of Reactive Dual-Ink Binders:** This research delves into the comprehensive characterisation of the reactive inks that mix to form dual-ink binder systems. Thorough evaluation of the properties of each reactive ink formulation, led to advanced insights into which of formulations would be suitable for the RBJ process. Additionally, reactive inks behaviours observed during inkjet printing informed further ink formulation development and optimisations for the RBJ printing process.
- ii **Portfolio of Print Parameters for RBJ Part Consolidation:** A wide range of printer settings, including waveforms, voltage inputs, and temperatures, were explored and optimum parameters mapped out for each of the viable reactive inks selected to form a dual-ink binder system. Initial powder printing produced Single-Powder Layer (SPL) samples were analysed, providing feedback around the uniformity and saturation of a single print layer. This iterative optimisation process not only improved the quality of RBJ parts but also established guidelines for consistently achieving fully consolidated 3D RBJ parts in different operating conditions.
- iii **Baseline Performance Indicators for RBJ Printed Parts:** This research characterised the surface quality and mechanical properties of 3D RBJ printed parts for the first time. These evaluations contributed to a deeper understanding of the performance characteristics of RBJ printed parts, providing an initial insight into potential use cases and thus revealing pathways to commercialisation of this low-temperature process follow further developments.

1.3 Aims and Objectives

The purpose of this research is to explore a novel ink-based powder AM process which utilises highly reactive dual-ink binder system to form three-dimensional (3D) composite polymer parts. This novel process has been designed to remove the need for high

temperature processes, or other energy inputs, to consolidate powder and achieve 3D parts. Powder AM technologies typically rely on laser beams, ultraviolet (UV) or infrared (IR) lamps to elicit a fully consolidated part. Therefore, the primary aim of this PhD project is to demonstrate the novel Reactive Binder Jetting (RBJ) process is a feasible low-temperature alternative to manufacture functional PU parts.

Objectives:

- i Identify printable reactive ink formulations and suitable dual-ink binder pairings for RBJ printing.
- ii Demonstrate RBJ printing suitability of the reactive dual-ink binder systems using commercial inkjet printing equipment on non-porous substrate.
- iii Establish a portfolio of print parameters for each reactive ink to expand the breadth of suitable dual-ink binder systems.
- iv Validate RBJ printing through single-powder layer consolidation using a reactive dual-ink binder.
- v Print multi-powder layer RBJ samples suitable for mechanical testing, including compression and tensile testing.

1.4 Thesis Structure

This thesis is organised into eight chapters, each designed to provide a logical progression of information, from contextual background to research findings and their implications. A brief overview of the chapters is provided below:

Chapter 1: Introduction

Chapter 2: Literature Review

Chapter 3: Experimental Methods and Materials

Chapter 4: Development of Reactive Dual-Ink Binder System for Inkjet Printing

Chapter 5: Performance and Printing Optimisation of Single Powder Layer (SPL) Parts

Chapter 6: Validation of Reactive Binder Jetting (RBJ) via Multiple Powder Layer (MPL) Printing

Chapter 7: Discussion

Chapter 8: Conclusions and Future Work

2 | Literature Review

The purpose of this chapter is to provide the reader with an overview of the current research related to the project focus. Critical analyses are presented throughout, including an assessment of the advantages and limitations of established powder-based processes. Finally, knowledge gaps in the field are identified and later used to plan future work.

2.1 Inkjet Printing Technology

2.1.1 Early Developments

In 1951, Elmqvist and Bromma¹⁰ successfully patented the first inkjet printer, initially used to record analogue voltage signals. In the early 1960s, R. G. Sweet demonstrated ink droplets of uniform size and spacing could be produced by applying a pressure wave to an orifice, becoming the first to use continuous inkjet (CIJ) technology.¹¹ In 1972, Carl Hellmuth Hertz discovered gray-scale images could be produced by varying the volume of ink distributed at each pixel, thus leading to the invention of coloured inkjet printing.^{12–14} In 1976, International Business Machines (IBM) licensed CIJ technology and launched the IBM 4640 inkjet printer.¹⁵ The Siemens PT-80 was introduced one year later as the first drop-on-demand (DOD) printer which used a squeeze mode piezoelectric printhead.¹⁶

Until the late 1980's, inkjet technology had predominantly been developed for the traditional printing industry, including publishing and label manufacturing, with thermal inkjet printers dominating three quarters of the market.¹⁶ However, inkjet printing technology has evolved beyond traditional printers over the last two decades toward advanced manufacturing techniques, eliciting novel 3D parts. Among these newer ap-

plications piezoelectric inkjet printers have become the most popular printhead type to use within the AM sector, particularly within academic settings. The inkjet technologies most relevant to the focus of this project are discussed later in Section 2.2.2.1 which include an analysis of the Hewlett-Packard (HP) Multi Jet Fusion (MJF) printer launched in 2016.

2.1.1.1 Printhead Technology

Inkjet printheads are typically composed of an ink reservoir and a nozzle or array of nozzles which, depending on the application, may have tens or hundreds of nozzles in a single printhead. As such, several different droplet generation methods have been investigated with both DOD printers proving to be the most successful within AM, followed by CIJ technologies.

DOD printers generate droplets by sending an impulse to the printhead when ink deposition is required whilst CIJ printers continuously eject ink droplets even when not required. To overcome this, CIJ printheads selectively apply an electric charge to unwanted droplets, causing them to deflect into a gutter as they pass through an electric field. Both CIJ and DOD technology can be further classified by the actuation mechanism responsible for droplet generation as shown in Figure 2.1 which provides an overview of the established CIJ and DOD technologies available for inkjet printing.

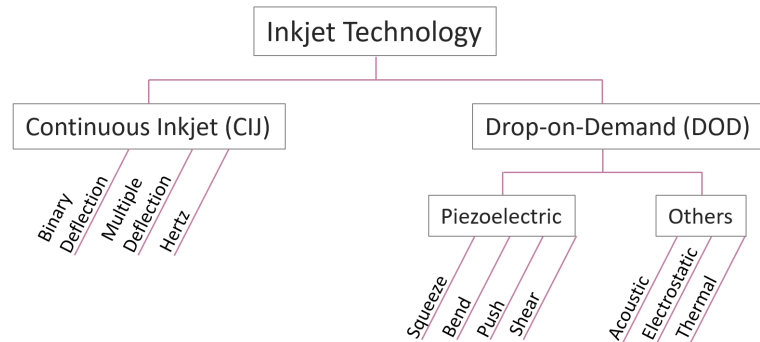


Figure 2.1: Classification of inkjet printing technology within the additive manufacturing industry (adapted from Le¹¹.)

Piezoelectric drop-on-demand (PDOD) printheads generate droplets by applying intermittent pressure to the outer walls of each nozzle chamber using a small piezoelectric device and as such are the most widely applied inkjet technology within the AM industry. When an electric impulse is received the piezoelectric component in the PDOD

printhead deforms, squeezing the nozzle chamber to eject an ink droplet. When the impulse is removed the piezoelectric component resumes its original position, drawing fresh ink into the nozzle chamber from the reservoir. Thus, the phenomenon responsible for droplet formation in PDOD printheads is known as the piezoelectric effect. Various PDOD printhead designs exist with different piezoelectric component configurations, however the four most common types can be seen in Figure 2.2.

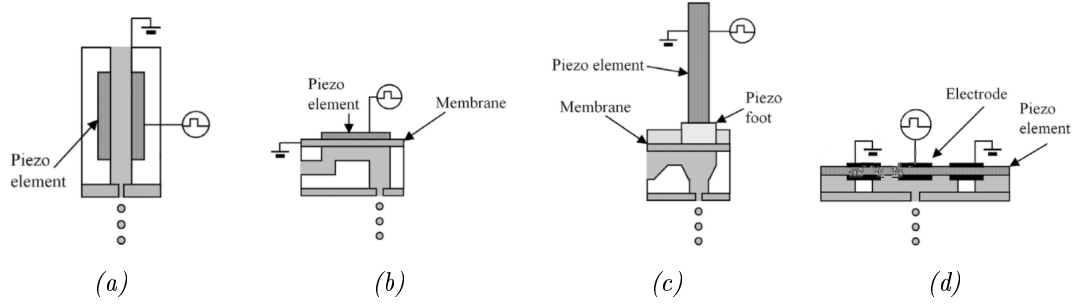


Figure 2.2: Configurations for piezoelectric drop-on-demand printheads in (a) squeeze, (b) bend, (c) push and (d) shear mode (adapted from Houben¹⁷).

The intensity and frequency of these piezoelectric deformations is influenced by the amount of voltage applied to the piezoelectric component. Typical PDOD printheads are capable of generating droplets at a rate between 0.1-10 kHz¹⁸ with velocities in the range of 5-8 m s⁻¹.¹⁹ Thus, voltage waveforms can be optimised for each ink based on their intended application. An example of a generic voltage waveform is shown in Figure 2.3.

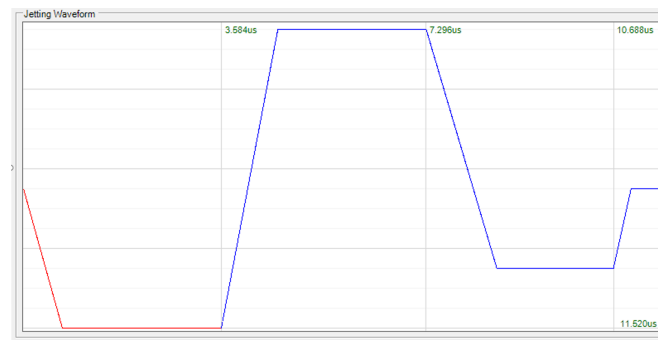


Figure 2.3: Example of a voltage waveform with four distinguishable voltage segments.

By understanding the rheological properties of a given material, the waveform can be tailored to produce droplets of a desired morphology, volume and velocity. However, successful ink deposition onto a substrate is dependent on the energy present within

the droplet system. Further information on ink rheology and energy requirement of a droplet is discussed within Sections 2.1.2 and 2.1.3, respectively.

2.1.2 Ink Rheology

The relationship between viscosity, surface tension and density of a material is defined by the Z parameter. This dimensionless number provides a quantitative method for comparing and predicting the printability of new materials for inkjet printing. The underlying equations and theory to support this relationship can be found in Section 2.1.2.3.

2.1.2.1 Viscosity Behaviours

The rheological properties of an ink have a significant impact on the formation of new material surfaces during droplet generation. Viscosity can be defined as the resistance to flow due to the internal friction between fluid particles.²⁰

Therefore, a highly viscous material will resist separation of its constituents more effectively than an inviscid material. For inkjet applications, it is critical for the ink to be sufficiently inviscid to allow separation of the ink from the nozzle orifice whilst exhibiting enough viscosity to maintain an ideal droplet morphology after ejection. For example, viscosity should ideally be between 10 - 12 mPa s for any ink jetted from a Fujifilm Dimatix Materials Printer (DMP), however it is still possible to achieve droplets up to 30 mPa s.²¹

The viscosity of a material can be optimised by manipulating the jetting temperature since both properties are inversely proportional. Therefore, viscosity is lowered by applying heat to a material which increases the internal energy thus making it easier for the constituent molecules to slide past one another. Most modern commercial printheads have a mechanism which allows the user to apply moderate heat to the nozzle chamber in order to temporarily reduce the ink's viscosity before attempting to generate a droplet.

A rheometer is an instrument that measures the flow or deformation of a material in response to applied forces. It is typically used to measure the viscosity for a given material, often over a range of temperatures. This is utilised during ink optimisation

for inkjet printing applications with capabilities to control the temperature of ink during droplet ejection. Further information about characterising the rheological properties of both powder and ink can be found in Section 3.2.3.

2.1.2.2 Impact of Surface Tension of Inks

Surface tension is responsible for the droplet geometry of a liquid, thus it is a material's ability to overcome gravitational forces and maintain a given shape. To elicit a change in the droplet shape, work must be applied to the material in order to overcome the tensile forces present at the droplet surface. According to the Young-Laplace equation, a relationship exists between a droplet's radii of curvature and surface tension, σ . By applying this relationship, we obtain Equation (2.1) which performs an energy analysis of the droplet system.

$$\sigma = \frac{\text{work}}{\text{droplet volume}} = \frac{\rho g h}{\left(\frac{1}{R_1} + \frac{1}{R_2}\right)} \quad (2.1)$$

where ρ is density, g is gravitational constant, h is vertical drop height and R_x is radii of curvature.

A tensiometer is an instrument designed to measure the surface tension of a liquid by analysing the shape produced by a droplet undergoing an appropriate method, such as bubble pressure, pendant drop or sessile drops. A Drop Shape Analyser (DSA) is commonly used to determine the surface tension and weight of a droplet by suspending the liquid from a needle to form a pendant drop to be analysed. This instrument can also be used to analyse sessile drops whereby the a given volume of liquid rests atop a flat surface. Contact angle measurements are performed by analysing the droplet curvature in relation to its substrate.

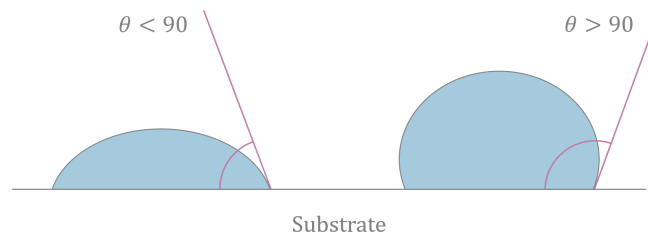


Figure 2.4: Droplet shapes for materials with contact angles less than and greater than 90° , respectively (adapted from Wenzel²²).

Figure 2.4 provides a visual representation of the relationship between contact angle and droplet shape. For example, materials with low surface tensions produce 'flatter' droplets with contact angles $< 90^\circ$.

2.1.2.3 Dimensionless Parameters

The surface tension, inertia and viscosity of an ink significantly influences the formation and behaviour of droplets during inkjet printing. In 1984, Fromm²³ obtained an approximate solution for droplet dynamics during ejection using simplified derivatives of the Navier-Stokes equations including Reynolds number. Reynolds number is a dimensionless value that represents the ratio between inertial and viscous forces present within a liquid system as seen in Equation (2.2).

$$Re = \frac{\text{inertial forces}}{\text{viscous forces}} = \frac{\rho d V}{\eta} \quad (2.2)$$

where ρ is density, d is characteristic length, V is velocity and η is viscosity.

The second Navier-Stokes derivative used to analyse droplet dynamics is Webers number, the ratio between a fluid's inertial forces to surface tension. The variables required to solve this dimensionless value are displayed in Equation (2.3).

$$We = \frac{\text{inertial forces}}{\text{surface tension}} = \frac{\rho d V^2}{\sigma} \quad (2.3)$$

where σ is surface tension.

Both derivatives are used to predict a fluid's suitability for inkjet printing applications. The ratio between the Reynolds number, Re , and a square root of the Weber number, We , is used to derive the inverse Ohnesorge number, Oh^{-1} , as seen in Equation (2.4). This value is often referred to as Z , a dimensionless parameter independent of fluid velocity.

$$Z = Oh^{-1} = \frac{\sqrt{\rho d \sigma}}{\eta} \quad (2.4)$$

A fluid with an inverse Ohnesorge Number, Z , in the range $1 \leq Z \leq 10$ is predicted to be suitable for inkjet printing according to work by Reis and Derby²⁴. The aim of their work was to investigate the influence of material properties on inkjet behaviour for particulate suspensions by using computational fluid dynamics modelling supplemented by parallel in-situ experiments. The lower Z boundary was defined by the dissipation of outward propulsion from the nozzle whilst upper boundary conditions were defined by the presence of satellite droplets after ejection as seen by Figure 2.5.

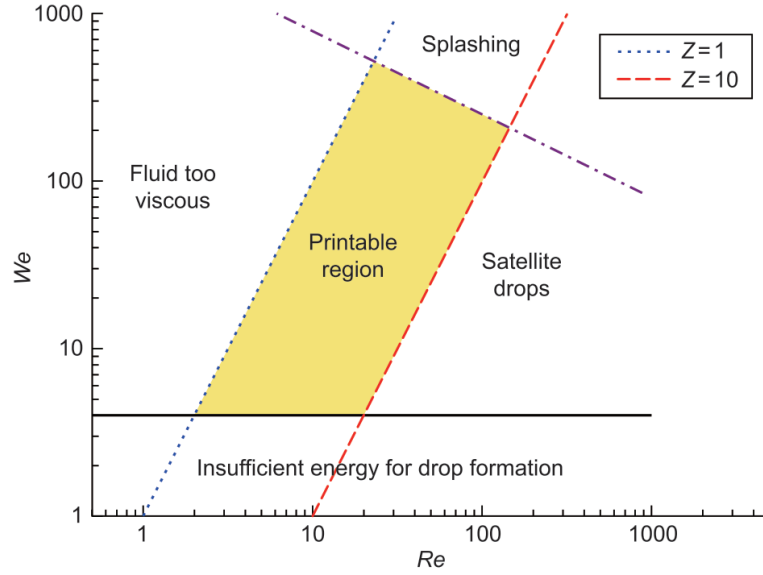


Figure 2.5: Representation of the printable region $1 \leq Z \leq 10$ where fluid properties are optimal for droplet formation.²⁵

Nearly a decade later, research conducted by Jang *et al.*²⁶ concluded that a more appropriate printing range is $4 \leq Z \leq 14$. An in-situ experiment was conducted for a range of inks containing varying concentrations of ethylene glycol and thus a range of Z values. Droplet formation dynamics were monitored for each ink resulting in a collection printing parameter data which included single droplet formability, positional accuracy and maximum allowable jetting frequency characteristics. Thus, the Z parameter range was redefine based on purely experimental data.

However, by comparing the properties of the materials investigated in each study, data obtained by Jang *et al.*²⁶ is more relevant to the scope of the project. Ethylene glycol has a similar composition to butanediol, where both materials contain hydroxyl function groups and a polymer chain composed of repeating $-\text{CH}_2$ monomers whilst the particulate suspension investigated by Reis and Derby²⁴ is less comparable to butanediol.

Although the Z parameter is indicative of printing viability, it is worth noting some materials are exempt from this rule such as water. Therefore, Z parameter measurements should not be relied on solely to determine a material's printability but rather used as a tool to guide ink selection.

2.1.3 Droplet Formation

As discussed in Section 2.1.2, droplet formation and behaviour is governed primarily by the rheological properties of an ink. The energy applied to an ink must be enough to overcome the resistive forces present in the system. A liquid with high surface tension will resist motion more effectively than one with lower surface tension due to intermolecular forces which bind a liquid to itself and any surface it makes contact with. Thus, resistance to motion of an ink is caused by friction between the liquid and inner walls of the nozzle chamber and the individual molecules within the ink. By applying the conservation of energy to a simple inkjet system, the minimum energy required to generate a droplet of ink can be estimated using Equation (2.5).

$$E_{imparted} = E_{loss} + E_{surface} + E_{kinetics} \quad (2.5)$$

where $E_{imparted}$ is energy applied to droplet, E_{loss} is energy lost during droplet motion, $E_{surface}$ is surface energy of the droplet and $E_{kinetics}$ is kinetic energy of the droplet.

Therefore, any ink droplet that forms successfully will have an imparted energy, $E_{imparted}$, greater than or equal to the total energy lost in the system during ejection. So, if the net energy present within an inkjet system is negative, the ink will struggle to push outward beyond the orifice and separate from the nozzle completely to form a droplet. Thus, the propulsive energy produced by pressure exerted onto the nozzle chamber is tailored so as to overcome the losses of energy due to resistive forces present in the system. By adjusting the voltage waveform applied to a PDOD printhead, the pressure exerted by the piezoelectric device can be optimised to form ideal droplets. A time-lapse of ideal droplet formation can be seen in Figure 2.6.

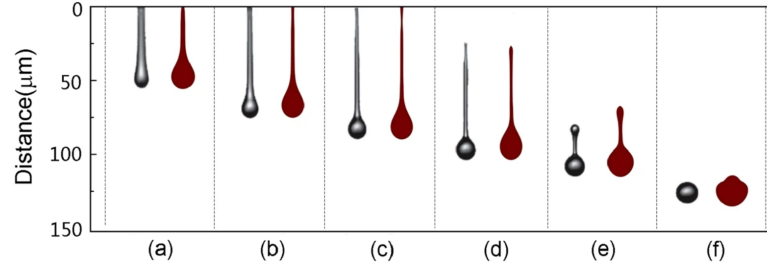


Figure 2.6: Droplet formation for experimental results (black droplets) at (a) $9 \mu s$, (b) $15 \mu s$, (c) $21 \mu s$, (d) $27 \mu s$, (e) $33 \mu s$, (f) $42 \mu s$ and simulation results (red droplets) at (a) $8.9 \mu s$, (b) $14.9 \mu s$, (c) $21 \mu s$, (d) $27 \mu s$, (e) $34.3 \mu s$, (f) $43.4 \mu s$.²⁷

If too much energy is imparted onto a droplet undesirable characteristics may develop, including a high impact velocity which may lead to ink splatter or substrate displacement in the case of powder beds. Additionally, the droplet may become segmented due to ligament instability, forming two distinct droplets - the primary and a satellite - as seen in Figure 2.7.

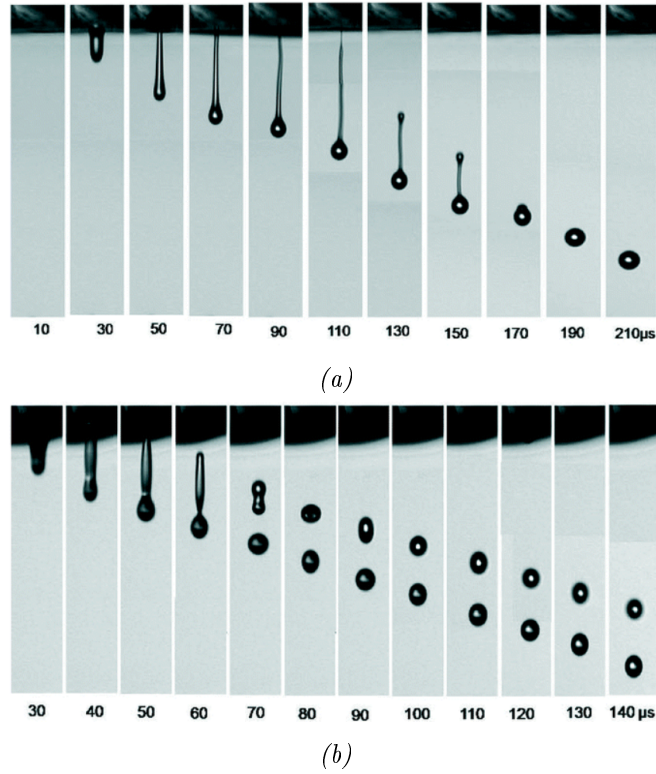


Figure 2.7: Satellite droplet formation at (a) $Z = 3.57$ where partial separation occurs before joining primary droplet and (b) $Z = 17.32$ where complete separation occurs.²⁸

This phenomenon occurs when the surface tension of an ink is not sufficient to cause complete collapse of the droplet ligament after ejection. Typically, a separated satellite droplet will trail behind the primary droplet at a slower vertical speed²⁷ as seen in

Figure 2.7b by the increase in separation over time. However, it is possible for a satellite to rejoin the primary droplet during flight given enough time before impact as seen in Figure 2.7a. For DOD printing, it is normal to print with a stand-off distance of 1-3 mm between the printhead and substrate.²⁵ It is worth noting this distance may be larger for powder bed substrates which have potential to displace particles which can clog printhead nozzles if too close.

2.2 Ink-Based Powder Additive Manufacturing (AM)

With reference to Figure 1.1, there are two established families of powder-based additive manufacturing (AM) techniques - Powder Bed Fusion (PBF) and Binder Jet (BJ) printing. Within PBF printing, consolidation is achieved either via energy-absorbing inks, lasers or electron beams. For the purposes of this project, only PBF methods which deposit energy-absorbing inks were considered, thus omitting methods which apply lasers or electron beams. Such ink-based PBF techniques include Multi Jet Fusion (MJF), High Speed Sintering (HSS) and Selective Mask Sintering (SMS) which are discussed later in Section 2.2.2.1.

Whereas BJ printing applies a liquid bonding agent which is selectively deposited to join powder materials, according to International Organization for Standardization (ISO) 17296.²⁹ The liquid bonding agent is often referred to as a binder ink due to its ability to consolidate powder. Similar to ink-based PBF printing, BJ printers also utilise inkjet printing to deposit liquid binder onto a powder bed substrate, generating a 'green' part which often undergoes post-processing techniques to increase part density and dimensional accuracy. This is discussed further in Section 2.2.2.2. However, it should be noted that polymers have rarely been studied as a material for BJ printing compared to ceramics and metals, likely due relatively poor mechanical properties and high porosities.³⁰

The BJ techniques offers several advantages, including high throughput as demonstrated by Bai and Williams³¹ with a 100-nozzle printhead manufacturing parts at up to 200 cm³ min⁻¹. BJ does not face the same challenges around residual stresses, warping, and shrinkage commonly observed in laser-based powder AM parts.^{31,32}

Despite applying fundamentally different consolidation methods, both BJ and ink-based PBF techniques share similar challenges to do with powder layer recoating, ink deposition reliability and recycling unconsolidated powder. Both printing techniques rely on the capabilities of inkjet printing to deposit binder onto a powder bed substrate, thus both ink formulations are subject to the same hardware limitations.

2.2.1 Powder Recoating

The handling and delivery of powder plays an important role in print quality, including geometrical accuracy and mechanical properties, as well as processing time for powder AM processes.³³ Thus, to achieve functional AM parts from powder feedstock, printers must be capable of achieving repeatable, uniform layer thicknesses. The powder material makes up the bulk of powder AM parts, however these processes are unique in that the powder bed provides build support during layer-by-layer printing thus increasing design freedom while reducing excess material usage. Depending on the powder-based technology, particles sizes of commercial powders will typically range from 10-150 μm in diameter.³⁴ The powder delivery system requirements according to Gibson *et al.*³ are outlined below:

- i Ensure enough powder in reservoir to achieve maximum build height.
- ii Transport the correct volume of powder from reservoir to build platform.
- iii Minimise shear forces during spreading to avoid damaging the previously layer.
- iv Ensure powder flows smoothly with minimal clumping.

To produce high quality parts, it is essential for powder handling equipment to be accurately calibrated to ensure the powder layer thickness inputted by the user is achieved as desired. The powder delivery system must be capable of executing the relevant commands to both raise the powder reservoir and lower the build platform to appropriate heights. Precision ensures the required volume of powder is carefully transported from the reservoir during spreading without damaging the previously processed layer above the build platform. Therefore, it is important to process powder with appropriate flow properties to ensure the layer height is both accurate and consistent across the build platform.

2.2.1.1 Spreading Mechanisms

To evenly distribute powder across a build platform to form a new powder layer, a spreading mechanism is applied for all powder-based AM techniques. Rollers or blades are the most commonly used mechanisms, in particular the counter-rotating roller and doctor blade shown in Figure 2.8.

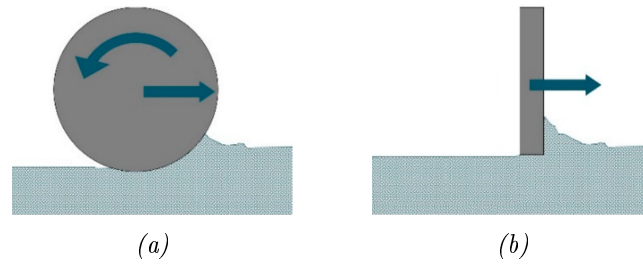


Figure 2.8: Spreading mechanics for the (a) counter-rotating roller and (b) doctor blade (adapted from Beitz et al. ³⁵).

During forward lateral motion, the counter-rotating roller (Figure 2.8a) displaces powder from underneath the mechanism to the front. The bulk powder becomes fluidised during this process due to the counter-clockwise rotation of the roller. This approach tends to increase powder flowability, resulting in more uniform powder layers during spreading.³⁵ A doctor blade (Figure 2.8b) scrapes powder from the reservoir to the build platform. Due to applied shear forces, doctor blades tend to compress rather than fluidise the powder, leading to more densely packed powder layers.

2.2.1.2 Packing Density of Powder Bed

The bulk rheological properties, such as particle size distribution (PSD) and surface morphology, impact the spreadability of a given powder. An ideal powder for AM, should flow freely to achieve a uniform layer thickness and packing density, thus minimising potential part defects following post-processing. Bai *et al.*³⁶ found coarse powders were most suitable for spreading and packing but led to poor part densitification after sintering. Whereas finer particles sintered more effectively. However, fine powders are found to have low flowability, leading to agglomerations and poor packing.

Powder can also be treated with flow additives to improve both the spreading behaviour and functionality of processed parts. Clayton *et al.*³⁷ found polyoxymethylene

powder containing additives led to more efficient part densities, indicated by a high Basic Flowability Energy (BFE), compared to pure polyoxymethylene powder. However, the additives used in the research were not disclosed so the validity of this data is uncertain. Further information about the characterisation of bulk powder flowability is discussed in Section 3.2.3.1.

Drummer *et al.*³⁸ investigated the impact of recoat speed on powder bed packing density, concluding that an increased speed led to higher part density due to the compressive forces applied during spreading. Thus, highlighting the impact of powder properties and print parameters on powder bed packing and part densities.

2.2.1.3 Effect of Particle Sizes

Using fine particles elicits thinner print layers, thus diminishing the stair staircase effect³⁹, as well as smoother surfaces due to decreased peak-to-valley ranges on the powder bed surface.^{36,40} However, finer particles of $< 20 \mu\text{m}$ is not typically used due to poor flowability and efficient layer recoating.⁴¹

Clares *et al.*⁴² demonstrated that bimodal size distributions led to a 20% increase in density and 170% increase in ultimate flexural strength when compared to the highest performing unimodal powder groups. Powder bed packing density significantly impacts part performance, whereby low densities tend to produce parts with poor mechanical strength.⁴³ However, powders with irregular shapes tend to have higher mechanical interlocking properties, causing challenges during powder spreading.⁴⁴ Thus, the challenge is to achieve highly packing densities with powders that are able to flow freely during the recoating process.

2.2.2 Powder Consolidation Mechanisms

Existing commercial powder AM printers typically apply one of four consolidation methods as outlined in Figure 2.9.

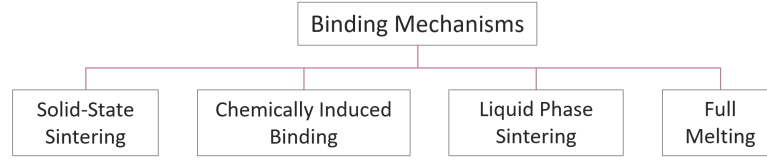


Figure 2.9: Four distinct classifications of powder binding mechanisms (adapted from Kruth et al.⁴⁵).

The most common is solid-state sintering whereby the surface of each particle melts coalescing into a solid part without full melting. To selectively consolidate polymer powder particles, the powder must reach a temperature between $\frac{1}{2} T_{\text{m absolute}} - T_{\text{m absolute}}$ ⁴⁵, thus limiting the range of printable materials, particularly composite powders with variable thermal sensitivities. Whereas, chemically induced binding techniques offer a low temperature alternative for powder consolidation. Existing polymer consolidation techniques which utilise radiation-absorbing materials and binder solutions to achieve powder consolidate are discussed in Sections 2.2.2.1 and 2.2.2.2, respectively.

2.2.2.1 Energy-Absorbing Inks

High Speed Sintering (HSS) is a powder AM process developed at Loughborough University by Hopkinson and Erasenthiran⁴⁶ which employs inkjet printing to selectively deposit specially formulated ink onto a bed of powder. However, specialised HSS inks do not immediately consolidate particles but rather act to transfer energy from a lamp that emits infrared radiation (IR) with wavelengths between $0.78 \mu\text{m} \geq \lambda \leq 1000 \mu\text{m}$. The IR lamp is swept across the powder bed, causing only the particles coated in specially formulated ink to absorb the minimum energy required to sinter.⁴⁷ A diagram of the HSS setup can be found in Figure 2.10a.

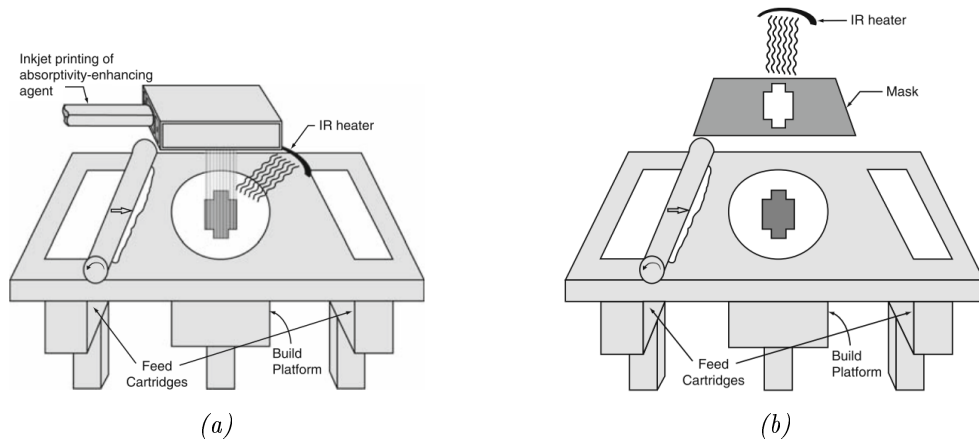


Figure 2.10: Schematics for two sintering processes including (a) High Speed Sintering (HSS) and (b) Selective Mask Sintering (SMS).³

The specially formulated ink applied in HSS was developed whilst using Selective Mask Sintering (SMS) technology (Figure 2.10b) to investigate the effects of IR absorption-enhancing materials, such as carbon black. In 2005, Thomas *et al.*⁴⁸ investigated the effects of 2 wt % carbon black on a bed of polyamide 12 (PA12) powder as carbon had been known to increase the rate of sintering. Due to carbon's ability to quickly absorb and transfer energy emitted from the IR lamp to the surrounding PA12 particles, entire layers were found to be processed within 5 seconds.⁴⁹ This work led to the development of Radiation Absorbing Material (RAM), specially formulated ink which could be selectively deposited onto powder before exposing the build platform to IR radiation.

Energy absorbed by RAM causes the surface of powder particles coated in the ink to melt, causing only RAM-coated particles to fuse. However, this process is susceptible to partial sintering of uncoated particles due to thermal radiation emitted from both the adjacent RAM-coated particles and the IR lamp. Therefore, particles located at the boundary between coated and uncoated powder and at the powder bed walls will likely absorb more radiation than the rest of the uncoated powder. This may lead to rough surface features and poor dimensional accuracy of the printed parts.

Another polymer powder AM process which uses IR radiation to bind particles is the HP MJF printer. This technique employs a fusing agent which activates upon contact with IR radiation later emitted by a lamp. Although similar to HSS and SMS technology, MJF deposits two additional inks - detailing and transforming agents - which

significantly increases part versatility. The printing process for the HP MJF printer is outlined in Figure 2.11.

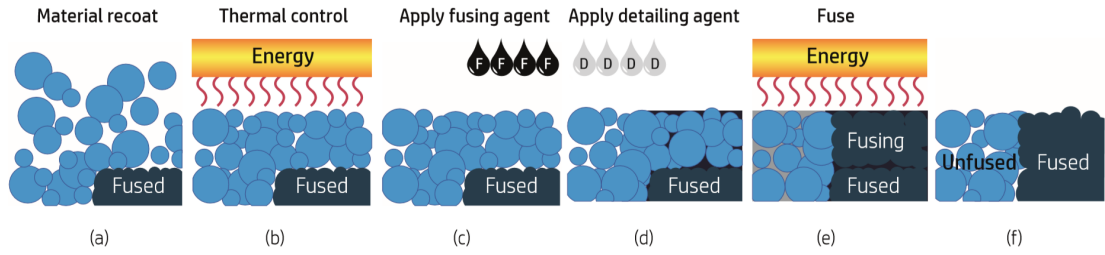


Figure 2.11: Step-by-step printing process for the HP Multi Jet Fusion (MJF) printer.⁵⁰⁾

The detailing agent is typically deposited around the contours of the desired part geometry to inhibit heat transfer in those regions, preventing selected powder particles from sintering in the presence of IR light.⁵⁰ These patented ink formulations contain 1 - 3 wt% of colourant incapable of absorbing wavelengths between 650 - 2500 nm.⁵¹ By selectively depositing these inks onto the powder bed before applying the fusing agent, a barrier is created against unwanted spreading of the fusing agent during both initial deposition and subsequent sintering processes. Resulting surface finishes, or roughness (R_a), for PA12 have been reported in the range of $2.54 \mu\text{m} \geq R_a \leq 10.29 \mu\text{m}$.⁵²

The transforming agent is a unique feature that enables the user to control the interaction between fusing and detailing agents as well as modify the properties of consolidated powder.⁵³ The HP MJF printer utilises a multiple-inkjet system, capable of producing functionally-graded parts due to the range of transforming agents that HP have made commercially available. By utilising these transforming agents, HP claims MJF printers can control the following part properties:

- i Surface roughness including texture and friction coefficient.
- ii Tensile strength, flexibility and hardness.
- iii Electrical and thermal conductivity.
- iv Opacity or translucency.
- v Colour, both embedded and at the surface.

Contrary to most AM inkjet printers, the MJF printer uses thermal inkjet technology whereby inks are heated to their boiling point to generate internal bubbles that lead to droplet ejection.¹⁶ Thus, the range of suitable ink materials for MJF printers is more

limited, particularly for volatile or thermally sensitive materials, compared to the more commonly used piezoelectric printheads.

2.2.2.2 Binder Inks

Binder Jet (BJ) printing employs special inks called binders to selectively bind powder particles together. Conventionally, binder inks would be used to temporarily form 'green' parts with low relative density. Typically, 'green' parts are fragile with poor mechanical properties, thus further processing at temperatures high enough to elicit powder sintering is typically performed.

Binders most commonly used are primarily composed of polymers designed to burnout of the 'green' part during post-processing via sintering.⁵⁴ However, due to the brittle nature of 'green' ceramic BJ parts, the risk of cracking is highest during sintering due to the low decomposition temperatures of the polymer binder and the high sintering temperature of ceramic, leading to the binder burning out before the ceramic powders have fully consolidated.⁵⁵ Further information about 'green' parts is covered in the Section 2.2.2.3.

Bai and Williams⁵⁶ introduced nanoparticle suspensions as an alternative to conventional polymeric binders for metal powder consolidation. In this approach, deposited nanoparticles were sintered at a low temperature via a heated powder bed to provide strength to the printed 'green' part before removal.

Recent work by Oropeza and Hart⁵⁷ introduced a thermally reactive binder that would withstand thermal heating for longer before decomposing, providing support to the ceramic 'green' part during sintering for much longer. Additionally, the binder residue was designed to enhance the mechanical properties of the final sintered part. The inspiration behind this mechanism, stemmed from the challenge within BJ around binder decomposition temperatures being lower than the sintering thresholds of the bulk powder. Thus, the structural support of traditional polymer binders during sintering of ceramic powders is limited given the binder decomposes before the ceramic powder begins to sinter.

No prior research could be found which explored polymeric dual-ink chemically reactive

binders which remained in-situ, forming a composite 'green' part that did not require sintering. Thus, further highlighting the novelty of the research contained within this thesis. However, chemically reactive inks for material jet (MJ) printing has been explored previously and has been discussed further in Section 2.3.2.3.

2.2.2.3 'Green' Part Sintering

Densities of 'green' state parts vary drastically depending on the powder and binder materials. Existing literature has reported 'green' part densities between 40 % - 85.5 % for metal BJ printed parts prior to furnace sintering.^{3,31,58,59} Generally, 'green' parts are more fragile at lower saturation levels and require extra care during post-processes such as debinding and sintering.⁵⁶

Before 'green' parts are sintered, loose powder is removed from all accessible surfaces and cavities. Often pressurised air or water is used to remove unbound particles. It is at this stage the part is most prone to failure due to the low binding strength of the binder ink. Additionally, defects which develop during the printing process reduce the integrity of the 'green' part.⁶⁰ It is only after the sintering process, during which densification occurs, that the effects of internal defects are mitigated.

During furnace sintering, the residual binder material burns off, leaving the powder particles to undergo liquid-phase sintering. The remaining powder binds together, increasing the part density, structural stability and strength of the BJ printed part. Typically, the sintering process leads to part shrinkages in the region of 15 - 20 % for metal BJ printed parts.⁵⁵

More recently, Hot Isostatic Pressing (HIP) has been investigated as an alternative densification technique whereby high pressures are uniformly applied to the 'green' part at high temperatures. HIP has been found to lead to higher part densification and geometric accuracy compared to traditional furnace sintering. Kumar *et al.*⁶¹ stated a 'green' part composed of copper powder with a mean bulk density of 55 % reached a final part density of 99.7 % after applying both traditional furnace sintering and HIP. Additionally, anisotropic shrinkage between 16-20 % was observed following the two-stage sintering technique.

2.2.3 Ink Infiltration Mechanics

When an ink droplet impacts a powder bed substrate, the particles that make contact with the ink tend to either shift under the droplet or be ejected from the bed entirely.²⁷ This depends on several factors including the packing density of the powder, any inter-particle forces at play and the size of individual particles. Parab *et al.*²⁷ postulated that the major mechanisms for powder bed disturbance in spherical (free flowing) and irregular (cohesive) particles were impact cratering and powder bed compression, respectively.

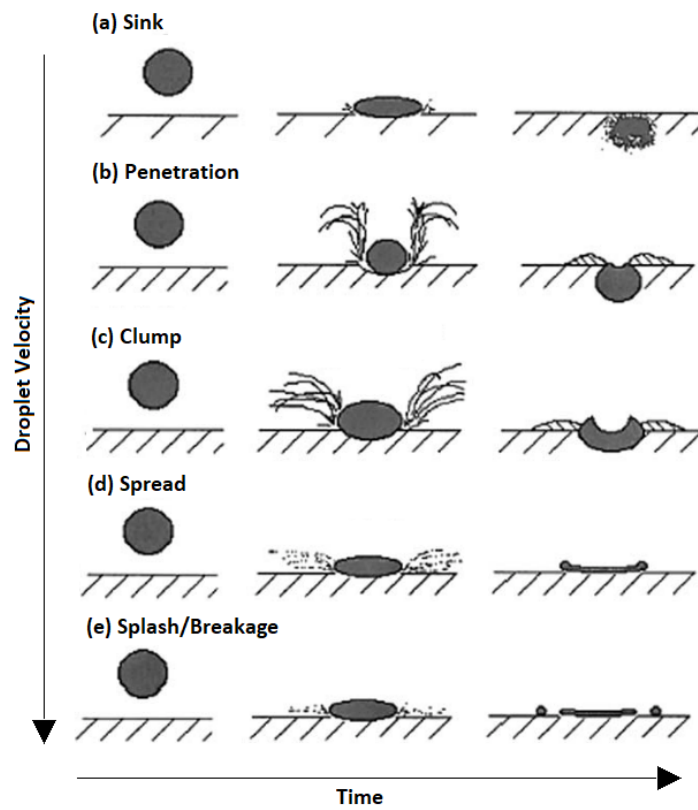


Figure 2.12: Droplet impact outcomes for powder bed substrates at increasing drop velocities (adapted from Qiao *et al.*⁶²).

Additionally, droplet velocity plays a critical role in ink-powder dynamics, including how ink spreads and penetrates into the powder bed as shown in Figure 2.12. Thus, highlighting the importance of optimising ink deposition parameters to minimise the formation of part defects caused by impact velocity during printing. Finally, ink-powder behaviours are also attributed to the rheological properties of the bulk powder which are directly influenced by the shape and size of the individual particles.

2.2.3.1 Ink Spreading on Powder Substrate

Upon deposition onto a powder bed substrate, ink will spread outward along the x and y axes before receding as the ink penetrates the powder bed in the z direction. The spreading and infiltration properties of a low-viscosity aqueous polymer onto porous ceramic powder beds with particles ranging in size between 0.3-1.70 μm and mean pore sizes between 0.07-0.53 μm was investigated by Holman *et al.*⁶³. Prior to impact droplets were found to be travelling at 4 m s^{-1} with an average diameter of 54 μm . The theoretical maximum spreading of the droplets was then predicted using Equation (2.6).

$$r_e = \left(\frac{3V \sin^3 \theta}{\pi (1 - \cos \theta)^2 (2 + \cos \theta)} \right)^{\frac{1}{3}} \quad (2.6)$$

where r_e is equilibrium spreading radius, V is droplet volume and θ is equilibrium contact angle.

The experimental data obtained by Holman *et al.*⁶³ supports a linear relationship between maximum droplet spreading behaviour and initial droplet diameter as seen in Figure 2.13. This extrapolation can be used to predict the maximum spreading that will occur for droplets with initial diameter in the range of 20-80 μm . Therefore, this tool can be used for theoretical optimisation of droplet volumes for a range of powder-based processes.

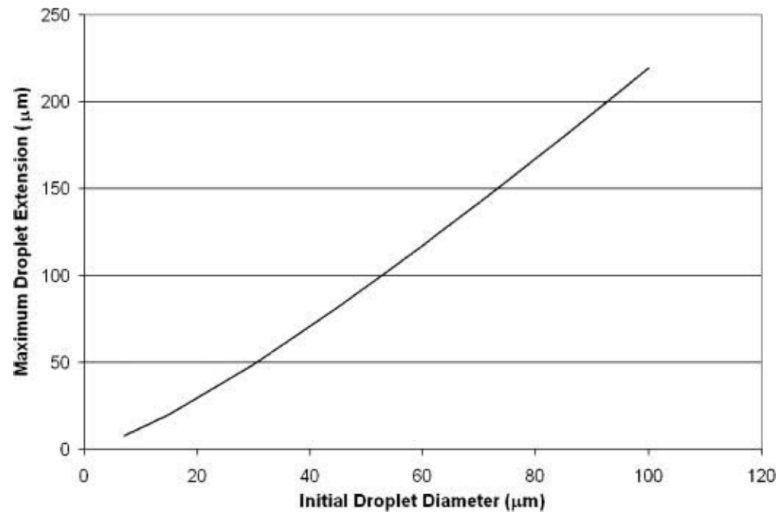


Figure 2.13: Relationship between ink droplet diameter before impact with the substrate and maximum droplet spreading diameter after impact.⁶³

Inks which spread outward beyond the desired print geometry may result in poor part resolutions. However, spreading cannot be managed by adjusting the printing parameters, thus undesired spreading can be controlled by applying a detailing agent along the print boundaries. As previously discussed in Section 2.2.2.1, detailing agents promote a high part resolution but limit the recyclability of unused powder due to contamination. The depth of downward ink penetration influences the adhesion between print layers thus insufficient layer saturation may lead to part delamination during shearing. Penetration depends on both the rheological properties of the ink and mean pore diameter of the powder bed.

2.2.3.2 Ink Saturation of Powder

Ink-based powder AM processes must balance both ink deposition volume and powder layer thickness and packing density to achieve optimum saturation levels for a given ink-powder system. For BJ printed parts, as saturation levels rise, 'green' part densities increase, however so does the risk of print layer warping or distortion. Zhang *et al.*⁶⁴ observed a gradual reduction in the degree of curling in BJ printed parts composed of silk powder as powder layer thickness increased from 0.1 mm to 0.2 mm as shown in Figure 2.14.

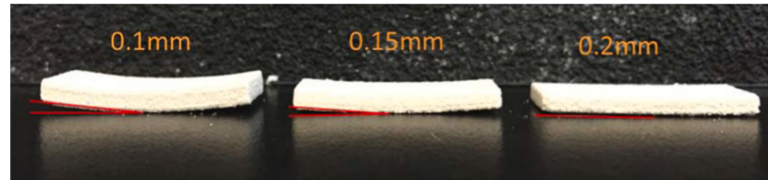


Figure 2.14: Warping in single print layer 'green' parts at powder layer thicknesses 0.1 mm, 0.15 mm and 0.2 mm..⁶⁴

Riechmann *et al.*⁶⁵ investigated the relationship between saturation level and tensile strength of BJ printed parts. This work identified a linear relationship existed for BJ printed parts composed of commercially available polymer powder and binder ink. However, the authored observed that for parts which exceeded saturation equilibrium, tensile strength plateaued at 19 MPa and bleeding increased, thus reducing the geometry accuracy of oversaturated parts. Vaezi and Chua⁶⁶ observed a similar trend, whereby increasing part saturation led to increased tensile strength. However, the flexural strength and surface quality of the parts decreased as saturation increased.

Separately, Crane⁶⁷ found the geometric accuracy of metal BJ printed parts increased as binder ink drying time decreased, thus reducing the window in which the binder ink could bleed. This was tested by comparing both single (1 mm) and multi-layer (5 mm) printed parts under two conditions - heated between print layers and unheated. Figure 2.15 below highlights the impact reduced bleeding has on part geometry.



Figure 2.15: Comparison of geometric accuracies for unheated and heated BJ parts composed of single (1 mm) and multiple (5 mm) layers.⁶⁷

Equation 2.7 can be used to estimate the saturation level of a given binder ink in a bed of powder.⁶⁸

$$S = \frac{V_{binder}}{V_{air}} = \frac{V_{binder}}{(1 - PR)V_{solid}} \quad (2.7)$$

where S is binder saturation and V_{binder} , V_{air} and V_{solid} are the volume fractions of binder, air and powder, respectively.

Miyanaji *et al.*⁶⁹ investigated an alternative approach based on capillarity to determine the equilibrium saturation for a given binder-powder system. The model presented is predicated on the assumption that binder ink infiltration will stop when a balance of capillary pressures is achieved.

Overall, balancing both ink deposition volume and powder layer thickness and packing density to achieve optimum saturation levels for a given ink-powder system is critical for part performance.

2.2.3.3 Recyclability of Processed Powder

For powder AM processes, unconsolidated powder is often recycled for future use, especially for metals which tend to have a higher associated cost compared to ceramic and polymer powder alternatives. The exposure to excessive binder splashing and the tendency for binder to migrate out of the desired print area limits the amount of powder that can be used following BJ printing.^{27,70}

Measures are often taken to ensure maximum recovery of powders throughout the manufacturing process, including the removal of loose powders from orifices and internal chambers during post-processing.⁷¹ However, these processes are found to be inefficient, unreliable and heavily reliant on specialised technical personnel.⁷² Other common challenges associated with powder AM processes, include ineffective removal of loose, unused powder from complex parts, binder contamination and thermal ageing, all of which either reduce powder recover rates or compromise integrity of the powder itself.

The intrinsic properties of polymers alter when processed at temperatures near to the material's crystalline melting point.⁷³ Thus, recyclability of polymer powders is limited when processed at temperatures near their melting points due thermal degradation, or powder ageing, compromising the quality and strength of final parts. A powder AM technique where recyclability is a major concern is Selective Laser Sintering (SLS) whereby powder temperature is maintained at just below the sintering temperature between 180-380 °C throughout the printing process.⁷⁴

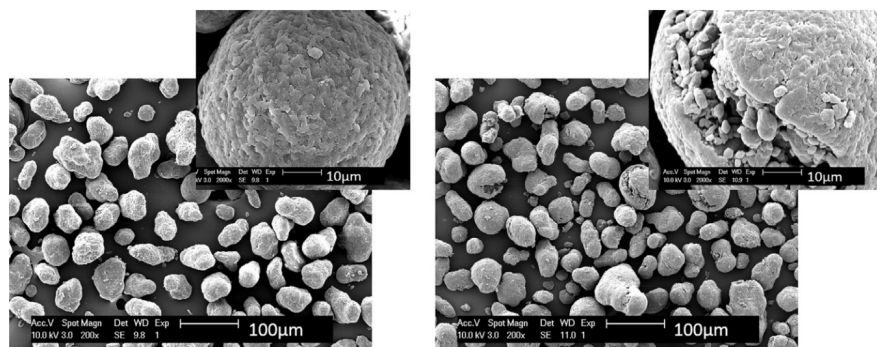


Figure 2.16: SEM image of (a) virgin and (b) aged polyamide 12 (PA12) powders used for Selective Laser Sintering (SLS) processes.⁷⁵

The primary characteristics of aged powder include increased particle cracking and a

reduction in bulk flow of the powder as shown in Figure 2.16. This often leads to spreading difficulties when applying new powder layers, resulting in parts with a rough surface finish similar to orange peel.⁷⁵ Therefore, it is not always beneficial to recover polymer particles that have been repeatedly processed due to the negative effects of thermal degradation, or ageing.

Overall, there is a clear gap in the polymer powder AM space to develop low temperature consolidation processes which minimise thermal degradation and maximise recyclability potential.

2.3 Polyurethane

In 1849, the first urethane was synthesized by Charles-Adolphe Wurtz.⁷⁶ However, Otto Bayer was the first to record the production of polyurethane (PU) in 1937 following the development of the polyisocyanate-polyaddition process.⁷⁷ Initial PU was developed as an alternative to elastic rubber. However, due to the versatility of PU, other materials, such as woven fibres and metal, were also replaced.⁷⁸ Further information about the widespread applications of PU has been outlined in Section 2.3.1.3

By the 1950s, PU synthesis had reached an industrial scale and foam applications had been firmly established within the market, growing steadily until the 1990s.⁷⁹ Throughout the 2000s, manufactures adopted low-emission materials and processes for foam production, including the use of double metal cyanide instead of potassium hydroxide.⁸⁰ By 2011, Asia Pacific accounted for 40.4 % of the total PU market, followed by Europe and North America.⁷⁹

In 2016, PU was ranked 6th among all polymers with a global production of 18 tonnes, demonstrating a strong, established market demand for PU products.⁶ Recent reports, valued the global PU market at \$ 103.08 billion in 2024 and estimated to have a compound annual growth rate (CAGR) of 13.5 % up to 2033.^{81,82}

2.3.1 Chemistry of Polyurethane

Fundamentally, PU is composed of a chain of co-polymer blocks formed from alternating molecules of isocyanates and alcohols. A urethane linkage forms when an available

[–OH] group binds to an [–NCO] group. The process of polymerisation repeats, lengthening the chain of co-polymer blocks to form a chain of repeating urethane linkages, or PU. For full polymerisation to occur between reactive PU components, optimum stoichiometry should be achieved. According to Gogoi *et al.*⁸³ this is 1.2 : 1 for isocyanate to hydroxyl groups, respectively.

Polymerisation is a process by which polymers composed of macromolecules form through reactions between monomers or a mixture of monomers.⁸⁴ Addition polymerisation occurs when a polymer chain lengthens exclusively via reactions between the monomers and reactive sites on the polymer chain, regenerating reactive sites at the end of each growth step.⁸⁴ Thus, individual monomers link to form PU without generating by-products during synthesis.

2.3.1.1 Molecular Structure of Polyurethanes

Polyurethane (PU) versatility is attributed to the molecular structure which consist of co-polymer blocks composed of alternating ‘soft’ and ‘hard’ segments. Fundamentally, PU is composed of organic methylene chain units (–CH₂–) separated by repeating urethane linkages (–NHCOO–). Thus, to form long PU chains, there must be two or more available functional groups on each of the core components. The simplest mechanism would be a reaction between a diisocyanate molecule which contains two or more isocyanate (ISO) groups (–NCO) and a diol molecule containing two or more hydroxyl groups (–OH) as summarised in Figure 2.17.

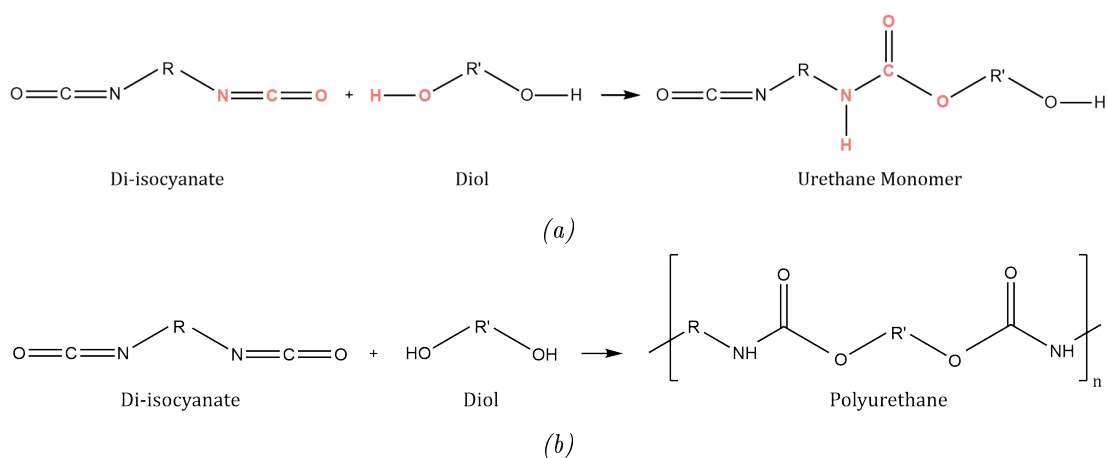


Figure 2.17: Chemical reaction (a) between single di-isocyanate and hydroxyl molecules with functional groups highlighted in red and (b) for repeating urethane units to form polyurethane (PU).

By swapping out the individual segments with compatible alternatives, a range of physical and chemical properties can be elicited in the final part. PU versatility is further explored throughout Sections 2.3.1.2 and 2.3.1.3. Overall, it is possible to manufacture either rigid and flexible or thermoplastic and thermoset PUs. However, classification of PU materials is determined by the alcohol used during synthesis. Table 2.1 below summarises the general impact each component has on the properties of the final part.

Table 2.1: *Summary of common polyurethane (PU) components including their respective influences.*^{78,85}

Component	Influence
Isocyanate (ISO)	Increase reactivity.
Polyols	Elasticity or stiffness.
Catalysts	Speed up reaction times.
Pigments	Colour for identification or aesthetics.
Chain Extenders	Tensile strength and hardness.
Fillers	Improve stiffness and reduce costs.

2.3.1.2 Impact of Polyurethane (PU) Components on Part Properties

As introduced in Table 2.1, the ISO component of PU directly influences reactivity. ISO molecules can be categorised into two primary types - aliphatic and aromatic. With reference to their chemical structure, aliphatic ISO molecules are linear, open chains without a benzene ring whereas aromatic ISO molecules contain a cyclic benzene ring.

Common aromatic isocyanates including toluene diisocyanate (TDI), specifically isomers 2,4-TDI and 2,6-TDI, and methylene diphenyl diisocyanate (MDI), specifically the isomers 4,4'-MDI and 2,4'-MDI.⁸⁰ Due to the delocalised negative charge found in the benzene rings, aromatic ISO compounds are more reactive than aliphatic.⁸⁶

Common aliphatic isocyanates include hexamethylene diisocyanate (HDI), isophorone diisocyanate (IPDI) and will typically form thermoplastic polyurethane TPU due to linear, open carbon chains.^{80,87} Thermoplastic polymers, such as TPU, harden during cooling and melt under heat, unlike thermoset polymers which permanently deform under heating.

Polyol molecular weight (MW) is a critical factor influencing the properties of PU materials. Low MW polyols produce hard, rigid PUs with a high concentration of urethane groups, whereas high MW polyols (2000 - 10000 gmol^{-1}), with fewer hydroxyl groups and longer alkyl chains, produce softer, more flexible PUs.^{78,85,87,88}

Polyols are classified as either polyester or polyether and the exact type plays a significant role in the final properties of PU parts. Polyester polyols, known for their strong hydrogen bonding, contribute to higher tensile strength and hardness in PU products. However, they are often more viscous and expensive than polyether polyols.

Polyether polyols, such as polyethylene glycol (PEG), are commonly used as soft segments in PU block copolymers, enhancing flexibility and hydrolytic resistance. PEG typically ranges in MW between 1000-5000 gmol^{-1} ^{89,90}.

Chain extenders are low MW diols or diamines (400 gmol^{-1}), such as 1,4-butanediol (BD).⁸⁹ BD reacts with ISO molecules to form part of the 'hard' segment, thus tuning the mechanical properties of the final part.

Most PU reactions will occur in the presence of a catalyst, such as dibutyltin dilaurate (DBTL). Catalysts lower the activation energy required to break bonds and initiate the reaction. PU reactions are exothermic, meaning the energy absorbed to break bonds is less than the energy released to form new bonds, thus heat is transferred to the surrounding environment during synthesis. For the reaction in Figure 2.17b, the bond energies for C=N and C=O are 615 kJ mol^{-1} and 743 kJ mol^{-1} ⁹¹, respectively. As such, the C=N bond is easier to break during synthesis.

2.3.1.3 Applications and Properties

PU elastomers typically have good flexibility, resistance to abrasion, chemicals or heat, and high load-bearing potential.⁹²⁻⁹⁴ Owing to the versatility and low relative cost, PU has been widely applied across a wide range of industries including medical, building, automotive, sport, energy, nautical, defence, footwear, electronics, packaging and many more.⁹⁵⁻⁹⁷ Figure 2.18 provides a breakdown of the five primary applications categories for PU materials.

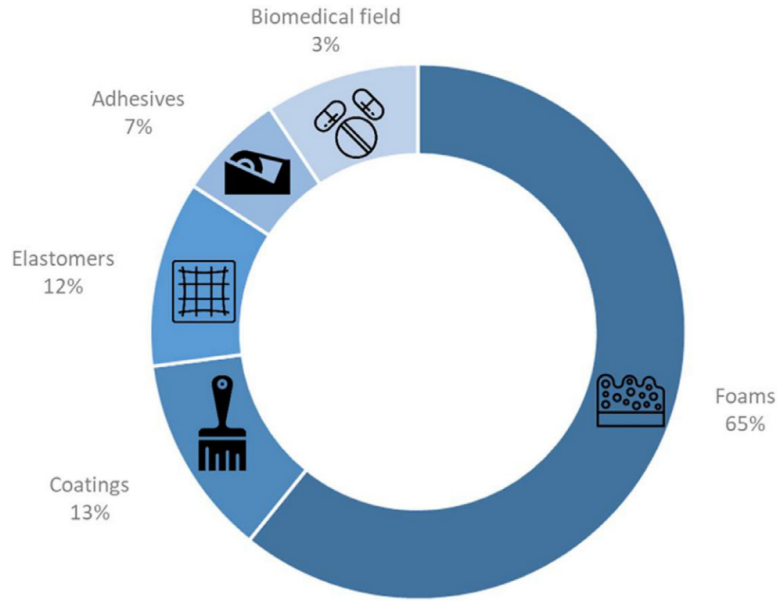


Figure 2.18: PU Market categorised into five application segments.⁸⁶

Foams make up the majority of PU applications at 65 % with the more common use case being insulation foams which exhibit low relative thermal conductivities values of less than $25 \times 10^{-3} \text{ Wm}^{-1} \text{ K}^{-1}$ ^{79,80} Table 2.2 provides a summary of common PU foam applications including tuned properties.

Table 2.2: List of common applications for polyurethane (PU) foams including their inherent properties (adapted from Oppon⁸⁵)

Applications	Properties
Cushioning	Density, flexibility, fatigue resistance.
Shoe Soles	Flexibility, abrasion resistance, strength, durability.
Building Panels	Thermal insulation, strength, lifetime.
Artificial Heart Valves	Flexibility, biostability.
Medical Implants	Toughness, biocompatibility, biodegradable.
Electronics	Electrical insulation, tough, oil resistance.

Foams are also used for applications in adsorption, water purification, piezo-resistive pressure sensors, templates for ceramic foam catalysts, soft body armours, tissue engineering scaffolds, sports equipment, self-healing materials, EMI shielding, and porous electrodes.^{96,98} The versatility, durability and elasticity of PU parts lend themselves well for Shape Memory Polymer (SMP) applications, whereby with an appropriate stimulus

a PU part will recover its original shape following large stains.⁹⁹

Additional PU applications commonly found within the building industry include textiles, lights, paints, furniture, adhesives and various coatings which overlap with the built environment.^{95,97} Whereas, within the medical industry PU is often used for biodegradable implants, drug delivery carriers, biocompatible scaffolds, synthetic skin and body fluid transport devices.^{96,97} Szarlej *et al.*¹⁰⁰ demonstrated how AM could be used to manufacture wound dressings from PU, delivering excellent flexibility and antibacterial properties.

Additionally, PU can be used to manufacture high-performance coatings excellent resistance to solar radiation, abrasion and corrosion.¹⁰¹ Typically aliphatic ISOs are used to produce superior weather resistance coating which elicit higher oxidative and ultraviolet stabilities, which their aromatic counterparts do not offer.⁸⁷

2.3.1.4 Sustainable Alternatives

Most of the polyols that are used in the production of PU foams are derived from petroleum feedstocks.⁷⁶ Market trends suggest a growing preference to use materials that have been derived from non-polluting resources, are recyclable or have a lower carbon impact.⁷⁶ The green and bio-polyols market is projected to be worth \$ 6.9 billion by 2027 with a CAGR of 9.5 %, between 2022 and 2027.¹⁰²

PU components which use fossil fuel-based feedstocks include EG and BD, however chemical companies have in recent years successfully synthesised bio-based versions of these materials that retain the same molecular structure and therefore same effects on final PU parts.⁸⁶ Alternative bio-based polyols that have been researched to date stem from renewable resources, such as biomass residues, vegetable oils, and industrial by-products, namely crude glycerol.^{76,103}

Isocyanates are commonly derived from a reaction of amine with highly toxic phosgene. As ISOs have been reported as a leading cause of occupational asthma worldwide and are suspected to be carcinogenic, efforts have been made to explore alternative synthesis routes.^{104–106}

Bio-based cyclic carbonates are a promising alternative to ISOs, capable of producing renewable non-isocyanate polyurethane (NIPU), such as polyhydroxyurethane.^{6,106,107} However, the low reactivity of bio-based polyhydroxyurethanes is a major limitation.¹⁰⁵ Further research to develop more efficient catalysts specialised to NIPU syntheses will reduce the negative impact. Finally, Sternberg and Pilla¹⁰⁸ introduced a protocol to manufacture highly sustainable PU containing 100 % bio-based carbon content using biomass as a feedstock for both the lignin precursor and curing agent.

2.3.2 Polyurethane Manufacturing Techniques

Conventional PU manufacturing methods involve moulds, high temperatures or solvents, all of which can reduce design freedom, sustainability and applications.¹⁰⁹ Whereas, AM techniques enable better material utilisation, cost savings, and customisation, further widening potential PU applications. For examples, Srivastava *et al.*¹¹⁰ observed a significant economic advantage (>50 %) in using AM over conventional techniques within the aerospace and automotive industry.

2.3.2.1 Conventional Methods

As discussed in Section 2.3.1.3, PU foams are the most commonly used format, totalling 65 % of the PU materials. According to Gama *et al.*⁷⁶, PU foam is conventionally manufacturing using the three methods outlined below:

- i **Moulding:** Reactive mixture is injected into a mould cavity.
- ii **Slabstock:** Reactive mixture is continuously poured into a moving conveyor.
- iii **Spraying:** Deposit liquid PU onto an external surface or within a cavity.

The most common conventional manufacturing technique is injection moulding (IM). A major disadvantage of using this technique is the high cost associated with tooling which reduces design freedoms and eliminates cost-effective customisation of parts. However, aside from the initial tooling costs, over its lifetime the cost per part drastically reduces due to the high volume output potential that IM offers.

2.3.2.2 Additive Manufacturing (AM) Methods

Marco *et al.*¹¹¹ demonstrated excellent performance in ultimate tensile strength (UTS)

and elongation at break (A%) for PU parts manufactured via Fused Deposition Modeling (FDM) and MJF techniques. The best performing parts exhibited an A% of 1162 % (± 2 %) and a UTS of 50 MPa (± 1.8 MPa). The significance of these results is demonstrated in Figure 2.19 which draws direct comparisons between three AM techniques - MJF, FDM, and SLS - and conventional manufacturing technique - IM.

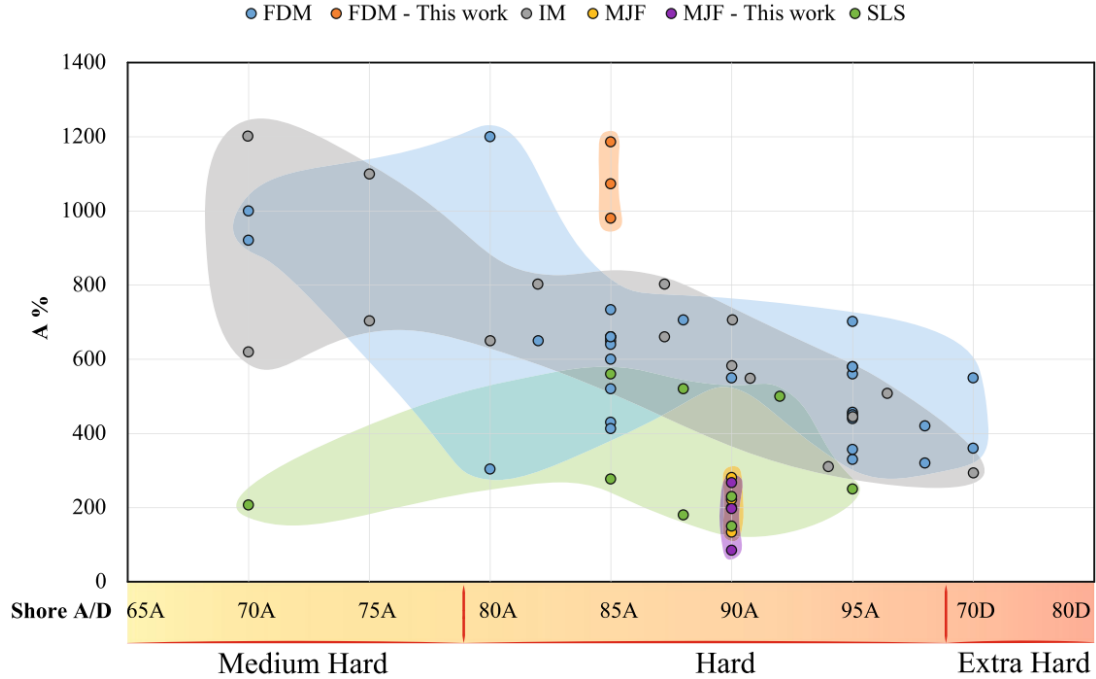


Figure 2.19: Elongation at break (A %) versus Shore hardness of different TPU materials manufactured via FDM, MJF, SLS and IM processes.¹¹¹

To date, material extrusion of TPU using FDM printers has been explored. For this AM process, TPU feedstock is heated to just below the melt point to enable malleability. Feedstock may come in the form of a solid filament^{112,113} or composite slurry¹¹⁴, both of which are extruded via a nozzle. PU parts formed via FDM are often ready to be used once removed from the build plate, requiring no further post-processing or heat treatment.

Ge *et al.*¹¹⁵ applied FDM printing to commercial TPU filament which was heated to 220 °C to print Kevin foam structures composed of repeating tetrakaidecahedral cells. This study found FDM printed TPU foams demonstrated similar resilience to deformation compared to rubber, a material that is 4x denser.

Separately, TPU-cork composites manufactured from a slurry via FDM printing demon-

strated a weight reduction of 21.3 % compared to pure TPU.¹¹³ However, with cork as a filler, maximum deformation and stress of the composite parts was reduced by 37.3 % and 53.5 %, respectively.

Additionally, Caracciolo *et al.*¹¹⁶ utilised MJF to manufacture biodegradable polyurethanes, demonstrating that flexural strength of the 'green' parts could be controlled using a thermally-activated crosslinked binder system.

Another AM technique known to manufacture PU is a form of VAT polymerisation called rapid projection polymerisation. Warner *et al.*¹⁰⁶ utilised the AM technique to print tunable NIPU parts composed of thiol crosslinkers.

2.3.2.3 Reactive Inkjet Printing

At present there is limited data available and no previous literature which addresses the interactions between ISO and DIOL inks on a powder substrate. However, data exists for similar PU reactions via inkjet printing but onto a flat, non-porous substrate. For example, Kröber *et al.*¹¹⁷ investigated the reactive inkjet printing of two separate inks, one containing IPDI and the other consisting of polypropylene glycol, a catalyst, and a cross-linking agent. The reaction conversion results found in Figure 2.20 were obtained from this experiment. For catalyst concentrations ranging from 0.1-2.0 wt%, PU conversions of 60-70 % were obtained after only three minutes. This data demonstrates how PU reactivity, or rate of reaction, changes over time, providing an indication of total reaction time to achieve full polymerisation, or PU conversion.

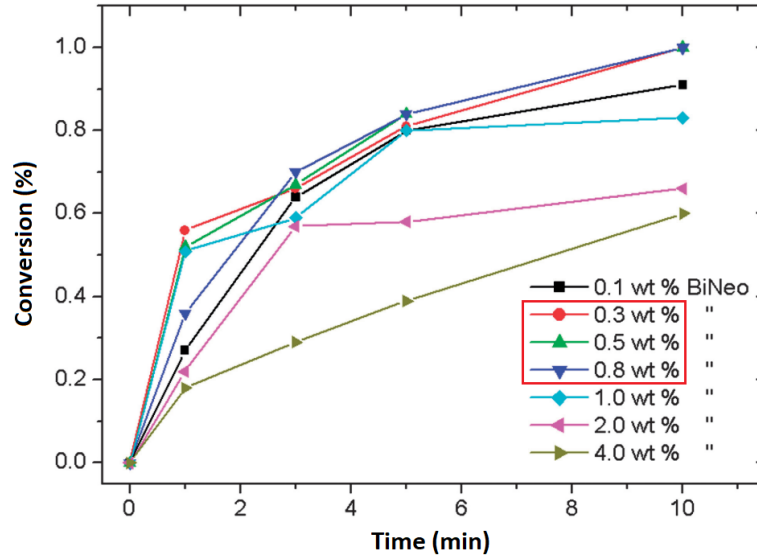


Figure 2.20: In situ reaction kinetics of polyurethane conversions for reactants containing catalyst concentrations between 0.1 - 2.0 wt%.¹¹⁷

A non-PU reactive polymers that have been inkjet printed include polydimethylsiloxane, a silicone elastomer widely used within industry due to its low cost, biocompatibility, and optical transparency.^{Sturgess *et al.* ¹¹⁸, Sturgess ¹¹⁹} This research identified common challenges associated with inkjet printing two-part reactive systems, including effective mixing, printable viscosities and curing times.

Finally, Müller *et al.*¹²⁰ studied the printability of reactive PU inks via inkjet printing, demonstrating that the mechanical properties could be altered by changing mixing ratio during printing. This led to theory of gradient materials by leveraging the versatility of PU. Additionally, Zawadzki *et al.*¹²¹ introduced a novel technique for synthesising polyurea via in-air collision of reactive ink droplets. This work further demonstrated the potential reactive inkjet printing has to produce parts with tunable mechanical properties via controlled ink deposition and mixing strategies.

2.4 Research Gaps and Opportunities for Innovation

Colton and Crane¹²² demonstrated interactions between the ink-powder system is complex and depends on many printing parameters, such as droplet volume, velocity and spacing as well as print frequency, which existing literature has often overlooked. Thus, highlighting a clear gap in our understanding of ink-based powder AM techniques.

Chapters 5 and 6 attempt to address this knowledge gap by showcasing the impact of print parameters, including droplet volume and spacing, on the mechanical properties and geometrical accuracies of parts manufactured via Reactive Binder Jetting (RBJ). Literature around ink dynamics on porous substrates exists^{123–125}, however limited experimental work has been done to better understand how ink infiltrates a bed of powder, justifying further research in the space of ink-based powder AM to achieve better print control and part performance.

Regarding reactive BJ printing systems, some research exists in the space but is primarily focused on reactive inkjet printing (RIJP)¹¹⁸ on to non-porous substrates. Although, Oropeza and Hart⁵⁷ introduced a 'reactive' binder ink, this process still required thermal post-processing which elicited the reaction between the metal-salt binder and metal powder. To date, there has been no research published that explores a polymer-based reactive dual-ink binder system which reacts without thermal post-processing and remains in-situ to form a final composite part. Thus, further highlighting the novelty around RBJ printing and justifying the work on custom reactive dual-ink binder systems. An additional benefit of the RBJ printing process, is the potential to reduce powder waste as the low-temperature process can preserve the lifetime of recycled powder for longer. Finally, with a dual-printhead, RBJ is capable of fabricating PUs with gradient properties, similar to work conducted by Müller *et al.*¹²⁰, thus leveraging the versatility of PUs to unlock new applications, such as within the biomedical sector (e.g. biodegradable drug-delivery implants).¹¹⁶

The PU market has traditionally used harmful raw material and manufacturing processes, including toxic isocyanates and catalysts as well as CO₂-emitting foaming techniques. However, market trends over the last few decades have seen manufacturers take deliberate measures to minimise the negative effects that PU manufacturing has on human and environmental health. In more recent years, we have seen an increase in research publications that explore more sustainable raw materials, including bio-based alternatives to isocyanates.

3 | Materials and Methods

This project built upon prior research conducted at the University of Nottingham, including a patent published in 2018 by researchers based within the Centre for Additive Manufacturing research group.⁷ Constituent materials use throughout this project were selected based on the disclosures noted in the patent. Aligning with the patent was a deliberate decision, enabling the exploration of commercial applications and licencing opportunities. Section 3.1 below provide a detailed account of the materials used and methods applied throughout, including the printing process and characterisation of materials.

3.1 Materials

A summary of key properties for all constituent materials used in the formulation of dual-ink reactive binder systems is located in Table 3.1.

Table 3.1: Key properties of constituent materials used in dual-ink binder systems.^{126–131}

Chemical	Molar Mass (g mol ⁻¹)	Density (g cm ³)	Viscosity (mPa s)	Boil Point (°C)
hexamethylene diisocyanate	168.2	1.05	2.5	255
poly(hexamethylene diisocyanate	—	1.13	1700	—
ethylene glycol	62.1	1.11	—	198
poly(ethylene glycol)	400	1.13	12	200
1,4-Butanediol	90.1	1.02	83	230
dibutyltin dilaurate	631.6	1.04	72	250
stannous octoate	405.1	1.25	—	200
dimethylethanolamine	89.1	0.89	3.9	136

3.1.1 Reactants

A number of reactants were used to formulate the reactive inks explored throughout this research. These inks were prepared to elicit an immediate polyaddition reaction upon contact, thus leading to the formation of a TPU binder system.

3.1.1.1 Isocyanates

Isocyanates (ISO) contain isocyanate functional groups, $[-NCO]$, which are highly reactive in the presence of compounds containing $[-OH]$ groups, such as diol or water molecules. In the presence of a diol molecule, the isocyanate undergoes poly-addition polymerisation to form polyurethane (PU). Alternatively, when ISO reacts with amine molecules, step-growth polymerisation occurs to form polyurea, a variant of PU whereby the reactive constituents consist of isocyanate $-NCO$ and amine $-NH_2$ molecules, respectively. Finally, ISO molecules react with water to produce CO_2 , a technique commonly used to manufacture PU foams.¹³² All three reactions are formed via addition polymerisation.

ISO are highly reactive compounds, often associated with a range of adverse health effects following exposure, including sensitisation or inflammation of the respiratory tract, hypersensitivity pneumonitis and cancer.¹³³ These compounds are highly flammable and may form explosive mixtures with air at elevated temperatures above the flash point. Thus, applications for parts containing ISO compounds should be carefully considered.

Both 1,6 - hexamethylene diisocyanate (HDI) and poly(hexamethylene diisocyanate) (PHDI) were used as received by Sigma-Aldrich to formulate a range of reactive isocyanate (ISO) inks. The ISO ink formulations were composed of varying ratios of HDI and PHDI to enhance control of reactive ink viscosity for inkjet printing and reactivity for powder consolidation speed, both being critical criteria for successful ink-based AM processes. Additionally, taking a dual-ISO formulation approach offered more flexibility over the physical and chemical properties elicited by PU parts. Further details about the impact of molecular structure on part properties can be found in Section 2.3.1.2.

Generally, HDI, along with other aliphatic ISO molecules, are less reactive than aromatic

ISO molecules, such as toluene diisocyanate and methylene bisphenyl diisocyanate. A lack of aromatic rings in HDI results in a lower melt temperature, making HDI an ideal ISO selection for inkjet printing applications whereby ink viscosity often determines the printability of a given formulation.

The chemical structures for HDI and PHDI can be found in Figures 3.1a and 3.1b, respectively.

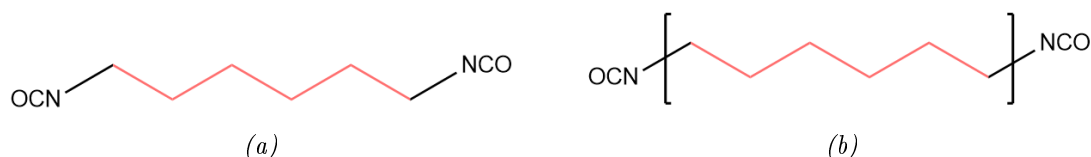


Figure 3.1: Chemical structure for (a) hexamethylene diisocyanate (HDI) and (b) poly(hexamethylene diisocyanate) (PHDI).

3.1.1.2 Alcohols

Polyols contain hydroxyl functional groups, $[-OH]$, which may react with available ISO groups, $[-NCO]$, to form a urethane linkage. Typically, to synthesise elastomeric PU parts, polyether or polyester polyols with molecular weights ranging from 1000 to 4000 $g\ mol^{-1}$ are reacted with ISO molecules.¹³⁴ The structure and chain length of polyols impact the final properties of PU. The large number of compatible, commercially-available polyols widens the range of achievable PU properties. It is this versatility that has led to the widespread adoption and application across dozens of industrial sectors.

Ethylene glycol (EG) and Poly(ethylene glycol) (PEG) EG is widely used in industry with commercial applications as antifreeze, paint and cosmetics. It is relatively cheap to manufacture and has excellent thermal properties. Although, EG readily absorbs water molecules when exposed to air, the low molecular weight has the advantage of reducing the viscosity of a diol (DIOL) ink, leading to a wider range of printable reactive inks. If necessary, measures can be taken to minimise exposure to moisture by preparing reactive inks in low-humidity environments.

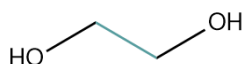


Figure 3.2: Chemical structure for ethylene glycol (EG).

3.1.1.3 Catalysts

Dibutyltin dilaurate (DBTL), stannous octoate (SO) and dimethylethanolamine (DMEA) were used as received by Sigma-Aldrich to catalyse the polyaddition reaction between the DIOL and ISO inks.

Dibutyltin dilaurate (DBTL) Conventionally, dibutyltin dilaurate (DBTL) has been widely used within industry to speed up polyurethane reactions due to its versatility in different reactive systems.¹³⁵ For this reason, it was selected as a catalyst in the reactive binder system. However, recent labelling changes and regulatory discussion regarding limitations to the use of organotin products, such as DBTL, has encouraged industry to consider alternative catalysts due to concerns regarding toxicity to humans, animals and the environment.¹³⁵

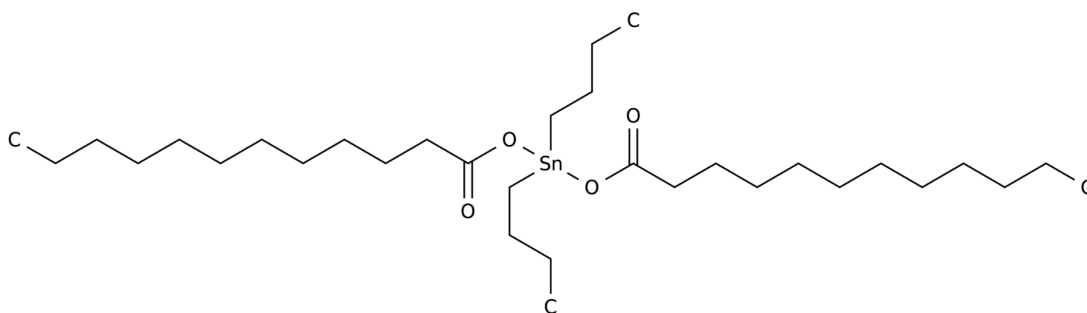


Figure 3.5: Chemical structure for dibutyltin dilaurate (DBTL).

Stannous octoate (SO) Stannous octoate (SO), or more commonly known as tin(II) 2-ethylhexanoate, was selected as a more sustainable tin-based alternative to DBTL. This is due to SO being more environmentally friendly, less toxic, and exhibiting a longer pot-life when used in a binder system.¹³⁶

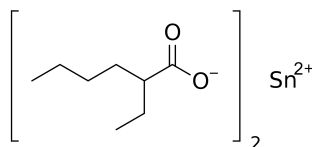


Figure 3.6: Chemical structure for stannous octoate (SO).

Dimethylethanolamine (DMEA) Dimethylethanolamine (DMEA) is an effective, economical catalyst for the manufacture of both flexible and rigid PU parts. DMEA is thought to disperse polyol ink components, aiding with the miscibility of reactive inks.

DMEA is recognised within the epoxy resin industry as an effective viscosity reducing agent, an important property for inkjet printing applications.

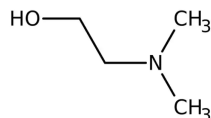


Figure 3.7: Chemical structure for dimethylethanolamine (DMEA).

3.1.1.4 Dyes

Two commercial Dimatix Model Inks were purchased from FujiFilm in colours red and blue. Both were used as received to dye the ISO and DIOL reactive ink formulations, respectively. Adding pigmentation to the ink formulation provided visual feedback during Reactive Binder Jetting (RBJ), indicating when jetting stability declined. This allowed the user to take immediate action to mitigate the effects of a stoichiometry imbalances within the reactive dual-ink binder system.

Blue Model Ink was added to DIO inks at 2.5 wt% to pigment the ink formulations blue. Similarly, Red Model Ink was added to ISO inks at 2.5 wt % to pigment the ink formulations red. When both reactive inks combined as a dual-ink binder system, the final pigmentation appeared purple. When printhead nozzles malfunctioned e.g. clogged, part pigmentation appeared less intense, non-uniform or skewed in colour toward either blue or red.

3.1.2 Polyurethane Powders

Commercial powders - Ultrasint™ TPU01 and UNEX TPU 80-240 - were used as received from BASF 3D Printing Solutions GmbH and Dakota Coatings, respectively.

UNEX UNEX TPU is a commercially available medium transfer powder designed to be used as a scatter coating on the back of plastisols to improve fabric adhesion. The received packaging indicated particles ranged in size from 80 - 200 µm in diameter.

Ultrasint™ TPU01 Ultrasint TPU01 is a commercially available PU powder designed by HP for use in the Multi Jet Fusion (MJF) print system to produce parts with good flexibility, shock absorption and fine geometric detail. According to the technical

data sheet the mean particle sizes range from 70 - 90 μm in diameter.

3.1.3 Printheads

Printing was performed on a FujiFilm DMP-2830 Dimatix inkjet printer (Santa Clara, CA, USA) using disposable Dimatix Materials Cartridges (DMCs).

Throughout this project two types of printheads were used - DMC-11610 and Samba. The latter was introduced halfway through the project due to a discontinuation of the DMC-11610 printhead model by Fujifilm. Therefore, experiments were conducted from Oct 2019 - June 2021 using DMC-11610 printheads whereas the DMC-Samba printheads were used from July 2021 - Dec 2022. Images of both printhead models can be seen in Figure 3.8



Figure 3.8: *FujiFilm printheads (a) DMC-11610 and (b) DMC-Samba (adapted from FujiFilm Dimatix Inc.²¹ and Fujifilm¹³⁷)*

The external appearance of both printheads was similar, however the internal hardware such as the nozzle array and heating element, fundamentally differed. The most relevant performance outputs that had changed following the switch from DMC-11610 to DMC-Samba model included a reduction in:

- Total number of addressable nozzles (16 down to 12)
- Native drop volume (10 pL down to 2.4pL)
- Maximum internal heating (70 °C down to 60 °C)

A combined reduction in nozzles and drop volume led to an estimated 43 % reduction in net ink volume output per unit time, thus affecting total print time and powder bed saturation levels. The lower heating capability of the Samba printhead meant 22 %

of the reactive inks initially investigated could no longer be printed. Table 3.2 below outlines the critical differences between the two Dimatix printhead types.

Table 3.2: Key differences between two types of Dimatix Material Cartridges (DMCs) used in this project.

Printhead	Nozzles	Drop Volume (pL)	Ink Viscosity (pL)	Max Temp (°C)
DMC-11610	16	10	10 – 12	70
DMC-Samba	12	2.4	4 – 8	60

3.2 Methods

3.2.1 Overview

To develop an effective dual-ink binder system, the following criteria were hypothesised as critical for RBJ printing and, therefore, needed to be considered throughout the ink development process:

1. Reliable inkjet printing via DMC-11610 and DMC-Samba printheads.
2. Reactivity to ensure inks rapidly and completely polymerise to form PU.
3. Desired functionality and mechanical performance of printed parts.

To achieve these criteria, several iterative cycles of ink reformulation followed by print parameter optimisation were conducted for each reactive ink to ensure the final binder system was effective. The critical print parameters were investigated to achieve an optimum droplet via inkjet printing with a focus on droplet size, shape, coalescence and velocity.^{138,139}

Once inks began to jet optimally, the molar density, or number of moles per droplet of ink, was estimated to allow for molar ratio calibrations between reactive inks. The flowchart in Figure 3.9 outlines part of the process taken to achieve reliable jetting (criteria 1) and a desired molar mass (criteria 2) for a single reactive ink. Additional method details can be found in Sections 3.2.4 and 3.2.4.2, respectively

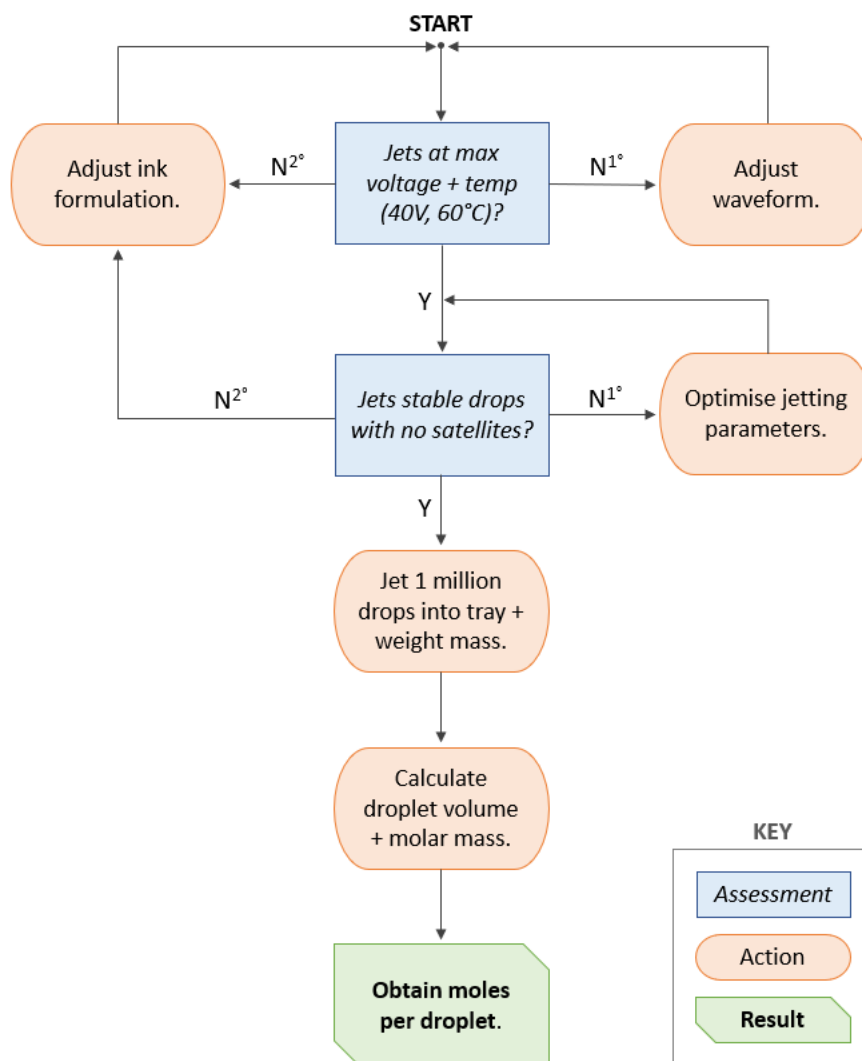


Figure 3.9: Method for optimising reactive ink formulations and obtaining the moles per droplet to calibrate the molar ratio within a dual-ink binder system.

3.2.2 Ink Preparation

3.2.2.1 Diol Inks

In this research, three polyester polyols - ethylene glycol (EG), poly(ethylene glycol) 400 (PEG) and 1,4 - butanediol (BD) - were used as received by Sigma-Aldrich to formulate a range of reactive diol (DIOL) inks. Three different catalysts - dibutyltin dilaurate (DBTL), stannous octoate (SO) or dimethylethanolamine (DMEA) - were used as received by Sigma-Aldrich. Blue Model Ink was purchased from FujiFilm and used as received to dye the DIOL inks a medium shade of blue.

Before the reactive inks were prepared, a 12 mm poly(tetrafluoroethylene) (PTFE) magnetic stirrer was added to an empty 20 mL glass vial. The stirrer and vial were

then placed on a mass balance located in a fume hood and the net weight zeroed.

Once the constituent materials had been added to the vial and homogeneously mixed via stir plate and bar, a 5 mL Braun syringe, 0.45 μm Millipore Millex filter and 125 μm Dimatix fill tip was used to extract and filter the final ink formulation before it was injected into an empty printhead cartridge.

DIOL Ink Formulations - B and B1 For B-type DIOL ink formulations, 2 mL of BD was extracted from a 500 mL bottle using an 80 mm green BD Microlance needle of 0.8 mm diameter and a 2 mL Braun syringe. BD was then added to the prepared vial and weighed.

For B1-type DIOL ink formulations, EG was extracted from a 100 mL bottle using a 40 mm green BD Microlance needle of 0.8 mm diameter in combination with a 2 mL Braun syringe. PEG was extracted from a 200 mL bottle using a 5 mL Braun syringe equipped with a 125 μm Dimatix fill tip. The larger syringe capacity and fill tip diameter was selected due to PEG having a higher viscosity than EG. Both reactants were then added to the vial and weighed one at a time.

The required concentration, or percentage weight, of the catalyst was calculated based on the net mass of reactants present. The mass balance was then zeroed before adding the catalyst, one of either DBTL, SO or DMEA. A 20 - 200 μL Fisherbrand™ adjustable-volume pipette equipped with a 200 μL yellow Fisherbrand™ polypropylene pipette tip was used to extract the selected catalyst before being added to the vial containing the DIOL reactant(s). Net weight of the catalyst was noted before the vial was removed from the scale, capped and placed on a hot plate stirrer set to 800 rpm.

Once constituents had fully mixed, approximately 2.5 wt % of blue Model Ink was added to the clear DIOL ink mixture to improve visibility. Extraction of the Model Ink was performed following the same process outlined previously, including using the same pipette and tip setup, for catalyst addition. The dye added was weighed and the vial returned to the hot plate stirrer for final mixing.

Once fully homogenised following stirring, 1.5 mL of a given DIOL ink was extracted from the mixing vial using a 5 mL Braun syringe, 0.45 μm Millipore Millex filter and

125 μm Dimatix fill tip before being transferred to a DMC cartridge. All contaminated equipment, including vial, stirrer, filters, syringes and needles, were washed repeated with acetone before being disposed of accordingly.

3.2.2.2 Isocyanate Inks

In this research, two isocyanates - poly(hexamethylene diisocyanate) (PHDI) and 1,6 - hexamethylene diisocyanate (HDI) - were used as received by Sigma-Aldrich to formulate a range of reactive isocyanate (ISO) inks. Red Model Ink was used as received from FujiFilm to dye the ISO inks a bright shade of red.

The A-type ISO ink formulations were prepared under a fume hood in ambient lab conditions using a mass balance, 20 mL capped vial, 12 mm PTFE stirrer and stirring plate. Vials and stirrers were dried in a vacuum oven at 100 $^{\circ}\text{C}$ for 60 minutes to remove moisture before preparing ISO inks.

PHDI and HDI were each extracted and added to the vial to achieve at desired stoichiometric ratio. The ISO formulation was then capped and stirred at 200 rpm for 5 minutes. A lower stir rate was chosen as it was observed to be most effective at dislodging the stir bar from the restrictive grasp of viscous PHDI ink. After 5 minutes of stirring, the stirrer would begins to rotate freely, at which point the stir speed was increased to 800 rpm for 30 minutes.

To prepare the ISO ink for printing, a 5 mL Braun syringe equipped with a 125 μm Dimatix fill tip was used to extract the final ISO ink from the vial. A 0.45 μm Millipore Millex filter was added between the syringe and fill tip before injecting the ISO ink into an empty printhead cartridge.

3.2.3 Characterisation Methods

Rheological data was obtained for the constituent inkjet materials in their monomeric and pre-polymeric states. Viscosity measurements for increasing shear rate and temperature were analysed to predict the printability of a given reactive ink and can be found in Section 4.1.2.

3.2.3.1 Rheological Behaviours of RBJ Materials

Fluid Rheometer A Kinexus pro+ fluid rotational rheometer (Malvern Instruments Ltd., Malvern, UK) equipped with a 4 °- 40 mm cone and parallel plate setup was used to measure the shear viscosity of each formulation of reactive ink to assess the changes to flow in response to applied forces. The first of two measurements applied torque to the ink at increasing shear rates of 10 - 1000 s⁻¹ which was conducted at three fixed temperatures of 50 °C, 60 °C and 70 °C for each formulation. The second measurement focused on the viscoelastic behaviour of the ink by applying a compressive force at a frequency of 10 kHz at increasing temperatures between 25 - 70 °C at 5 °C increments. Measurements were taken for a temperature of 70 °C or less to reflect the applicable heating range for both DMC printheads.

Powder Rheometer An FT4 powder rheometer (Freeman Technology, Tewkesbury, U.K.) was used to measure the stability and variable flow rate of the two commercial TPU powders. Before each measurement, the powder samples were conditioned to ensure a standardised packing state and remove any residual compaction or air between runs. This was achieved by traversing a 23.5 mm blade along the vertical into a 25 mL powder container before lifting the blade out. Each powder type was measured three times using the combined stability and variable flow rate method. The approach was applied as suggested in the Freeman Technology manual dated 2007.¹⁴⁰ Further justification is supported by existing literature investigating powder rheology.^{141,142}

Particle Size Analyser A Mastersizer 3000 (Malvern Instruments Ltd., Malvern, U.K.) was used to measure the particle size distributions of the two commercial TPU powders - Ultrasint™ and UNEX - and one custom TPU powder. Three repeat measurements were taken for each sample run. A wide range of particle sizes between 10 nm - 3500 µm can be accurately measured using this equipment according to the manufacturer.¹⁴³

3.2.3.2 Composition of RBJ Materials

Fourier-transform infrared (FTIR) Spectroscopy A Frontier Fourier-transform infrared (FTIR) spectrometer (PerkinElmer Ltd., Beaconsfield, U.K.) equipped with an

attenuated total reflectance (ATR) accessory was used to predict the presence of specific functional groups by their respective transmission peaks. Before each scan, both the pin and ATR crystal were wiped with isopropanol (IPA) followed by a background measurement of 4 scans. A pin is required to press the sample into the ATR crystal before calculating the average of 20 scan measurements between $4000 - 700 \text{ cm}^{-1}$ at a resolution of 4 cm^{-1} . The shifting and depth of characteristic transmission peaks were measured to compare the degree of polymerisation between reacted samples.¹⁴⁴ Before analysing a set of spectra, a baseline correction was applied followed by a smooth factor of 2.

Table 3.3: Characteristic FTIR frequencies of bonds present in isocyanates, alcohols and polyurethane ranging from $3600 - 1600 \text{ cm}^{-1}$.^{145,146}

Wavenumber (cm^{-1})	Vibration Type	Bond	Assignment
1750 - 1600	Stretching	C=O	Urethane
2275 - 2250	Stretching	NCO	Isocyanate
3550 - 3200	Stretching	OH	Alcohol

Thermogravimetric Analysis (TGA) A thermogravimetric analysis (TGA) instrument (PerkinElmer Ltd., Beaconsfield, U.K.) was used to investigate the thermal decomposition profile of TPU powders and printed parts during gradual heating ($10 \text{ }^{\circ}\text{C min}^{-1}$). Nitrogen was used to purge the sample of oxygen to mitigate oxidation reactions from occurring at elevated temperatures.

For PU systems, thermal decomposition will typically occur in three stages as outlined below:^{133,147–149}

- i **Pre-Decomposition** (0 - $200 \text{ }^{\circ}\text{C}$): Blowing agents and other small molecules, such as water and unreacted isocyanates, are released.
- ii **Hard Segment Decomposition** ($> 200 \text{ }^{\circ}\text{C}$): Urethane bonds (in hard segment) are broken first, releasing large quantities of isocyanate and polyol compounds.
- iii **Soft Segment Decomposition** ($> 300 \text{ }^{\circ}\text{C}$): Remaining residue and polyol compounds decompose into volatiles, such as CO, CO₂, and monomeric alcohol.

Example thermal profiles of commercial TPU powders - Ultrasint™ and Unex - are shown in Figure 3.10 for context.

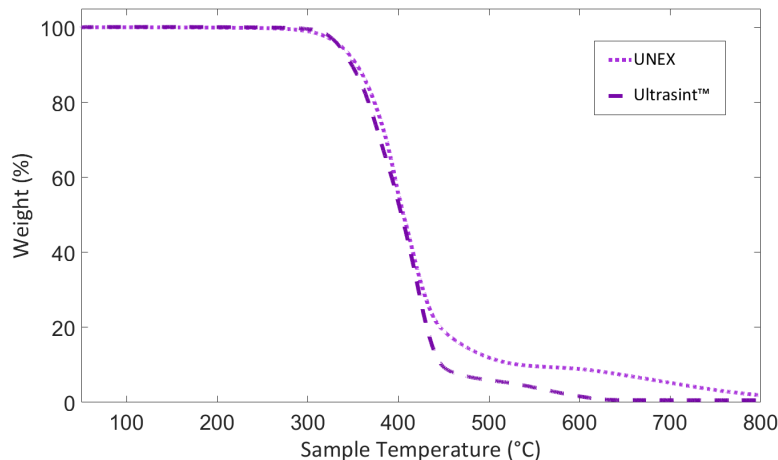


Figure 3.10: Example TGA plot profiling the thermal decomposition of commercial TPU powders - Ultrasint™ and UNEX - at $20\text{ }^{\circ}\text{C min}^{-1}$.

3.2.3.3 Morphological Characterisation of RBJ Printed Parts

Scanning Electron Microscope (SEM) Imaging The surface morphology of printed PU samples and their constituent TPU powders were obtained using a Philips XL30 Scanning Electron Microscope (SEM) (FEI Company, Hillsboro, OR, US) configured with a 10 kV beam and spot size of 4. With DMC printheads capable of depositing pico-litre droplets, it is necessary to apply SEM characterisation techniques capable of capturing nano-scale features.

Commercial TPU powder samples were prepared using a pair of stub gripper tweezers to scoop aluminium stubs prepared with carbon tape through loose powder contained within a vial. A thin layer of TPU powder is captured at the stub surface via adhesion to the carbon tape.

Printed PU samples were prepared using a pair of tweezers to place a single-layer PU sample onto the exposed carbon tape at the surface of an aluminium stub. The smooth side of the tweezers were used to apply gentle pressure onto the top surface of the sample to ensure it remained fixed to the tape. All prepared samples were blasted with pressurised nitrogen gas within the confines of a fume hood to ensure loose particles are safely removed before sputter coating each sample in platinum at 2.2 kV and 18 mA for 90 s.

X-ray Computed Tomography (XCT) An MCT 225 (NIKON CORPORATION, Tokyo, Japan) X-ray computed tomography (XCT) system was used to obtain hundreds of 2D images to reveal the internal and external features of printed CPU samples. Part density is a critical performance feature for powder AM parts, thus XCT enables accurate void percentage measurements and therefore part quality predictions without needing to damage the part.

The parts were placed vertically in the manipulator and scanned with a 2 second exposure rate. The electrical inputs were set at 88 kV and 177 μ A. The voxel size was set to 0.022632540038229 mm for each dimension (X, Y, and Z). No filter was used. Scan parameters were defined by the technician responsible for managing the XCT equipment based their expertise and technical know-how.

Sets of 2D images were processed and compiled in MATLAB to form a 3D computational structure using the built-in Volume Viewer application. To enhance contrast between the PU part and air, individual images were binarised, thus enabling more accurate calculations for part density and binder saturation.

3.2.4 Inkjet Printing of Reactive Inks

3.2.4.1 Printer Set Up

Environmental Control Ambient print conditions were monitored using a hygrometer (Testo SE & Co. KGaA, Lenzkirch, Germany) with a relative humidity (RH) range of 2 - 98 % and accuracy of $\pm 2\%$ Both the DMP and custom LP50 printers were housed within their respective glove box each equipped with an adjacent antechamber, nitrogen inlet, extraction and sufficient lighting (refer to Figures 3.11 and 3.12). The humidity was controlled by purging the chamber with nitrogen gas until the RH dropped to 10 %. Intermittent purging continued throughout printing to maintain RH conditions between 10-13 %. Ambient temperatures within each glove box was controlled between 21 - 24 °C during printing.

Dimatix Glove Box Printer Drop Watcher View with the Dimatix Drop Manager software was used to observe droplet formation and deposition velocity, confirming ink printability and allowing for cartridge settings to be tailored for individual inks.

Jetting waveforms were optimised in Waveform Editor to ensure stable droplet formation occurred for each ink formulation. Subsequently, the cartridge temperature, cleaning cycle settings and jetting voltages for individual nozzles were all configured in Cartridge Settings to synchronise droplet ejection times and travelling velocities. Pattern Editor within the Dimatix Drop Manager software was used to generate patterns to be printed and allow the droplet spacing to be defined.

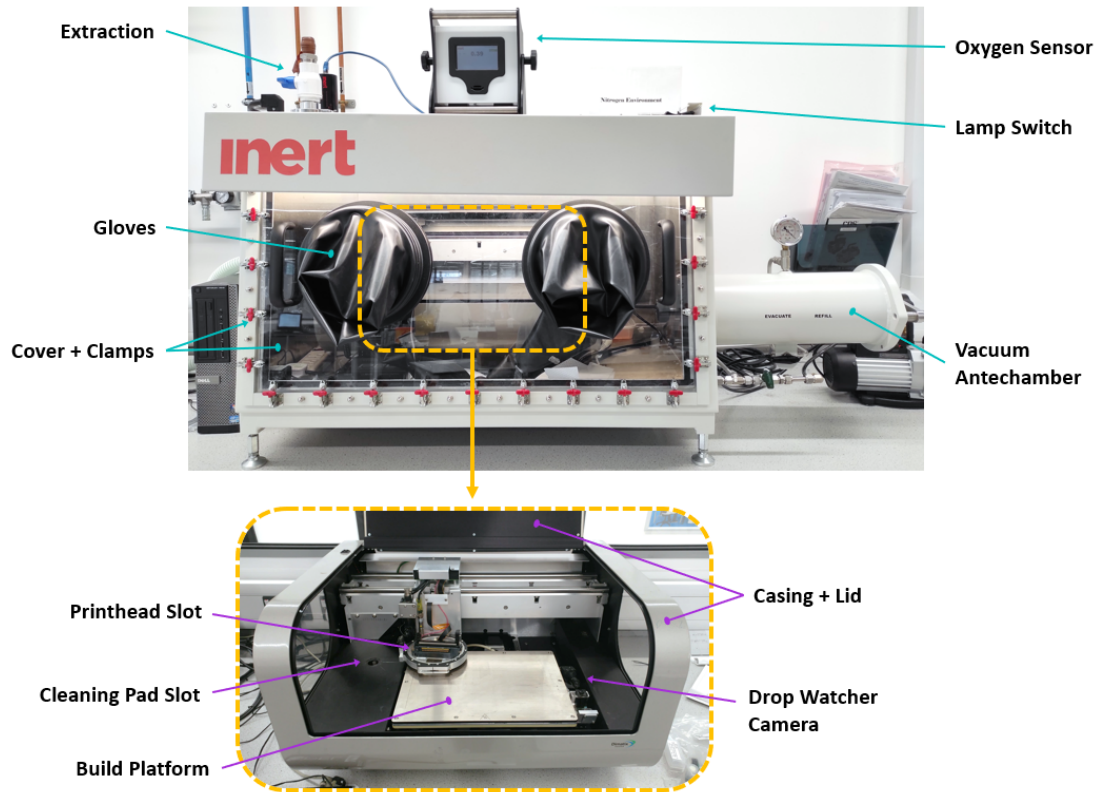


Figure 3.11: Full Dimatix Inkjet Printer setup in glove box with antechamber (top) with internal part labels (bottom).

Modified LP50 Printer A modified LP50 3D printer, originally designed for inkjet printing, had several hardware and software upgrades to enable RBJ printing, including a custom CNC-machined powder bed with a depth of 1 cm, servo motors to drive precise powder bed movements, a 3D printed PLA doctor blade for controlled powder spreading, and a dual-printhead assembly holder for increased printing efficiency. Figure 3.12 provides an overview of the various key components that made up the RBJ-compatible printer.

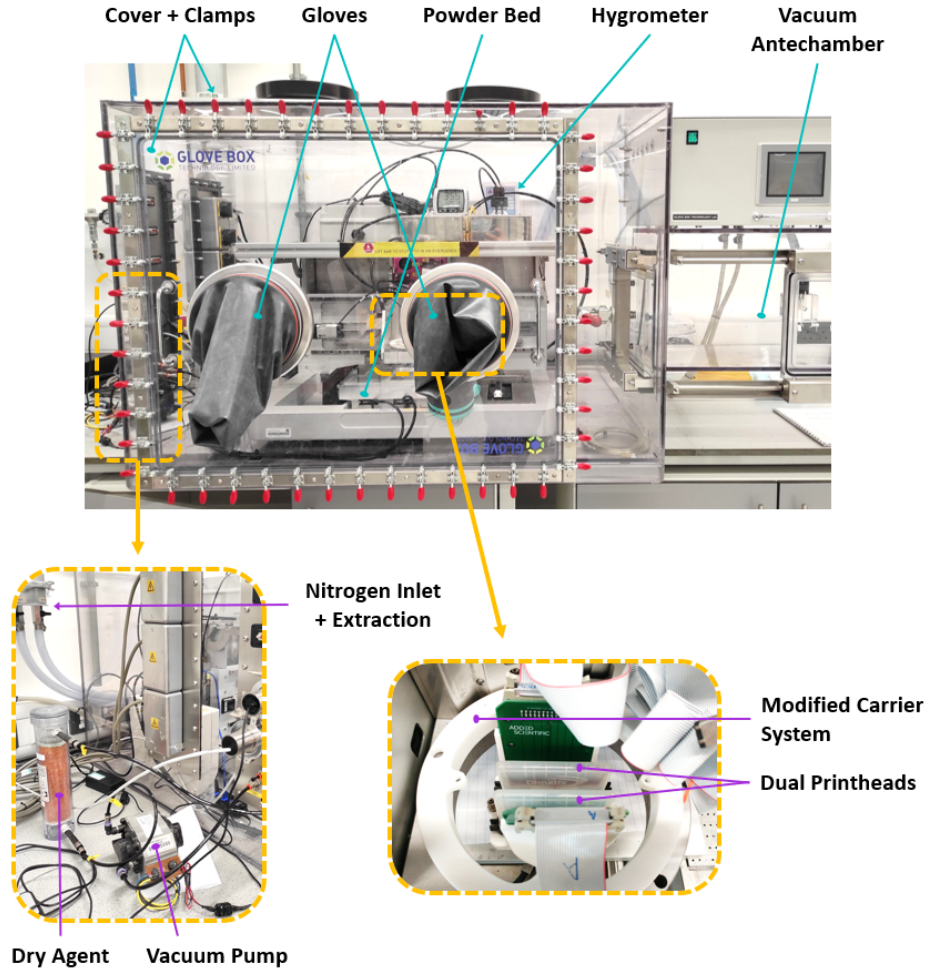


Figure 3.12: PiXDRO LP50 inkjet printer modified with a dual-printhead, vacuum, and powder bed system.

Overall, the printer modifications provided flexibility and control over the printing process, enabling fine tuning of several printer settings including recoat speed, build platform and/or powder feed reservoir height and print location or offsetting. These printer advancements provided more freedoms than the original LP50 commercial graphic user interface (GUI) across the entire printing process from inkjet printing to powder recoating, enabling more advanced experimentations.

The key printer features following modifications have been outlined below:

1. **Powder Bed Platform:** Built-in servo motors actuate a custom powder bed system, whereby the height for both the build platform and powder feed reservoir are moved up and down along the z-axis at discrete increments.
2. **Powder Recoating Blade:** A polymeric blade collects powder from the powder

feed reservoir and spreads it across the build platform, moving right to left. Grooves have been strategically placed along the edges of the platform to collect excess powder that may overflow during recoating.

3. **Dual-Printhead Assembly Holder:** A dual-printhead holder was designed to accommodate two DMC-Samba printheads to enable effective deposition of the dual-ink binder system. The rig was 3D printed via SLS and retrofitted to fit the existing infrastructure.

3.2.4.2 Controlling Stoichiometry of Reactive Dual-Ink Binder System

To achieve an optimal reaction for each dual-ink binding system, the net molar mass deposited by each ink within a single print pass is measured. The full process is outlined in Stages 1a and 1b below. The process for optimising jetting parameters was previously outlined in Figure 3.9. The step sequence highlights the importance of first generating reliable ink droplets before proceeding to the printing stage to maximise the chance of reaching the desired stoichiometric ratio. If fewer than 1 million droplets were jetted onto the tray during molar calibrations, the molecular weight per droplet calculations would become inaccurate, impacting final part properties.

Stage 1a

1. Select Reactive Ink Formulation
2. Estimate density for selected formulations.
3. Determine printable voltage range between 18 - 40 V for each formulation.
4. Jet 1 million droplets across range of jettable voltages for each formulation
5. Determine individual droplet volumes for each dataset via the following equation:

$$\text{Single Droplet Volume} = \frac{\text{Total Droplet Mass}}{\text{Formulation Density}} * \frac{1}{1,000,000}$$

Stage 1b

1. Estimate the molecular weight of each formulation.
2. Estimate the number of moles per droplet for drop volume datasets in Stage 1a for each formulation .

Stage 2a

1. Repeat Stage 1 for increasing waveforms (1x, 2x and 3x) for each ink.
2. Identify relationship between waveform sets for each formulation.
3. Obtain gradient for change in volume/moles with increasing waveform sets.

Stage 2b

1. Extrapolate moles per drop for dataset in Stage 1b using the gradient identified in Stage 2a.
2. Estimate the net moles per drop for each ink at all jettable voltages across all three waveforms.
3. Plot all datasets on one graph, determine the maximum net moles per drop for each formulation.
4. Identify all print parameter combinations (voltage + waveform) which achieve an optimal molar ratio between reactive inks.
5. Remove unfeasible or suboptimal datasets.

The resulting methodology has been summarised below with the corresponding results outlined in Sections 4.2.2.1, 4.2.2.1, and 4.2.2.2, respectively.

1. Determine moles per drop for each ink formulation.
 - i Assess printable voltage range for each formulation.
 - ii Measure drop volume at all printable voltages for each formulation.
 - iii Estimate formulation densities and molar masses.
 - iv Calculate the moles per droplet for all datasets.
2. Extrapolate viable ink datasets for multi-waveform printing.
 - i Using a stable print parameter, measure drop volume at 1x, 2x and 3x waveforms for each ink.
 - ii Plot and identify gradient between drop volume and waveform sets for each ink.
 - iii Extrapolate moles per droplet at 1x, 2x and 3x waveforms for all datasets within each ink formulation.

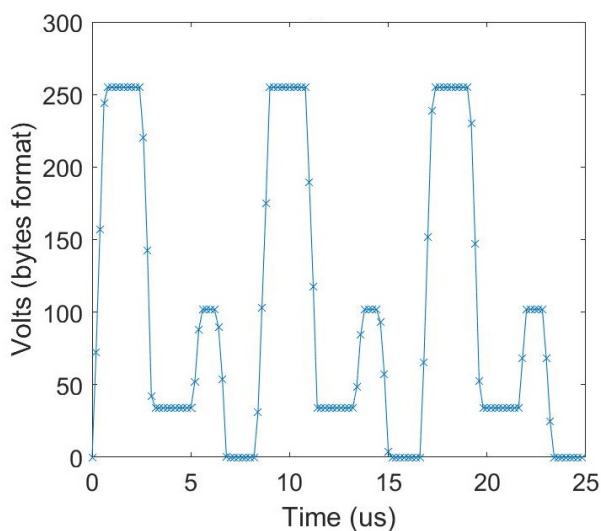


Figure 3.13: Example of a multi-set jetting waveform with three repeating droplet generation segments.

3. Determine optimal ink combinations for printing.
 - i Plot all viable moles per droplet datasets onto a bar graph.
 - ii Identify all compatible reactive ink combinations between A-B and A-B1 where bar heights are similar.
 - iii Eliminate ink combinations with $> 5\%$ error in molar ratio.
 - iv Eliminate ink combinations where at least one ink formulation exhibits $> 10\%$ error in jetting reliability.
 - v Present remaining ink combinations as optimal for RBJ.

Optimal reactive ink combinations were identified and taken forward for further research. The formulation process for each reactive ink was repeated following the specifications outlined in this section, minimising experimental errors between ink formulation batches. Further investigation into optimal parameters for inkjet printing onto PET and powder substrates have been continued in Chapters 5 and 6.

4 | Development of Reactive Dual-Ink Binder System for Inkjet Printing

To validate the commercial suitability of Reactive Binder Jetting (RBJ) for advanced manufacturing applications, specialised ink formulations were developed and optimised for powder consolidation. Contrary to traditional Binder Jet (BJ) processes, the RBJ reactive dual-ink binder system remains in-situ, forming a final composite part. The reactive ink acts as a permanent binding mechanism that does not get burned off during thermal post-processing.

RBJ binder is composed of two functionalised ink formulations which readily react together, in the presence of a catalyst, to form a thermoplastic polyurethane (TPU). The components that make up each of the reactive ink formulations can be tailored to achieve a range of part properties, ranging from flexible and strong to rigid and brittle. Rigorous formulation development and printing optimisation was necessary to successfully produce a functional dual-ink binding system capable of producing three-dimensional (3D) polyurethane (PU) parts.

Existing research demonstrates a wide range of routes to synthesis, highlighting the versatility of PU systems and suggesting a variety of reactive ink formulations could prove suitable for RBJ printing. In this research, three reactive ink families were explored based on prior work in the spacing.^{7,78,117} The first was an isocyanate (ISO) formulation derived from hexamethylene diisocyanate (HDI) which was selected to react with one of two diol (DIOL) inks composed of either butanediol (BD) or ethylene glycol (EG), including the polymer derivative polyethylene glycol (PEG). Table 4.1 provides an overview of all reactive ink formulations considered in this chapter.

Table 4.1: Summary of composition of all reactive ink formulations investigated.

Formulation			Constituent Materials		
Family	Identifier	Ratio	1	2	Catalyst
A	A01	1:9	PHDI	HDI	-
	A02	1:4	PHDI	HDI	-
	A03	3:7	PHDI	HDI	-
	A04	2:3	PHDI	HDI	-
	A05	1:1	PHDI	HDI	-
B	B01	-	BD	-	DBTDL
	B02	-	BD	-	SO
	B03	-	BD	-	DMEA
B1	B101	1:9	PEG	EG	DBTDL
	B102	1:4	PEG	EG	DBTDL
	B103	3:7	PEG	EG	DBTDL
	B104	2:3	PEG	EG	DBTDL
	B105	1:1	PEG	EG	DBTDL
	B106	1:9	PEG	EG	SO
	B107	1:4	PEG	EG	SO
	B108	3:7	PEG	EG	SO
	B109	2:3	PEG	EG	SO
	B110	1:1	PEG	EG	SO
	B111	1:9	PEG	EG	DMEA
	B112	1:4	PEG	EG	DMEA
	B113	3:7	PEG	EG	DMEA
	B114	2:3	PEG	EG	DMEA
	B115	1:1	PEG	EG	DMEA

Each formulation was characterised to identify the ink most suitable for inkjet printing of PU films. A range of stoichiometric ratios for reactive inks A and B1 were explored, aligning with the ratios outlined in the patent that inspired this project. Additionally, different catalytic concentrations for inks B and B1, were tested in three critical areas – miscibility, viscosity, and reactivity. The results were used to make an informed selection of the best-suited reactive ink pairings capable of reliable jetting, homogeneous mixing, and reactivity to consolidate powder in RBJ printing.

Selected reactive inks were optimised for jetting parameters using commercial Dimatix Material Printers (DMPs) manufactured by FujiFilm. Section 4.2 provides an overview of the performance of selected reactive inks across a range of inkjet printing parameters, such as temperature, jetting voltage, and waveform profile. These performance insights allow for precise control of stoichiometric ratios and droplet velocities by adjusting ink deposition parameters, including net volume, speed, and droplet shape. Inkjet printing parameters significantly impact the quality of RBJ-printed parts. The definition of

'quality' varies depending on the specific application. Key quality metrics for RBJ-printed parts include net part geometry, ink saturation density, and interparticle or interlayer binding strength, which can be assessed to determine part suitability for a given application.

A comprehensive understanding and control of the RBJ printer system enabled the identification of optimal inkjet printing parameters for fabricating thin films of fully polymerised dual-ink binder. This chapter presents results demonstrating the applicability of reactive dual-ink binding systems as a low-temperature alternative for material consolidation through inkjet printing.

4.1 Evaluation of Reactive Inks

Before proceeding to inkjet printing of a new reactive ink formulation, the printability of each ink was evaluated for RBJ printing suitability. The three ink properties deemed most critical for successful RBJ printing have been outlined below.

- i **Miscibility:** To effectively mix constituent ink materials and minimise nozzle clogging due to precipitation.^{150–152}
- ii **Viscosity:** To achieve stable jetting and reliable ink deposition.^{70,153,154}
- iii **Reactivity:** To maximise reactive binder polymerisation and minimise part failures during multi-layer printing.^{121,150}

The output ranges outlined in Table 4.2 were proposed to simplify the reactive ink selection process. By converting the qualitative and quantitative results into either a 0, 5 or 10, a weighted matrix could be applied to identify the theoretically optimum reactive ink formulations.

Table 4.2: Selection criteria for reactive inks suitable for Reactive Binder Jetting (RBJ).

	Miscibility	Viscosity	Reactivity
0	Immiscible	> 30 Mpa s	< 25 % Change
5	Partially Miscible	12 - 30 MPa S	25 -50 % Change
10	Miscible	< 12 MPa S	> 50 % Change

These material properties were deemed most influential when assessing whether a new reactive ink formulation would be suitable for RBJ printing at the early stages of for-

mulation development. Ink selection criteria will differ depending on the application, print system, printhead type, ink composition and, if relevant, reaction mechanisms.

4.1.1 Miscibility

Miscibility between constituent materials was visually assessed for all reactive ink families to ensure ink homogeneity and stability. For ink B formulations composed of only one monomer, miscibility checks were performed before and after mixing of the catalyst. Initially, when the catalyst had just been added, the bulk solutions for each of the three catalysts were clear despite observing segments of shiny, more refractive liquid swirling within the vial. However, once the formulations were mixed via a stir bar at 1000 rpm, visual markers became apparent to the naked eye immediately for some formulations.

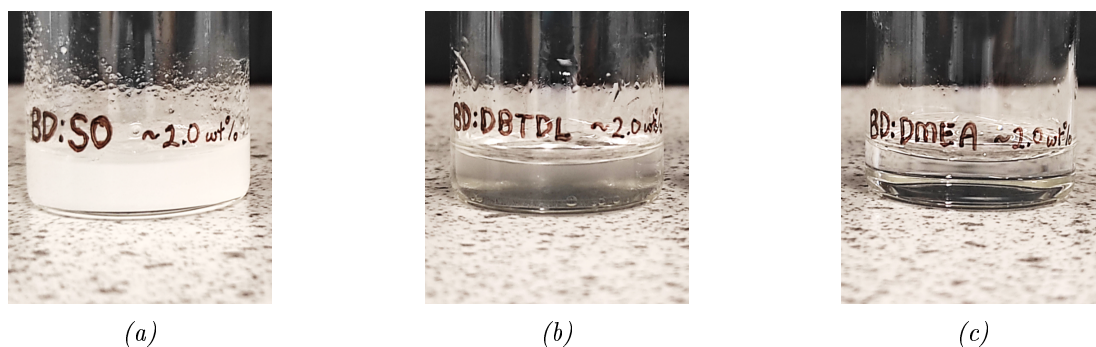


Figure 4.1: Ink B formulations containing 2.0 wt % (a) stannous octoate (SO), (b) dibutyltin dilaurate (DBTL), and (c) dimethylethanolamine (DMEA).

Figure 4.1 provides a visual snapshot of ink B miscibility for formulations composed of three different catalysts – DBTL, SO and DMEA – at 2.0 wt% in butanediol stirred at 1000 rpm for 15 minutes and left to rest for another 15 minutes. Other catalyst concentrations, including 0.5 wt%, 1.0 wt% and 1.5 wt%, were assessed but not included in the results as no visual differences were observed. All three formulations were distinguishable based on degree of transparency and amount of precipitate adhering to the vial walls.

Figure 4.1a indicates that SO was immiscible, as evidenced by the formation of white precipitates within the solution, resulting in a white, opaque mixture. For this reason, SO was removed from the ink formulation selection pool due to the increased risk of printhead nozzles clogging during printing. Catalyst DMEA appeared to be completely miscible with BD as evidenced by the ink transparency in Figure 4.1c. For DBTL,

Figure 4.1b indicated partial immiscibility, evidenced by the reduced transparency and blurred appearance. While no visible precipitates formed on the vial walls, the opacity was less pronounced than that of SO. Given the perceived low risk of nozzle clogging caused by immiscibility for DBTL-containing ink B formulations and its widespread use within the PU industry, DBTL was selected for further evaluation alongside DMEA.

For inks A and B1, more than one constituent material (excluding the catalyst) was used to form the bulk of the ink. As such, a separate miscibility check was performed to confirm the constituents formed a clear, homogenous solution before a catalyst, or any form of colourant, was applied. The preparation method applied before visual assessment was consistent with that used for catalyst miscibility checks performed on ink B. Thus, ink A and B1 formulations were stirred for 15 minutes at 1000 rpm and left to rest for 15 minutes following the assembly of constituent bulk materials and before the addition of any catalysts or colourants.

For ink A, only mixtures of poly(hexamethylene diisocyanate) (PHDI) and hexamethylene diisocyanate (HDI) at molar ratios less than 1:1, including formulations A01-A04, were assessed for ink miscibility. A01-A04 appeared transparent and completely clear of precipitates or other forms of liquid separation. Thus, all ink A formulations passed initial miscibility checks.

For ink B1, only mixtures of poly(ethylene glycol) (PEG) and ethylene glycol (EG) at molar ratios less than 1:1, including B101-B104 and B111-B114, were visually assessed for ink miscibility. All ink B1 formulations appeared transparent and completely clear of precipitates or other forms of separation. Similarly, for ink B formulations, an additional miscibility check was performed once catalysts were added to the bulk composition. However, to reduce the experimental dataset, a fixed molar ratio of 2:3 for ink B1 was chosen for each of the three catalysts being tested. Thus, formulations B104, B109, and B114 were investigated for catalytic miscibility. The visual assessment results mirrored those observed for ink B formulations further supporting the conclusion that DBTL and DMEA were the most suitable catalyst options for alcohol-based reactive inks.

4.1.2 Viscosity

Viscosity of a new ink formulation is often measured as an early indicator of how well the ink will resist the shear forces experienced at the inner nozzle walls during jetting. For all three reactive ink formulation families - A, B, and B1 - the viscosity was measured using a rheometer to simulate two measurement conditions relating to shear rate and temperature to predict rheological behaviour that might occur during inkjet printing.

For the discontinued (June 2021) DMC-11610 printheads, manufacturers had advised inks with viscosities of ≤ 30 mPa s could be jetted but reliability would increase at ink viscosities of 10 - 12 mPa s. This printhead had been able to heat inks up to 70 °C, further reducing ink viscosity. For the new DMC-Samba printheads introduced to the project from July 2021, printhead temperatures were capped at 60 °C with the manufacturer recommending the use of inks with viscosities between 4-8 mPa s. The viscosity ranges were used as a guide only, as prior research has demonstrated successful jetting of high molecular weight (MW) inks.¹⁵⁵ Parameters that could critically impact performance included ink viscosity, surface tension, and temperature.

4.1.2.1 Increasing Shear Rate

The first measurement condition subjected a thin layer of ink to increasing shear rates from 10 – 1000 s⁻¹ at a fixed temperature. This parameter was investigated to highlight how each ink might behave during drop generation during which the ink is predicted to experience high shear forces as it transitions from the ink reservoir to printhead nozzle where the change in volume is significant. The rheometer used was limited to a shear rate of 1000 s⁻¹, thus this value was selected as the maximum threshold when investigating the impact of shear rate on shear viscosity. This type of measurement was taken for three temperatures – 50, 60 and 70 °C which sufficiently covered the range of printing temperatures required to form PU using the two sets of reactive dual-ink systems. This selection was backed by reactivity tests using hot plate temperatures of 45 °C or more which had elicited a faster reaction. Finally, the upper temperature limit for viscosity tests was defined by the maximum printhead threshold of 70 °C for the DMC-11610 printheads, thus it was not necessary to measure viscosities beyond this point. However, since conducting these tests, the DMC-11610 printheads had been

discontinued and replaced by the DMC-Samba printhead which were found to have a lower maximum temperature threshold of 60 °C.

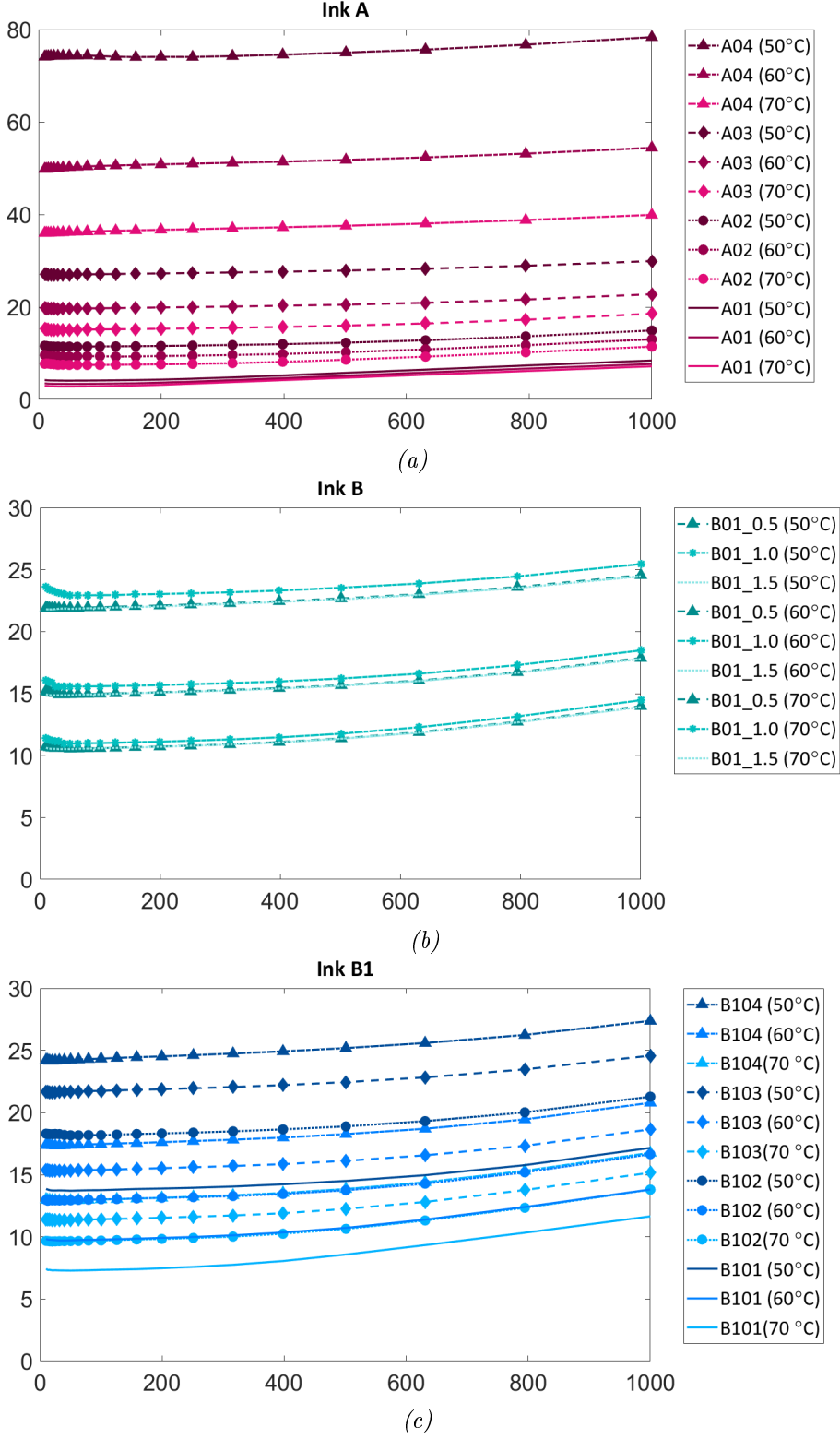



Figure 4.2: Shear viscosities for reactive inks (a) A (PHDI:HDI), (b) B (BD:DBTL) and (c) B1(PEG:EG:DBTL) at increasing shear rates from 10 - 1000 s⁻¹ at 50 °C, 60 °C, and 70 °C.

Figures (4.2a-4.2c) shows the shear viscosity at increasing shear rate from 10 - 1000 s⁻¹ for of all three reactive ink types. A clear decrease in mean viscosity was observed at fixed measurement temperatures – 50 °C, 60 °C and 70 °C – for all datasets. All three ink formulation datasets showed an increase in shear viscosity with increasing shear rate from 10 to 1000 s⁻¹. For inks A, B and B1, the largest shifts in shear viscosity were 4.60 mPa s, 3.29 mPa s and 4.22 mPa s, respectively. However, for both inks B and B1 this was observed at the highest measured temperature of 70 °C while for ink A it was at 60 °C for formulation A04. This data set presented an unusual trend compared to the other datasets that showed a consistent upward trend as measurement temperature increased from 50 °C to 70 °C.

Table 4.3: Coloured arrays for all ink formulations highlighting the (a) final viscosities (mPa s) at 1000 s⁻¹ and (b) percentage increases (relative to initial shear rates of 10 s⁻¹).

Lowest 				Highest			
	50 °C	60 °C	70 °C		50 °C	60 °C	70 °C
A04	78.3	54.4	39.9	A04	6%	9%	11%
A03	29.9	22.8	18.6	A03	11%	15%	21%
A02	14.9	13.0	11.4	A02	29%	35%	48%
A01	8.4	7.7	7.2	A01	101%	120%	144%
B01_0.5	24.6	17.9	14.0	B01_0.5	12%	17%	30%
B01_1.0	25.5	18.5	14.5	B01_1.0	8%	15%	27%
B01_1.5	24.5	17.8	13.9	B01_1.5	12%	19%	31%
B104_1.0	27.4	20.8	16.8	B104_1.0	13%	19%	29%
B103_1.0	24.6	18.7	15.2	B103_1.0	13%	21%	33%
B102_1.0	21.3	16.7	13.8	B102_1.0	16%	28%	43%
B101_1.0	17.2	13.8	11.7	B101_1.0	24%	40%	57%

(a) (b)

Table 4.3a quantifies the final viscosity values observed in Figures (4.2a-4.2c) at $x = 1000$ s⁻¹. Colour shifts from highest (red) to lowest (green) suggests viscosity consistently dropped as operating temperatures increased across all ink formulations. For example, although ink A01 is shaded in green throughout, the same trend is observed as the viscosity transitioned from 8.4 mPa s at 50 °C to 7.7 mPa s and 7.2 mPa s at 60 °C and 70 °C, respectively. An additional trend was observed for specific temperature datasets for inks A and B1 only whereby the viscosity values were highest when formulation ratios were 2:3 but then consistently dropped as the ratios decreased to 1:9.

Table 4.3b quantifies the percentage increase in viscosities at 1000 s⁻¹ relative to the

starting rate of 10 s^{-1} for each formulation. For all datasets, the percentage difference in viscosities gradually increased from $50 \text{ }^{\circ}\text{C}$ through to $70 \text{ }^{\circ}\text{C}$ as seen by the colour shift from green to red along each row. A significant percentage increase in inks A and B1 was observed for formulation ratios decreasing from 2:3 to 1:9.

Inks that exhibited large increases in viscosity between 10 s^{-1} and 1000 s^{-1} (red highlight in Figure 4.3b) were primarily in the $70 \text{ }^{\circ}\text{C}$ temperatures range. This was an unexpected results given viscosity for these ink formulations have been observed to decrease with increasing temperature. It is possible the rheometer is less accurate at measuring viscosity at high shear rates. Alternatively, these ink formulation experienced shear thickening, meaning the molecules clustered under shearing preventing flow and increasing resistance.¹⁵⁶ With reference to the average MW of each reactive inks in Table 4.4a, reactive ink family B was observed to have the lowest MW but the highest disparity in viscosity.

Viscosity data in Figure 4.3a demonstrated most reactive inks reached viscosities below 30 mPa s across the temperature range tested (excluding reactive ink A04), increasing the probability of these reactive inks jetting successful. However, shear thickening was observed at high shear rates of 1000 s^{-1} and should be taken into account when selecting print parameters or a printhead to use in later developmental stages.

Table 4.4: Estimated molecular weights for inks (a) A and B1 across four monomeric ratios and (b) B across three catalytic concentrations.

Ratio	MW (g mol^{-1})		Concentration	MW (g mol^{-1})
	Ink A	Ink B1		Ink B
1 : 9	199.2	95.9	0.5 wt%	92.8
1 : 4	230.3	129.7	1.0 wt%	95.5
3 : 7	261.3	163.4	1.5 wt%	98.1
2 : 3	292.3	197.2	2.0 wt%	100.7

(a)

(b)

Formulation MW was estimated for each of the reactive inks as summarised in Table 4.4a. Inks A and B1 formulations with a 1:9 molar ratio (A01 and B101) were estimated to have a lower MW since only 10 % of the formulation contained higher viscosity derivatives PHDI and PEG, respectively. This estimation correlated with the mean viscosity data shown in Figures 4.2a and 4.2c whereby both 1:9 formulations consistently

had the lowest viscosities for each temperature measurement. Although ink B does not exhibit the same trend with increasing catalyst concentration, a significant increase in the net MW between formulations is observed in Table 4.4a. However, the deviation between these values is ± 0.27 which is negligible hence why no clear trend is observed in Figure 4.2b. Whereas both inks A and B1 experience MW deviations of ± 4.0 or more between formulations, correlating with discreet temperature shifts within the datasets.

A relationship between operational temperature and MW can be defined whereby reactive ink formulations composed of lower MW will exhibit larger percentage increases in viscosity (see Table 4.3b) at higher operational temperatures when subjected to increasing shear rates. Therefore, higher operational temperatures may exacerbate any tendencies toward shear thickening, especially as the MW of the formulation decreases. Higher MW reactive inks are likely to display more stability during inkjet printing as shear rates are expected to be high during nozzle ejection. This further justifies the need for rheological testing of inks to ensure a balance between jetting stability and reliability, especially as higher MW formulation may improve stability but then jetting reliability if the viscosity becomes too great.

4.1.2.2 Increasing Temperature

The second measurement condition investigated the impact of increasing temperature at a fixed shear rate on shear viscosity. As stated previously, the Dimatix printheads used at the start of this project (DMC-11610) were capable of heating ink up to 70 °C whereas the next generation printhead (DMC-Samba) used in the second half of this project was limited to 60 °C. Thus, there was no need to take viscosity measurements above these expected operating temperatures.

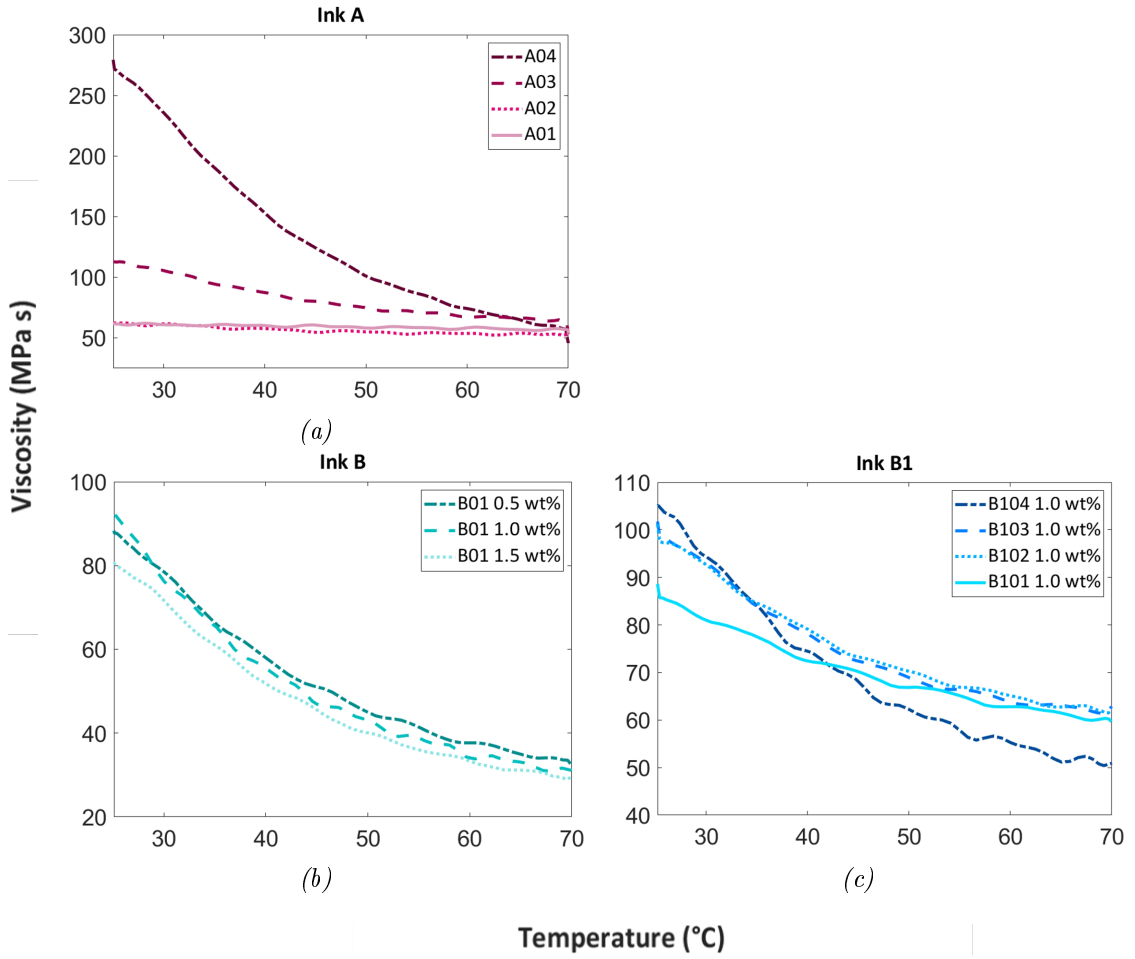


Figure 4.3: Shear viscosity of reactive inks (a) A, (b) B, and (c) B1 at increasing temperatures ($5\text{ }^{\circ}\text{C min}^{-1}$) between $25 - 70\text{ }^{\circ}\text{C}$ at 1000 s^{-1} shear rate and 10 Hz oscillation frequency.

Figure 4.3 summarises shear viscosities for reactive inks A, B and B1 at fixed shear rate (1000 s^{-1}) undergoing heating from $25 - 70\text{ }^{\circ}\text{C}$ at a rate of $+5\text{ }^{\circ}\text{C per minute}$. All formulations were seen to decrease in viscosity as temperatures increases from room temperature. All formulations start with a higher viscosity value at $25\text{ }^{\circ}\text{C}$ before decreasing as temperatures increase, confirming that all inks have the potential to be jetted within the desired viscosity range at an achievable temperature condition. However, some formulations have been observed to follow a negative exponential rate of change during heating, including A04, B104 and all ink B formulations.

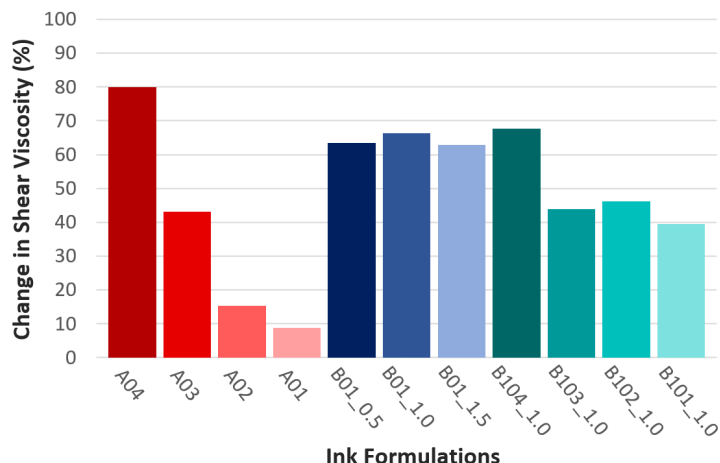


Figure 4.4: Reduction in shear viscosity from start (25 °C) to finish (70 °C) for all reactive ink formulations.

Figure 4.4 provides a visual representation of the percentage difference in viscosity for each ink at 70 °C compared to the first data point at 25 °C. The tiered bars shaded in red, indicate ink A formulations experienced a larger reduction in viscosity during heating for formulations containing higher concentrations of PHD, as demonstrated by A04 with a 80 % reduction. It is commonly understood that liquid viscosity reduces with increasing temperature. Akhanova *et al.*¹⁵⁷ observed non-Newtonian shear thinning behaviour in HDI when sample viscosity decreased with increasing shear rate, suggesting polymer chain alignment and disentanglement via shearing led to reduced viscosity.

It is hypothesised that reactive ink formulations containing larger concentrations of long chained polymers components, such as PEG and PHDI, are prone to greater chain entanglement. Therefore, they exhibit higher viscosity outputs at fixed shear rates due to increased tangling. Additionally, existing literature suggest a strong correlation between MW and viscosity as well as mechanical strength.¹⁵⁸ Hence, within their datasets, formulations A01 and B101_{1.0} exhibited the smallest reduction in viscosities at 8.8 % and 39.4%, respectively. This behaviour suggests reactive inks with lower MWs exhibit better stability across the full range of printhead temperatures (25 - 70 °C). This is likely a result of there being fewer chain entanglements to remove, and therefore the impact of increasing temperature having less impact on formulation viscosity since the bulk molecular structure is generally simpler with less PEG and PHDI present.

Initial analyses had suggested formulation B104 was an outlier compared to the other

inks in the B1 dataset. However, assessing the change in viscosity datasets for ink A and ink B1 and comparing to the extrapolated trend presented by the ink A dataset, *B103* would be expected to fall within the 50 – 60 % range to bridge the gap between *B102* and *B104*. This assessment is supported by research conducted by Yanen *et al.*¹⁵⁹ which demonstrated the correlation between viscosity and MW for liquids containing PEG. As ink *B103* was composed of a larger concentration of PEG compared to *B102*, the MW and therefore the initial viscosity would be expected to be greater. This would then correlate theoretically with a greater change in viscosity as demonstrated by ink *A03*.

Finally, a consistent decrease in viscosity between 62.9 – 66.4 % (± 1.9) for ink B was observed during heating, suggesting minor changes in catalyst concentration (± 0.5 wt%) did not significantly impact ink stability during heating from 25 °C to 70 °C at high shear rates of 1000 s⁻¹. Overall, adjusting jetting temperature during printing will be the most effective on ink A formulations, especially for higher MW inks.

4.1.3 Reactivity of Dual-Ink Binder System

Polyaddition reactions were expected to occur between reactive ink pairings to form PU, continuing until no more [–OH] and/or [NCO] groups were available in the mixture. Over time functional group availability is expected to decrease over time while the number of urethane linkages increase throughout the PU sample.

4.1.3.1 Compositional Changes during Reaction Time

FTIR spectroscopy offers insight into the quantity and type of bonds present within a sample. Multiple separate measurements can be taken for a single sample over time. Spectral scans were run at set intervals of time for the same sample during polymerisation. An initial scan was run immediately to provide a baseline measurement at time 0 minutes followed by further scans at 3, 6, 25 and 60 minutes. The spectral data were collated and the rate of reaction observed by quantifying the change in transmission peak intensities across targeted spectral ranges. This process was followed for all reactive ink combinations, including reactive ink combinations A-B and A-B1, as shown in Figures 4.5 and 4.6, respectively.

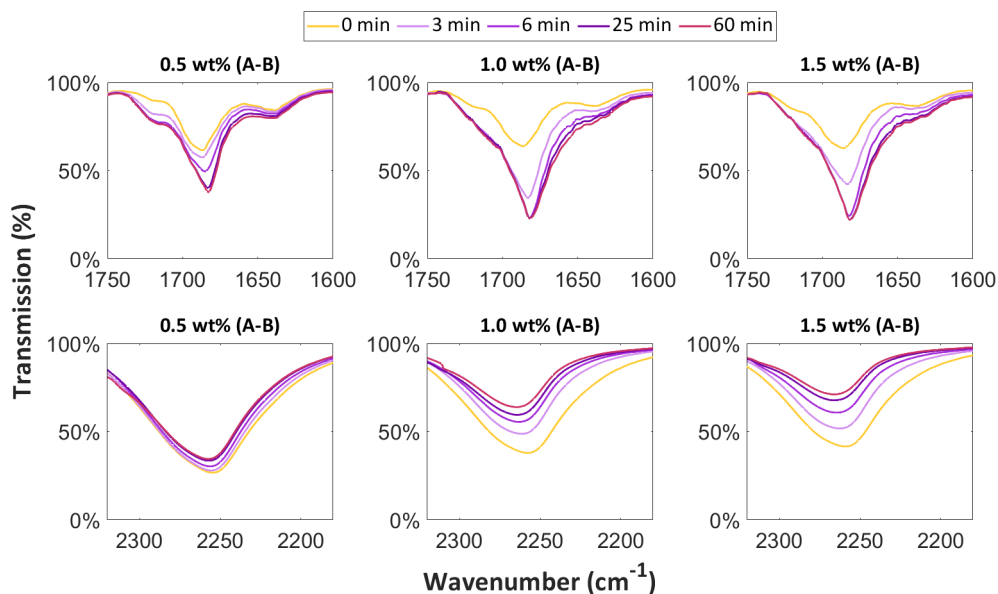


Figure 4.5: Changes in transmission peak intensities at 1750 - 1600 cm^{-1} (top) and 2325 - 2175 cm^{-1} (bottom) from 0 - 60 mins for reactive inks A03 and B01 at different DBTL concentrations.

Figure 4.5 shows the shifting of transmission peak intensities (%) from 0 - 60 minutes for reactive inks A03 and B01. Peaks which indicate the presence of isocyanates appear between 2325 - 2175 cm^{-1} (bottom row) as NCO stretching, whereas the presence of urethane linkages are associated with C=O stretching peaks between 1750 - 1600 cm^{-1} (top row).^{144,160,161} A reduction in isocyanate peak intensity at 2269 cm^{-1} is attributed to the consumption of NCO groups in the presence of hydroxyl groups found in polyols, such as polypropylene glycol, to form PU resins.¹⁵⁷ Longer reaction times lead to increased isocyanate transmission peaks along the bottom row as the number of available NCO groups reduce following reactions with hydroxyl groups.¹⁵⁸

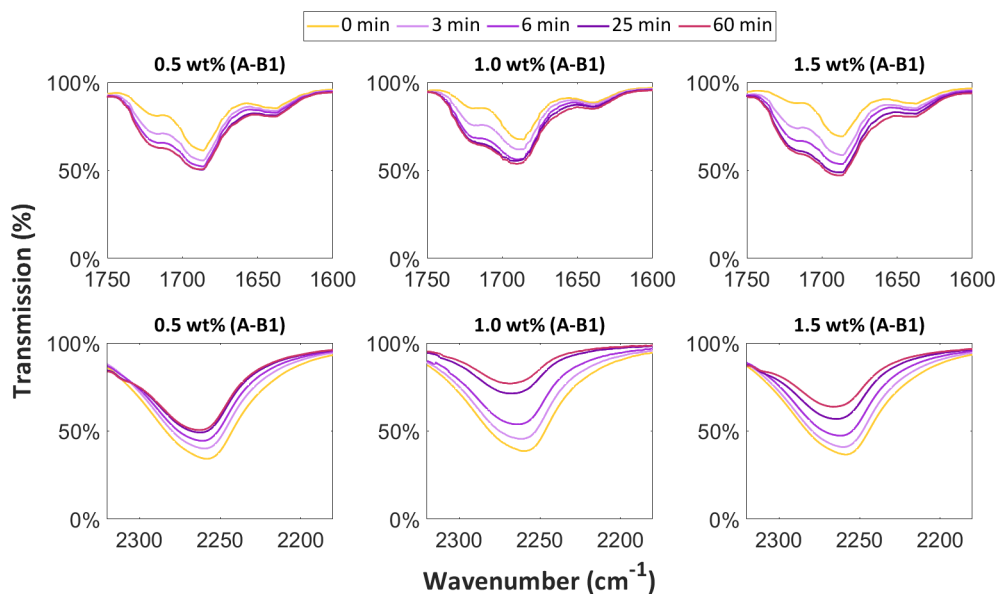


Figure 4.6: Change in transmission peak intensities at 1750 - 1600 cm^{-1} (top) and 2325 - 2175 cm^{-1} (bottom) from 0 - 60 mins for reactive inks A03 and B104 at different DBTL concentrations.

Composition identification based on peak transmission are assessed across a spectral ranges to account for variations in the chemical structures of isocyanates, polyols and polyurethanes. Existing literature promotes FTIR analyses for characterising different molecules present within blend systems as dipole-dipole interaction and hydrogen bonding elicit transmission peak changes and wavenumber shifts.¹⁶² For example, Badri *et al.*¹⁶¹ concluded the carbonyl group in urethane linkages shifted to the left as isocyanate content reduced across four PU samples, leading to weaker urethane bonds. Whereas, Hong *et al.*¹⁶³ found a wavenumber reduction, or shift to the right, for urethane linkage transmissions within the spectral range of 1750 - 1600 cm^{-1} indicated an increase in hydrogen bonding.

Each molecule has a unique spectral fingerprint defined by chemical bonds which each absorb IR at specific absorption wavelengths, aiding identification of material compositions.¹⁶⁴ Thus, based on FTIR results presented in Figures 4.5 and 4.6, there is robust evidence to support the hypothesis that PU had formed for all datasets. This is demonstrated by the reduction in isocyanate groups over time, as seen by the increasing transmission peak intensities located between 2275 - 2250 cm^{-1} (bottom rows) and decreasing peak intensities between 1750 - 1600 cm^{-1} . This inverse shifts suggest isocyanates are converting to urethane linkages over time as discuss earlier. Further

composition analyses via Thermogravimetric Analysis (TGA) are outlined in Section 5.2.3.3 for RBJ part characterisation.

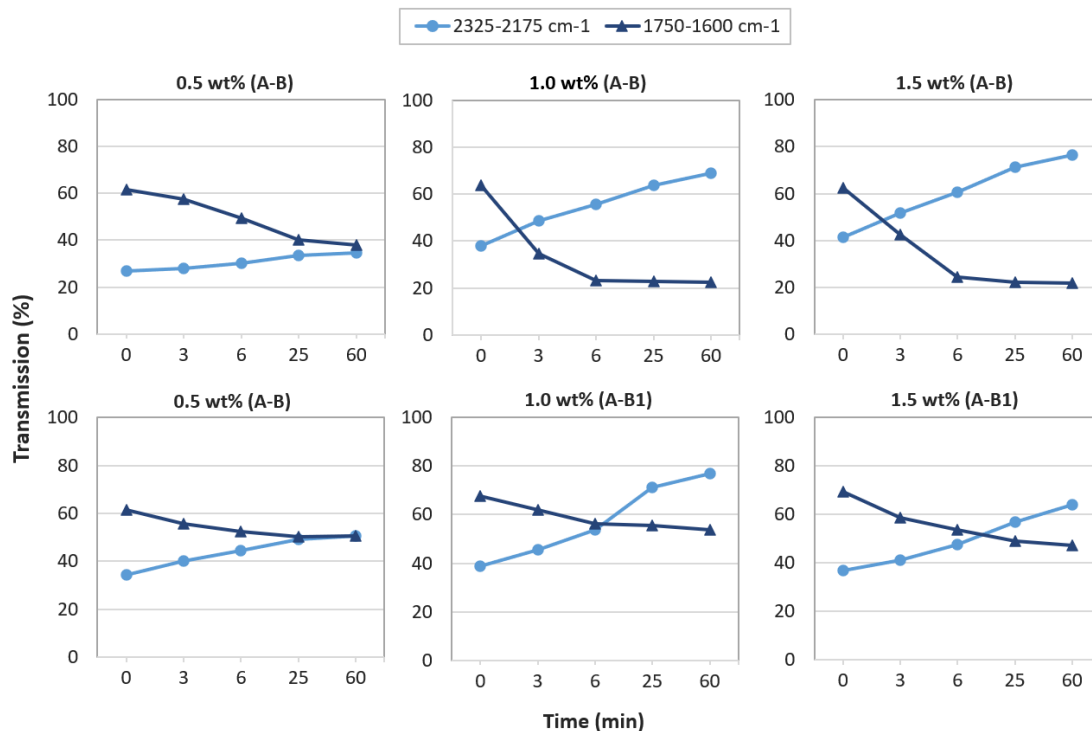


Figure 4.7: Change in intensity of transmission peak minima (by wavenumber) at 1750 - 1600 cm^{-1} and 2325 - 2175 cm^{-1} for reactive ink combinations A-B (top) and A-B1 (bottom) from 0 - 60 minutes.

Figure 4.7 compares the transmission intensities for peak minima at each time point (0, 3, 6, 25 and 60 minutes). Percentage transmission of $[-\text{NCO}]$ groups increased between 2325 - 2175 cm^{-1} while the percentage transmission for $[-\text{CO}-]$ groups between 1750 - 1600 cm^{-1} decreased proportionally. An inverse correlation was observed, suggesting polymerisation had occurred and an increasing amount PU formed over time. Similar trends have been observed for other research that characterised PU materials also composed of HDI, PEG and BD.^{159,165}

Based on PU reactivity research conducted by Kröber *et al.*¹¹⁷, rate of reaction or polymerisation will plateau over time (refer to Figure 2.20 in Section 2.3.2.3). This indicates at least one of the reactive inks has run out of available functional groups to elicit a reaction between the $[-\text{OH}]$ and $[\text{NCO}]$ present. Similarly, lines that plateau in Figure 4.7 are an indication the dual-ink binder system is no longer reacting. Assuming stoichiometry was maintained throughout, reactive ink pairings that plateau

the fastest, such as A-B at 1.0 wt% DBTL, formed PU the quickest. For powder AM techniques, powder layer consolidation time is critical for reducing printing times as well as increasing geometric accuracy and 'green' part stability.¹⁶⁶

Table 4.5: Percentage difference in peak transmission from 0 - 60 minutes.

Reactive Ink Combination Catalyst Concentration	A03 + B01			A03 + B104		
	0.5 wt%	1.0 wt%	1.5 wt%	0.5 wt%	1.0 wt%	1.5 wt%
Shift @ 2325 - 2175 cm^{-1}	29.2%	82.1%	84.5%	47.2%	99.2%	73.9%
Shift @ 1750 - 1600 cm^{-1}	38.7%	65.0%	65.5%	17.6%	20.5%	31.9%
Shift Difference	± 9.6%	± 17.1%	± 19.0%	± 30.3%	± 78.7%	± 42%

Polymerisation occurred across all reactive pairings between ink A03 and different catalytic concentrations of ink B from 0.5 - 1.5 wt %. Table 4.5 suggests degree of conversion was much higher for catalyst concentrations of 1.0 wt % or greater due to a significant percentage change over time for both functional groups.

Finally, given FTIR scans were conducted in ambient conditions, there was an exposure risk to water, thus polyurea may have formed in addition to PU. According to Wang *et al.*¹⁶⁷, secondary amide bond stretching at 1520 cm^{-1} could be an indication of either polyurea or PU. Therefore, to confirm compositional purity, FTIR analyses can be expanded to other wavenumber ranges in future work. It had not been necessary to pursue at this stage in project as the focus had been to confirm whether PU had formed and not search for impurities.

4.1.4 Selection of Suitable Reactive Inks for Reactive Binder Jetting (RBJ)

Selecting the most suitable reactive inks and respective dual-ink binder system pairings was based on three criteria deemed most critical to successfully apply Reactive Binder Jetting (RBJ) for manufacture PU. Weighted matrices were used to assess reactive ink data against miscibility, viscosity, and reactivity as summarised in Tables 4.6a, 4.6b and 4.6c. The selection criteria and their respective boundaries were summarised in Table 4.2 located in Section 4.1. Ink suitability across all datasets were rated either 0, 5, or 10 based on the defined boundaries.

Table 4.6: Weighted matrices (a) 'Miscibility', (b) 'Viscosity', and (c) 'Reactivity' for reactive ink A, B and B1.

Reactive Ink	Miscibility		Weight
	Bulk	Catalyst	
A04	10	-	10
A03	10	-	10
A02	10	-	10
A01	10	-	10
B01_1.0	-	5	5
B02_1.0	-	0	0
B03_1.0	-	10	10
B102_1.0	10	5	7.5
B107_1.0	10	0	5
B112_1.0	10	10	10

(a)

Reactive Ink	Viscosity		Weight
	60 °C	70 °C	
A04	0	0	0
A03	5	5	5
A02	5	10	8
A01	10	10	10
B01_0.5	5	5	5
B01_1.0	5	5	5
B01_1.5	5	5	5
B104_1.0	5	5	5
B103_1.0	5	5	5
B102_1.0	5	5	5
B101_1.0	5	10	8

(b)

Reactive Ink Combination	Catalyst Conc.	Reactivity		Weight
		[NCO]	[CO]	
A03 + B01	0.5 wt %	5	5	5
	1.0 wt %	10	10	10
	1.5 wt %	10	10	10
A03 + B103	0.5 wt %	5	0	3
	1.0 wt %	10	0	5
	1.5 wt %	10	5	8

(c)

Performance of each reactive ink and their respective pairings were assessed and given a rating. Average weightings are located along the right-hand column. Samples deemed most suitable within each selection criteria were highlighted green (rating 10), whereas those highlighted in red (rating 0) were considered least suitable, if not at all, for RBJ applications. This selection approach was used to identify which reactive ink

formulations to take forward for further testing via inkjet printing.

Miscibility for reactive inks containing stannous octoate (SO) at 2.0 wt % was the lowest for ink B, while ink B1 was more middling being valued at 5. Based on visual assessment alone, SO was deemed an unsuitable catalyst option due to visible white precipitates adhered to the internal surface of the vial. Rule of thumb to achieve jetting stability is to keep precipitates $< 1/10$ th of the nozzle orifice.¹⁶⁸ Other literature suggests $< 1/50$ th is more appropriate.¹⁶⁹ Based on this, no further characterisation was deemed necessary to rule out SO given the white precipitates were visible to the naked eye and appeared larger than the nozzle orifices located on the DMC-Samba printhead. With reference to Table 4.2, DBTL and DMEA were deemed suitable for further testing given no visible precipitates were observed following visual assessments for miscibility. It is noted that DIOL inks which contained DBTL were not as transparent compared to DMEA. Wang *et al.*¹⁴⁴ demonstrated successful inkjet printing of PU containing both DBTL and SO, supporting their case for RBJ suitability.

The top highest viscosity ratings were for inks A01, A02 and B101, suggesting these formulations would be most promising. However, if the DMC-Samba printhead is used the ratings applied at 60 °C should be taken into account instead. Thus, ink A01 was the safest option given it scored 10 across both temperature conditions. The lowest rated ink formulation was A04 which had fallen outside the printhead manufacturer's recommended viscosity range for both temperature conditions with 39.9 mPa s at 70 °C being the lowest datapoint.^{21,137} Thus, ink A04 was excluded from further testing. However, this viscosity criteria fails to consider the potential impact on droplet deposition of non-Newtonian fluids at high shear rates ($> 1000 \text{ s}^{-1}$). In this case, reactive ink demonstrated shear thinning at 1000 s^{-1} which is 2-3x lower than the expected shear rates during printing, suggesting there may be a greater viscosity tolerance for reactive inks.²⁰ Remaining ink formulations rated an average of 5, suggesting print parameter optimisation may improve jettability.

Reactivity tests were conducted on reactive ink pairing A-B and A-B1. Pairings that exhibited the greatest percentage change in transmission were rated highest (10) as it may lead to faster consolidation times and better geometric accuracy, addressing some

of the challenges associated with BJ.^{30,31,122} This was based on the hypothesis that a greater percentage in transmission peaks would lead to faster reactions. Ink combinations $A03 + B01_0.5$ and $A03 + B01_1.0$ had the largest average increase and reduction of [CO] and [NCO] groups, respectively. Across all datasets, an upward trend in reactivity ratings were observed for reactive inks with higher catalytic concentration. These results correlated with existing literature around PU chemistry.^{117,120} However, each catalyst will have a different effective reactivity concentration so further formulation testing should be done on a wider range of catalyst concentrations. For examples, compared to DBTL, SO has a very low efficiency at 0.01 wt % but then drastically increases disproportionately in effectiveness when a higher concentrations of 0.2 wt % is used.¹⁴⁴

One of each reactive ink family was selected to take forward into the next stage of development. Reactive ink $A01$ was selected based on lowest viscosity results to maximise the chance of successful jetting of reactive inks. However, ink A formulations that were rated 5 should also be considered in future work given the observed shear thinning tendencies in Section 4.1.2. Literature also suggests that viscosity can be too low for inkjet printing, especially powder AM where the ink might disperse easily, compromising geometric accuracy.²⁸

For the DIOL inks, $B01$ and $B102$ were selected to take forward. Based on the reactivity data outlined in this section, a catalytic concentration of 1.5 wt% was taken forward. However, it should be noted that during later-stage inkjet printing experiments outline later in this chapter, a higher concentration of 2 wt% was found to be more effective at producing fully reacted PU films. Additionally, Wang *et al.*¹⁴⁴ found that SO performed best 0.2 wt % with the lowest efficacy occurring at very low concentrations close to 0.01 wt %. As an iterative optimisation approach was taken throughout the development stage of the reactive inks discussed in this chapter, reformulations to improve printability were expected. With a strong correlation presented in Table 4.6c between increased catalytic concentration and faster reaction speeds, it was deemed unnecessary to repeat the time consuming FTIR tests for the new 2.0 wt% formulations. Instead extrapolations were made with confidence and were backed by the experiment results being obtained during inkjet printing. Finally, given the nature of powder AM processes, it

is especially critical for the reactive inks to react quickly before the next powder layer is recoated, further justifying the decision.⁶⁵

4.2 Inkjet Printing Optimisation for Reactive Inks

When preparing a new ink formulation for inkjet printing, particularly with a reactive aspect, critical criteria should be considered throughout the developmental phases including experimental testing. For the reactive dual-ink binder system presented in this thesis, the two most critical aspects considered are outlined below. Depending on the intended application, other criteria may be assessed to further optimise jetting performance and reliability.

- i **Droplet Generation:** Optimising print parameters (printhead temperature or jetting voltage) and waveform patterns to improve print quality.
- ii **Molar Ratio:** Calibrating net ink volumes to maintain optimal stoichiometry throughout the dual-ink printing process.

4.2.1 Droplet Generation

Generating optimal and reliable droplets is a common challenge encountered during jetting experiments for new ink formulations. As discussed in Section 2.1.3, the process of droplet formation is complex and variable between materials. Upon ejection, an ink may break up into small, discrete droplets called satellites. This is often attributed to several factors, including the presence of large particulates which obstruct nozzles, high viscosity inks with restricted mobility, and suboptimal waveforms that result in inadequate energy inputs. Many jetting issues can be mitigated by applying good laboratory practice and various optimisation methods. For example, risk of printhead clogging can be minimised by removing debris, contaminants, precipitates or other agglomeration by using a filter before loading the ink into a printhead cartridge.

Reactive inks selected for further testing in Section 4.1.4 were chosen based on independent experiments which tested for miscibility, viscosity and reactivity. The next stage of work focused on applying these reactive ink formulations to real inkjet printing conditions to generate optimal droplets. Jetting suitability was assessed based on

droplet formation and reliability as variable outputs could lead to a higher probability of RBJ print failures due to incorrect stoichiometry leading to incomplete reactions and therefore poor powder consolidation.

Jetting temperature, voltage, and waveform profile were deemed the three most critical parameters to be assessed to achieve successful RBJ printing and part performance. To validate the suitability of selected reactive inks for inkjet printing, these parameters were optimised to elicit reliable droplet generation. Results obtained during jetting optimisation are outlined later in this section.

Finally, optimised print parameters for DMC-11610 printheads were later re-optimised to be compatible with DMC-Samba printheads. Print parameters optimised for the latter have been presented throughout.

4.2.1.1 Impact of Jetting Temperature

Printhead temperatures for the selected reactive inks were set at 60 °C for ink *A01* and 55 °C for inks *B01_2.0* and *B102_2.0*, respectively. All temperature tests had been conducted between 30 °C and 60 °C following the transition from DMC-11610 to DMC-Samba printhead halfway through the project. Jetting behaviour, was visually analysed using mostly videos of the droplet between 50 and 200 μs .¹⁷⁰ It was observed during temperature scanning that ink *B1* droplets were more prone to spraying at an angle to the central axis at the higher temperatures. This behaviour was exaggerated when the voltage was increased as well. Several small, disconnected droplets, or satellites, would continuously jet until the printhead surface was flooded by sprayed ink, agglomerating at the nozzle orifices and preventing further droplet generation. The only way to recover the printhead functionality at this stage was to wipe the nozzle array clean with a felt-free cloth.

4.2.1.2 Impact of Jetting Voltage

Maintaining a desired stoichiometric ratio between reactive ink pairings was a critical objective to achieve effective polymerise.¹⁴⁴ Therefore, jetting voltage optimisation was conducted to achieve reliable droplet generation and deposition. Jetting quality was assessed across the full range of available DMP printing voltages ranging from 18-40 V

and presented in Figure 4.8 against predefined performance boundaries.

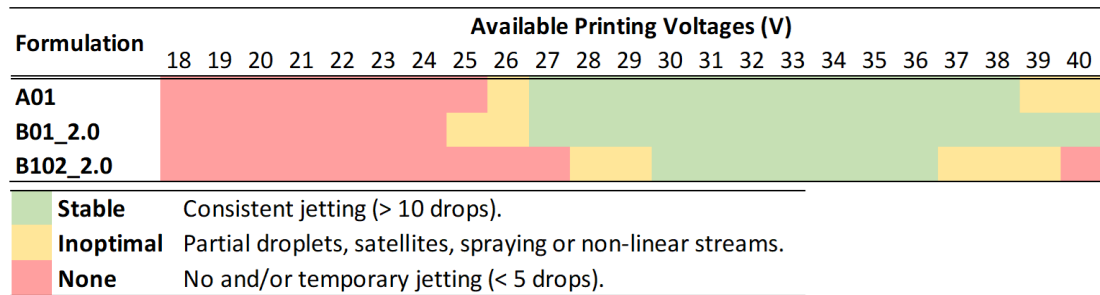


Figure 4.8: Colour mapping of print performance across the full range of available voltages from 18-40 V with key.

The most stable printing voltages were able to jet more than 10 identical droplets without requiring intervention, such as purging or wiping the printhead nozzles. For ink A01 and B01_2.0 the most suitable voltage ranges were observed to be between 27-38 V and B01_2.0, respectively. A much narrower range of 30-36 V was observed for ink B1_1 : 4.

4.2.1.3 Impact of Waveform Profile

Waveform profiles impact droplet formation so must be optimised for each ink. By adjusting the peak height, or percentage of maximum input voltage, and the width, or duration, of each peak and trough, optimal droplets can often be achieved. Both the material properties and the net energy going into the system must be accounted for during this process. For example, with an ink of the same composition, a maximum jetting voltage of 40 V should theoretically generate larger droplets than when the voltage is set at 30 V.^{16,171-173} This is due to a larger ejection force being exerted through nozzle, causing a greater pressure difference between the ink reservoir and the nozzle orifice. In other words, a greater distance is created between the two piezoelectric surfaces located on opposite ends of the printhead ink cavity.

Throughout the optimisation process, trade-offs between droplet volume, ejection speed, and jetting reliability were considered. For example, to generate larger droplets the rate of ejection may decrease due to longer waveform times. Alternatively, higher voltages may be used to overcome the resistive forces in an ink but then cause to satellite droplets or spraying to occur. This highlights the importance of optimising the print settings

and waveform pattern to suit a given ink with its own unique material properties.

Within the Dimatix software suite, the *Waveform Editor* tool was used to create and edit waveforms up to 24 μs . Figure 4.9 provides an example of a single waveform pattern of 8 μs which had been optimised for use with reactive ink *B102_2.0*.

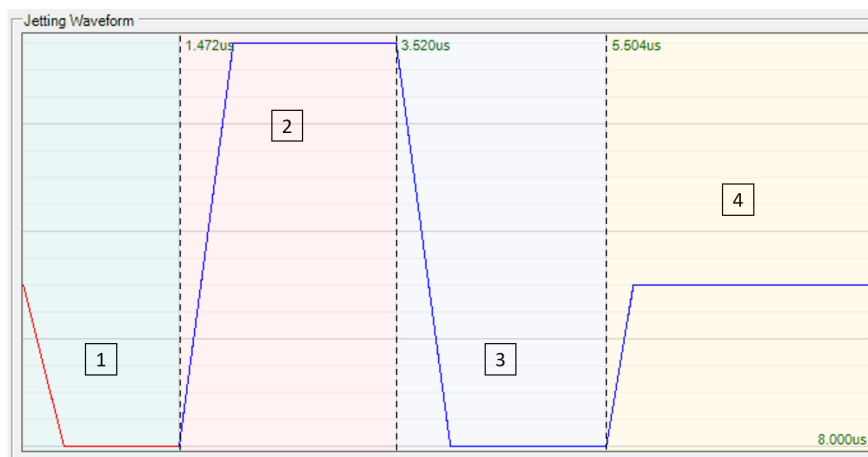


Figure 4.9: Example of a single waveform pattern with labelled segments.

Each peak and trough, including the rate of transition (gradient lines), count as a single segment. Typically, a minimum of two segments - one peak and one trough - are required to eject a droplet. An extensive waveform optimisation process was applied to each reactive ink family, starting with a simple three-segment profile similar to the one shown in Figure 2.3. From there trials were conducted using live droplet viewing software for a range of voltage parameters. This was then repeated for every additional segment added up to five. Four segments were found to be sufficient to achieve reliable droplet generation for all reactive inks.

4.2.2 Molar Ratio of Dual-Ink Binder System

To achieve high quality 3D parts using reactive inks, it was essential to maintain the desired stoichiometric ratio between ISO and DIOL reactive inks during printing. Minor stoichiometric variations in PU systems leads to very different materials property outputs, thus for the purposes of this research a baseline stoichiometry of 1:1 was chosen.¹⁷⁴ However, there is scope in future to test different ratios to see how RBJ part properties change. Finally, new methodologies were developed to achieve a desired molar ratio for all ink combinations (A-B and A-B1). These have been summarised in Section 3.2.4.2.

4.2.2.1 Number of Moles per Droplet

To determine the number of moles in a single jetted droplet of a specified ink formulation and associated print parameters, the following calculation were applied:

$$\text{Moles per Droplet} = \frac{\text{Average Droplet Mass}}{\text{Estimated Molar Mass}} \quad (4.1)$$

Average Droplet Mass To obtain an average droplet mass, 1,000,000 droplets were jetted into a weigh boat using the integrated *Drop Volume Measurement* tool within the Dimatix software suite. The net mass was sufficient for a scientific mass balance to take an accurate measurement and the number of repeated droplet ejections was high enough to ensure the average mass of a single droplet could be considered reliable. An essential step in the process was for the boat to be weighed before the 1,000,000 droplets were deposited. The respective weight of the empty boat was then subtracted from the measured mass of both the boat and 1,000,000 droplets.

Repeated measurements were taken for all three reactive inks across all suitable print voltages and summarised in Figure 4.10 below. For reference, Section 4.2.1.2 summarises the process and corresponding results for assessing suitable print voltage ranges.

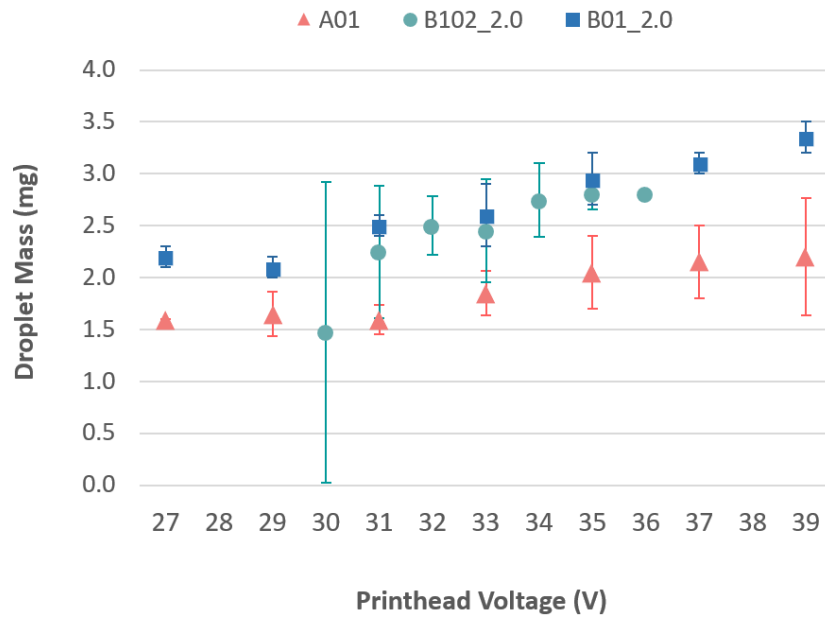


Figure 4.10: Droplet mass with error bars for reactive inks - A01, B01_2.0, and B102_2.0 - at suitable print voltages.

Finally, each measurement was divided by 1,000,000 to obtain an average mass per droplet then divided again by the formulation molar mass to obtain an estimate for the number of moles present in a single jetted droplet. Jetting reliability and relevant error margins have been assessed and discussed in Section 4.2.2.2.

Estimating Molar Mass The molar ratio of a reactive ink required careful consideration to ensure the desired material properties were obtained following the PU reaction. Due to the compositional complexity of reactive inks, the formulation molar mass was estimated using Equation 4.2 below. Thus, formulation molar mass (FMM) of the reactive inks was calculated based on constituent molar masses (CMM).

$$FMM_{(X_Y:Z)} = \frac{y}{y+z} * CMM_{(X1)} + \frac{z}{y+z} * CMM_{(X2)} \quad (4.2)$$

where X is the reactive ink family composed of monomers $X1$ and $X2$, $Y : Z$ is molar ratio of the reactive ink, y is one fraction of the molar ratio, z is the other fraction of the molar ratio,

$X1$ is the constituent molar mass of monomer $X1$ and $X2$ is the constituent molar mass of monomer $X2$.

With reference to Table 4.7, which summarises constituent material properties, the formulation molar mass for $B1_1 : 4$ was calculated by applying Equation 4.2 as follows:

$$FMW_{(B1_1:4)} = \frac{1}{5}(400) + \frac{4}{5}(62.1) = 129.68g\ mol^{-1}$$

Table 4.7: Summary of constituent materials properties for reactive inks A01, B01_2.0, and B102_2.0.

Property	Units	Constituent Materials					
		PHDI	1,6-HDI	PEG ₄₀₀	EG	BD	DBTDL
Molar Mass	g mol⁻¹	478.6	168.2	400.0	62.1	90.1	631.6
Density	g cm⁻³	1.12	1.05	1.13	1.11	1.02	1.07

A summary of molar mass estimations for all three reactive inks can be found in Table 4.4 located in Section 4.1.4 whereby optimal ink formulations were selected for fur-

ther development. For ease, molar masses for these optimal formulations have been summarised in Table 4.8 below:

Table 4.8: Summary of molar masses and densities for reactive inks A01, B01_2.0, and B102_2.0.

Property	Units	Formulations		
		A01	B102_2.0	B01_2.0
Molar Mass	g mol^{-1}	199.2	129.7	100.7
Density	g cm^{-3}	1.06	1.11	1.02

Moles per droplet across the full range of suitable print voltages for each ink formulation was calculated using Equation 4.1. Each dataset was plotted with error margins in Figure 4.15 and discussed further in Section 4.2.2.2.

Increasing Moles per Drop Print settings were adjusted to access a wider range of moles per droplet outputs to maximise the probability of finding compatible reactive inks pairings of optimal stoichiometry. Jetting waveforms were manipulated to achieve larger droplet volumes and, thus, more moles per print layer.

Utilising the *Waveform Editor* tool integrated into the Dimatix software suite, waveforms were tailored to each reactive ink family. The maximum waveform time allowed within a single plot for DMPs was 24 μs which allowed a pattern of peaks and troughs to be repeated within a single waveform file. Figure 4.11 provides an example of a waveform file produced with three repeating waveform patterns of duration 8 μs each.

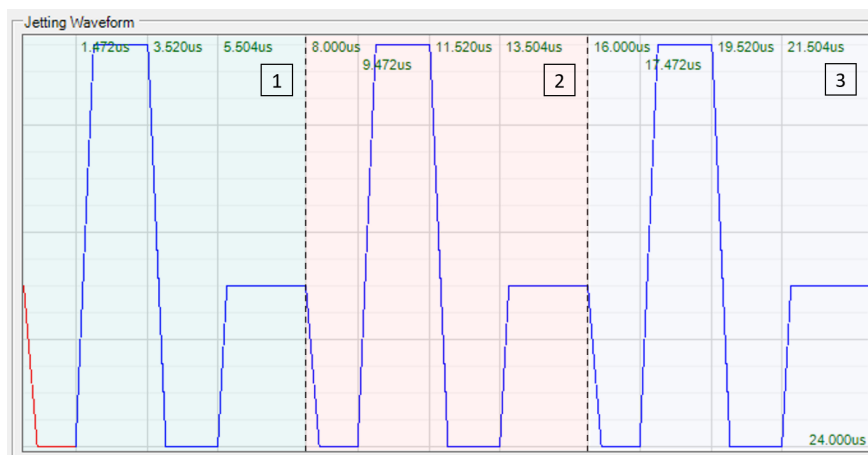


Figure 4.11: Example of a multiple-pattern waveform (MPW) with each of the three repeat patterns labelled.

Stationary images from a video recording were collated and labelled in Figure 4.12, highlighting the evolution of droplet generation for the multiple-pattern waveform (MPW) shown in Figure 4.11 when applied to ink *B102_2.0* at 32 V.

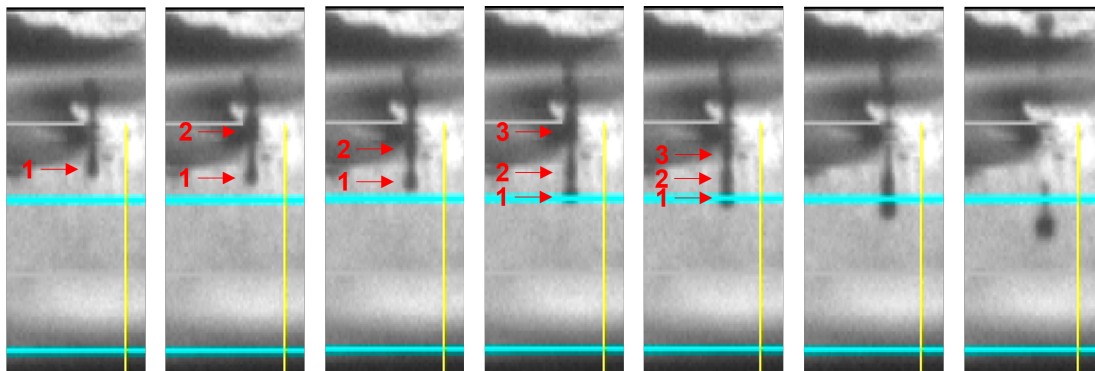


Figure 4.12: Array of still images from a slow-motion recording of a droplet generated using a triple multiple-pattern waveform (MPW).

With an aim of achieving a stoichiometric ratio of 1:1 between ISO and DIOL inks, MPWs were explored as a mechanism for control molar ratio during jetting. For examples, moles per droplet measurements for *A01* were found to be in the range of 8.03 - 11.04, whereas inks *B102_2.0* and *B01_2.0* ranged from 11.38-21.60 and 22.42-34.14, respectively. Thus, to achieve the desired stoichiometry ink *A01* would benefit from generating larger droplets using MPWs.

To streamline waveform developments, print settings including maximum voltage input, were selected based on qualitative observation of jetting reliability and remained fixed throughout. Once 2x and 3x MPWs were created for both inks, the built-in Dimatix *Drop Volume Measurement* tool was used once again to calculate the total droplet mass and, following the same approach in Section 4.2.2.1, the number of moles per MPW droplet.

The MPW results for inks *A01* and *B102_2.0* were plotted against their respective baseline values in Figure 4.13. The gradients between 1x, 2x and 3x waveform pattern were measured and the value applied to rest of the ink baseline datasets. For example, reactive ink *B01_2.0* was found to deliver 26.50 moles with every drop at 33 V for a single-pattern waveform (see Figure 4.15). However, by applying a multiply factor of 2.06 (gradient) to the baseline value, an extrapolated droplet volume, or molar density, was estimated with this model and summarised in the plot below.

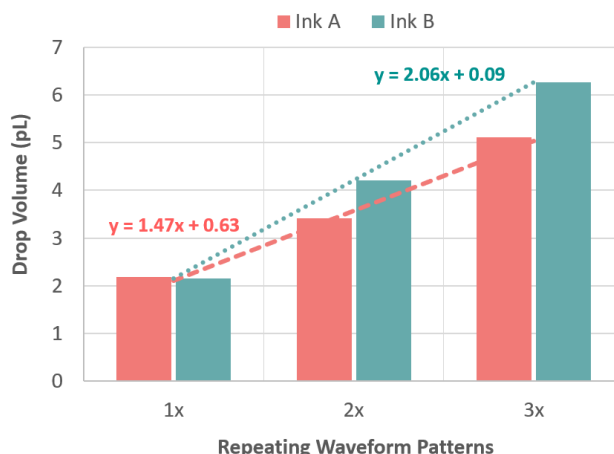


Figure 4.13: Measured droplet volumes for reactive inks A01 and B102_2.0 at 1x, 2x, and 3x waveforms.

As highlighted above, extrapolated moles per droplet values for inks A01 and B102_2.0 within the printable jetting voltages have been summarised in Figure 4.14, alongside the ink B01_2.0 baseline values.

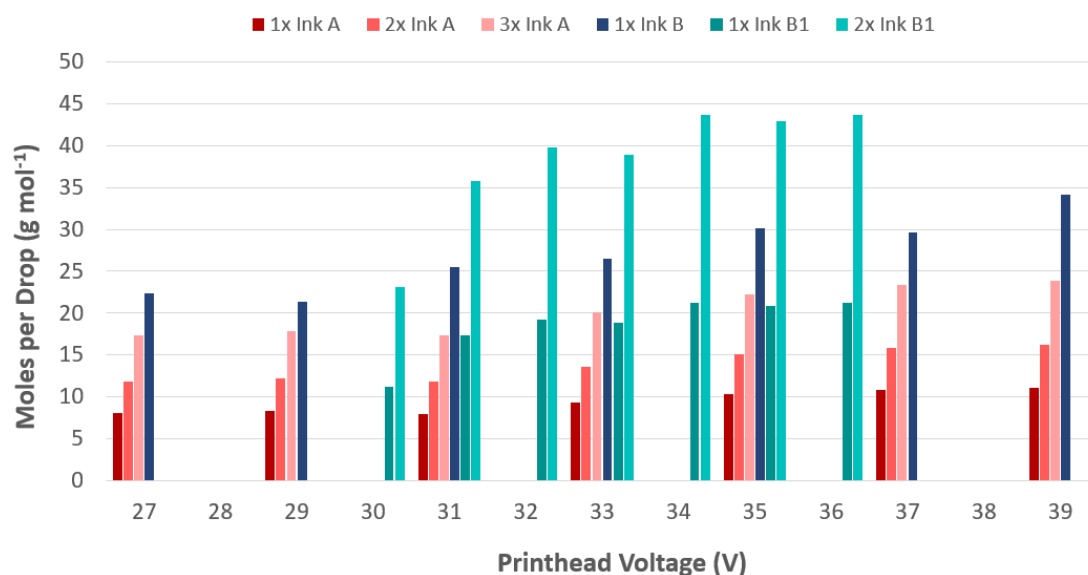


Figure 4.14: Histogram of moles per droplet measurements for reactive inks A01, B01_2.0, and B102_2.0 across their respective suitable printhead temperatures ranges outlined in Figure 4.8.

4.2.2.2 Stoichiometry Calibration of Dual-Ink Binders

This section focused on further optimising the reaction efficiency between reactive inks. The results obtained in previous sections were assessed based on percentage error, or printing reliability, with the most reliable ink settings taken forward. Therefore, print

parameters which proved to be unstable were removed. From the remaining datasets, reactive inks were optimally paired and their deviation from an optimal 1:1 molar ratio measured. Any ink combinations which fell outside of the acceptable compatibility boundaries previously discussed in Section 2.1.2.3 were eliminated. Any ink combinations which remained were considered to be optimal and would maximise the probability of successful printing.

Jetting Reliability As a continuation to Section 4.2.2.1, the average moles per drop for each reactive ink were plotted below in Figure 4.15 with error bars. Datasets circled in yellow exhibited large percentage errors of over 10 %. Thus, these print parameters were eliminated from the selection pool due to poor jetting reliability and an increased risk of undesired molar ratios.

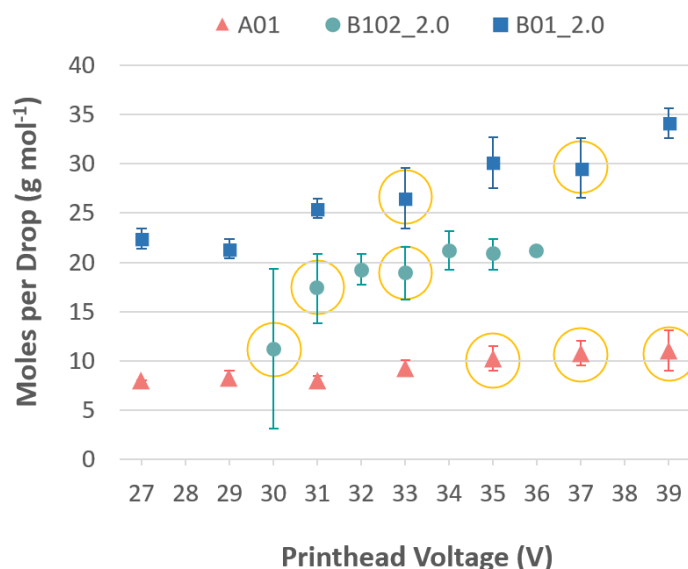


Figure 4.15: Moles per droplet measurements with error bars for reactive inks A01, B01_2.0, and B102_2.0 at suitable print voltages.

For inks A01 and B102_2.0 errors occurred at the ends of their respective printable voltage ranges, correlating with the qualitative trends observed on Section 4.2.1.2. It is possible with some minor adjustments to their waveforms that jetting reliability could be improved in those regions but it would likely arise at the expense of jetting reliability at the opposite end of the printability spectrum.

For ink B01_2.0, there was no error trends observed. Random error occurrence suggested the jetting issue was either with the formulation itself or variations in printhead

performance between batches. Given the disposable nature of Dimatix printheads and the number of faults reported each year, it is very likely that the specific printhead used for this experiment were not performing optimally. This theory is supported by ink *B01_2.0* results outlined in Section 4.1, which demonstrated stable temperature-based viscosity outputs.

Extrapolated datasets (e.g. 3x Ink *A01*) were subjected to the same standard deviations but at the larger moles per drop values. Figure 4.16 provides a histogram of reliable data points only, omitting data with significant errors (<10 %).

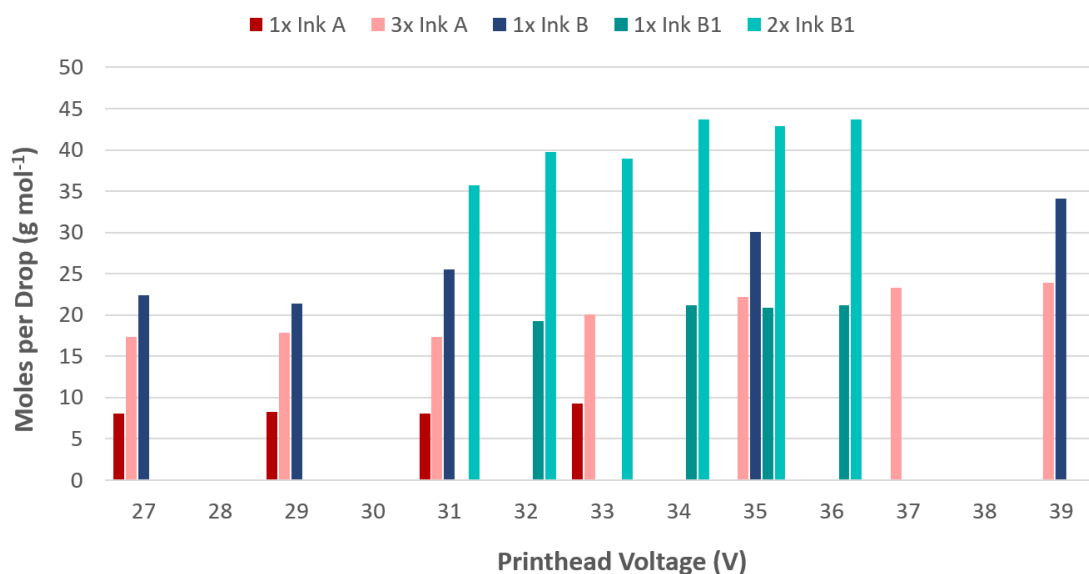


Figure 4.16: Plot of moles per droplet measurements at suitable printhead voltages for selected reactive inks associated with reliable jetting characteristics (<10 % deviation from mean).

With reference to Figure 4.8, jetting voltage outputs for *B01_2.0* were obtained on the same day with the same formulation batch and printhead. Given jetting stability was observed between 27 V to 40 V, data variability at 33 V and 37 V was unexpected. However, the molar ratio calibration experiments were conducted over several days, thus increasing the chance of printing failing between tests.

Reaction Pairing Following the removal of unreliable data points, the remaining isocyanate values were paired with the nearest suitable DIOL ink value for both inks B and B1, respectively. Given the optimal molar ratio of 1:1, percentage differences for each pairing were calculated and any pairings with more than 10 % error were eliminated. The remaining optimal reactive ink pairings have been listed in Table 4.9.

Table 4.9: Colour mapping of all suitable reactive ink pairings with key.

	Ink A	Ink B	Ink B1
	3x 33 V		1x 32 V
			1x 35 V
	3x 35 V	1x 27 V	1x 34 V
		1x 29 V	1x 36 V
	Optimal Meets all conditions without concern.		
	Cautionary Jetting reliability concerns with parent dataset.		

For pairings highlighted in orange, it was recommended for users to proceed with caution regarding the jetting reliability of applying MPWs. However, in all cases final selection of ink pairings were always validated before use as slight variations in equipment, material, and environmental conditions had potential to negatively impact the reaction mechanism.

Going into the next stages of development one pair of reactive inks were selected to streamline experimentations. Based on results in this section, inks *A01* and *B1_1 : 4_2.0* performed best throughout with reliable jetting and optimal molar matching. For ink A, a MPW composed of three repeating patterns jetted at a maximum voltage of 33 V is selected. For ink B1, a simple waveform with no repeating pattern is selected to be jetting at 35 V.

Table 4.9 indicated ink B1 jets optimally at 32 V, however numerical data indicated 35 V was superior in performance with a 7.4 % error in jetting reliability compared to 8.0 % at 32 V. Additionally, deviations in molar mass for 35 V was 3.8 % compared to 3.9 % for 32 V. Thus, 35 V consistently outperformed 32 V despite both parameters meeting the minimum requirement for selection.

4.3 Validation of Reactive Inks on Non-Porous Substrate

Previous reactive ink developments and selections were validated via inkjet printing onto non-porous substrates, including polyethylene terephthalate (PET) and glass. The primary objectives were to confirm jetting reliability and degree of conversion between inks A and B1. Printing parameters, such as droplet spacing, working distance, nozzle

purging frequency, and more, were considered throughout the process. Observations are shared later on in Chapters 5 and 6.

The modified LP50 printer described in Section 3.2.4 was introduced at this stage, complete with a glove box, nitrogen system and hygrometer. Both Dimatix and LP50 printers were used in combination, the former to perform quality checks on the DMC disposable printhead and the latter to instantaneously jet consecutive reactive ink droplets onto a chosen substrate. In this section, the custom build platform designed for powder AM were set up for non-porous substrate printing by taping PET film to the adjustable metal build plate.

4.3.1 Initial Quality Checks

Following printhead quality checks, which often involved repeatedly purging and wiping nozzles, each printhead was carefully removed from the Dimatix printer and glove box. These were then transferred into the LP50 glove box where they were fixed into the custom dual-printhead module.

Based on the observations made during quality checks, nozzles exhibiting persistent undesirable characteristics were disengaged via the LP50 settings. Once printer calibration and set up was complete, jetting accuracy and quality was assessed through signature prints shown in Figure 4.17.

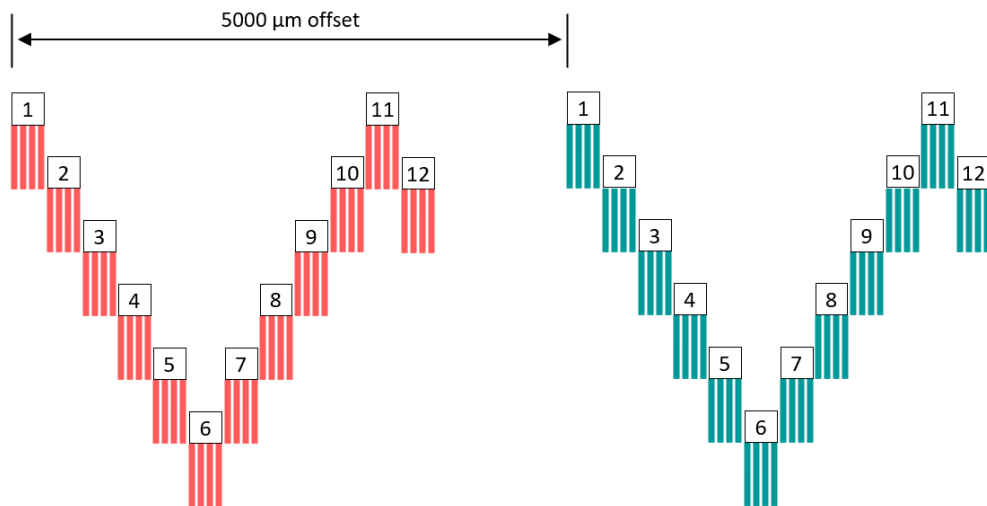


Figure 4.17: Print pattern ('signature') and layout used to assess nozzle functionality of each printhead.

Each segment was associated with one of the twelve nozzles on a given printhead as per the labels. During printing all nozzles jetted simultaneously over four vertical print passes, creating four columns of droplets as seen in Figure 4.18.

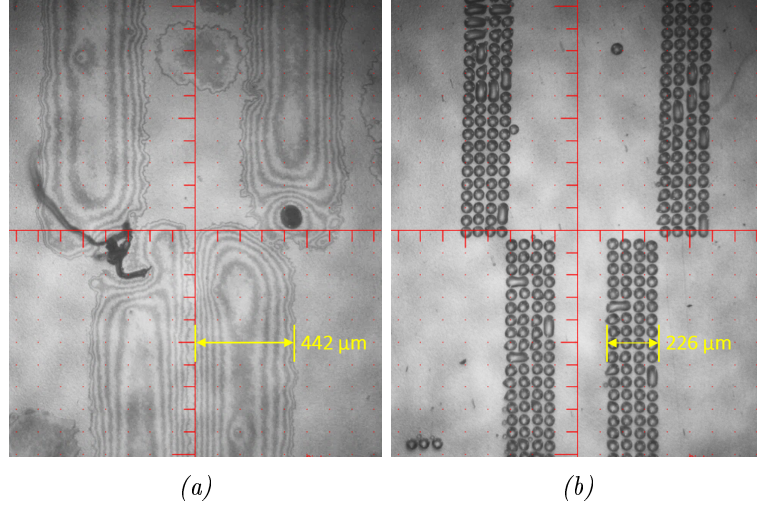


Figure 4.18: Images of print signatures for ink (a) A01 jetted at 32 V/55 °C using 3x MPW and (b) B102_2.0 jetted at 35 V/60 °C via 1x waveform; captured using an LP50 integrated camera.

From these images, nozzles 4, 5, 7, and 8 were functioning effectively for ink A (Figure 4.18a) as well as the ink B1 (Figure 4.18b) printheads as indicated by the individually defined segments and minimal splattering of ink droplets in the print peripherals. Ink A01 was observed to have a wider footprint by approximately 2x compared to that of ink B102_2.0. Additionally, individual droplets could not be distinguished due to coalescence toward the centre of each segment indicated by the ringed edges. HDI and PET are hydrophobic while EG is hydrophilic. Therefore, Ink A wetting was likely caused by the strong attractive forces experienced at the interface of two hydrophobic surfaces.

This behaviour continued with increasing print layers, or net ink volume deposited, as seen in Figures (4.19a-4.19c). However, by 10x single-ink layers of ink A (Figure 4.19d), there were no ringed edges and the print appeared generally more uniform across the surface. Contrarily, ink B1 droplets appeared to retain their original position and coalescence locally between neighbouring droplets, resulting in a clearly defined corner by 10x single-ink layers (Figure 4.19h).

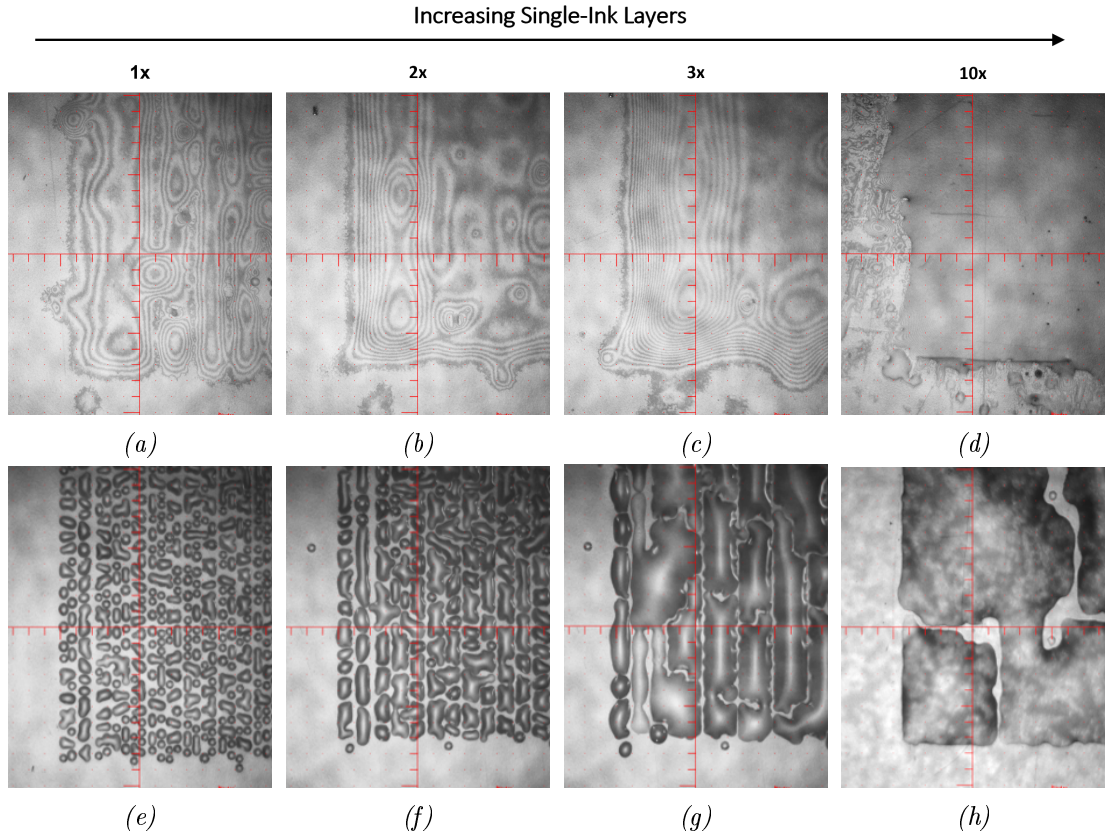


Figure 4.19: Images of single-ink layers at 1x, 2x, 3x, and 10x for (a)-(d) ink A01 printed at 33 V/60 °C using a 3x MPW and (e)-(h) ink B102 printed at 35 V/55 °C via 1x waveform; red hatched lines are spaced 100 μm apart for scale.

Compared to ink B1 in Figures (4.19e-4.19h), the geometric accuracy of ink A was on average poorer as seen by the uneven edges throughout. Additionally, droplets were noted in the print peripherals suggesting ink A was not performing optimally whereas ink B1 was. There were many potential causes for why ink A did not print accurately including:

- i Printhead had one or more nozzles clogged and required cleaning to prevent ink spraying outside the intended print area.
- ii Reactive ink has been formulated incorrectly and/or the constituent materials used were compromised causing unpredictable performance.
- iii Print parameters and/or waveform was unstable and required further optimisation to improve jetting reliability.

4.3.2 Mixing Behaviour

Figure 4.20 highlights the impact clogged or dysfunctional printhead nozzles had on the bulk print. In this specific situation, an ink A printhead nozzle malfunctioned based on the distinct visual characteristics of each reactive ink. However, this not only skewed the molar ratio but also compromised the cohesion between print lines, reducing the overall print quality.

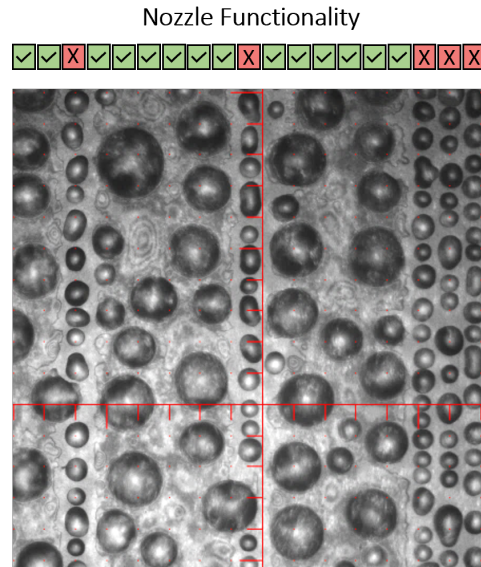


Figure 4.20: Demonstration of dysfunctional nozzles for a 1x dual-ink print layer on PET substrate composed of ink A01 printed at 35 V/60 °C using a 3x MPW and B102 printed at 33 V/55 °C using a 1x waveform; red hatched lines are spaced 100 μm apart for scale.

Additionally, this image provided insight into the mixing behaviour of both inks. In areas where both inks were successfully deposited, a faint ink A residue had visibly adhered to the film with minimal spreading as seen by the clean edges adjacent to ink B print lines. It is theorised that both ink A and ink B agglomerated to form larger droplets ranging from 213 μm to 1000 μm in diameter, thus explaining the lack of outward ink A spreading.

To confirm these predictions, 10x reactive ink layers were printed with a 500 μm offset on PET film. The result can be seen in Figure 4.21 whereby three distinct regions - ink A only, ink A with ink B1, and ink B1 only - were observed.

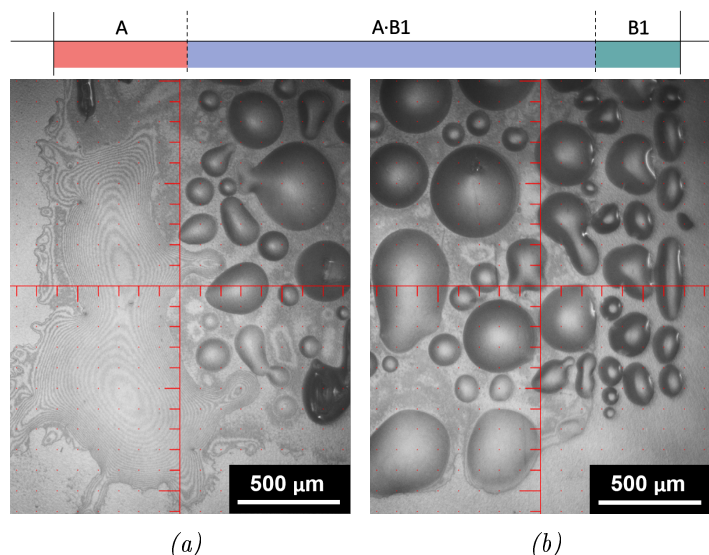


Figure 4.21: Images of 10x dual-ink 10 mm square print at a 500 μm offset to show ink behaviour in the dual-ink, (a) ink A only, and (b) ink B1 only regions; red hatched lines are spaced 100 μm apart for scale.

From this image, it is clear ink A had a higher tendency to spread, unevenly and outward in all directions. Additionally, ink A presented few individual droplets, suggesting a higher affinity to itself and, thus, a tendency to coalesce. Finally, within the overlapped region, ink A residue was visible on the film and droplets formed with a profile similar to that of ink B droplets but were instead 2-5x larger in diameter. This confirmed, both ink A and ink B mixed to form much larger droplets in regions where both inks had been successfully printed.

4.3.3 Degree of Polymerisation

Following several print iterations, optimised print parameters and waveform patterns were applied to assess print quality. Thus, 15x overlapped, alternating dual-ink layers were printed onto PET at a net 1:1 molar ratio. Quality was assessed both visually and via FTIR spectroscopy analysis of the following characteristic peaks:

- 3320 cm^{-1} (bonded N-H)
- 2260 cm^{-1} (N=C=O)
- 1690 cm^{-1} (urethane linkage)

Figure 4.22 provided both an image of the 15x dual-ink layer printed on PET film and three FTIR transmission scans across the sample. Reactive inks A01 jetted at 32 V/55

$^{\circ}\text{C}$ via 3x MPW and B102 jetted at 35 V/ 60°C via 1x waveform were applied to form the film. Most importantly, there were no peaks present at 2260 cm^{-1} indicating all isocyanate groups had reacted. However, this did not necessarily mean PU had formed.

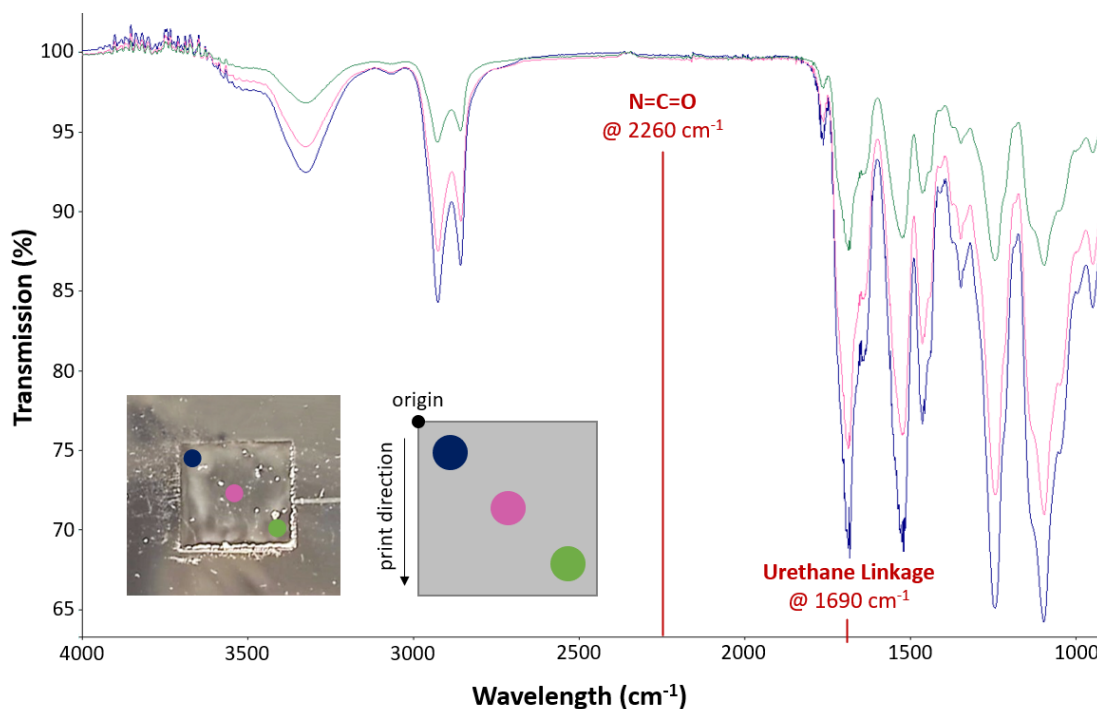


Figure 4.22: Collated image of three FTIR transmission scans at colour coded points across a PU film printed on PET composed of reactive inks A01 jetted at 32 V/ 55°C via 3x MPW and B102 jetted at 35 V/ 60°C via 1x waveform.

The PU film was printed inside a glove box with humidity ranging between 10-12 % at the start of printing. Often, the glove box would begin leaking immediately, raising the humidity over time as indicated by the hygrometer placed in the glove box. As such, it was not possible with the equipment available to completely remove moisture from the enclosed space to start with, nor was it possible to maintain a constant humidity level over time. With an increased risk of isocyanate groups reacting with water present in the glove box, there was concern that the reactive inks did not fully polymerise and that PU had not successfully formed.

FTIR spectra results presented in Figure 4.22 suggest PU was present as indicated by the peak transmissions located at 1690 cm^{-1} .^{144,160,161,163} These are often associated with C=O stretching in urethane linkages. However, these peak transmission intensities appear to increase over time, suggesting the amount of urethane present at the green dot is lower than at the navy dot nearest the print origin. Thus, degree of polymerisation

to PU was proportionally lower as the scanning point moved diagonally away from the print origin.

It is theorised that as the humidity levels in the glove box increased, ISO groups in the ISO ink began reacting with H_2O to form CO_2 instead of reacting with the available hydroxyl groups present in the DIOL ink.¹³² This is further supported by the lack of transmission peaks at 2260 cm^{-1} which would indicate NCO stretching and therefore the presence of isocyanates. Therefore, at the start of printing when there was less moisture in the glove, the conversion to PU was greatest as indicated by the navy spectrum and associated dot near the print origin on the film.

Finally, through physical touch there was no tackiness or smudging and a light scratch across the surface resulted in no visible damage to the print except to the PET film. Further supporting the hypothesis that PU had formed following the subsequent deposition and mixing of two reactive inks to form a dual-ink binder system without the presence of powder.

Reactive inkjet printing on non-porous substrate was validated in this chapter following incremental developments and optimisations to the reactive ink formulations and printing processes. Finally, the suitability of these reactive inks for powder-based printing, specifically Reactive Binder Jetting (RBJ), is discussed further in Chapters 5 and 6.

4.4 Summary

The results presented in this chapter delved into the feasibility of using novel RBJ printing techniques within PU manufacturing. Experiments focused on the development and optimisation of specialised ink formulations capable of consolidating powder via a dual-ink reactive binder system. Contrary to conventional BJ printing processes, where binders are applied temporarily to keep the powder consolidated during sintering, RBJ utilises a reactive dual-ink binder system to form consolidated PU parts without the need for further post-processing. Thus, this chapter underscores the importance of rigorous development and exploration of various reactive ink constituents to ensure the dual-ink binder performs reliably during jetting.

Research commenced by selecting three distinct families of reactive ink formulations grounded in existing PU research. These formulations were characterised to identify the most promising options for successful inkjet printing. Critical parameters, including temperature, voltage, and waveform profile, were meticulously optimised to enhance control over reactive ink deposition and maximising the probability of successful manufactured parts of good quality.

To ascertain the printability of the selected formulations, a thorough analysis of reactive ink properties, including miscibility, viscosity, and reactivity, was conducted. This multifaceted evaluation facilitated the identification of the most suitable ink formulations by leveraging weighted matrices to weigh and rank the various outputs deemed most desirable for the dual-ink binder system to be effective.

Further experimentation focused on generating stable droplets and calibrating molar ratios between reactive inks. Both voltage outputs and waveform patterns were systematically optimised to achieve stable droplet jetting across each of the three reactive inks. Following this, dual-ink binder calibration protocols were implemented to match molar ratios between reactive ink components, thus maximising the probability of full polymerisation for each dual-ink binder system.

Initial validation of RBJ printing suitability was conducted by jetting the dual-ink binders onto a non-porous substrate to assess binder composition and reaction times. Initial quality checks and assessments of ink mixing behaviour underscored the efficacy of the selected ink formulations. The degree of polymerisation for the binder systems were measured using FTIR spectroscopy and TGA equipment to validate whether TPU had been successfully formed. Finally, this chapter concluded with plans to progress developments forward toward powder-based AM using the selected reactive ink pairings to validate the suitability of RBJ printing of PUs.

5 | Performance and Printing Optimisation of Single Powder Layer (SPL) Parts

This chapter focused on Reactive Binder Jetting (RBJ) process optimisation using a systematic investigation of printing parameters and their impact on powder consolidation. Single Powder Layer (SPL) experiments were conducted to evaluate critical printing parameters, including droplet spacing, jetting voltage, and waveform profiles. These parameters were optimised to achieve consistent droplet deposition, effective ink-powder interactions, and controlled saturation levels. Findings from these experiments provided insights into the complex dynamics of ink deposition on powder substrates and established a baseline RBJ print strategy to take forward into multiple powder layer (MPL) experiments discussed in Chapter 6.

5.1 Suitability of Commercial Thermoplastic Polyurethane (TPU) Powders for Reactive Binder Jetting (RBJ)

The bulk flow of a powder has a direct impact on its suitability for powder-based additive manufacturing (AM) processes due to the spreading requirements during recoating. If particles cannot smoothly flow past each other the powder will experience compressive forces which compact the powder during recoating, causing a higher packing density which directly effects the saturation potential.¹⁷⁵ In this section, commercial thermoplastic polyurethane (TPU) powders – Ultrasint™ (HP) and UNEX (UX) – had the following three powder characteristics assessed:

1. **Flowability:** To ensure uniform spreading of new layers during powder recoating.
2. **Particle Size Distribution:** To control packing density and minimum powder layer thickness (PLT).
3. **Morphology and Roughness:** To determine surface properties and compatibility with a reactive dual-ink binder system.

Powder flow was deemed the most critical characteristic, whereas particle size and shape informed the optimisation processes for reactive materials and printing parameters. Based on information provided by the manufacturers, out of the two TPU powders, it was predicted that HP powder would exhibit optimal printing properties since it had been designed to be compatible with HP Multi Jet Fusion (MJF) printers. Contrarily, UX powder was commercially used as a transfer powder for clothing via scatter coating. Each commercial powder was characterised to assess their suitability for the Reactive Binder Jetting (RBJ) process. Bulk powder properties, such as void percentages for reactive ink saturation calculations and minimum powder recoating layer thicknesses, impact the quality and performance of RBJ parts, including geometric accuracy and compressive strength.¹⁴¹

5.1.1 Flowability for Powder Recoating

Powder flowability is similar to ink viscosity whereby it is a quantification of the ease in which individual particles slide past each other and the inner walls of their container when subject to external forces, including compression and shearing.¹⁷⁶ A powder rheometer is typically used to evaluate powder flow under different conditions and will output the following rheological properties:

- **Basic Flow Energy (BFE):** To assess resistance to confined, downward flow; impacted by mechanical interlocking of particles and friction.
- **Stability Index (SI):** To assess bulk powder stability between repeated dynamic flow measurements; impacted by clumping of particles.
- **Specific Energy (SE):** To assess resistance to unconfined, upward flow; impacted by interparticle forces, including cohesion and gravitation friction.
- **Conditioned Bulk Density (CBD):** To assess the apparent density of powder; impacted by physical properties, including particle shape and texture.

These properties were when assessing the suitability of a powder for AM applications.

Often friction between particles, mechanical interlocking, and interparticle forces have the most significant impact on flow.¹⁷⁶ Other characteristics, such as particle size, morphology, and roughness, have also been evaluated to provide a holistic understanding of the bulk properties of each TPU powder.

Table 5.1: Powder flow measurements - Basic Flow Energy (BFE), Stability Index (SI), Specific Energy (SE), and Conditioned Bulk Density (CBD) - for commercial polyurethane powders - Ultrasint™ (HP) and UNEX (UX).

Powder	BFE (mJ)	SI	SE (mJ g ⁻¹)	CBD (g mL ⁻¹)
HP	227	0.90	4.70	0.51
UX	730	0.84	8.15	0.54

Table 5.1 summarises rheology results for both HP and UX powders. All measurements were repeated three times and the averages (mean values) presented for each dataset. Established research indicates that HP powder demonstrates superior fluidity, evidenced by low BFE and SE values of 227 mJ and 4.70 mJ g⁻¹, respectively, combined with a high SI of 0.90.¹⁴¹ Contrarily, UX powder exhibited a higher BFE value of 730 mJ, meaning on average 222 % more energy had been exerted on the powder by the rheometer during compressive flow measurements. Comparatively, the SE value for UX powder was 8.15 mJ g⁻¹ which was 73 % higher than HP. This suggests flowability for the UX powder was impacted more by particle shape due to disproportionately higher BFE values compared to SE. When BFE measurements were taken the powder volume had been confined during downward rotation of the rheometer blade, forcing closer contact between particles and leading to mechanical interlocking, or resistance to flow. When measuring SE, the blade moved upward through the bulk of the powder, allowing particles to move freely. Thus, cohesion between particles and gravity were the most significant resistive forces at play.

CBD values of 0.51 g mL⁻¹ and 0.54 g mL⁻¹ for HP and UX, respectively, suggested gravity was not a likely cause for the disparity highlighted previously. The powder was homogenised by the blade during the conditioning sequence of CBD measurements so powder clumps and air pockets were likely removed, thus increasing the density and uniformity of the powder.¹⁷⁶ This suggests UX particles are generally more irregular in

shape or present a rougher surface than HP particles based on the higher SE value.

While a perfectly stable powder will exhibit an SI of 1.00, it is typical within powder AM processes to allow a $\pm 10\%$ deviation between stability tests.¹⁷⁷ Thus, powders which measure between $0.90 > \text{SI} > 1.10$ are deemed stable during flow. For the HP and UX powders, the stability indices were 0.90 and 0.84, respectively. Suggesting HP powder was a more suitable powder for powder bed AM processes due to stable flow properties. However, 0.90 is at the threshold of an acceptable SI value with a UX value only 0.06 units away from being acceptable. However, the UX powder was not so unstable as to justify removing it from the RBJ printing development process. Additionally, the higher BFE value for UX powder may prove to be an advantage for mechanical performance of RBJ parts later. Both powder exhibit properties which suggested flow during layer recoating would be reliable, leading to smooth, uniform layer thicknesses to print on.

5.1.2 Particle Size Distribution

A powder will exhibit poor flow properties when particles are $\leq 5.0\ \mu\text{m}$ due to inter-particle forces which cause higher cohesive forces and to particle clustering.¹⁷⁸ Increasing particle sizing raises the achievable minimum powder layer thickness (PLT), compromising geometric accuracy.⁷⁴ Chen and Zhao¹⁶⁶ confirms larger particles reduce the maximum layer packing density and lead to poorer part resolution. The “stair-stepping” phenomenon presented by Onuh and Hon³⁹ demonstrates how finer printed layers lead to higher quality parts that more accurately resemble the desired geometry. A higher powder packing density leads to fewer voids present in printed parts, and therefore better mechanical performances.³⁶ To determine if a powder would be suitable for powder AM applications, particle size distribution (PSD) was investigated in addition to the flow properties and packing densities.

Based on existing literature, bimodal particles with particle size differences and weight ratios of coarse to fine particles between 80:20 and 60:40, elicit optimum packing densities.^{31,179} Further work in the area of powder selection is recommended to achieve higher packing densities, thinner powder layers and smoother flow.

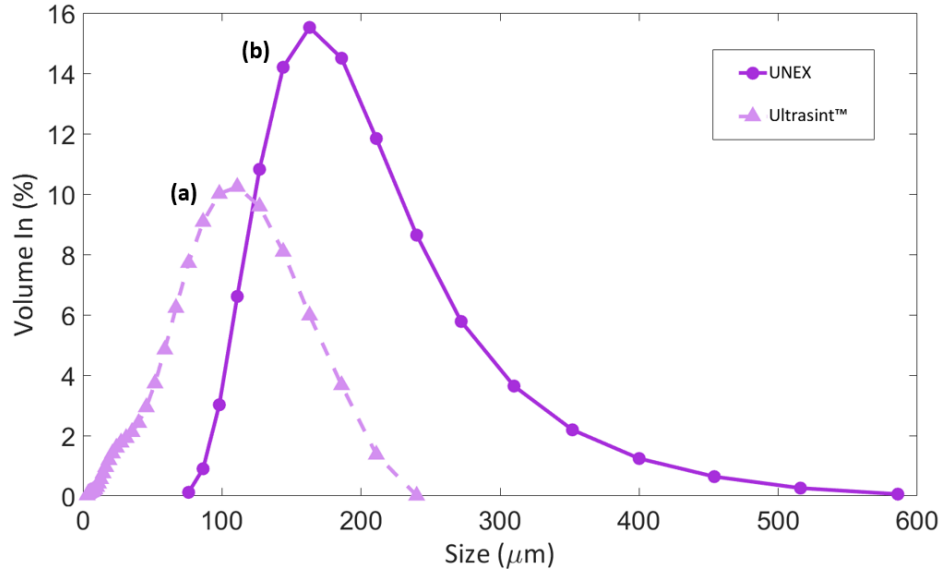


Figure 5.1: Particle size distribution (PSD) for two commercial thermoplastic polyurethane (TPU) powders (a) Ultrasint™ (HP) (δ), and (b) UNEX (UX) (\circ).

The full distribution of particle sizes for both HP and UX powders can be seen in Figure 5.1. For UX powder the PSD was widest with particle sizes ranging from 76 – 586 μm . There was a strong positive skew of 1.09 exhibited with a median particle size of 184 μm as outlined in Table 5.2.

Table 5.2: Summary of the particle size distribution (PSD), skewness and specific surface area for (a) Ultrasint™ (HP), and (b) UNEX (UX) powders; data collected using a Mastersizer 3000.

Powder	Particle Sizing			Population Skewness	Surface Area (m^2kg^{-1}) (μm)
	$D_x(10)$	$D_x(50)$	$D_x(90)$		
HP	31	96.7	167	0.53	86.1
UX	125	184	296	1.09	30.5

For HP powder, the PSD was much narrower ranging from 3 – 240 μm and a positive skew of 0.53, suggesting HP powder could be used to form thinner powder layers to generate higher resolution prints. However, packing density potential was low given the BFE was measured at 227 mJ. While for UX powder, the maximum particle size was 586 μm .

Mcgeary⁴⁴ suggests optimal packing density can be achieved if there is at least a sevenfold difference between the smallest and largest particle diameters. Given the largest particle measured was 79x larger than the smallest, HP powder would be theoretically

well equipped for optimal packing. For UX powder, there was a 6.7x increase in size from the smallest to largest particle.

The powder samples used to measure PSD came straight out of the container provided by the manufacturer. No pre-processing, such as sieving, grinding or aerating was conducted before use. Therefore, it was possible the righthand side distribution (tail) of UX powder was elongated by the presence of powder clumps present in the samples. The lefthand side of the HP powder showed a large quantity of fine particles ($< 10\text{ }\mu\text{m}$), including powder fragments and debris of *leq* $4\text{ }\mu\text{m}$. Particles at the far ends of the PSD distribution ($\leq 0.1\%$ Volume) were discounted as debris, resulting in an adjusted PSD range of $5.2 - 211\text{ }\mu\text{m}$ and $76 - 516\text{ }\mu\text{m}$ for HP and UX, respectively. A more accurate calculation of the packing density potential for a fresh supply of powder was 39.6x and 5.8x for HP and UX, respectively. This suggested that HP powder had greater packing density potential despite having a much lower BFE value compared to UX powder. Both powders require further investigation to validate packing densities as other factors, such as mechanical interlocking and particle cohesion, could also influence flow and packing behaviour.

5.1.3 Morphological Characterisation of Commercial Powders

As discussed in Section 5.1.1, individual particle morphology and roughness affect the bulk properties of a powder. By analysing powder particles at micro-scale, expected surface profile and texture becomes clearer. To produce robust parts via RBJ, there must be sufficient wetting with reactive inks. If particles are smooth, a constant spreading rate would be expected, whereas for rougher particles, a logarithmic rate of spreading would be expected due to capillary effects at troughs.¹⁸⁰ Given reactive inks polymerise to form a solid dual-ink binder while simultaneously spreading throughout the powder bed, wetting rate has potential to impact the mixing efficiency of reactive inks and therefore the degree of polymerisation. Incomplete polymerisation could reduce mechanical properties and part integrity due to insufficient binding between particles and print layers. Ink wetting and rate of reaction are considered to allow reactive inks sufficient time to penetrate the powder bed before solidifying.

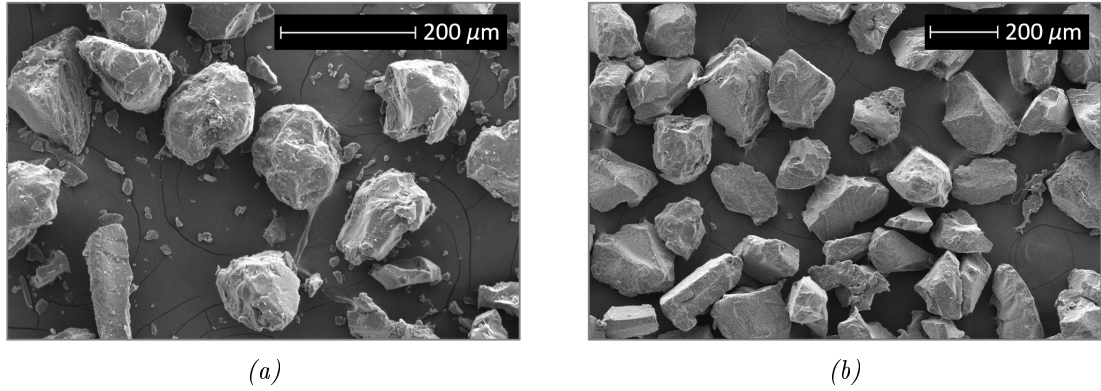


Figure 5.2: SEM images of commercial powders (a) Ultrasint™ (HP) at 400x magnification, and (b) UNEX (UX) at 200x magnification..

SEM images of the commercial TPU powders – HP and UX – can be seen in Figure 5.2. Qualitative assessments suggested HP particles were rounder, compared to more angular features of UX particles. Shadows and highlights on the particles suggest UX particles appeared faceted with sharp edges and smooth, flat planes leading to clear boundaries of dark and light. Contrarily, HP particles possess fewer flat surfaces and smaller transitions in plane direction, resulting in a rough, rounded surface with a patchier distribution of light and dark profiles.

Additionally, small particles were visible on the surface of carbon tape between larger particles with a powder median of 184 μm. These smaller particles were either pieces of debris generated during powder production or fragments that have broken away from the larger particles during sample preparation. The HP powder had been developed for Multi Jet Fusion (MJF) printing, thus it was very likely the powder had been coated in an additive to aid flowability properties. It is also probable these small particles were fragments of a different material used to coat the powder, potentially explaining why they appeared in the shape of shavings or long shards that had sheared away from the parent particle. Finally, if additives had been used to condition the powder flowability, it was concluded these foreign materials were not likely to have a stronger bond to TPU than the TPU powder itself, however further characterisation would be required to confirm this prediction.

Table 5.3: Summary of mean particle sizing and deviations in each dataset for (a) *Ultrasint™* (HP), and (b) *UNEX* (UX) powders; data collected using ImageJ software on SEM images.

Powder	Image Particle Sizing (μm)	
	Mean	Deviation
HP	138	18
UX	207	33

ImageJ software was applied to the powder SEM images in Figure 5.2 to verify the accuracy of PSD data collected via laser diffraction in Section 5.1.2. A summary of the particle measurements taken using ImageJ software, following minimal image processing, has been outlined in Table 5.3. For each sample set, the minimum and maximum particle sizes were measured for each powder sample, falling within the distribution ranges quoted previously, suggesting the PSD data was valid. However, HP PSD data was likely skewed by the presence of smaller particle fragments or debris.

Using SEM imaging, the largest particles for UX powder were measured at $239.5 \mu\text{m}$ which was 59 % smaller than the largest particle measured via laser diffraction (Mastersizer 3000). This observation supported the theory that UX powder would tend to clump, forming agglomerates. It was theorised, the laser was unable to distinguish the individual particles from the agglomerated masses. However, clumps could be reduced by running the powder through a powder rheometer in aeration mode or apply manual grinding via mortar and pestle to loosen the agglomerates.

5.2 Single Powder Layer (SPL) Printing

Building upon the foundational research presented in Chapter 4, optimisation of process parameters and material formulation were investigated to enhance mechanical properties and thermal stability. Reactive inks were printed onto a powder substrate to produce Single Powder Layer (SPL) parts. Sample identifiers based on compositions and droplet spacing have been outlined in Table 5.4.

Table 5.4: Summary of single powder layer (SPL) samples investigated.

Formulation		Ink Combination		Droplet Spacing
Family	Identifier	ISO	DIOL	(μm)
UX	UX01	A03	B01	6
	UX02	A03	B01	8
	UX03	A03	B01	10
	UX04	A03	B104	6
	UX05	A03	B104	8
	UX06	A03	B104	10
HP	HP01	A03	B01	6
	HP02	A03	B01	8
	HP03	A03	B01	10
	HP04	A03	B104	6
	HP05	A03	B104	8
	HP06	A03	B104	10

5.2.1 Experimental Set Up for Single Powder Layer (SPL) Printing

Transitioning from non-porous PET film to TPU powder as a substrate, required adaptations to the printing systems. Key alterations, including the introduction of miniature powder bed sample frames and ink pigmentation, have been highlighted in this section.

5.2.1.1 Ink Visibility and Jetting Feedback

Visibility of reactive inks on white TPU powder was limited due to the transparent nature of the inks. An insignificant amount colourant (<2 wt %) was added to the reactive inks with red being added to ISO inks and blue being added to DIOL inks. This proved to be a necessary adaptation of the reactive ink formulations as it provided immediate visual feedback about jetting health for each ink and associated printhead. For example, when both inks were jetting correctly the final part would appear purple due to equal mixing of red and blue inks.

Figure 5.3a shows the colour of each reactive ink before subsequent jetting followed by Figure 5.3b which demonstrated how both inks create a purple hue when combined within a powder bed. Deposition origins had not been calibrated correctly, resulting in a slight horizontal offset with blue ink visible on the left edge and red ink on the right. Separately, further LP50 calibrations were performed to regain alignment before printing continued.

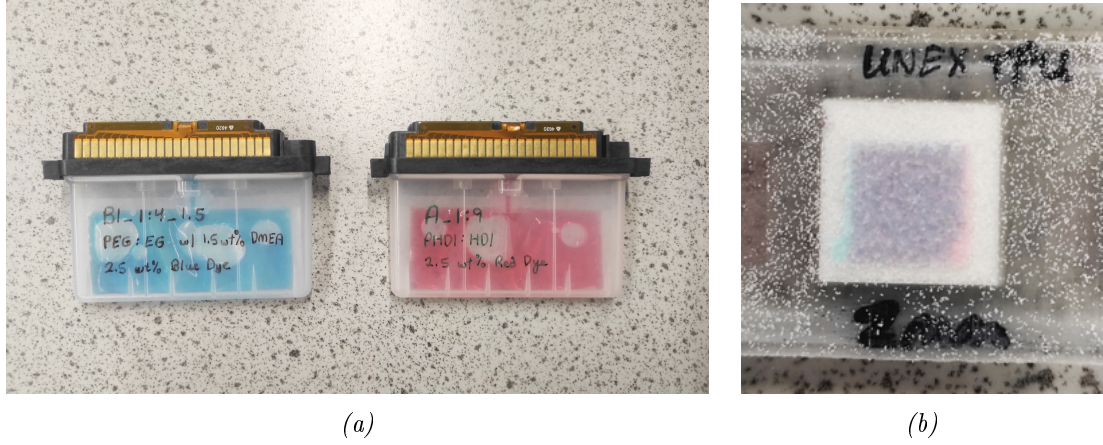


Figure 5.3: Visual representation of dyed (a) reactive ink formulations and (b) a powder bed following subsequent jetting of both reactive inks.

5.2.1.2 Custom Powder Bed Samples

At this stage in the project, the most suitable printer available was the Dimatix Material Printer (DMP). The built-in tools, such as Droplet Viewer and Waveform Editor, enabled the user to optimise jetting waveforms and printing parameter. An LP50 inkjet printer was modified later in the project to test multiple powder layer (MPL) printing techniques, as outlined in Chapter 6 .

The Dimatix Printer was inherently a inkjet printer and was not suitable for powder AM printing. To get around this, a set of custom powder holders were 3D printed using a Stratsys Objet30 printer. Known for its dimensional accuracy, the Objet30 printer was used to control powder bed depth, incrementally increasing sample frame depth from 1-5 mm as shown in Figure 5.4a. Each frame was comprised of three individual 10 mm square powder beds.

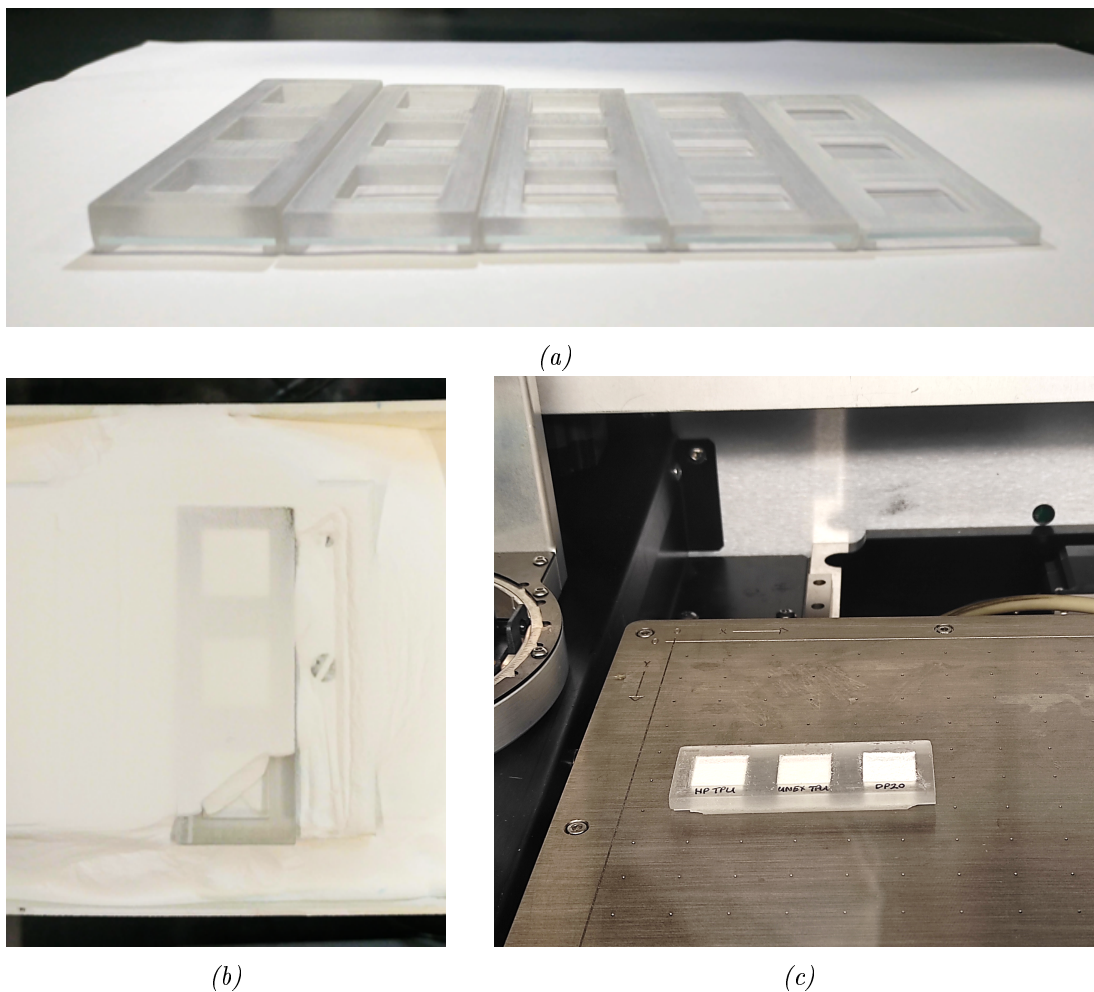


Figure 5.4: Custom powder holders demonstrating (a) variable bed depths from 5mm to 1mm (left to right), (b) partially filled powder cavities following recoating and (c) fully prepared powder samples atop a Dimatix printer build platform.

To ensure the particle packing arrangement was comparable to traditional roller-based powder beds, the miniature powder bed sample frame was fitted to the build platform of a powder recoating system as shown in Figure 5.4b. To completely fill all three powder beds, 2-3 sweeps of the recoater were often required. Excess powder around the sample frame was carefully removed with a brush and damp paper towel before being moved into the glove box housing the Dimatix printer. Prepared sample frames were then placed on the build platform with edges running parallel as shown in Figure 5.4c.

5.2.1.3 Summary

Overall, UNEX powder was found to be the easiest to spread when preparing the sample frames, however the powder layer surface was visibly rougher compared to HP powder. These observations correlate with existing literature which suggests coarse powders

were more suitable for spreading and packing.³⁶ However, according to Table 5.2 of Section 5.1.2, HP powder presented with a much smaller mean particle size of 96.7 μm , approximately half that of UNEX powder, suggesting RBJ part densities will be greater with HP than with UNEX powder.

5.2.2 Initial Printing via Sample Frames

Based on the powder characterisation data detailed in Section 5.1, initial printing parameters were selected to evaluate the suitability of the reactive dual-ink binders developed in Chapter 4 for use with powder bed substrates. Transitioning inkjet printing from a flat, non-porous substrate, such as PET film, to a textured, porous powder bed introduced complexities that necessitate print parameter optimisation to achieve successful powder consolidation. Achieving optimal ink saturation is critical for binding powder particles and forming a cohesive printed layer.^{58,69} Critical parameters influencing part consolidation have been outlined in Section 5.2.2.3, while the deposition sequence of reactive inks and its impact on the geometry and integrity of Single Powder Layer (SPL) parts have been covered in Section 5.2.2.1.

5.2.2.1 Deposition Sequence

The compositional differences between the ISO and DIOL ink formulations result in distinct properties, making the interactions between each ink and the TPU powder inherently unique. Consequently, the isolated interaction of ISO ink with TPU powder was likely to differ significantly from that of DIOL ink with TPU powder.

This experiment tested two deposition sequences to evaluate these differences. In Sequence 1, the ISO ink layer was deposited first, followed by the DIOL ink layer (see Figure 5.5a). In Sequence 2, the order was reversed, with the DIOL ink layer deposited first and the ISO ink layer applied second (see Figure 5.5b).

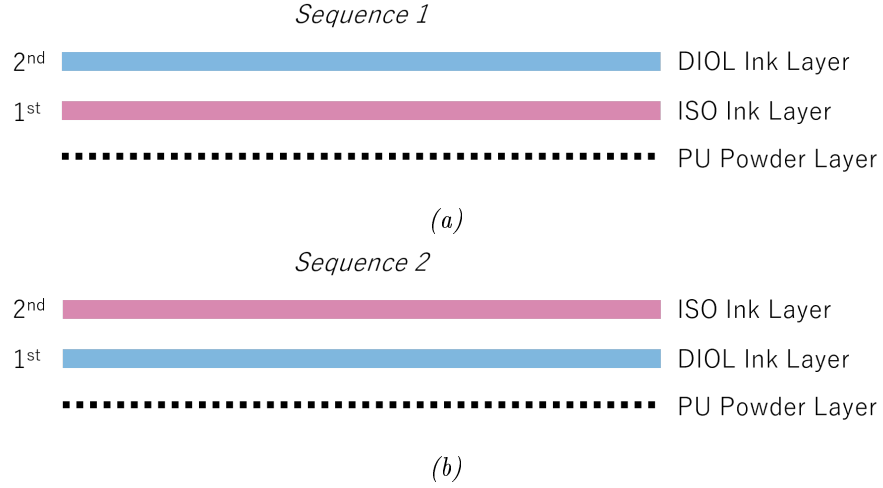


Figure 5.5: Deposition sequencing for ISO and DIOL reactive inks.

Using the optimised jetting parameters established in Chapter 4, two samples were printed onto a UX powder substrate, each corresponding to one of the deposition sequences. Results are shown in Figure 5.6, with the left image representing the output from Sequence 1 and the right image from Sequence 2. No discernible differences in geometry, colour, or size were observed between the two samples.

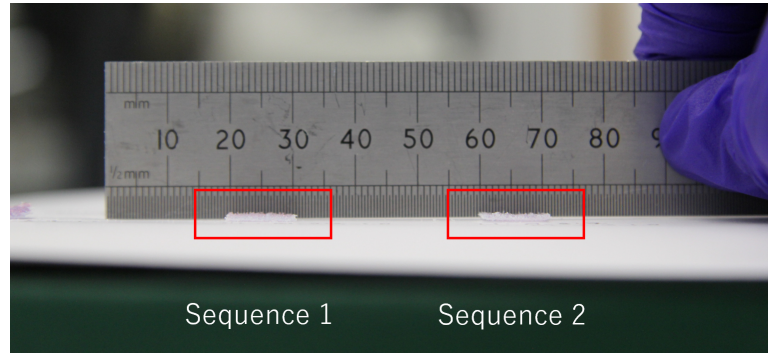


Figure 5.6: Comparison of single-powder layer (SPL) samples between Sequence 1 (ISO ink 1st) and Sequence 2 (DIOL ink 2nd)

In subsequent experiments (see Section 5.2.4.1), visible layer deformation was observed in samples printed using the Sequence 2 deposition order. Specifically, the printed layer curved downward, forming a dome-like structure when placed on a flat surface. This warping became increasingly prominent as the number of Reactive Ink Layers (RILs) deposited onto the same powder layer increased. In contrast, samples printed with Sequence 1 exhibited no noticeable deformation. These findings suggested that

Sequence 1 should be adopted for future experiments to minimise the risk of print failures and maintain part quality.

5.2.2.2 Single Powder Layer (SPL) Validation

Using the custom sample frames introduced in Section 5.2.1.2, a range of droplet spacing (DS) parameters were evaluated to identify which inputs resulted in a consolidated print layer, thereby establishing the range of suitable DS parameters for RBJ. At this stage, no parameter optimisations were applied; the default settings for the ISO and DIOL inks were 33 V at 60 °C using a 3x Multiple Waveform Pattern (MWP) and 35 V at 55 °C using a single waveform pattern, respectively.

Initially, for the reactive dual-ink system, the DS inputs tested were 10 μm , 20 μm , and 30 μm . Two sample frames were prepared, one using UX powder and the other with HP powder. Of the three parameters tested, only the 10 μm DS setting led to a success SPL print for both TPU powders. DS directly impacts ink saturation so it was concluded that a 20 μm and 30 μm DS delivered an insufficient volume of ink to consolidate the powders. A narrower range of DS inputs were selected for further testing as discussed in Section 5.2.3.



Figure 5.7: Image array of a fully consolidated single powder layer (SPL) sample of 0.82 μm thickness printed using binder system A01 – B102; A01 jetted at 35 V/60 °C and B102 jetted at 33 V/55 °C.

Figure 5.7 highlights a successful SPL print composed of a fully consolidated layer of UX powder printed using a 10 μm DS. Evidenced by fine white cracks visible throughout the printed sample, the image on the far right demonstrates poor powder packing. However, for a 'green' part consolidated with no thermal processing, this 0.82 mm thick SPL sample could be handled without deteriorating. This was a critical milestone in

the project.

Thus, the reactive dual-ink system developed in Chapter 4 was successful in demonstrating powder consolidation, further validating suitability for RBJ. However, due to the inherent gaps present in the powder bed substrate, these initial results suggest a smaller droplet spacing (DS) should be applied. This adjustment ensures sufficient ink saturation and powder consolidation, addressing the challenges posed by the textured and porous nature of the powder bed.

Existing literature suggests a 20 μm DS to be optimal for BJ in the case of metal salt binders.⁵⁷ However, the ceramic powder used in this research had a nominal particle size of 20 μm , leading to a higher packing density and therefore fewer voids to fill compared to UNEX and HP powders.

5.2.2.3 Critical Parameters to Adjust for Powder Substrate

Deposition sequence experiments revealed that print layer deformation increased proportionally with the number of Reactive Ink Layers (RILs), suggesting the powder had been over-saturated. Zhang *et al.*⁶⁴ observed similar curling in SPL parts and found that as powder layer thicknesses increased, warping reduced proportionally. Therefore, by reducing either the net ink volume deposited or increasing the available pore space, warping can be minimised through saturation level optimisation. The number of RILs was identified as a critical parameter, requiring further investigation in Section 5.2.4.

Print layer deformation increases the risk of part failure occurring during RBJ printing. For instance, upward warping above the horizontal plane of the build platform was observed to increase the likelihood of impact with the powder recoating system. This could result in the displacement of the part within the powder bed, causing layer misalignment or tearing soft, unreacted layers across the powder bed surface. Part failure modes that occurred during multiple powder layer (MPL) printing and recoating are discussed in Chapter 6.

Ink saturation levels significantly influence the quality of the printed part. Early DS experiments demonstrated that low saturation levels, particularly at DS values of 20 μm or higher, resulted in wetter but unconsolidated powder layers. A minimum saturation

level, driven by the ratio of net ink volume and void percentage in the powder bed, was required to successfully print SPL samples. DS can be adjusted to control pixel density and, consequently, the total ink volume deposited per unit area.

5.2.3 Impact of Droplet Spacing (DS)

Throughout this section, a smaller range of DS inputs were applied based on the results outlined in Section 5.2.2.2. To assess the impact of higher powder saturation levels on print layer quality, DS parameters of 6 μm , 8 μm and 10 μm were investigated. Previously, the lowest DS input applied was 10 μm , while existing BJ literature demonstrated successful saturation levels were achieved with DS parameters as low as 5 μm .¹²²

5.2.3.1 Printed Powder Comparison

Initial DS experimentations at 10 μm , 20 μm and 30 μm were conducted on both HP and UX powder bed samples. The ink deposition approach applied across all datasets was Sequence 1. Therefore, in this second wave of DS experimentations, six samples frames were prepared in total - three frames filled with UX powder and the remaining with HP powder. The DS inputs applied included 6 μm , 8 μm and 10 μm , with the latter included as a control having previously demonstrated SPL consolidation with both TPU powders.

Images of SPL samples formed using a DS of 10 μm can be found in Figures 5.8a and 5.8b below, including repeats for reliability. Printed samples in Figures 5.8c and 5.8d applied a DS of 6 μm . These samples are visibly more saturated as seen by the darker shade of purple.

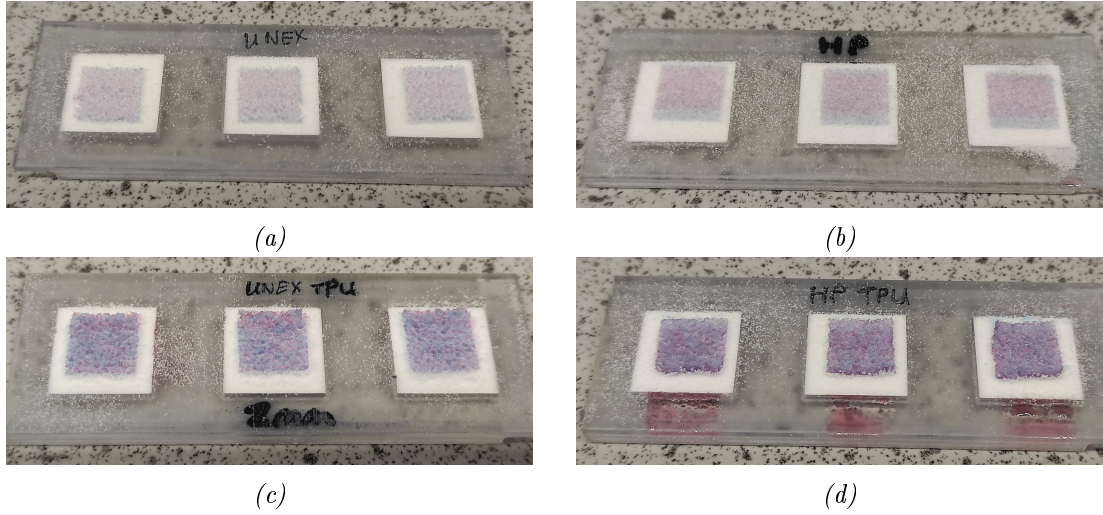


Figure 5.8: Single-powder layer (SPL) samples printed with droplet spacings (DS) (a)(b) $10\ \mu\text{m}$ and (c)(d) $6\ \mu\text{m}$ using commercial powders (a)(c) UX and (b)(d) HP using binder system A01 – B102; A01 jetted at $35\ \text{V}/60\ ^\circ\text{C}$ and B102 jetted at $33\ \text{V}/55\ ^\circ\text{C}$.

Additionally, there was a distinct difference in the print layer texture along the top surface layer between the UX powder samples in Figures 5.8a and 5.8c and HP powder samples in Figures 5.8b and 5.8d. Across all three DS inputs, the printed layer samples composed of HP powder were consistently smoother compared to the rougher surfaces featured on the UX powder samples.

Based on the particle size distribution (PSD) data outlined in Section 5.1.2, the median particle size, $Dx(50)$, of a given UX powder batch was $184\ \mu\text{m}$, nearly doubling that of the HP powder which was measured at $96.7\ \mu\text{m}$. Thus, there is a higher probability of producing a high-resolution print layer using HP powder compared to UX powder. This is due to have a lower achievable minimum PLT.

Across both powder datasets at $10\ \mu\text{m}$ and $8\ \mu\text{m}$, the geometric accuracy of SPL samples were good with no visible signs of deformation occurring. It was observed at the highest ink saturation level, when the DS was $6\ \mu\text{m}$, that the SPL samples composed of HP powder began to curl upwards along the top and bottom edges with the top left and bottom right corners rising highest above the horizontal print plane ($z = 0$).

Thus, print layer quality was more consistent across a wider range of saturation levels for UX powder compared to HP powder which exhibited early signs over saturation at a DS of $6\ \mu\text{m}$. Printing on HP powder produced a more aesthetic print surface at a DS

of 8 μm or higher.

5.2.3.2 Droplet Spacing (DS) Comparison

To take a closer look at the surface, printed samples for each of the six datasets were prepared for SEM imaging following the method outlined in Section 3.2.3.3. The microstructure of each sample surface can be found in Figure 5.9. Each sample is labelled in accordance with the compositions and DS outlined in Table 5.4.

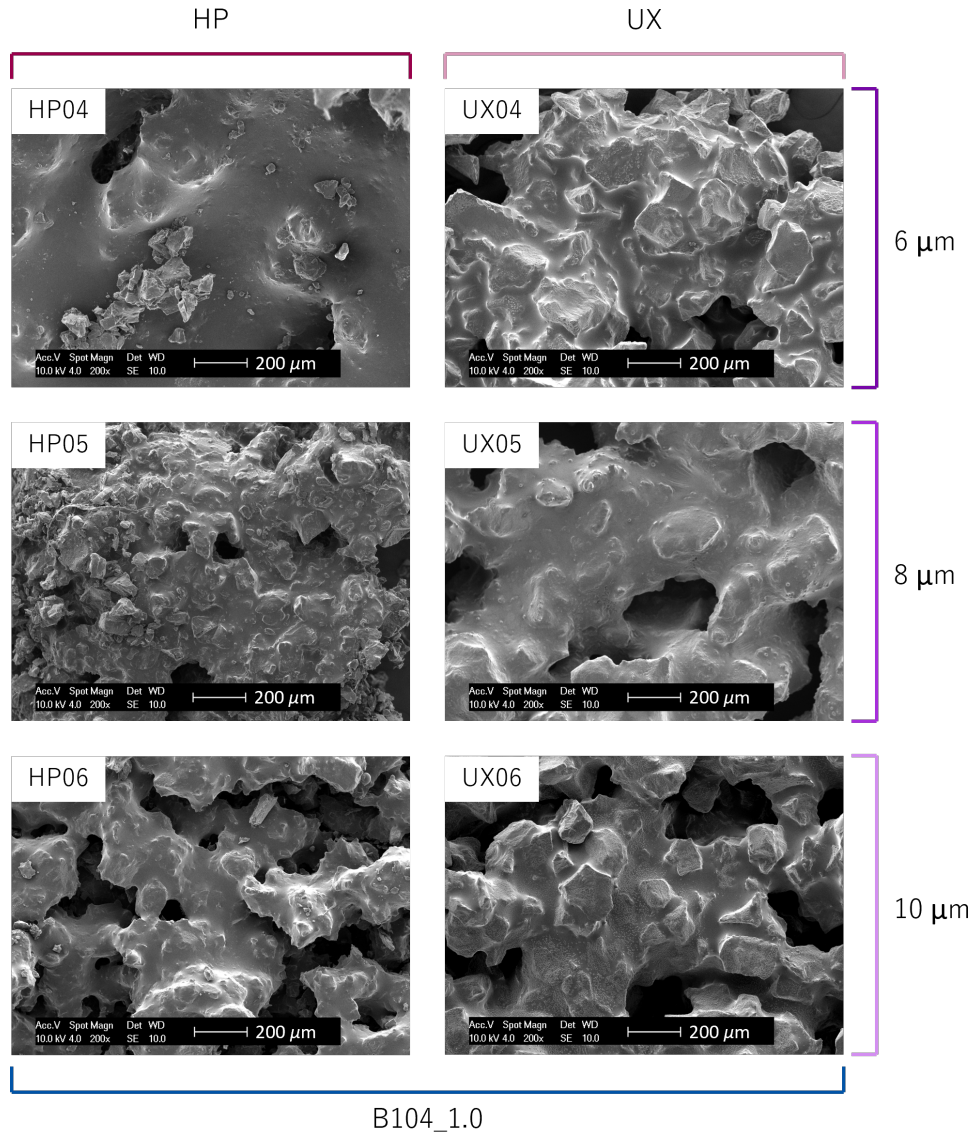


Figure 5.9: SEM images at 200x magnification for six SPL samples printed using a DS of 6, 8, and 10 μm for both UX and HP powders.

Black localised voids were observed across all datasets. Additionally, the number of voids presented within the samples rose as DS increased with the fewest number of

voids occurring in sample HP01 and the highest in samples HP03 and UX03.

Across all datasets, only sample HP01 exhibited a large area of a smooth surface texture akin to setting glue. Where particles protruded from the smooth surface, the features were more rounded and less obtrusive compared to the other UX samples. However, the lack of dark voids presented at the surface of sample HP03 suggested the print layer was very close to the maximum saturation point.

Saturation limit for a given sample volume can be estimated by quantifying the amount of unoccupied space within the sample space.^{68,69} Further parameter optimisation was conducted to widen the range of printable saturation levels. The aim was to achieve a minimum print layer quality that enables MLP printing while maximising powder layer saturation. To successfully produce a three-dimensional (3D) part, multiple print layers are required. Therefore, it is crucial for print quality to be consistent with each subsequent layer to ensure the 3D part can form a uniform, consolidated RBJ part, void of defects, including print layer delamination or print layer offsets. These results are further explored in Chapter 6.

Based on the literature for traditional BJ printing processes, achieving the maximum binder saturation is often desirable as parts perform better with higher part densities.^{65,66} This extends to materials engineering, whereby metal parts with fewer defects, including voids or cracks, traditionally perform better too. However, given the potential functionality and versatility of RBJ printing, high density RBJ parts may not always be desired. Covalent bonds between $-OH$ and $-NCO$ that form within the powder are what lend ink-based AM processes their strength. By maximising the saturation level to achieve high density parts, the contact points between the reactive inks and the powder particles also increase leading to more robust parts.

5.2.3.3 Compositional Analysis via TGA and FTIR

The dual-ink binder system was designed to form covalent bonds between each other to form urethane linkages, and between the powder particles which have both $-OH$ and $-NCO$ groups present on the surface to form direct bond with the individual ISO and DIOL inks, respectively. Chemical characterisation techniques - TGA and FTIR - were

applied to validate the chemical composition of each printed sample.

A dual characterisation approach was taken to analyse the composition of printed samples whereby TGA and FTIR data was measured and analysed. The rationale behind using a dual approach was to minimise error as neither characterisation approach on its own could offer the level of confidence needed to confirm PU had formed.

As isocyanates are highly reactive to hydroxyl groups, they will readily react with both polyols to form PU as well as water to form polyurea.⁷⁷ Given the high exposure risk to moisture during printing, it is important to understand if PU or polyurea has formed in the final part. Given both materials have very similar chemical compositions, TGA on its own would not necessarily help us differentiate. Whereas FTIR measurements only measure the composition of the surface up to a few micrometers, failing to capture the composition of the bulk part. Therefore, applying both compositional analyses ensures a more holistic result for part characterisation is achieved.

Figure 5.10 demonstrates the thermal degradation profiles of both the TPU powder samples (UX and HP) and all SPL printed samples. In this case, both powder samples were measured to act as a baseline (yellow and orange lines). The composition of both powders are known to be TPU, therefore if the reactive dual-ink system has polymerised to form TPU the thermal degradation profile should be similar to the powder. Existing literature suggests PU materials will typically thermally degrade in three stages with the final stage (soft segment decomposition) occurring at $>300\text{ }^{\circ}\text{C}$.^{133,147-149}

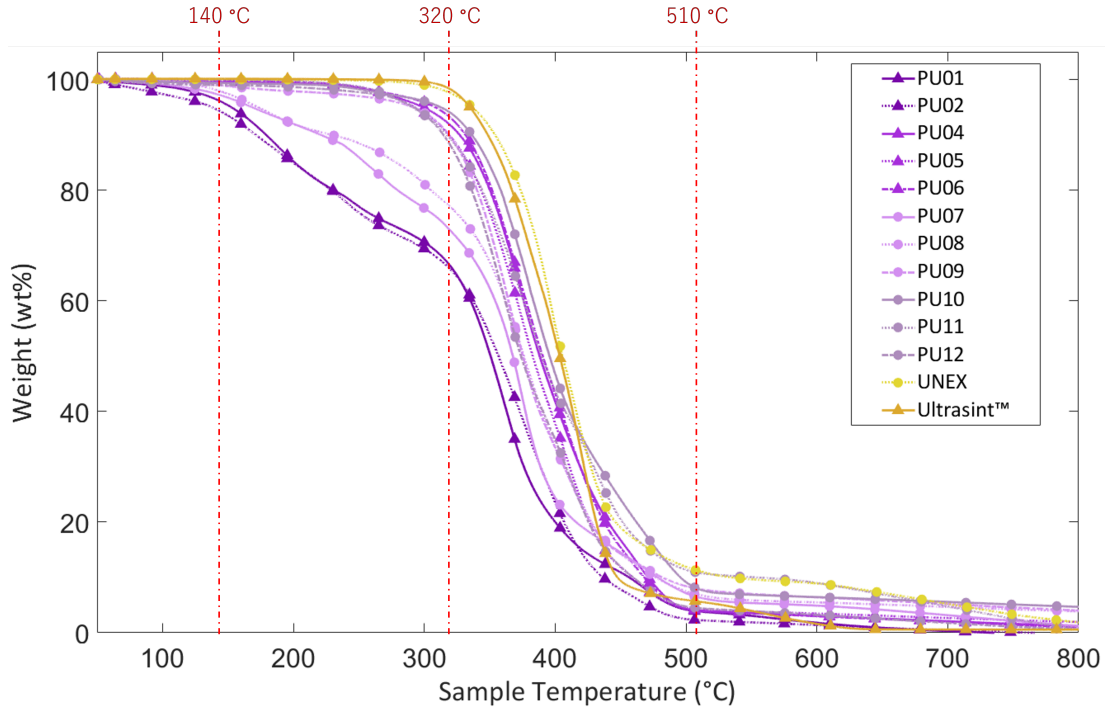


Figure 5.10: Thermogravimetric analysis (TGA) of single print layer (SPL) composite polyurethane (CPU) prints heated from 50 - 800 °C at 20 °Cmin⁻¹ in a nitrogen atmosphere.

According to the data, both UX and HP powder follow a similar degradation profile, degrading at 320 °C as expected. However, the rate of degradation drops significantly around 450 °C and by 475 °C the HP powder has experienced a larger loss in weight of approximately 94 % compared to UX powder at 85 %. This highlights a subtle compositional difference between the two powders. It is highly likely that the UX powder contain additives or more complex molecules which form stronger bonds capable of resisting thermal stresses for longer. Typically, at this point in the degradation profile, only carbon remains of the original sample.

With references to the printed samples - UX01-UX03 and HP01-HP03 – from Figure 5.9, degradation profiles across all datasets follow a similar profile compared to the TPU powders. Similarly, the highest rate of degradation occurring between 320 °C – 510 °C. However, the thermal profile of the printed samples differs to that of the powder samples between 220 °C - 320 °C. Typically, from 140 °C onwards, any water molecules present on the sample will begin to evaporate. It is highly likely that the printed samples more readily absorb moisture than the powder samples which were stored in a dry, airtight container. By 320 °C, the printed samples had experienced an additional 5-10 % weight

loss compared to the powder samples at this stage in the process. All three of the printed samples containing HP powder (HP01-HP03) experienced the largest weight loss compared to the other three samples which contained UX powder.

Degradation profiles of the printed samples follow a similar profile to the TPU powders. Based on TGA data alone, it cannot be concluded whether polyureas were also present at this stage as the degradation profiles of both materials are similar. The data suggests all printed samples had fully reacted and, therefore the reactive dual-ink system, including catalyst choice and concentration, were working effectively.

Figure 5.11a provides FTIR scans for both the UX powder and print samples UX01-UX03 while Figure 5.11b is of a scan for HP powder and print samples HP01-HP03. Transmission peaks between wavenumbers 1800 cm^{-1} and 1600 cm^{-1} were analysed as the bond types associated with urethane groups, including C=O, C–O and N–H, can be identified within this range.

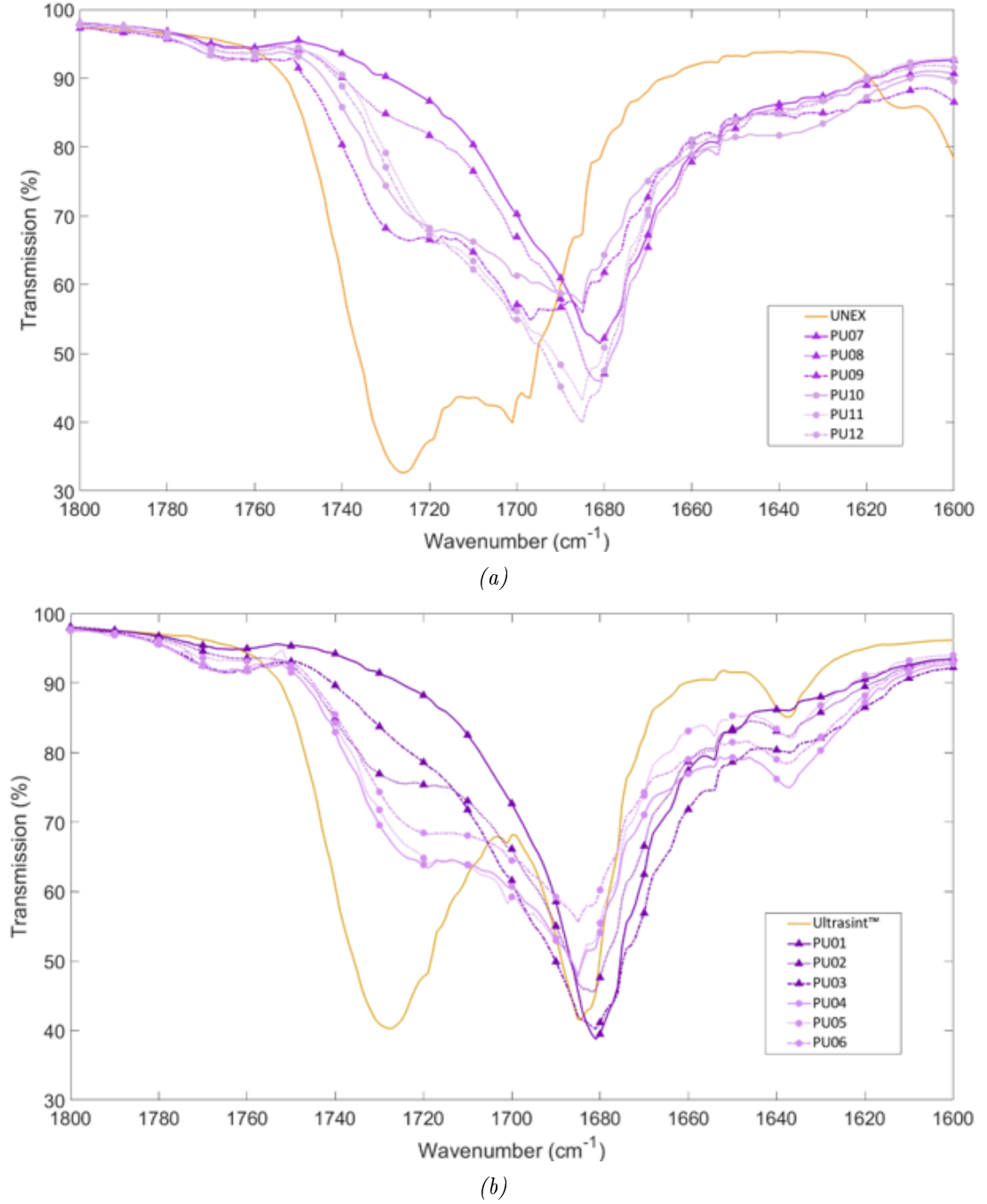


Figure 5.11: Transmission peak intensities between 1800 - 1600 cm^{-1} for (a) UX powder with samples UX01-UX03 and (b) HP powder with samples HP01-HP03.

TGA measurements for both powder samples were taken to act as baseline datasets. For the UX powder (orange line in Figure 5.11a), two peaks are observed at 1726 cm^{-1} and 1701 cm^{-1} with the latter peak less prominent than the first. For the HP powder (yellow line in Figure 5.11b), there are three peaks present in this range with locations at 1728 cm^{-1} , 1685 cm^{-1} , and 1637 cm^{-1} .

The most prominent peak was located near 1725 cm^{-1} for both datasets. Additionally, the general shape and curvature of both primary peaks were nearly identical with a slight kink located at 1720 cm^{-1} just before the peak curves begin to differentiate. The secondary peak for UX powder was small, indistinct, and wavy which was contrary to the secondary peak of the HP powder which was offset by 15 cm^{-1} and instead resembled a smooth, pronounced curve. Finally, there was no third peak observed for the UX powder, however there was a very short, discreet peak observed in the HP powder. Each sample was repeatedly scanned (minimum of 5x), minimising potential errors in the measurements.

With reference to printed samples UX01-UX03, there was one distinct peak present at 1685 cm^{-1} . All three samples followed a similar profile with varying transmission peak intensities. Sample UX01 had the smallest transmission peak of 57.2 %, followed by UX02 at 43.2 % and UX03 at 39.9 %. Different peak intensities indicated a varying degree of polymerisation within the printed samples. It was possible that a higher DS led to a higher conversion or more effective reaction between the reactive inks during printing.

Additionally, for printed samples HP01-HP03 the primary transmission peak was located at 1685 cm^{-1} with a shallow, secondary peak at 1719 cm^{-1} . Within this dataset the primary peak intensity for HP02 was the smallest with a transmission of 47.6 % followed by HP01 at 47.9 % and HP03 at 55.6 %. However, the scan profile and peak intensities for all three printed samples were nearly identical, suggesting the composition of each sample was the same. The primary peak was consistently located at 1685 cm^{-1} across all six print sample datasets, confirming the same bond type had formed following RBJ printing.

As isocyanates react to form polyurethane, the C=O bond evolves into a urethane group which leads to the formation of C–O and N–H bonds. Within this urethane group, both ester (–COO–) and amide (–CN–) linkages are present. However, identification of polyurethanes in this system can be difficult due to the potential presence of polyurea which readily forms when ISO groups react with water. However, while polyurea groups are comprised of amide (–CN–) linkages, ester (–COO–) linkages do not form, thus

differentiations may be found at the C=O bond. Table 5.5 below provides a summary of relevant transmission peaks found within the scanning range of 1800 - 1600 cm^{-1} .

Table 5.5: Range of wavenumbers for relevant peak transmissions between 1800-1600 cm^{-1} .

Wavenumbers (cm-1)	Vibration	Group Name
1740 - 1730	C=O Stretch	1° Urethane
1725 - 1705	C=O Stretch	2° Urethane
1690 - 1680	C=O Stretch	3° Urethane
1680 - 1630	C=O Stretch	2° Amide
1630 - 1610	N-H Bend (out-of-plane)	1° Urethane

During a PU reaction, the number of bonds associated with the carbonyl group (C=O) of an ISO molecule increases as linkages form, leading to the formation of an N-H bond as the C=N bonds breaks. Therefore, primary urethanes will typically form transmission peaks between 1740 – 1730 cm^{-1} and 1630 – 1610 cm^{-1} . However, the N–H bond disappears when secondary and/or tertiary urethane groups are formed.

With reference to Figure 5.11b, both the HP powder and printed samples (HP01-HP03) shared a peak at 1685 cm^{-1} . All UX printed samples (UX01-UX03) in Figure 5.11a exhibited a peak at 1685 cm^{-1} , however the UX powder sample did not. This value was consistent across multiple samples, thus the results were deemed unreliable, however the peaks did not fall within any of the scan ranges summarised in Table 5.5. Therefore, it is possible this value was an average peak of both secondary urethanes and secondary amides present in the sample. Alternatively, the FTIR machine may not have been calibrated at the time measurements were taken, leading to an incorrect wavenumber output.

5.2.4 Impact of Increasing Reactive Ink Layers (RILs)

Net ink volume, or print layer saturation, was increased by multiplying the number of Reactive Ink Layers (RILs) deposited per layer of powder layer. A single reactive ink layer was composed of one DIOL ink layer and one ISO ink layer as shown in Figure 5.12.



Figure 5.12: Composition of a single Reactive Ink Layer (RIL), totalling one DIOL ink layer and one ISO ink layer, in any deposition sequence.

These reactive ink layers could be multiplied whereby the deposition sequence was repeated in alternating sets of DIOL and ISO ink layers. Figure 5.13 provides a layer breakdown of a 3x RIL print whereby a total of six full inkjet printing passes were completed subsequently atop the same powder layer. Similar to the multiple-pattern waveforms (MPWs) technique introduced in Section 4.2.2.1, to increase the number of moles per droplet, the net droplet volume could be increased by applying multiple RILs to increase print layer saturation.

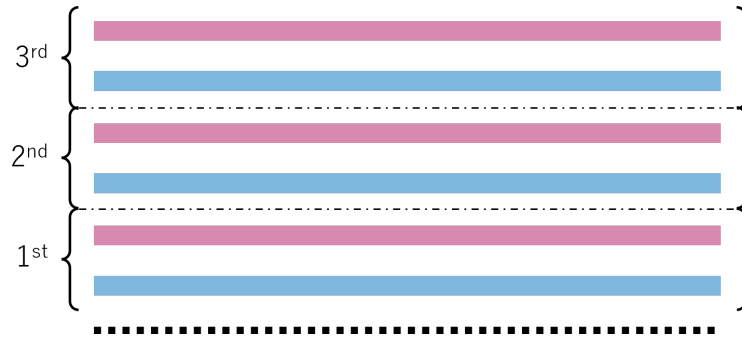


Figure 5.13: Composition of 3x Reactive Ink Layer (RIL), totalling three DIOL ink layers and three ISO ink layers, alternating in any deposition sequence.

A powder bed sample frame with a depth of 2 mm (see Section 5.2.1.2) was prepared with UX powder. The frame was then placed within the printer glove box and onto the DMP build platform for printing. Three print samples were prepared with 1x, 2x and 3x RILs, respectively. The DIOL ink - B112 - was first printed atop the UX powder bed with a simple, 1x waveform patten. This was then immediately followed by a print layer of ISO ink - A01 - with a MPW of 3x repeats. This deposition sequence was then repeated with the same ink formulations up to 3x. Once all samples had been printed they were left in the glove box overnight to minimise exposure to water during the polymerisation phase.

5.2.4.1 Visual Analyses of Reactive Ink Layer (RIL) Samples

Figure 5.14 provides a visual summary of six 1 cm square printed samples with varying RILs of 1x (Figure 5.14a,5.14d), 2x (Figure 5.14b,5.14e), and 3x (Figure 5.14c,5.14f) printed onto UX powder. Each image shows a sample pair which was comprised of the same number of RILs but with a different deposition sequence. The sample located at the top has been printed using Sequence 1 whereby the ISO ink was deposited first followed by the DIOL ink as discussed in Section 5.5. The bottom sample was printed taking a Sequence 2 approach.

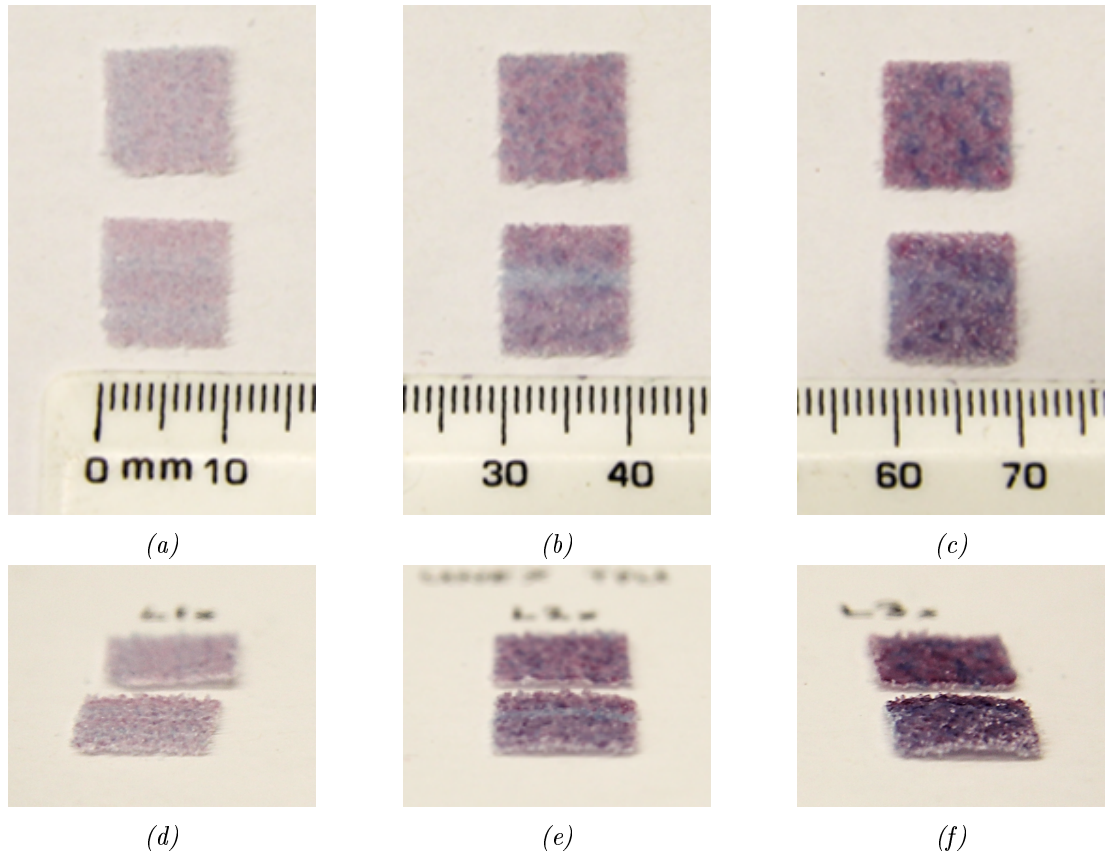


Figure 5.14: Various images of single powder layer (SPL) prints jetted with (a)(d) 1x Reactive Ink Layer (RIL), (b)(e) 2x RILs and (c)(f) 3x RILs onto UX powder.

Across all three RIL datasets a purple colour was observed, providing visual confirmation that both reactive inks had jetted successfully onto the powder substrate. With reference to Figures 5.14a-5.14c, aerial views of all six printed samples demonstrated the x-y dimensions were close to 1 cm and the geometry was mostly square with some rounding at the corners. However, there was a colour variation along the bottom row of samples (Sequence 2) as indicated by the blue horizontal stripes, suggesting the ISO

ink printhead was experiencing faults during the printing process which led to inconsistent ink deposition. The compromised sample area was located at the same point - approximately one-third of the distance down from the top edge - for all the Sequence 2 sample dataset. The top sample within the 3x RIL dataset displayed blue lines as seen by in clumps that had formed localised networks. This may be the result of DIOL ink pooling into deep voids along the printed sample surface or a printing fault during ink jetting.

Figures 5.14d-5.14f provide an angled view of all six samples, highlighting the variation in sample uniformity between datasets. At 1x and 2x RILs, samples were mostly flat, however significant deformation occurred at 3x RIL whereby the printed samples curled at the corners to create a bowl-shaped geometry. Based on earlier findings, printed SPL samples were experiencing significant warping as a result of increasing saturation level. However, deformation, or curling, appeared to occur in opposite directions within the 3x RIL dataset whereby the top sample (Sequence 1) curled slightly upward at the corners and the bottom sample curled downward creating a shallow dome-like shape. Thus, the deposition sequence may have played a significant part in the warping behaviour of saturated parts. Possibly, there were forces at play within the composite system that created tension along the ISO ink surface and compression along the DIOL ink surface. The impact of deformation appeared to be far less significant when Sequence 1 was applied as seen by the mostly flat sample exhibiting slightly curled corners.

Due to the cross-sectional uniformity, the 1x and 2x RIL sample sets were photographed with a ruler for reference as seen in Figure 5.15, respectively. As expected, the 1x RIL sample was smaller in all dimensions compared to the 2x RIL sample. However, the dimensional growth was not proportional whereby the cross-sectional thickness increased by 54 % while the width increased by 0.02 %. It was concluded that as the net ink volume increases, the reactive dual-ink binder system was drawn downward into the powder bed substrate more readily than spreading out horizontally. In addition to capillarity, gravitational forces may have also impacted the ink systems.

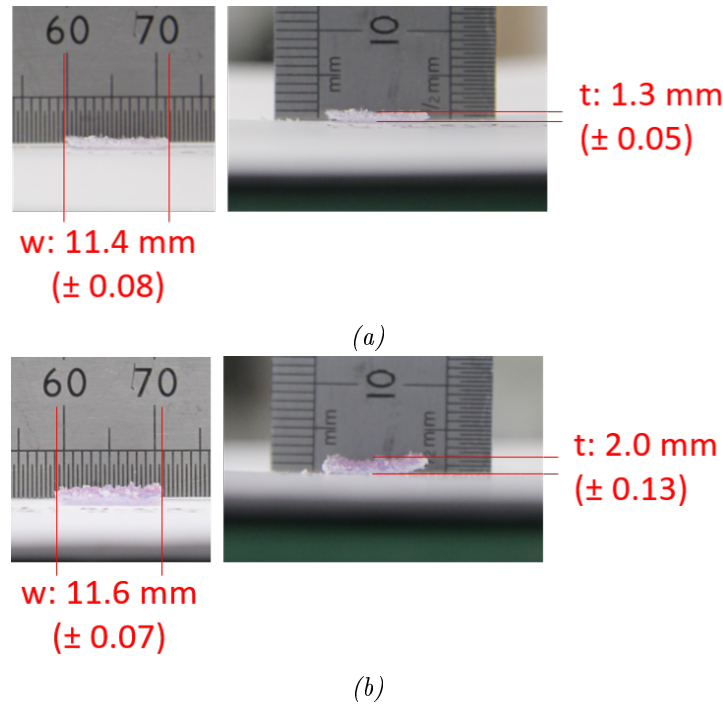
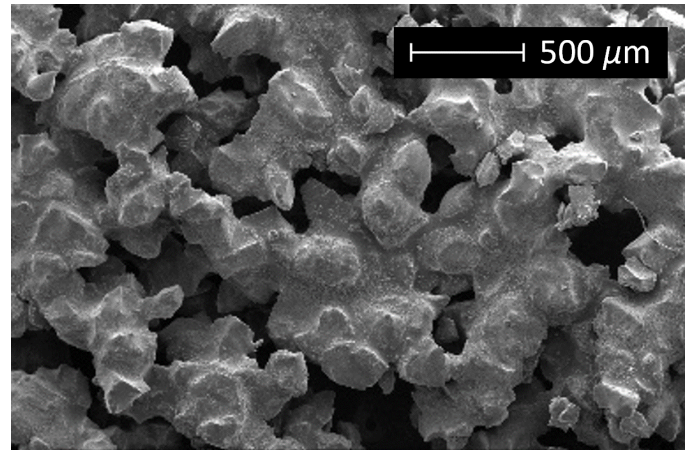


Figure 5.15: Images of SPL printed samples with dimensional annotations for (a) 1x RIL and (b) 2x RIL samples.

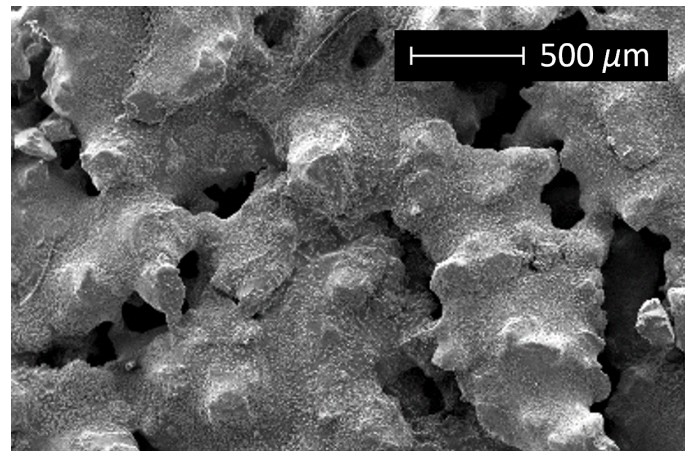
Furthermore, voids present in a powder bed substrate naturally form tiny channels or pores. These narrow microstructures lead to capillary action whereby a liquid, such as the reactive ink systems, are drawn through the channels before reacting and solidifying via polymerisation. A reduced surface tension between powder particles encouraged ink to spread through the powder substrate. However, as the net ink volume increased via increasing RILs, gravity appeared to dominant the intermolecular forces present in the ink-powder system due to a significant increase in printed sample thickness.

5.2.4.2 SEM Images of Reactive Ink Layer (RIL) Samples

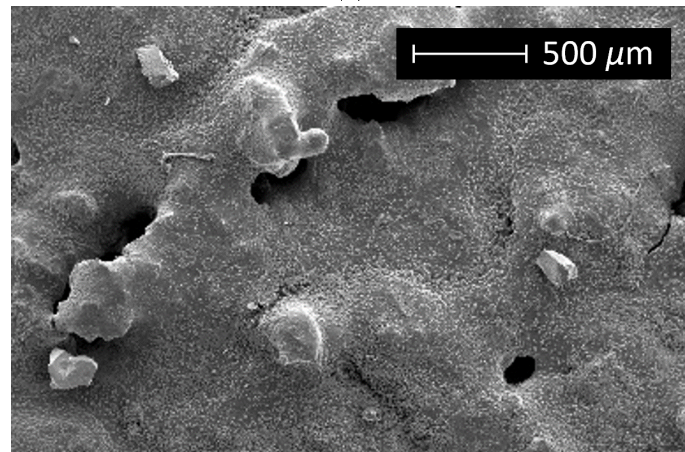
Each print sample was fixed to its own SEM stub using carbon tape as an adhesive. The fixed samples were coated in platinum following the method outlined in Section 3.2.3.3. SEM equipment was used to obtain micron-scale images of the sample surfaces. Each of the three samples can be seen in Figures 5.16a-5.16c.



(a)



(b)



(c)

Figure 5.16: Various SEM images at 100x magnification of single powder layer (SPL) samples printed with (a)(d) 1x Reactive Ink Layer (RIL), (b)(e) 2x RILs and (c)(f) 3x RILs onto UX powder.

As the number of RILs increased, the net volume of ink deposited onto the same location on the powder bed increased proportionally. The SEM images above highlight that with each additional RIL deposited, gaps or pores in the powder bed substrate decreased.

Thus, the powder bed surface became more saturated from sample 1 through to 3. This was confirmed visually via SEM imaging and numerically using X-ray Computed Tomography (XCT) scans to characterise cross-sectional density variation. The sections below outline the results from each method.

5.2.4.3 Cross-Sectional Sample Density Profiling

X-ray Computed Tomography (XCT) Arrays Printed samples were measured in three-dimensions via XCT to produce hundreds and thousands of 2D images. Each image was a representation of a thin cross-sectional slice of the sample. Each subsequent image incrementally shifted along the z-axis until a full suite of 2D images were produced. When compiled in MATLAB, these images formed a 3D image of the printed sample as seen in Figure 5.17. The applied XCT methodology can be found in Section 3.2.3.3.

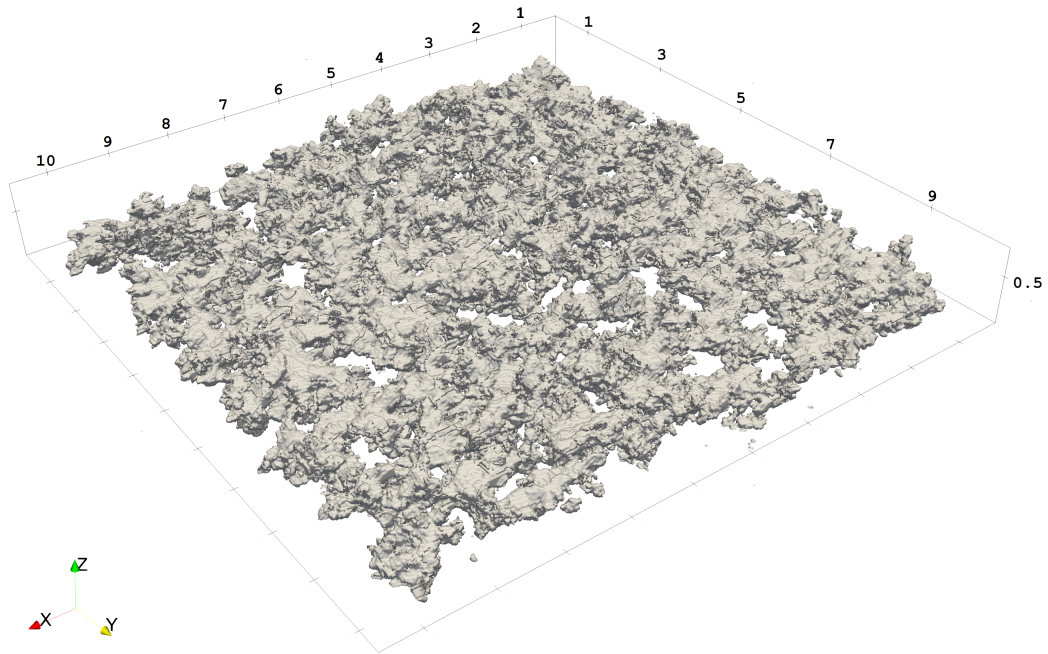


Figure 5.17: 3D reconstruction of multiple X-ray Computed Tomography (XCT) images for a SPL sample with a 1x RIL jetted onto UX powder; units in mm.

An array of ten 2D images were scanned from top to bottom as shown in Figure 5.18. In this format, variations in the sample thickness or geometry were more effectively observed. Layer 1 (L1) is displayed as a predominantly white image, indicating a high density relative to the surrounding ambient air. This can be interpreted as filled space

or, the presence of both PU powder and reactive inks in the printed sample. When compared to the top layer (L10), which had three separate high-density regions, it can be concluded that the geometry of the printed sample had warped into a bowl-shape, curling upwards for three of the four corners. This conclusion is further validated by layers six and seven (L6-7) where an empty black centre is distinguishable against the higher-density white detail framing the hole.

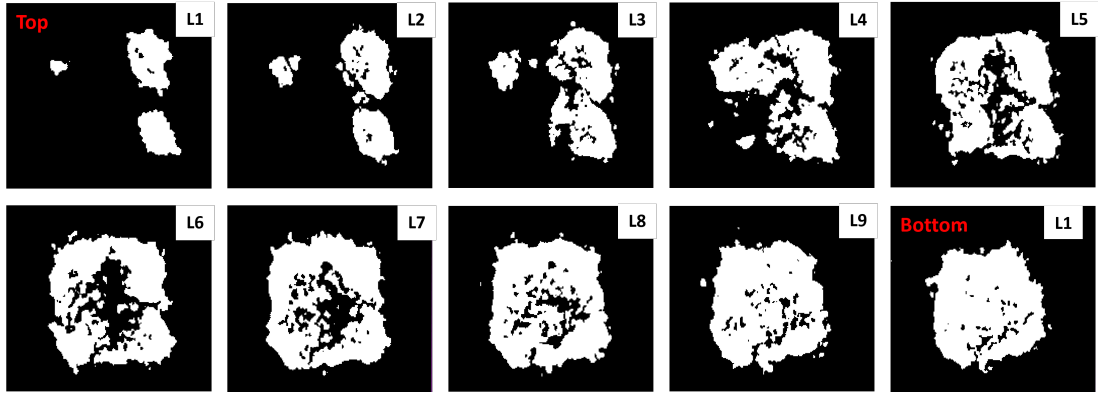


Figure 5.18: Array of X-ray Computed Tomography (XCT) slices displayed as x - y plane cross-sections between layers L1 - L10 for a single powder layer (SPL) sample printed onto UX powder.

Cross-Sectional Analyses Cross-sectional SEM images of the printed samples were obtained via cryo-fracturing and prepared using the same method outlined in Section 3.2.3.3. However, the sample holder used was not a standard SEM stub but instead a cubic holder with four clips on each side, thus mechanical force was applied to fix the samples instead of adhesive tape. Figures 5.19a and Figure 5.19b show the resulting fractured edges of print samples composed of 2x and 3x RILs, respectively. The 1x RIL sample was not shown as the material was too fragile to be prepared successfully for cross-sectional SEM analysis.

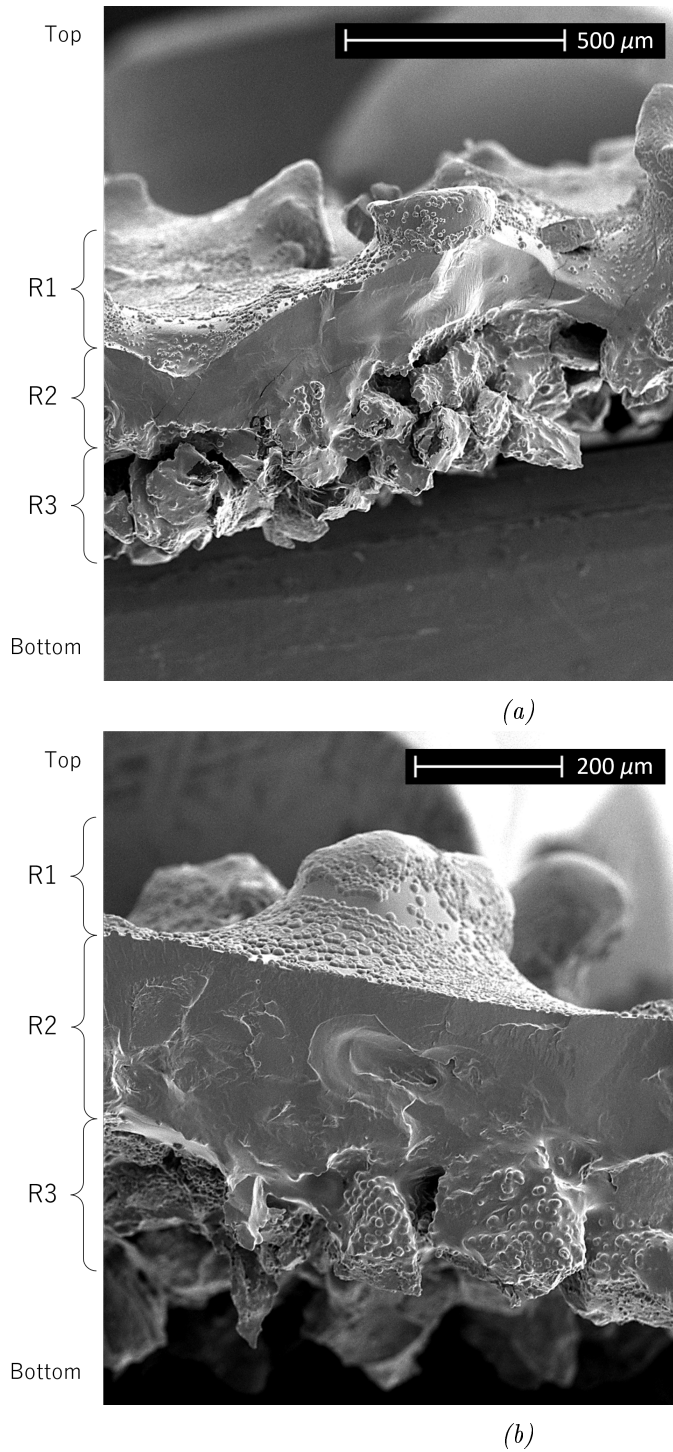


Figure 5.19: SEM images of cross-sectioned SPL samples with binder region annotations for prints (a) at 150x magnification for 2x RILs and (b) at 250x magnification for 3x RILs.

Across both printed samples, three distinct regions were observed. At the top was the outermost surface in which the reactive inks wetted the powder bed surface (R1) followed by a homogenous dual-ink binder layer (R2) and finally a jagged layer of unwetted powder particles (R3). The powder particles present in the printed sample were only

observed at R1 and R3, suggesting the dual-ink binder system had fully saturated the midplane of the printed sample. Previously, SEM images of the print surface always showed voids present regardless of the number of RILs used. Thus, the presence of a distinct binder layer provides insight into the ink-powder behaviours present in the system.

It is observed that the binder layer (R2) increases in thickness as the number of RILs increases. Using ImageJ software the average binder thickness was measured at $94.8\text{ }\mu\text{m}$ ($\pm 30.2\text{ }\mu\text{m}$) and $230.0\text{ }\mu\text{m}$ ($\pm 22.0\text{ }\mu\text{m}$) for both the 2x and 3x RIL printed samples, respectively. Thus, binder layer thickness as well as uniformity increased as net ink volume increased. The binder layer thickness did not necessarily increase proportionally due to a 143 % increase in average layer thickness between the 2x and 3x RIL samples. It is likely that the 1x RIL sample did not have a distinct binder layer (R2) present as the initial dual-ink layer coated the surface of the powder particles, lightly binding them together. During this stage, the reactive dual-ink binder system likely began to polymerise, turning from a liquid to a solid layer. The time required to complete the first full reactive ink layer using the DMP took between 10-20 minutes depending on the print settings applied. On average, it took 30 minutes and 45 minutes to print a 2x and 3x RIL sample, respectively.

Based on reactivity results summarised in Section 4.1.3, the rate of reaction dropped significantly after 6 minutes and by 25 minutes the reaction was mostly complete. Therefore, it may become harder for subsequent ink layers to pass the first RIL and penetrate deeper into the powder bed substrate. This may explain why the cross-sectional profile of the binder layer (R2) for the 3x RIL sample was more uniform and of consistent thickness; additional ink layers were blocked from spreading deeper into the powder bed so voids already present within the sample area were filled instead.

In both samples, powder particles were visible at R1 and R3. The roughness and angularity appeared much greater in R3 compared to R1 located at the top of the printed samples, highlighting the wetting behaviour between the reactive dual-ink system and the powder particles. Contrasts in particle sizes and shapes between R1 and R3 suggested good wetting had occurred, adding RILs to the particle surface which increased

the size of the particle while smoothing out the surface and rounding the sharp edges. Deposited ink layers settled at the join between horizontal binder layer (R2) and the vertical side of the powder particle creating a distinct curve where the ink had clung to the particle surface (see Figure 5.19b). This suggests there was a high surface energy at the interface between powder particle and ink, thus adhesive forces dominated over cohesive and gravitational forces.

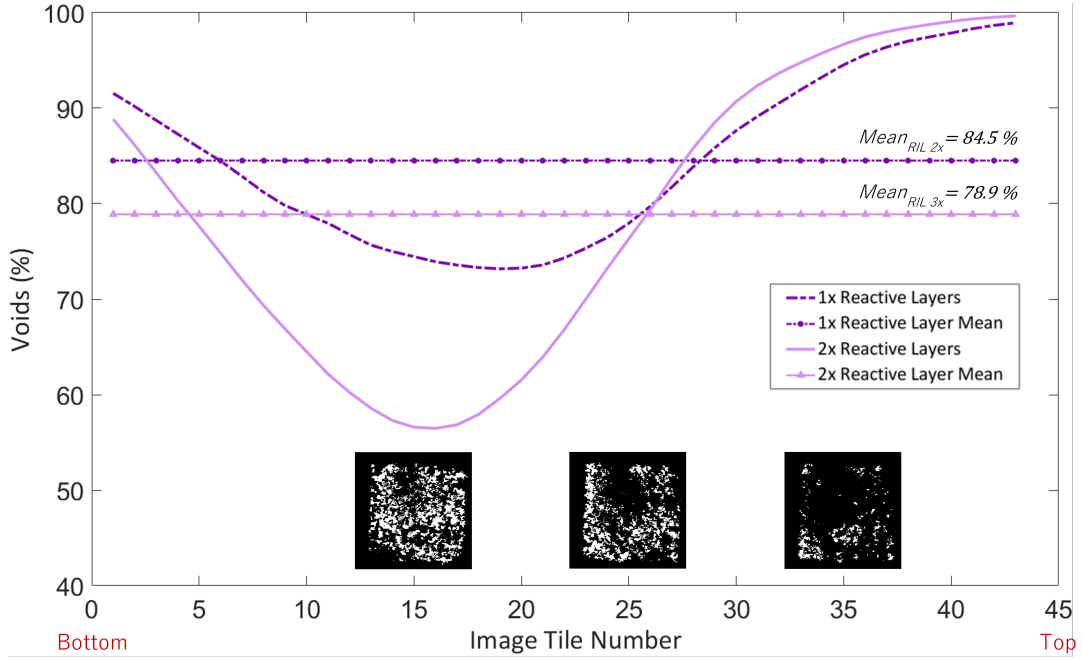


Figure 5.20: Cross-sectional profile of void percentage based on XCT images of 2x and 3x RIL samples from bottom to top along the z axis.

ImageJ and MATLAB software was applied to the raw XCT images of the 2x and 3x RIL samples shown in Figure 5.19. These tiles were manipulated in a similar way to those shown in Figure 5.18, allowing void percentage to be measured throughout the samples. This data was then extracted and plotted starting with the XTC images taken from the bottom of the sample. The result was plotted as shown in Figure 5.20, profiling the changes in saturation from bottom to top along the z axis.

It was observed that both samples started (tile number 1) and ended (tile number 43) at similar void percentages of approximately 90% and 99% , respectively. The sample with 3x RILs dropped significantly further than the 2x RIL sample with the lowest void percent values being 57% and 74%, respectively. This result was expected as the former sample received 50% more ink volume than the latter given it was three versus two RIL

passes. Based on the initial trend present, if the 1x RIL sample had been successful, its lowest void percent would have likely been near tile number 24 and near the 90% void mark.

With increased saturation of a given powder bed, the dual-ink binder system continued to penetrate deeper into the powder layer. This indicates the binder system was likely still in a liquid form by the time the final RIL layer had been deposited. Hypothetically, if the catalyst concentrations has been doubled, the location of the void percent peak would have possibly been further along the x-axis toward the sample top. This would have been due to the reactive inks polymerising too soon and acting as a barrier against further penetration into the powder bed.

With reference to the cross-sectional images shown in Figure 5.19, the highest saturation points within the SPL print were along the binder midplane. These sections of the prints were estimated to be 43% and 26% saturation for the 3x and 2x samples, respectively. This indicates that the middle layer of binder was not as solid as was originally theorised based on cross-sectional SEM images. It is likely there were pores or gaps running through the entire cross-section of the sample, including the binder midlayer, hence why the void percent through this section was so low. This suggests the SEM images of sample surfaces shown in Figure 5.16, could be representative of the whole sample, not just at the top surface. These results provided a deeper understanding of the ink-powder dynamics at play for RBJ printing of SPLs.

5.2.5 Summary

This chapter explored the properties of the commercial powders that would become the powder substrate. Particles sizing, flowability and morphology was characterised, providing fundamental information that later informed the initial powder recoating parameters. Optimised waveform patterns and printer parameters developed in Chapter 4 were applied to a powder substrate, eliciting a single consolidated print layer thus proving the dual-ink binder system was working.

Further optimisation was conducted around deposition sequencing, droplet spacing, cleaning cycles, and powder layer thicknesses. The focus throughout this section was

on enhancing print layer saturation while maintain geometric accuracy and, generally, trying to minimise print failures during powder recoating.

Saturation levels, particularly around how characterise and control them, was the final focus of the chapter. The impact of Reactive Ink Layers (RILs) and Droplet Spacing (DS) on print saturation levels were heavily explored. Additionally, the surface roughness and geometric accuracy was assessed, especially when challenges arose with sample warpage.

The experimental setup required both software and hardware modification to a commercial inkjet printer (LP50) to enable successful RBJ printing on powders. Results highlighted that greater RILs led to deeper binder penetration into the powder bed substrate as demonstrated in Figure 5.19 by a 3x RIL sample producing a 230 μm thick binder layer along the midplane. This led to an increased sample saturation level of 43 % (from 26 % for 2x RIL) and a 143 % thicker binder layer for a 3x RIL sample. However, higher RILs were also correlated with greater warping and deformation of printed samples. Typical layer thickness obtained via BJ printing falls within the range of 30 μm to 100 μm .¹⁸¹ However, these values are representative of the total thickness and not necessarily of the binder-only midplane.

Finally, a deeper understanding of the microscale features of single powder layer (SPL) RBJ samples was established through analyses of sample cross-sections and 3D dimensional models which provided key insights into void percentages and internal features of SPL samples. Additional insights can be drawn from existing literature which has demonstrated smaller particles lead to denser parts. Similarly, the more spherical a powder, the more dense the part will be.¹⁸² Therefore, highlighting the impact powder selection has on the void percentage potential of RBJ parts.

6 | Validation of Reactive Binder Jetting (RBJ) via Multiple Powder Layer (MPL) Printing

A full print layer (FPL) is comprised of a single powder layer and one or more reactive ink layers (RILs) as seen in Figure 6.1. Multiple powder layer (MPL) parts are achieved by subsequently printing multiple FPLs to form a three-dimensional (3D) part. The unique ink-powders dynamics involved in the process of MPL printing is explored throughout this chapter, building upon the single powder layer (SPL) printing knowledge outlined in Chapter 5.

Building on the insights gained from single powder layer (SPL) experiments in Chapter 5, this chapter explores the validation of Reactive Binder Jetting (RBJ) for multiple powder layer (MPL) printing, a critical step toward achieving fully consolidated 3D parts. The transition from SPL to MPL printing introduces additional challenges, including inter-layer binding, geometric accuracy, and the cumulative effects of Reactive Ink Layers (RILs) on part integrity. This chapter investigates these factors, focusing on optimising printer parameters, evaluating mechanical properties, and addressing common defects such as warping and misalignment. By systematically analysing MPL prints, this study aims to demonstrate the feasibility of RBJ as a scalable additive manufacturing (AM) process and provide foundational strategies for producing functional parts with high precision and reliability.

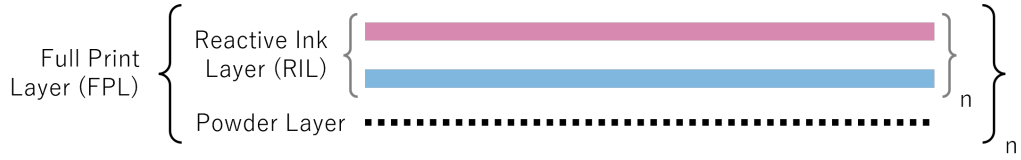


Figure 6.1: Graphic overview of a Full Print Layer (FPL) defined by a single powder layer and one or more Reactive Ink Layers (RILs).

6.1 Printer Set Up for Reactive Binder Jetting (RBJ)

Reactive Binder Jetting (RBJ) is a novel additive manufacturing process which requires the use of two or more reactive inks to consolidate powder particles to form a 3D part. Modifications to existing commercial printers were required to ensure the RBJ process could be applied throughout this research project.

6.1.1 Jetting Adjustments via LP50 (Software Modifications)

Modifications to a commercial LP50 machine were made by specialist consultants to customise the programme scripts to facilitate a transition between the DMP and LP50 printers.

6.1.1.1 Waveform Conversions

As a result of these changes, the original waveforms generated on the DMP for optimal jetting for each reactive ink were no longer compatible. Thus, a waveform conversion programme was developed to ensure printing voltages, segment durations and frequency were accurately transferred between commercial printer systems.

A script was prepared in MATLAB to convert the raw DMP waveform output to a simple waveform plot with minimal discrete data points. An example of a 3x multiple pattern waveform (MWP) plotted using this script can be seen in Figure 3.13 located within Section 3.2.4.2.

6.1.1.2 Droplet Spacing

The DMP system was designed to deliver a fine droplet spacing (DS) incrementally up to a 1 μm spacing. In Chapter 5, DS of 30 μm , 20 μm , 10 μm and later on 10 μm , 8 μm and 6 μm were investigated in SPL printing experiments. However, the LP50

printer does not have the same DS capacity, instead DS increments are 5 μm . As such, comparable DSs of 15 μm , 10 μm , and 5 μm were selected for the MPL printing experiments outlined in this chapter.

6.1.1.3 Pixel Density and Image Sizing

Changes in DS directly impacted the pixel density of a given ink, thus altering saturation levels per powder layer. As such, new printing parameters were selected to accommodate the shift from a 6 μm to 5 μm and 8 μm to 15 μm DS. The parameters for 10 μm DS remained unchanged between printers.

Print layer images like the one shown in Figure 6.2 were required to inform the printer where to jet ink and where not to. DS was altered by adjusting the angle that each printhead jetted at. For example, to increase the DS, the printhead angle should decrease with reference to the x-axis. An increase in DS would generate a larger print area as the image input was linked to a given number of pixels or droplets. To ensure the print output retained its original dimensions (e.g. 10 x 10 mm), the 5 μm DS print image size were scaled up while the DS increase to 15 μm required the image size to be scaled down.

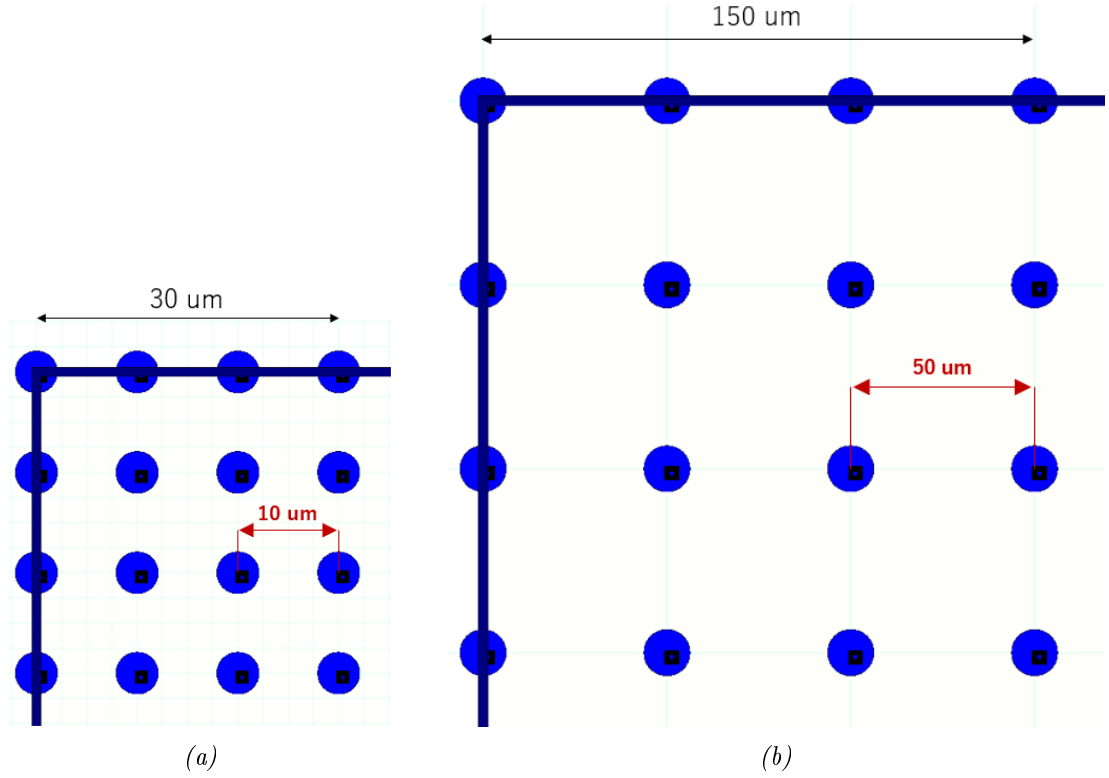


Figure 6.2: Print layer images for a Droplet Spacing (DS) of (a) 10 μm and (b) 50 μm to demonstrate pixel density changes.

6.1.2 Powder Recoating via LP50 (Hardware Modifications)

6.1.2.1 Powder Bed Platform

Commercial LP50 printers are commercial material jetting (MJ) printers equipped with a flat, non-porous metal build plate. To facilitate RBJ printing, a custom powder bed system was manufactured via CNC machining and assembled with two servo motors. With reference to Figure 6.3, the first motor moves the build platform up and down along the z-axis while the second motor is dedicated to moving the powder feed reservoir.

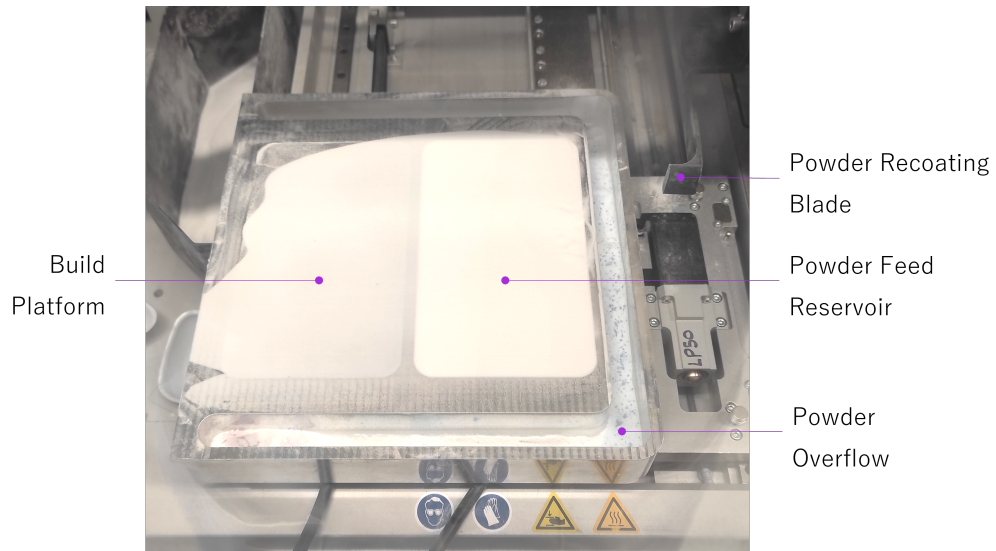


Figure 6.3: Custom powder bed for LP50 printer with part labels.

6.1.2.2 Powder Recoating Blade

As the printhead assembly moves along the x-axis, to enable powder spreading a 3D printed doctor blade was designed and manufactured to retrofit to the front of the printhead assembly as seen in Figure 6.4. As the printhead assembly and doctor blade moves gradually from right to left the excess powder from the powder feed reservoir is collected by the blade and pushed across the build platform, filling in the available space. In this image, a build-up of powder can be seen to the left of the blade. The powder overflow grooves located along three edges of the powder bed platform collect any powder that escape the doctor blade during recoating.

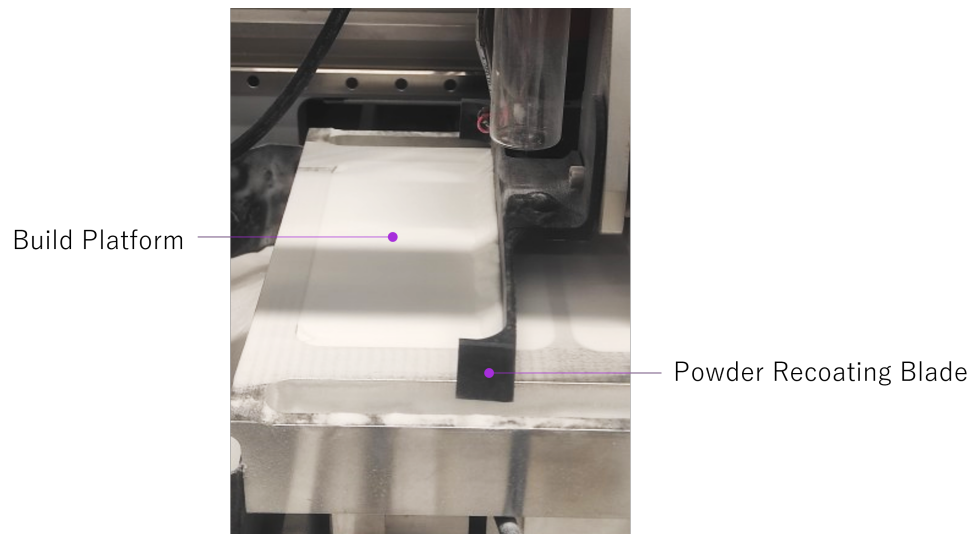


Figure 6.4: Custom LP50 recoater mechanism with part labels.

Additionally, the LP50 scripts were modified to enable the user to control the recoat speed and manually adjust the build platform and powder feed reservoir depths, thus controlling the amount of powder being displaced.

6.1.2.3 Dual-Printhead Assembly Holder

Due to the sensitivity of ISO inks and water, printheads are prone to clogging over time. Thus, DMC printheads were used as they are considered disposable due to the affordability of these printheads compared to other commercial printheads. Additionally, the minimum ink volume required for successful jetting is low. As such, modification to the LP50 printing scripts were made to integrate a dual-printhead system for DMC printheads.

An assembly holder was designed to secure two DMC printheads – Printhead A and Printhead B. The custom dual-printhead holder was 3D printed and retrofitted to the LP50 printer as seen in Figure 6.5. The offset in printhead locations required additional software modifications to ensure the print location, dimensions and deposition sequencing remained consistent with the built-in LP50 graphic user interface (GUI).

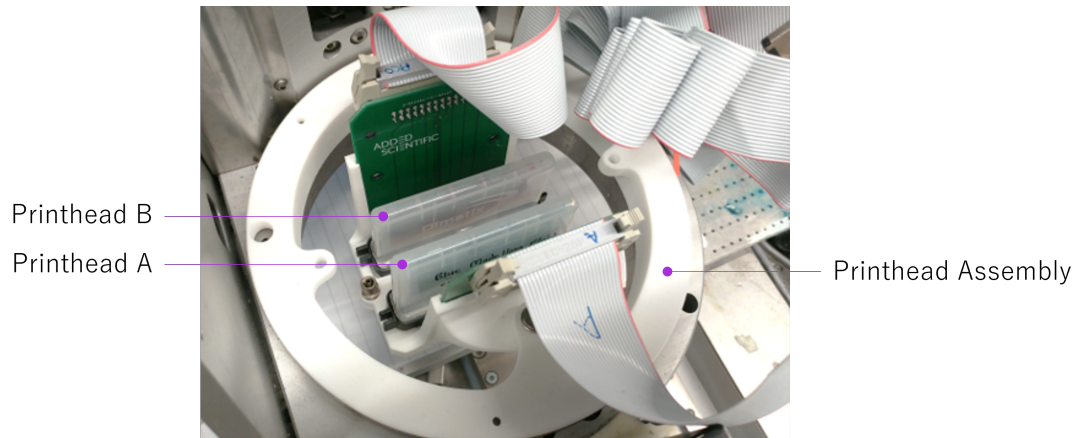


Figure 6.5: Custom dual printhead assembly holder for LP50 printer with part labels.

6.1.3 Printing Parameter Calibrations for Reactive Binder Jetting (RBJ)

Before RBJ printing could begin, final print parameters for both the inkjet printing and powder recoating processes needed to be selected and inputted into the LP50 GUI. Then to ensure the whole printer system was functioning correctly, a print test would

be conducted to enable the user to make a quick visual assessment of the printer set up quality.

6.1.3.1 Parameter Selection

Inkjet Printing As discussed previously in Section 6.1.1.3, the DS and pixel size of a print are directly linked. Additionally, the number of reactive ink layers (RILs) and DS directly impacts the saturation level of a given powder layer. Changes in saturation levels, or net ink volumes, between reactive inks directly alters the quantity of moles present, thus impacting the average molar ratio within each RIL. Moles for each reactive ink are also impacted by the jetting waveform whereby MPWs will typically increase with droplet size and therefore the number of moles ejected with every droplet.

As the parameters summarised above are linked to each other, a specific parameter selection process should be applied to ensure RBJ printing produces 3D parts as expected. Therefore, the following steps should be followed in order:

- (i) Determine desired molar ratio (e.g. 1:1 of $-OH$ to $-NCO$) and select an appropriate waveform for each reactive ink.
- (ii) Select an optimal droplet spacing (DS) for chosen powder, reactive ink set and jetting parameters.
- (iii) Determine desired part size and adjust image pixels based on chosen DS.
- (iv) Determine desired saturation level and select an appropriate number of reactive ink layers (RIL) per powder layer.

Powder Recoating Three powder recoating parameters require optimisation to successfully apply a new layer of powder atop a subsequent print layer. The first is the powder recoat speed which can be manually adjusted via a custom script followed by the build platform height, and powder feed reservoir height, both of which directly impact the powder layer thickness (PLT) as shown in Figure 6.6. In this case, the plate at the bottom of the powder feed reservoir is raised to bring a thin layer of powder above the neutral plane ($z = 0$). Simultaneously, the build platform is lowered proportionally to create space above the previous powder layer, allowing displaced powder particles to fill the gap during recoating.

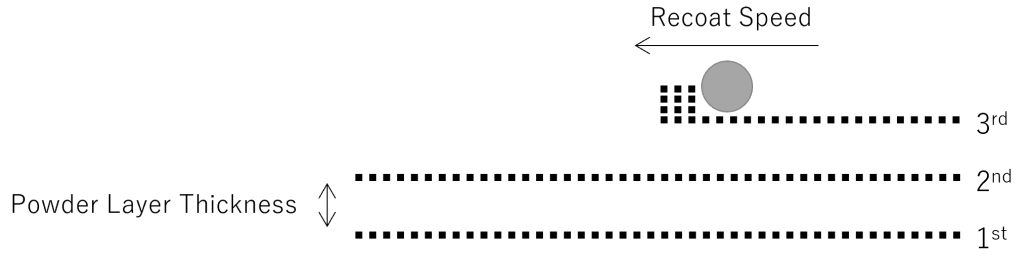


Figure 6.6: Overview of powder recoating process with key settings labelled.

These parameters are critical to get right for the chosen RBJ system, otherwise parts may become damaged during printing, develop geometrical defects, or delaminate throughout. Examples of printing failures due to poorly selected powder recoating parameters are outlined within Section 6.2.2.

6.1.3.2 Offset Print Testing

Once the inkjet printing and powder recoating parameters have been selected and inputted into the LP50 printer, an offset print test was conducted to confirm the RBJ set up process had been completed successfully. By applying a manual horizontal offset to the print origin location of Printhead B, the resulting print output resembled the image in Figure 6.7 whereby the purple region indicated an overlap of both the ISO and DIOL inks had occurred. The print dimensions could be measured at this stage to ensure the correct print size had been achieved. The jetting health of each printhead was visually checked to assess the colour outputs. If three distinct colour regions - red, purple, and blue - can be clearly observed and are in alignment, the RBJ system is ready for printing.

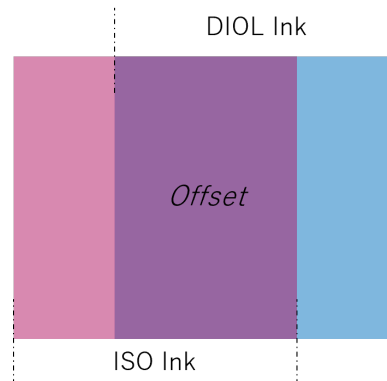


Figure 6.7: Visual summary of a horizontal offset print for ISO (red) and DIOL (blue) inks.

6.2 Three-Dimensional (3D) Printing Optimisation

Throughout this section, multiple print layers were printed to form simple 3D samples. The binding strength between print layers was explored in Section 6.2.1, including the impact of powder recoating parameters on part delamination. Additionally, print layers were found to misalignment or become offset in the first few print layers due to a dragging effect during recoating. Thus, location of the sample on the build platform was found to play a role in the degree of part deformation as outlined in Section 6.2.2.

6.2.1 Powder Recoating Parameters

The minimum powder layer thickness (PLT) was limited by the powder properties, including the particle size and morphology. Additionally, powder recoating parameters must be optimised for each powder sample to ensure the appropriate powder recoating parameters were used lest the part fail during printing. For example, if the bottom of a given powder recoating mechanism (roller or blade) is raised 80 μm above the neutral printing plane ($z = 0$) but the average powder particles have a diameter of 100 μm , the recoating process will likely lead to failure due to insufficient space for the powder to flow smoothly during recoating. However, if loose powder is present below the neutral plane of the build platform, it is more likely for the powder particles to create a larger gap by pressing down on the existing powder. This leads to powder displacement which causes damage to the previously printed layer(s).

Damage of this nature can still occur even if the recoating system is set to a gap size, or working height, that is greater than the largest particle diameter. This is because the local height of the previously printed print layer may rise above on the neutral build plane due to oversaturation of reactive inks, thus reducing the recoating gap to a value less than the working height inputted initially. Thus, it is important to evaluate powder recoating parameters only after reactive dual-ink systems and jetting parameters have been selected as changes to these may impact the powder recoating parameters.

6.2.1.1 Delamination

The optimum height of the recoating blade that enabled powder flowability while minimising PLT could be estimated using PSD data. However, this approach cannot be

relied on as initial experimentations which applied this method led to print layer damage during recoating between print layers resulting in part delamination shown in Figure 6.8 below.

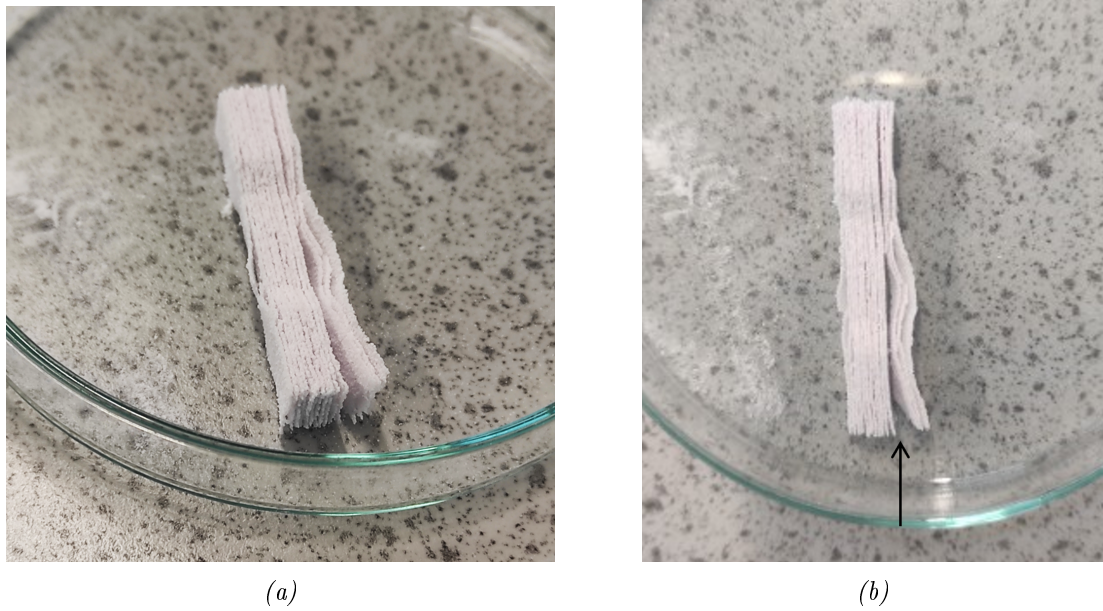


Figure 6.8: Example of delamination occurring in Reactive Binder Jetting (RBJ) printed dog bone composed of 18x RILs; scaled image of part is available in Figure 6.17b.

Although the sample bulk remained loosely connected, there was at least one major point of failure where the arrow in Figure 6.8b is pointed whereby the print layers had mostly disconnected. Up close visible gaps can be seen between the layers, especially along the edges as seen in Figure 6.8a. Thus, to prevent delamination there are two main approaches that can be taken. Firstly, the PLT can be reduced to shorten the distance the reactive dual-ink system needs to travel to reach the previous print layer before polymerising. This may not always be feasible since the powder particle size will limit the recoating height of the blade. Alternatively, when the PLT can not be lowered any further, the net volume of reactive ink can be increased to penetrate the powder layer deeper until it reaches the previously printed layer. The limitation with this approach is time as the dual-ink system will immediately start reacting, eventually ceasing powder layer penetration. Thus, there needs to be large enough quantities of each ink deposited in a minimum amount of time. To achieve this, the jetted reactive dual-ink system needs to fully saturate the newly deposited powder layer and reach the previous print layer within 6 minutes of the second reactive ink being deposited onto

the first reactive ink. Thus, multiple reactive ink layers (RILs) are applied to maximise reactive ink saturation within a short period of time.

6.2.1.2 Maximising Saturation

To determine the maximum number of RILs that could be printed without causing the printed sample to fail, a series of single layer prints (SLPs) were deposited at 1x, 2x, 3x, 4x and 5x RILs (samples 1-5, respectively) onto a bed of powder as seen in Figure 6.9a. A DS of 10 μm was used initially. At S4 and S5, the print layer can be seen to have failed immediately due to the visible warping upward at the corners and edges as seen in previous experiments (see Section 5.2.4). With reference to the agglomeration of wetted powder formed at the surface of both S4 and S5, a layer of ink remains behind within the original footprint. This suggests the first 1-2 RILs had sufficient time to react, thus binding the wetted powder together. Therefore, it is likely the powder layer became fully saturated by the 3rd RIL causing subsequent RILs to pool together rather than penetrate the powder bed, creating the dark purple agglomerations at the surface.

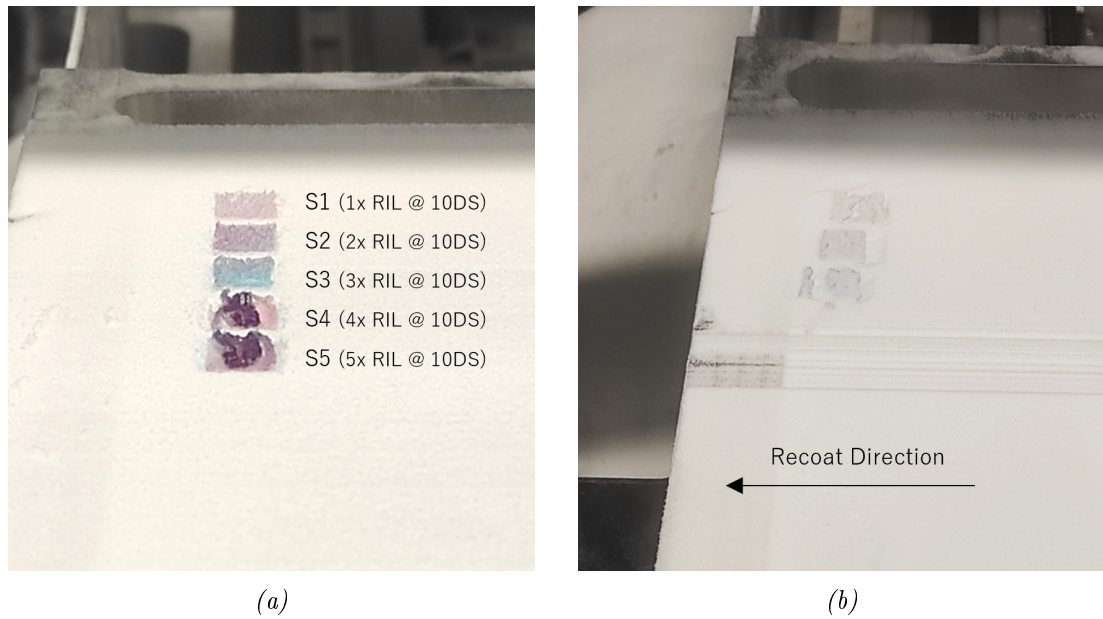


Figure 6.9: Single Powder Layer (SPL) samples S1 - S5 printed at a 10 μm DS with increasing Reactive Ink Layer (RIL) from 1x - 5x, respectively. (a) Print layers applied and (b) samples S1-S3 remain following powder recoating.

To assess whether any remaining print layer samples had become oversaturated a subsequent powder layer must be applied by the recoating mechanism at an optimal working height for the chosen powder type. If any of these samples experience a major failure at

this point, then those print parameters are deemed unsuitable for the selected powder and reactive dual-ink system. With reference to Figure 6.9b, print layer samples S1, S2 and S3, the previous print layers were either directly damaged or displaced from their original locations during the recoating process. Meanwhile samples S4 and S5 were fully displaced from the build platform and became stuck to the bottom of the recoating blade. Thus, two linear tracks were created as the blade returned to its starting position on the right side of the build platform. The samples likely became attached to blade because they had not fully reacted yet and therefore were still tacky. Overall, all samples S1-S5 had made contact with the blade during powder recoating process, suggesting the powder recoating parameters require further optimisation for these specific print parameters (10 μm DS).

If the cause of failure for samples S1-S5 was due to a combination of oversaturated powder layers and non-optimal powder recoating parameters (e.g. build platform height), then a reduced pixel density would lead to less saturate print layers. Another experiment was conducted following the same methodology used earlier in this section, however the DS was increased to 20 μm . The print result for RILs 1x - 5x at 20 DS can be seen in Figure 6.10 where each sample have been labelled T1 - T5, respectively. Immediately, it is apparent no significant warping has occurred. When the same powder recoating parameters are applied to this sample set only sample T5 is seen to clearly failure. Thus, this experiment highlights the impact of oversaturation on MLP, especially during the powder recoating process.

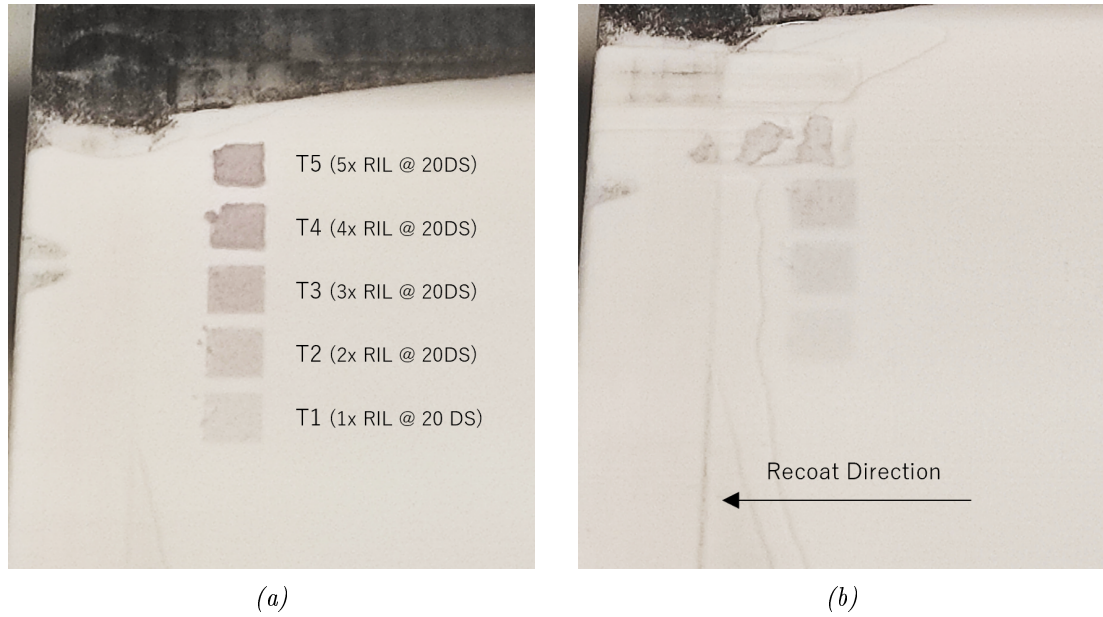


Figure 6.10: Single Powder Layer (SPL) samples T1 - T5 printed at a 20 μm DS with increasing Reactive Ink Layer (RIL) from 1x - 5x, respectively. (a) Print layers applied and (b) samples T1-T4 remain following powder recoating.

Warping & Splitting Print layer samples S1, S2, S3 along with samples T1 - T5 remained mostly flat, however slight curling at the corners occurred for S2 and S3 whereby degree of deformation increases with increasing RILs. During powder recoating, S1, S3 and T5 split down the middle along the vertical axis but retain their original position on the build platform. Whereas samples S4, S5 and T5 are visibly displaced from their original print location having been dragged to the left by the recoating blade. Both print layers have risen above the neutral plane ($z = 0$) and very likely higher than the chosen PLT for the new powder layer, hence catching the recoating blade at the print layer corners. However, the likely cause of print layer splitting is due to the downward pressure onto the print layer caused by the combined forces of powder buildup at the front of the blade as well as the recoating blade itself assuming the print sample height had increased. Additionally, sample S3 appears more visibly blue than purple relative to the rest of the sample set. Thus, there is a concern the dual-ink binder system is compromised thus weakening the binding between particles which may have contributed to the vertical split.

6.2.2 Print Stability on Build Platform

The results presented in Section 6.2.1.2 highlighted print layer samples experienced significant damage and/or displacement during powder recoating. Based on observation, one theory is that powder buildup at the front end of the recoating blade leads to a rotational downward force into the powder bed as loose powder is forced into the prepared powder layer void. Figures 6.11a-6.11d below summarise the recoating process, highlighting the suspected counter-clockwise rotational forces going into the build platform. The magnitude of the rotational force is expected to be highest at the right side of the build platform when the quantity of powder waiting to be spread is at a peak. The downward rotational force is expected to lessen linearly as the recoating blade moves across the build platform since the amount of powder buildup is lessened as seen in Figure 6.11d.

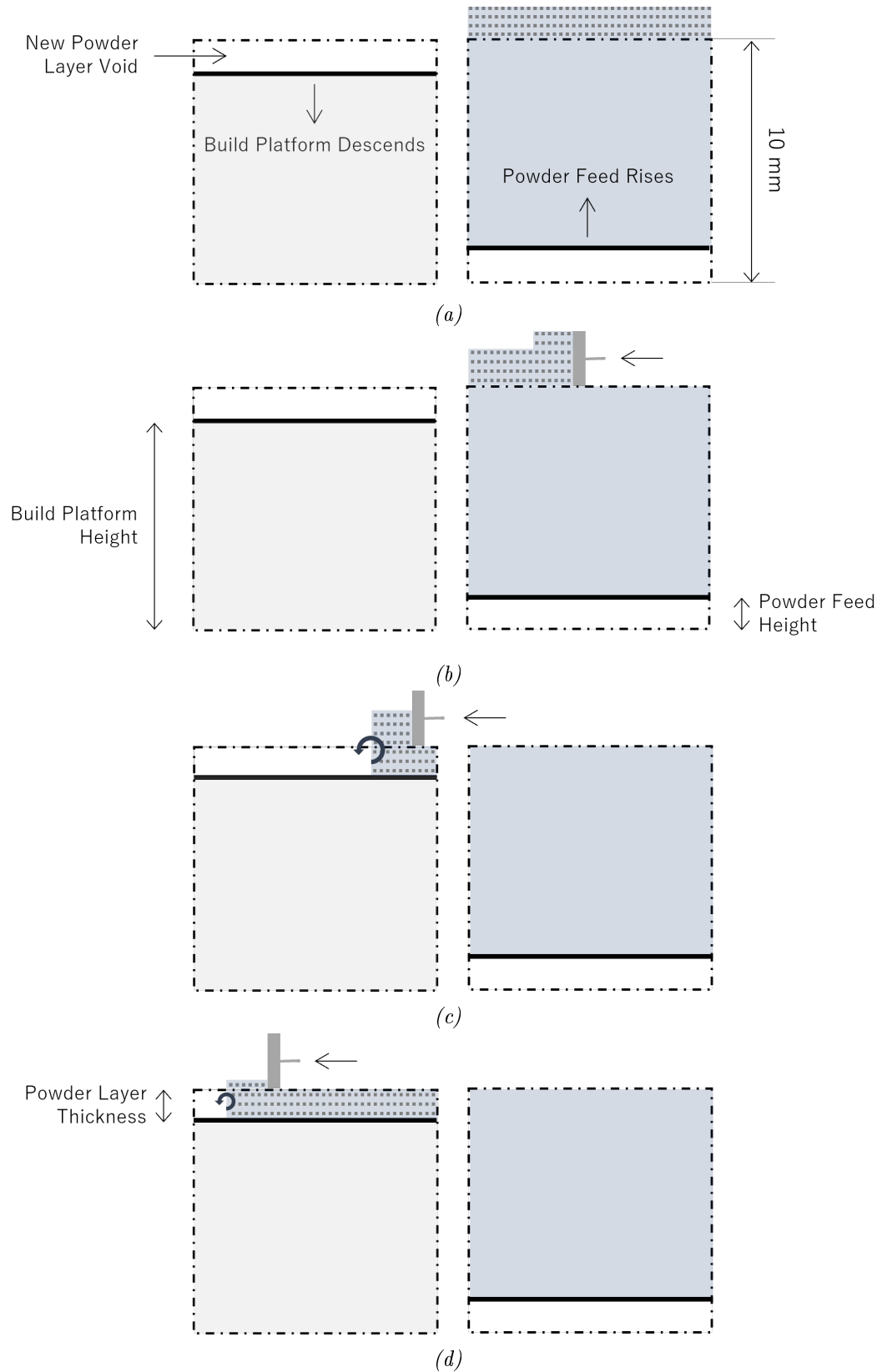


Figure 6.11: Summary of the recoating process from (a) powder feed rising to (b)(c) spreading powder from right to left leading to a (d) new powder layer.

6.2.2.1 Print Layer Displacement

To validate this theory, a simple experiment was conducted whereby four 1x RIL samples were printed using identical jetting parameters at four unique locations on the build platform. Rotational forces at each print location, labelled L1 – L4 in Figure 6.12, are expected to vary. The print layer quality following a single powder recoat can be seen in Figure 6.12b. Both samples L1 and L3, located the furthest away from the powder feed reservoir, experience minimal damage or displacement whereas L2 and L4 have been spread evenly across the powder bed to the left in the same direction of the recoating blade. Therefore, a large powder buildup at the front of the recoating blade can lead to poor print layer quality. Additionally, between samples L2 and L4, the latter is not as wide suggesting the forces are fewer at this location. This aligns with visual observations whereby there is less powder at the top and bottom of the recoating blade since any powder buildup tends to fall into the overflow grooves, thus limiting the powder recoating forces at the ends. Thus, the impact of poor recoating parameters can be mitigated through print location selection. Additionally, reducing the recoating speed was found to reduce print layer displacement.

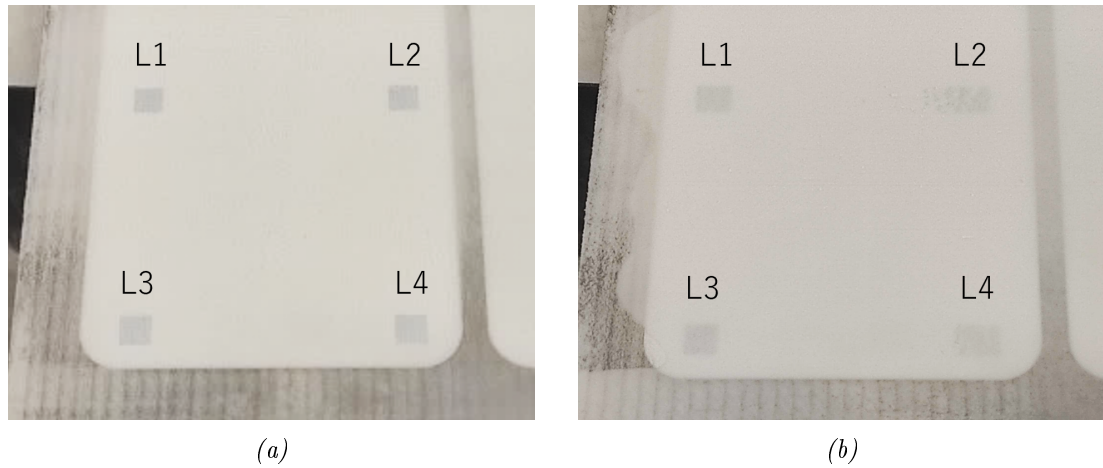


Figure 6.12: Four 10 mm square print layers in locations L1-L4. (a) Print layers applied and (b) print layers displacements following powder recoating process.

The impact of oversaturation and poor recoating parameters can lead to print layer displacement which leads to MPL samples like the ones shown in Figure 6.13. The first print layer had been dragged across to the left during recoating. However, subsequent print layers were seemingly unaffected by the print layer offset, resulting in a 3D part

with good layer binding. By observation, the first 1-3 print layers are often displaced during recoating before the part stabilises, remaining in the same location throughout the remainder of the whole printing process, including multiple powder recoating passes.

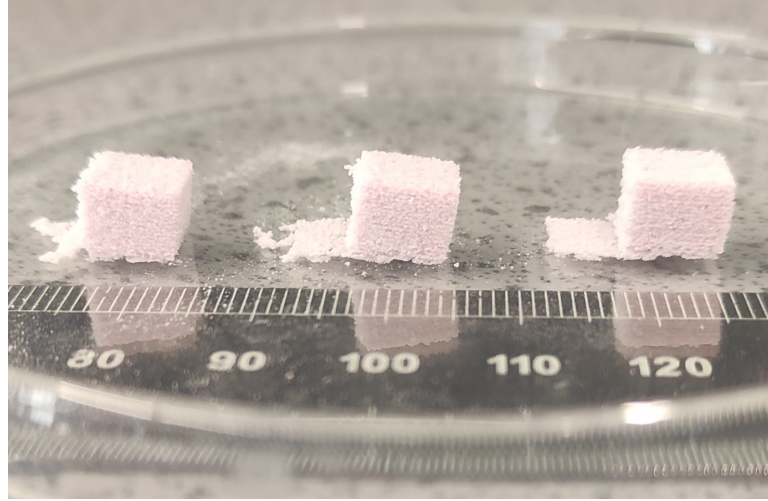


Figure 6.13: Print layer offset following RBJ printing of 18x RILs.

6.2.2.2 Printed Raft Stabilisation

To stabilise the first print layer of a 3D MPL part, a raft mechanism was applied whereby the first few prints of every print are designed to be detached from the main part. This was implemented by following the steps below:

- (i) Jet a single print layer using optimal parameters (e.g. 2x RILs, 20 DS) at the desired part location.
- (ii) Lower the build platform by 350 μm and raise the powder feed plate by 400 μm .
- (iii) Apply the recoating blade at a speed of 5 mm s^{-1} to generate a 350 μm powder layer.
- (iv) Repeat step i to produce a total of two print layers.
- (v) Lower the build platform by 500 μm and raise the powder feed plate by 550 μm .
- (vi) Apply the recoating blade at a speed of 5 mm s^{-1} to generate a 500 μm powder layer.
- (vii) Repeat steps i-iii continuously until the desired number of full print layers (FPLs) have been achieved and a 3D part has formed.

This raft mechanism was applied to the sample shown in Figure 6.14a which is composed of twenty FPLs in total. To the right of the black dotted lines, is a lightly bound raft. The raft was promptly and gently removed from the bulk of the 3D part using tweezers

to minimise surface damage as seen in Figure 6.14b. This resulted in a 3D rectangular part with good geometric accuracy and placement of all eighteen remaining FPLs.



Figure 6.14: Rectangular 3D RBJ part built above a supportive raft where (a) highlights the boundary with the dotted line and (b) demonstrates how the raft is removed during post-processing.

6.3 Part Quality and Performance

Following several iterations of powder recoating parameters to determine optimal settings for a given powder and reactive dual-ink system, a set of 3D parts were manufactured on the LP50 machine using the RBJ printing parameters outlined in Figure 6.16.

Two samples of each geometry – small cube, large cube, and rectangle – were produced to assess repeatability regarding both geometric accuracy and mechanical properties later in this section. Figure 6.15 provides images of the 3D parts manufactured using RBJ techniques, thus providing initial validation for RBJ printing as a feasible additive manufacturing (AM) technique.

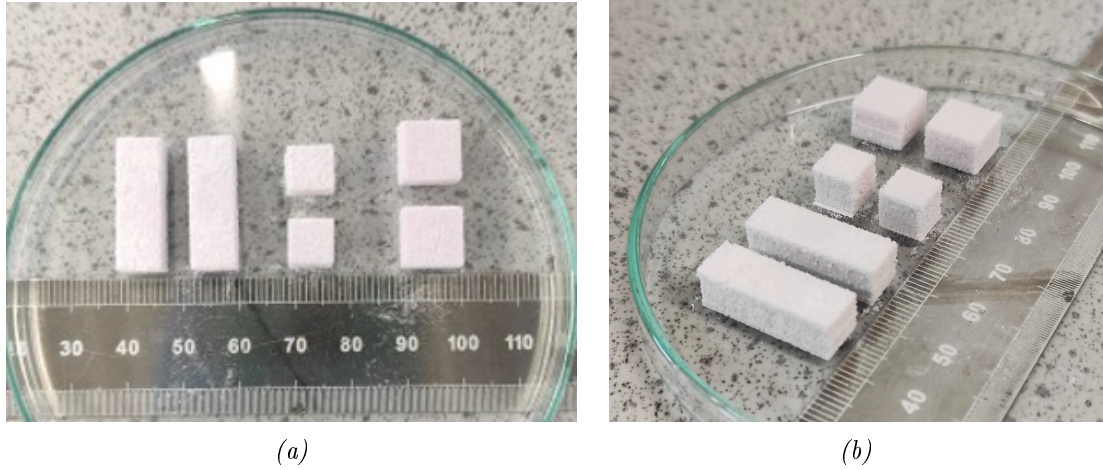


Figure 6.15: Images of 3D RBJ printed samples composed of the dual-ink binder system and UX powder.

6.3.1 Geometrical Analyses of Multiple Powder Layer (MPL) Printed Parts

AM is often applied over other traditional manufacturing techniques because of the design freedom it lends, meaning highly complex geometries can now be manufactured and at a cost-effective price point. Therefore, functionality is often more important than strength, especially for polymeric systems like the PU composites researched throughout this project. When assessing whether RBJ printing is a suitable technique, the print geometry is an important area of focus on to decide.

6.3.1.1 Uniform Shapes

Figure 6.16 outlines the target dimensions and settings for printing and recoating for each sample. Further to the SPL geometry measurements outlined in Section 5.2.4.1, the width and length are greater than the intended print size. Despite having a rough surface texture, especially along the sides where individual layers can be seen, the overall shape is well defined with sharp edges. Additionally, the print sample thickness is greater than predicted. However, this is expected given the reactive dual-ink system is designed to penetrate beyond the PLT to achieve sufficient layer-to-layer binding. The theoretical thickness is estimated by multiplying the number of print layers by the PLT (e.g. $18 \times 350 \mu\text{m}$).

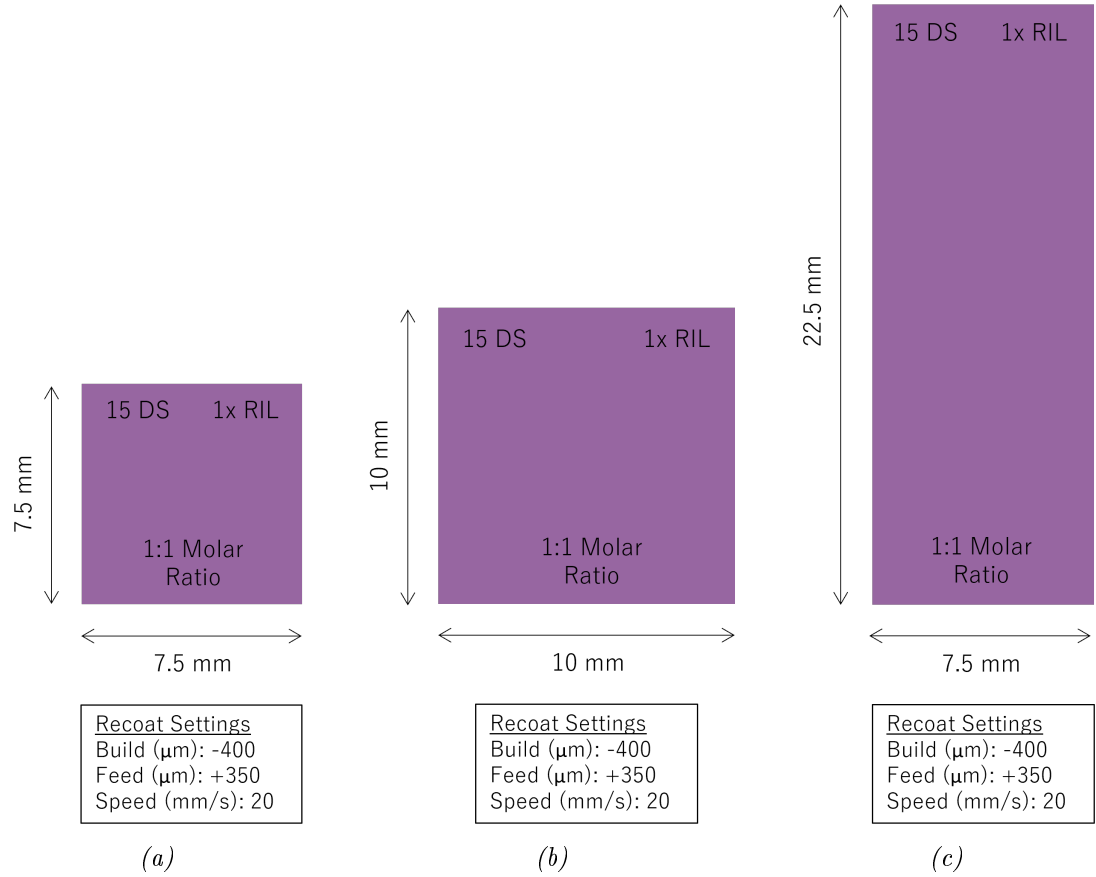


Figure 6.16: Overview of target dimensions and settings for printing and recoating for each sample.

6.3.1.2 Non-Uniform Shapes

The geometric accuracy and surface quality of non-uniform 3D parts manufactured via RBJ printing is relatively low cost compared to other AM techniques. This is likely related to the particle sizing of the selected powder rather than the technique itself. However, powders with smaller particles are more likely to warp or fail during printing due to oversaturation. The cubic out-out and dog bone geometries shown in Figures 6.17a and 6.17b, respectively, provide a visual overview of the geometry of non-uniform shapes.

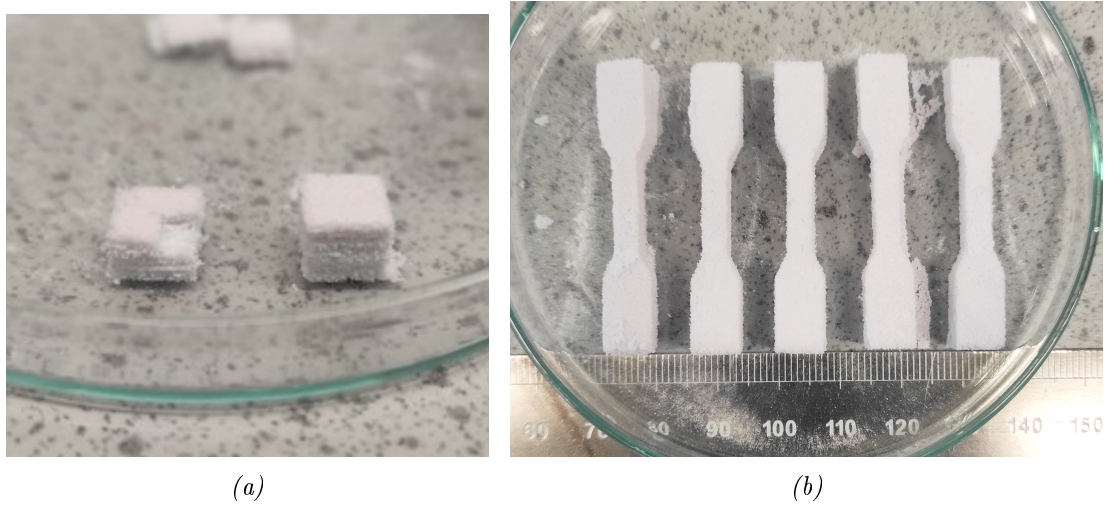


Figure 6.17: Images of RBJ printed parts in the shape of (a) 10 mm cube with an extruded cutout in the corner and (b) dog bones of length 22.7 mm.

6.3.2 Mechanical Analyses of Multiple Powder Layer (MPL) Printed Parts

A small sample set of 3D parts were prepared for mechanical testing to explore the tensile and compressive strengths that RBJ printing leads to.

6.3.2.1 Tensile Testing of Multiple Powder Layer (MPL) Printed Parts

The two rectangular samples 22.5 mm in length shown in Figure 6.15 are used to obtain a baseline tensile strength for MPL RBJ printed parts using optimal parameters. Close up images of these samples can be in Figure 6.18 below.

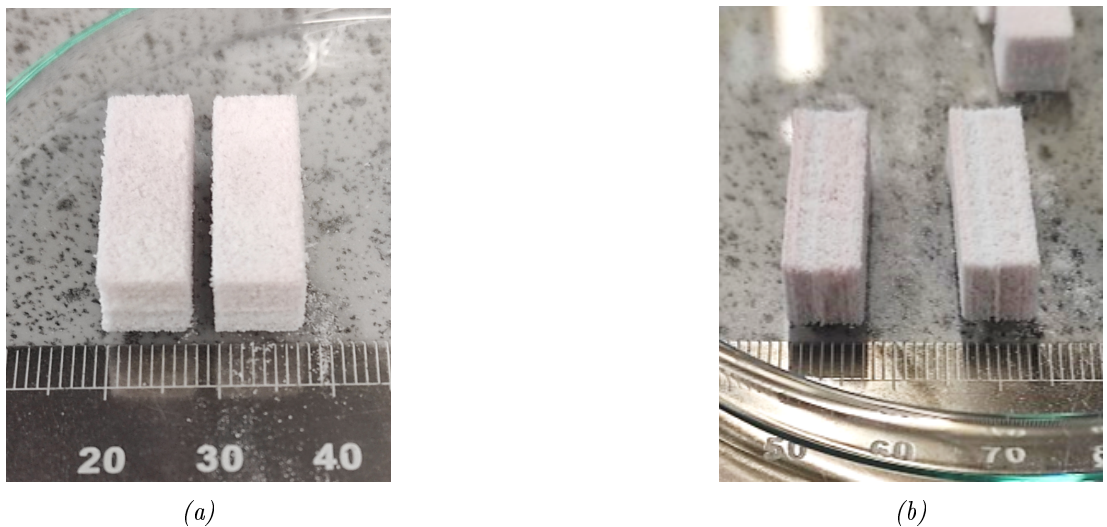


Figure 6.18: Images of two 22.5 mm rectangular RBJ parts positioned (a) upright with layers horizontal and (b) sideways with layers vertical.

The samples were prepared between the two sets of clamps as seen in Figure 6.19a. Due to part elasticity, flexible clamp holders were used to conform with the variable shape. A 50 kN load was applied at a constant rate of 0.5 mm min^{-1} until failure occurred. Rather than failing suddenly (e.g. snapping in half), individual print layers began to tear one at a time starting from the outside layers then working toward the midline of the parts. Initially, the part had slipped from the clamp holders, requiring minor adjustments at the start until a balanced grip was achieved whereby the part was not overly compressed or damaged but was sufficiently gripped by the clamp to allow tensile testing. Finally, the part reached a failure point as seen in Figure 6.19b which resulted in a mean Ultimate Tensile Strength of 35 kPa and Young's Modulus of 4 kPa. A stress vs strength plot for these samples can be seen in Figure 6.19c below.

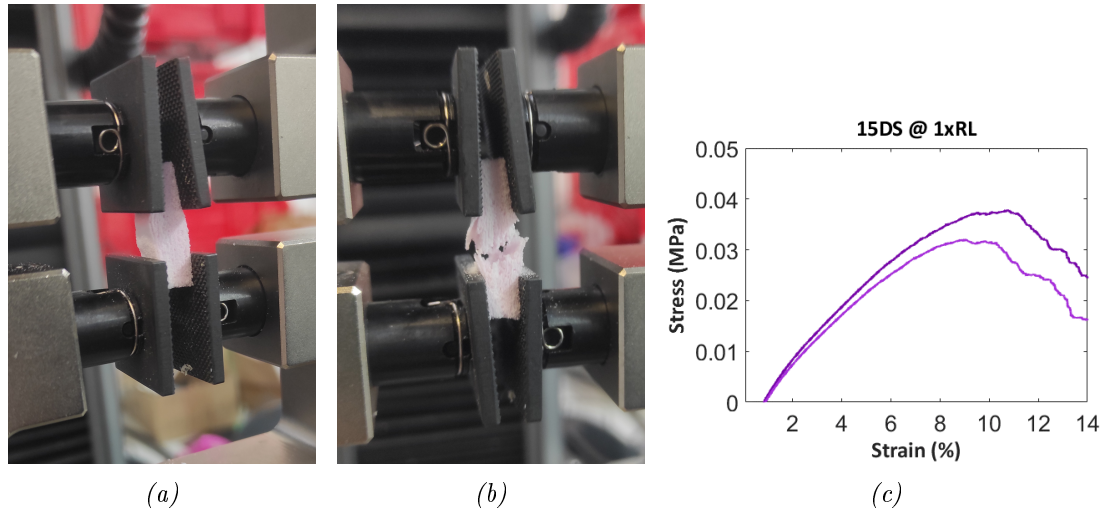


Figure 6.19: Tensile testing at (a) setup, (b) fail point and (c) results plotted in a stress-strain curve.

6.3.2.2 Compression Testing of Multiple Powder Layer (MPL) Printed Parts

Cubic samples were prepared at 10 mm in size for compression testing using the 100 kN load set up shown in Figure 6.20a. The first cubic sample (S1) follows the same printing and recoating parameters outlined previously in Figure 6.16b. However, the second sample (S2) applies the same recoating parameters but differs in DS and RIL whereby 20 and 2x are used, respectively. The two different sample were selected to highlight how elasticity varies between droplet densities given S1 is $4,444 \text{ px mm}^{-2}$ and S2 is $2,500 \text{ px mm}^{-2}$.

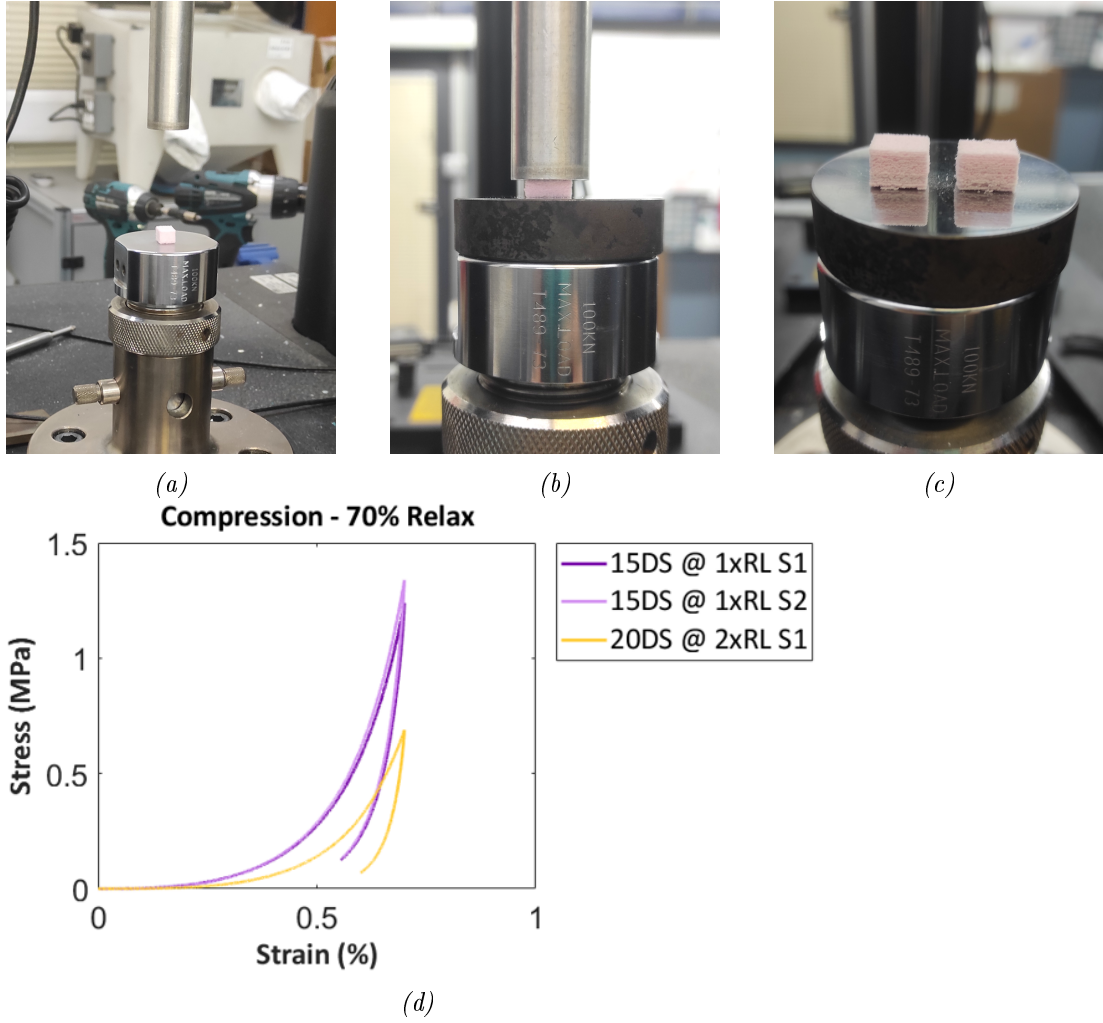


Figure 6.20: Compression testing at (a) setup, (b) 70 % compression and (c) a plotted stress-strain curve.

Each sample was compressed up to 70 % before the load was released. Figures 6.20b shows how during deformation, the cubic samples maintain sharp edges and flat faces throughout while the thickness decreases. The behaviour exhibited is akin to that of a sponge. As soon as the load is released the samples expanded, returning to nearly the same thickness before loading. Figure 6.20c shows two samples side by side whereby the part on the left has yet to be loaded while the one on the right has already undergone loading. A slight variation in thickness can be seen between the two samples, suggesting that plastic deformation is occurring during compressive loading. Upon closer inspection, some of the individual layers appear torn in the post-load sample. However, overall the samples appear highly elastic, retaining the majority of their original shape even after compression of 70%. The stress-strain curve for both S1 and S2 can be seen in Figure 6.20d. The sample S2 with the highest droplet density of $4,444 \text{ px mm}^{-2}$ was

found to have a Young's Modulus of 1.74 MPa which is nearly double that of sample S1 at 0.92 MPa with a droplet density of 2,500 px mm⁻². Thus, the Young's Modulus of a RBJ printed part is linearly proportional to the droplet density, or in other words, the saturation level of a given part.

6.4 Summary

This chapter Multiple Powder Layer (MPL) printing to produce fully consolidate 3D Reactive Binder Jetting (RBJ) printed parts capable of undergoing mechanical testing. The process was an extension of Single Powder Layer (SPL) printing discussed in Chapter 5 and introducing inter-layer binding as a new concept to explore.

RBJ required modifications to the commercial LP50 printers to accommodate both a powder bed and dual printheads for reactive ink deposition. The modifications involve software adjustments, including waveform conversions to ensure compatibility between printers, and hardware modifications for powder recoating.

For printing adjustments, factors like DS, pixel density, and image sizing were critical setting that required adaptations from the DMP to LP50 printer. Powder recoating mechanisms were optimised based on real-time feedback from the process, whereby printing failures from part delamination or deformation inform the solution. Powder recoating parameters are critical for successful printing. Print stability on the build platform was also affected by recoating parameters which led to displacement of print layers, and in some cases, samples were entirely pushed off of the powder bed.

However, to stabilise the first print layer, a raft mechanism designed and implemented. This feature involved printing 2-3 initial print layers to provide stability and support for subsequent print layers to build from. By preparing a sacrificial raft, initial damage to the final part was mitigated.

Finally, the chapter concludes with an assessment of part quality and performance. Geometric accuracy and mechanical properties, such as tensile and compressive strengths, were evaluated, highlighting the importance of saturation level on robust RBJ parts.

7 | Discussion

Previous research into reactive inkjet printing (RIJP) covers the physiochemical behaviours before, during and after the reactive inks make contact, however these experimentations have been non-porous substrates. Although, Reactive Binder Jetting (RBJ) shares many of the same challenges including stoichiometry, jetting stability and reactivity, RIJP does not investigate the added complexities associated with powder bed substrates. Thus, as the reactive inks physically penetrate the voids found in powder beds, these inks are simultaneously undergoing a chemical reaction which over time alters the physical state of the inks from liquid to solid. The result is a complex reactive dual-ink binder system that is extremely sensitive to changes in ink formulations, print parameters, powder bed properties, humidity levels, temperatures, and so on. Throughout this project, efforts were made to understand the impact these sensitivities had on the performance of these reactive dual-ink binder systems including the quality of parts fabricated via RBJ.

7.1 Reactive Inks

When developing new ink formulations for RBJ it is critical to consider the ‘printability’ of a material before successful printing can begin. In the case of Dimatix DMCs, it is predicted an ink will jet if the viscosity, η , falls within 10 – 12 mPa s, however it is also suggested droplets can still be generated at higher viscosities of up to 30 mPa s.^{21,137} Generally, it is challenging to predict printability for a given formulation due to system complexities including shear forces, surface energies, and molecular shape or size.

Original DMC printheads are capable of heating inks up to 70 °C, thus rheological measurements were taken only up to this temperature to ensure comparability. Similarly, a

maximum shear rate of 1000 s^{-1} was applied to simulate shearing experienced by inks as they are forced through a $21\text{ }\mu\text{m}$ nozzle at high velocity. However, it is clear from the two sets of viscosity data in Section 4.1.2 that temperature has the most significant impact on lowering ink viscosity while higher shear rates lead to slightly higher viscosities. This is likely caused by the onset of turbulence within ink flow.

Existing literature suggests printing stability is the critical factor to consider when formulating new inks for inkjet printing¹⁶⁹. This is especially critical for reactive inks which require optimum stoichiometry to be maintained throughout the printing process to maximise reaction efficiency.¹¹⁹

For traditional BJ printing, the purpose of the binder is to temporarily bind powder particles to a desired shape and to provide sufficient cohesive strength to withstand the powder removal process before debinding via sintering.^{55,183}

Thus, for the RBJ system presented in this document, the following material properties were considered to be critical to the viability of reactive inks:

- (i) **Miscibility**: To ensure effective mixing of materials leading to complete reactions.
- (ii) **Viscosity**: To ensure inks repeatedly jetted onto relevant substrates without clogging.
- (iii) **Reactivity**: To ensure the reactive inks formed a solid product or binder system.

However, in reality, DIOL inks with poor miscibility, particularly DBTL, was found to elicit full reactions over time. However, it was found the reliability of the system was significantly lower than DMEA which was hypothetical the most miscible of all three catalysts explored. Overall, there was a higher chance of incomplete reactions occurring with less miscible DIOL inks.

The viscosity of a reactive ink was deemed most critical since an ink that could not reliably eject from the printhead was fundamentally not viable. No matter how miscible and reactive an ink, it is entirely pointless if it can be printed, thus viscosity was found to be the most critical parameter to consider during selection.

The reactivity of a given ink and/or dual-ink system is critical to the performance of the final part. Additionally, poor reactivity was found to cause more printing failures

due to the poor binding between particles and powder layers, leading to deformation during recoating. Thus, ink reactivity is critical for RBJ to work, however even with poor reactivity there was still sufficient binding to produce 3D parts with very limited application potential. As such, reactivity was considered the second most critical parameter to assess reactive ink viability.

Arguably, based on the level of importance of each property, theoretically the selection sequence should be 1. Viscosity, 2. Reactivity and 3. Miscibility in order of most to least critical for successful RBJ. However, the decision to assess miscibility first is justified as it significantly reduces the number of experiments required in later stages, including reactivity characterisation since miscibility is directly linked to reaction efficiency and reliability. Thus, the selection sequence would not be altered for future experiments, however to simplify the process, removal of the miscibility step would be considered.

Finally, the dual-ink binder systems presented in this thesis have been designed to now only remain in the final part but to enhance its properties inherently, unlike with traditional binders for BJ printing which are burnout during sintering. According to literature, these binder systems require careful formulation and optimisation to ensure effective burnout of additives through multi-stage thermal treatment while preventing cracks.^{184,185} Following the de-binding process, binder leave residues which reduce structural integrity and mechanical strength.¹⁸⁶ Whereas with dual-ink binder systems for RBJ printing, the binder requirements are much simpler than for traditional BJ binders, potentially saving time, energy, and other operational costs within industry. However, further developments are still needed within RBJ printing for this AM technique to be considered comparable, let alone superior.

7.2 Printer Parameters

Print parameters for any inkjet system will often require initial optimisation to ensure the ink, or multiple inks, to be jetted are reliably deposited onto the desired substrate via a given printhead. However, changes to the ink formulation, printing conditions, print settings, printhead and even substrate itself will elicit variable results, thus requiring re-calibration following each change to achieve the desired print. In the case of RBJ,

changes in print parameters also directly impact the droplet volume and therefore the molar ratio between reactive inks. Thus, print parameter optimisation for RBJ systems must take into account both printing stability, to generate reliable droplets, and the droplet volumes of each ink to maintain a desired molar ratio between reactive inks.⁶⁰

To optimise for jetting reliability for each reactive ink, the two critical areas of focus were the waveform profile and jetting voltage for each ink. However, as previously highlighted in Section 4.2.1.3, there are often trade-offs to consider between droplet volume, ejection speed, jetting reliability and so on.^{20,187} For example, to generate larger droplets the rate of ejection may decrease due to longer waveform times. Alternatively, higher voltages may be used to overcome the resistive forces in an ink but then cause satellite droplets, or spraying, to occur. This highlights the importance of optimising the print settings and waveform pattern to suit a given ink with its own unique material properties.

Throughout the reactive ink selection process, optimum printhead temperatures had been determined to carry out the droplet volume measurements. These settings were taken forward to printer parameter optimisation whereby printhead temperatures were either maxed out at 60 °C (A01) or just under at 55 °C (B01 and B102). This is not surprising given the viscosity results shared in Section 4.1.2 highlighted a clear decrease in viscosity at higher temperatures. However, further analysis was needed to determine the optimum jetting voltage for each ink as previously a fixed voltage had been selected based on very quick stability checks. Thus, when a scan was performed Figure 4.10 it was found that the droplet volume became increasingly less reliable as the voltage changed. For reactive ink A01, the error margins increased as voltage increased, whereas with reactive ink B102, the error margins were high across most voltage settings, however there were on average a higher percentage of errors as voltage decreased. However, since the error margins for B102 across most voltage settings between 30 – 36 V are very higher and the viable printing range presented in Figure 4.8 is much narrower than the other two inks, it is likely that reactive ink B102 is generally less stable and more sensitive to voltage changes. Luckily, voltages 35 V and 36 V appear to deliver reliable droplet volumes, suggesting these printer parameters are most stable.

Although, literature confirms droplet volume is influenced by the actuating voltage,

whereby larger droplets are elicited from larger voltages, thus enabling additional control over molar ratios for reactive inks.¹⁵⁰ However, due to the limitation of the printhead hardware used, the range of viable printing voltages was narrow and, when compared to the increased ink deposition volumes achieved using MPW technique, the impact was insignificant. Thus, for this system, it made sense to prioritise jetting stability over droplet volume when it came to deciding optimum voltage settings.⁶⁰

In hindsight, it might have been worth revisiting the temperature setting for B102 as it is possible the ink was not receiving enough energy from the combined inputs of temperature and voltage to overcome resistive forces in the printhead, leading to jetting instability. However, in the case of reactive ink A01 where stability worsened with increasing voltage, it is more likely that too much energy was entering the ink system meaning which likely led to for the formation of satellite drops or spraying which would in turn impact the net droplet volume.¹⁵² Therefore, similar to reactive ink B102, a drop in the printhead temperature settings may have helped to increase the viable printing range. However, this change could also have caused the reverse issue whereby there is insufficient energy in the ink system.

Another major factor to consider here is the impact a waveform, or a voltage distribution profile, has on the ability for a reactive ink to eject reliably from the printhead nozzles. In this case, an optimum profile could leverage the temperature and voltage settings to eject a droplet whereas a simpler and/or less tailored waveform could completely suppress the droplets, stopping all droplet generation. Additionally, since the duration of a waveform is in the microseconds, it is possible to add repeating patterns within one waveform profile without significantly increasing the overall printing time. Thus, the development of multi-pattern waveforms (WPMs) enables a wider range of droplet volumes to be achieved and thus offering more control over molar ratios. The MPWs play a critical role in validating the viability of RBJ printing. When it comes to pairing reactive inks to achieve a target molar ratio of 1:1, the wider range of droplet volumes means at least two reactive ink combinations could be taken forward to the next validation stage of printing on powder. It is worth noting that without the introduction of these MPWs, there would have been no compatible molar ratio pairing based on the droplet volume obtained to date. Thus, a reformulation of inks would have

been necessary, consuming more time and resources to deliver a viable dual-ink binder system.

Furthermore, the process of applying a new powder layer is critical for successful printing of RBJ parts. Given the fragile nature of green parts consolidated by binder alone, inadequate powder recoating parameters often lead to part deformation due to high compressive forces or poor mechanical performance due to low powder bed packing densities. In this research, a blade was used to spread new powder layers which according to literature Beitz *et al.*³⁵ produces more densely packed powder layers which was considered desirable for RBJ printing. However, given commercial powders - UX and HP - had very large PSDs with finer particulates below 20 μm in diameter, a counter roller mechanism may have been more appropriate. Typically, rollers are used to break up agglomerations which often form with finer particles and reduces the downward force on the powder bed. Thus, in hindsight, to minimise part failures during recoating, a counter roller should have been trialled or finer particles removed by sieving the commercial powders before printing. The potential knock-on effect would have been more successful sample prints to characterise and therefore more data to feed to inform the iterative optimisation process for printing parameters.

7.3 Saturation Level

The quality and performance of 3D RBJ parts produced in Chapter 6 were assessed based on the geometric accuracy and mechanical properties of the prints, respectively. However, as this research project did not have a specific application for this novel printing technique, the performance parameters for assessing performance and quality may vary depending on the intended application. For example, RBJ has the potential to print parts with gradient properties if three or more inks are used to form the binder system, thus the desired mechanical properties for this type of part could be both stiff and flexible at the same time.¹²⁰ With a part like this, orthotic shoe soles could be explored as a potential application, at which point compressive strength and flexibility become critical properties to measure. Given this information, a more explorative approach was taken whereby a range of mechanical tests were conducted, some standard (e.g. compressive, tensile) and other not so (e.g. manual tearing or cutting).

The results following standard destructive mechanical testing, including compression and tension, suggested the strength of 3D RBJ parts are not currently comparable to other polymeric parts manufactured via other AM methods such as binder jet (BJ) printing. However, post-processing in the form of furnace sintering is often applied to the ‘green’ parts produced via BJ printing, which strengthens the part further.^{3,31,55,58,59} As RBJ is a low-energy process which does not apply IR or UV lamps, heated build platforms, lasers or a furnace, the mechanical properties are unlikely to ever surpass AM parts which has undergone physical changes due to high-energy processing. Thus, as a novel AM technique being explored for the first time, these results have provided a baseline from which to build from. Further points to be made in Future Work (Section 8.2).

It is very likely that both the performance and quality of the 3D RBJ parts could be improved by increasing the overall saturation level. By increasing the net volume of binder, more contact points form between the binder and the particles, thus, the internal binding strength increases due to more covalent bonds. Additionally, an increase in part density would likely increase the compressive strength of the part. Finally, with fewer voids present in the part, surface texture or roughness should appear more smooth, thus increasing the perceived quality of the part.

Literature states that within BJ printing applied saturation levels are often greater than 100% to increase the ‘green’ strength of a part.¹⁸⁸ Therefore, the mechanical properties including binding strength should increase proportionally with saturation level. Thus, the probability of printing failures occurring during recoating would also decrease as it had been observed that prints would often fail because the previous print layer would deform during powder recoating. This would continue to occur even after recoat speed and print layer thicknesses were optimisation, thus suggesting either there was poor consolidation, possibly due to incorrect molar ratios or ineffective mixing of inks, or insufficient saturation, possibly due to nozzle clogging during printing or the powder layer deposited during recoating was too thick. However, the commercial powders used were on average quite large in size ($>100\text{ }\mu\text{m}$), this the powder layer thickness has to be quite large to enable smooth recoating. Additionally, the powder layer thickness was often increased further to minimise the chance of print failure due to oversaturation,

warping or print layer deformation, thus skewing the saturation level to the lower end.

However, when attempts were made to maximise saturation either by applying multiple ink layers per powder layer or by maximising droplet volumes via MPWs, the part quality would become compromised. In other words, the geometric accuracy would decrease whereby print layers would begin to warp causing subsequent layers to fail as a result. Research conducted by Holland *et al.*¹⁸⁹ found a very similar curling behaviour would occur during BJ printing edible materials including cellulose, xanthan gum and glucomannan. This phenomenon is very common within BJ due to an inhomogeneous shrinkage across the part that occurs during build process as the part begins to shrinkage during the ink phase change from liquid to solid.¹⁹⁰

Finding the right saturation level was a challenge, especially given this value is different for each powder type. The properties of a powder, including morphology and PSD, influence the packing density of a given powder bed and therefore the percentage of voids present within a given volume of powder bed. However, to accurately characterise the void percentage of either of the two polymer powders used in this project – UX and HP – was a challenge as they are both of low density, white in colour and highly refractive, making it difficult to distinguish the individual particles from the internal pockets of air or voids. However, once particles are wetted by the reactive inks, it becomes easier to identify air pockets in the part using XCT as seen in Figures 5.18, 5.17.

Therefore, to optimise the saturation level, a successfully printed part must first be obtained and the void percentage measured via image processing of XCT data. The XCT images of two SPL samples of 2x and 3x RILs were analysed in Figure 5.20 where it was observed the mean void percentage for each sample was 84.5% and 78.9%, respectively. Thus, the saturation levels are theoretically 15.5% and 21.1%, respectively. However, it is likely the saturation level is actually higher as the image processing technique applied using MATLAB took into account the black empty space framing the sample, thus the amount of white pixels were compared to a much larger, inaccurate number of black pixels. As such, it would be sensible to apply a 30% adjustment factor proportional to percentage of black pixels outside of the sample footprint. Thus, corrected saturation levels would be closer to 22.1% and 30.1%, respectively.

Literature suggests that, for optimal bonding in Binder Jetting (BJ) printing, saturation levels around 60 % are typically required. However, it is recognized that reactive binders can achieve effective bonding at significantly lower levels, such as 20-30 %.¹⁹¹ While these lower saturation levels are promising for SPL printing, scaling to multiple-powder layer (MPL) printing presents a unique challenge. In MPL printing, the risk of over-saturation increases, as excess ink cannot penetrate deeper into the powder bed. This can lead to ink pooling on the surface or spreading laterally, potentially compromising part quality and mechanical properties.

In addition to XCT characterisation, visual assessments of the part surfaces were made via SEM. The results here suggested the dual-ink binder system would settle along the midplane of a single print layer as proven by the cross-sectional images presented in Figure 5.19. Although, viewing the cross-section of a part does not directly support any saturation level measurements, it does provide insight into some potential challenges regarding inter-layer binding. This result conflicts with other literature which found the top region of the print layer contained more binder than the lower.¹⁹² It is worth noting, this research investigated a completely different set materials including a metal powder substrate, thus the ink-powder dynamics at play are expected to be fundamental different, especially given the dual-ink binder system used is polymerising, and therefore changing material properties, over time. However, Hu *et al.*¹⁹² found that increasing droplet volume lead to an increase in binder spreading and penetration which does correlate strongly with geometric results presented in Figure 5.15. Overall, the dual-ink binder systems used in this research behave similarly to traditional binder systems.

Interestingly, increasing saturation levels did not result in a smoother surface finish. Microscopic examination revealed protruding particles on both 2x and 3x RIL samples. Instead, additional binder primarily led to a thicker and more uniform binder layer along the midplane. This maintained roughness can be attributed to the reactive inks' continued penetration into the powder bed, even with increased ink deposition. While theoretically, this could be mitigated by accelerating the reaction kinetics through reformulating the DIOL inks with a higher catalyst concentration, the current behavior is beneficial for Multi-Part Layer (MPL) printing. By maximizing inter-layer binding, the risk of delamination, where individual layers remain intact but lack connectivity, is

significantly reduced. This was evident in earlier trials with very low saturation levels, where parts often delaminated upon removal from the powder bed. Visual inspection of the delaminated print layers shown in Figure 6.8, were comparable to the single payer sample analyses conducted throughout Section 5.2 on SPL parts. Overall, print parameters, reactive ink formulations and even powder selection can be addressed to improve MPL part quality, starting with efforts to increase powder saturation to improve layer-to-layer binding while minimising part failures caused by over saturation of inks during RBJ printing.

Due to high failure rates following powder recoating, powder thicknesses were increased to prevent print layers from being displaced or deformed. However, by increasing the powder layer thickness the volume of binder required to sufficient bind particles and print layers together significantly increased. Several efforts had been made to increase droplet volumes, including the introduction of multiple Reactive Ink Layers (RILs), Multiple-Pattern Waveforms (MPWs) and reduced Droplet Spacing (DS), however despite these efforts delamination due to poor saturation would still occur at higher powder layer thicknesses.

Alternative powder options should have been explored sooner, particularly ones with smaller average diameters, to reduce powder thickness, and tailored PSDs for optimal packing densities and flowability. As an initial investigation in RBJ, it was preferred to keep the powder TPU to match the dual-ink binder system, however this decision drastically reduced the commercially available powders. The UX powder used throughout this research is a transfer powder, and therefore, had not been manufactured with AM powder-based processes in mind.

Finally, the DMC-Samba printheads were a major limitation in this project. However, with the disposal rates so high due to the sensitivities of ISO inks clogging nozzles, these were an economical choice. However, if the glove boxes available were more effective at keeping humidity low, the risk of printheads clogging would have been drastically reduced, opening up an opportunity to use higher-throughput printheads ejecting droplets of a more suitable printhead without budget concerns (e.g. Xaar 128). These unexpected challenges are addressed in the next section.

Despite the compounding hardware limitations, a limited number of fully consolidated 3D RBJ parts were successfully produced. These samples were characterised as effectively as possible given the limited number available. Mechanical testing was prioritised as this data can be used to set a baseline for RBJ printing from which to optimise the process the further. Additionally, mechanical testing is commonly done with manufacturing to assess performance and to compare results across a wide span of materials, processes and applications. Although, lacking in repeated datasets, the RBJ parts were found to demonstrate good compressive modulus of up to 1.74 MPa at 70% compression and a tensile strength of . During handling, the parts were observed to deform under pressure but then regain their original shape very quickly, potentially enabling Shape Memory Polymer (SMP) developments in future work.

As there is no existing literature on RBJ printing and their parts, directly relevant performance comparisons cannot be drawn at this stage, as the characterisation of RBJ parts presented in this thesis are completely novel. However, parts manufactured via BJ or from PU were considered sufficiently relatable to offer an approximate idea of where RBJ parts stand in relation to other competing manufacturing techniques.

Research conducted by Park *et al.*³⁰ investigated the mechanical properties of polymethyl methacrylate (PMMA) manufactured via warm isostatic pressing (WIP). The compressive modulus of the green part (G) was observed to be 11.5 MPa which is 6.6x higher than the RBJ parts. Additionally, research outside of AM conducted by D'Ovidio *et al.*¹⁹³ presented a novel composite PU material with a compressive modulus (at 50% compression) of 48.4 kPa for a PU system with a stoichiometric ratio of 1.0. Thus, the RBJ parts presented in Section 6.3.2 are estimated to have 35x more compressive strength. Although, both materials are composite PUs of the same stoichiometry, the constituent materials that formed PU are fundamentally different. Additionally, the test setting are not comparable as the RBJ parts were subjected to different loading forces, rates and percentage compressions.

7.4 Unexpected Challenges

Throughout this project, several unexpected challenges arose that had not been anticipated during the initial planning stage. These are outlined below:

- (1) **Printhead Discontinuation:** Dimatix DMC-11610 printheads being discontinued and replaced by the DMC-Samba printheads 22 months into the project. This change forced an immediate reduction in viable reactive inks options due to the reduced nozzle size and reduction in maximum printhead temperature, thus higher viscosity inks were scraped altogether. Additionally, printer parameters for those inks that were still viable had to be completely re-optimisation to account for the changes.
- (2) **Printhead Lifetime:** Although, both DMC printhead versions were considered more-or-less disposable due to the relative low cost compared to other inkjet printheads, the short lifetime of less than 1 day was not anticipated. The primary cause is presumed to be the hardware quality of the DMC-Samba printheads as the DMC-11610 predecessor has lasted up to 2-3 weeks at a time if cared for properly. However, the printheads containing ISO ink often did not last as long as this due to the sensitivity of isocyanate. However, the lifetime could have been extended if left overnight in low-humidity conditions. Unfortunately, the glove boxes for both the Dimatix and LP printers in the lab were not capable of bringing the humidity to less than 5%, let alone maintain the low-humidity conditions for extended periods. Within 24 hrs the humidity would usually be at 15-25% which likely led to accelerated polymerisation of the ISO inks, thus clogging the printhead overnight. A laboratory standard desiccator was purchased to maximise the printhead lifetime but it was not effective enough, and thus new ink formulation were prepared on a regular basis.
- (3) **Printhead Purging:** Although likely caused by a combination of challenges 1 and 2, the frequency of purging required to maintain jetting stability throughout the printing of a MPL part was much higher than anticipated. To ensure molar ratios were maintained and maximum saturation was being achieved, the print-

heads would undergo purging and the nozzles gently wiped with a paper towel to between each print pass. For context, a 3x RIL print layer would require three purging sequences with first one at the start of the first print pass. Thus, for a typical 3D RBJ part of say 20x print layers, a minimum of 60 purge and clean cycles would be required. Each purge cycle would take anywhere between 1-5 minutes to perform and potentially even longer if an insufficient amount of ink came following the purge. Often the printheads would get dislodged during the wiping stage, requiring manual adjustments until the electrical components regained sufficient contact.

- (4) **Net Droplet Volume:** Most definitely a knock on effect from the printhead change (challenge 1), but ultimately the average droplet volume decreased from 10 pL to 2.4 pL following the transition from the DMC-11610 to DMC-Samba printhead. Additionally, the number of nozzles per printhead went from 16 to 12, respectively. Thus, the net droplet volume potential per unit time decreased to 19% of the original output achieved by the DMC-11610 printhead that have been used for the first 20 months of the project. As a result, it became incredibly difficult to achieve the same quality of single-powder layer prints achieved with the DMC-11610 printhead due to insufficient saturation levels. Out of necessity, the MPW were developed to minimise the negative impact such a reduction in drop volume had on the RBJ part quality.
- (5) **Covid-19:** The lab was inaccessible for over 24 weeks from March to September 2020, completely stifling the potential to gain essential hands-on lab experience, training, and initial data. Additionally, even when the lab reopened, access was highly restrictive, thus between September – December 2020 only 23 full days were secured. Noting that just before the first lockdown, 4-5 days were being spent in the lab given the under-explored and highly practical nature of the project.

8 | Conclusions and Future Work

8.1 Conclusions

This research has demonstrated the feasibility of Reactive Binder Jetting (RBJ) as an innovative, low-temperature additive manufacturing (AM) process for polyurethane (PU) fabrication. By employing a reactive dual-ink binder system, RBJ facilitates in-situ polymerisation at ambient temperatures, thereby eliminating the need for energy-intensive processes or equipment. This advancement represents a low-temperature powder AM alternative for producing fully-consolidated, functional polymer parts.

The key conclusions are as follows:

(i) **Development of Reactive Inks:**

Comprehensive characterisation of reactive inks, focusing on viscosity, miscibility, and reactivity, was crucial in ensuring stable droplet formation and achieving the optimal stoichiometric balance during jetting. A total of 23 reactive ink formulations were characterised and of these two reactive dual-ink binder system pairings were selected for RBJ testing. This work provided vital insights into the interplay between ink formulation and deposition dynamics, establishing a foundation for further innovation in reactive binder systems.

(ii) **Optimisation of Printer Parameters:**

Detailed optimisation of printer settings, including jetting voltages up to 40 V, waveform profiles, and droplet spacings between 6 - 10 μm , ensured

consistent ink deposition and effective powder saturations for powder consolidation. The establishment of a robust parameter portfolio supports reliable part quality and scalability for commercial applications.

(iii) **Powder-Substrate Interaction:**

The influence of powder characteristics, such as particle size distribution and flowability, on ink spreading and saturation was thoroughly examined. Single Powder Layer (SPL) samples composed of 2x and 3x Reactive Ink Layers (RIL) demonstrated the ink-powder dynamics of reactive dual-ink binder systems on part geometry and void percentage for two different powders with unique characteristics.

(iv) **Performance of RBJ Parts:**

Mechanical testing validated the capability of RBJ to produce PU components with high compressive strength, inter-layer integrity, and geometric accuracy. The greatest Young's Modulus achieved was 1.74 MPa following compression testing, demonstrating excellent elasticity and binding strength with minimal plastic deformation. This work validates RBJ is capable of producing robust 'green' polymer parts at low temperature, potentially addressing challenges around 'green' part fragility for Binder Jetting (BJ) applications.

(v) **Sustainability and Versatility:**

The energy-efficient nature of RBJ, combined with its ability to reduce material waste via recycling, highlights its sustainability advantages over traditional powder AM techniques. This process paves the way for the use of thermally-sensitive powders and environmentally-friendly reactive multi-ink binder systems, aligning with the growing emphasis on sustainable manufacturing. Additionally, these results highlight the potential RBJ has in fabricating multifunctional parts with gradient properties.

8.2 Future Work

To summarise, future research should focus on the following:

- (I) Expanding the range of printable materials, including custom PU powders and non-toxic, sustainable inks. of Reactive Inks:
- (II) Scaling up the RBJ process by developing high-capacity printheads and industrial-grade systems.
- (III) Exploring advanced design capabilities, such as integrating multifunctional and gradient material properties for targeted applications in the medical, automotive, and aerospace industries.

The outcomes of this research represent a significant advancement in AM technologies, positioning RBJ as a transformative approach for polymer-based manufacturing. Further developments have the potential to revolutionise the production of complex, highly functional parts while supporting sustainability goals. Additional insights have been provided in the sections below.

8.2.1 Widening Printable Ink Range

Polyurethane are incredible versatile chemical systems capable of elicit properties on opposite ends of the spectrum of traditional mechanical properties, including parts ranging from very flexible and soft to hard and abrasion resistant. Interestingly, RBJ has the potential to capture the full range of properties that polyurethane exhibit a single print. By introducing more printheads, and therefore inks, to the RBJ process, it is possible to manufacture parts with either more complex binder systems composed of various segments or more variety of dual-inks binders in the same part by selectively depositing certain reactive ink combinations on to the powder substrate.

By having a wider range of printable reactive inks at our disposal, particularly constituent materials that form polyurethane systems, capable of eliciting variable properties within a single part, the number of potential applications increases significantly. For example, by fine tuning the exact molar ratios and deposition sequences, it is possible to produce fully customised orthotic footwear with firmer material in one location and them soft, flexible material in another to ensure optimal comfort and support for the

wearer.

Finally, the use of toxic materials including isocyanates and tin-based catalysts, increases the risk to human health and the environment if not handled correctly. This drawback also limits the potential scalability of RBJ printing, especially given the requirement for environmental control and expected costs associated with large-scale infrastructural changes to meet the requirements for the RBJ system. Additionally, given the unique selling point (USP) of this system is that it is significantly less energy intensive compared to other AM technique, it would be very fitting to explore more sustainable reactive ink materials to align with the general societal shift away from environmentally harmful chemicals and use of high-energy systems which require fossil-fuel based electricity to operate. Thus, it is strongly recommended that more sustainable alternatives to traditional polyurethanes should be explored further to minimise the negative impacts caused by handling isocyanates and enhance the USP of RBJ printing. Existing PU chemistry literature identified renewable ISO and DIOL constituent materials^{194,195}, non-isocyanate alternatives¹³², providing a platform from which further research could build from.

8.2.2 Exploring Alternative Powders

From the perspective of increasing binding strength between particles and individual print layers, synthesis of custom powders should be explored to increase the number of active sites available within the collective composite system. Although not presented within this document, initial work on reactive polyurethane powders was conducted, however the complexity of dispersion polymerisation led to inconsistent powder properties, including variable sizes, morphologies and flow behaviours, and low volume outputs insufficient to fill a powder bed. Hence, work on this front was paused. However, it is strongly recommended, that to improve the mechanical properties of the RBJ parts as well as reduce the probability of failure during recoating, reactive polyurethane powders should be developed followed by efforts to scale powder output. This work would widen the range of viable RBJ printing applications, potentially unlocking next generation RBJ parts exhibiting more robust properties.

Additionally, future research should explore the viability of using RBJ printing to bind

thermally sensitive substrates, such as pharmaceutical materials or polymers with low-melting points. However, to achieve full consolidation, reactive inks will require customisation on a chemical level to ensure bonding occurs not only between the reactive inks but the substrate particles as well. The low-temperature nature of RBJ printing lends itself well to completely novel AM parts, not previously possible to manufacture due to the requirement of high temperatures or energies to bind a particle substrate together.

A wider range of commercial powders, with different powder properties should be tested to better understand which packing arrangements, pore sizes and surface chemistries are most compatible with the dual-ink binder systems presented throughout this project. Explore compatible RBJ powders with potential for higher-packing densities may mean the net volume of ink or binder required to consolidate the powder is reduced, thus minimising print time while maximising part density.

Finally, powders with a reduced PSD range between 20-150 μm and a smaller average diameter nearer to 60 μm , will lend more readily to higher powder bed densities, leading to RBJ parts with more robust mechanical properties.⁴¹ Achieving non-uniform or irregular parts, similar to those demonstrated in Section 6.3.1.2, would potentially become easier to manufacture based on research which has investigated bi-modal powder beds.¹⁹⁶ Thus, mixing of various commercial powders may elicit better results and should be explored further, alongside alternative powder bed characterisation techniques to analyse optimal packing arrangements.

8.2.3 Higher-Volume Deposition Printheads

It is clear from the research presented that there are many challenges associated with the RBJ printing, particularly around achieving optimum part saturation. It is noted that the reactive nature of the binder system implies there is a limited amount of time available to deposit the desired net volume of dual-ink binder before the system fully reacts, thus becoming immobilised. It was found the hardware used in this project, particularly the DMC-Samba printhead which was found to generate droplets approximately 2.2 pL in volume across 12 nozzles, was not capable of depositing the reactive inks quickly enough or in large enough volume to deliver more saturated parts.

Thus, by exploring alternative printheads capable of generating larger droplets of 10 pL or higher, as was achievable with the discontinued printhead DMC-11610, deposition time is reduced, allowing reactive inks enough time to penetrate deeper into the powder bed before polymerising. This is expected to minimise the risk of delamination for powders comprised of larger particles which incidentally lead to thicker powder layers and therefore more voids to fill with binder. Additionally, the reactive inks are able to mix more effectively if the net volume of ink required for a given powder layer is delivered all at once versus incrementally over several minutes.

Finally, the incremental ink deposition approach taken in this research due to the limitation around droplet volumes, is believed to have caused SPL prints to warp. Since there are multiple sets of reactive ink layers each polymerising at different points in time, the stresses within the part are not balanced or uniform. Therefore, by depositing reactive inks more effectively using printheads capable of higher deposition rates (e.g. Xaar 128), the risk of print failures occurring due to layer deformation is theorised to reduce significantly, ultimately saving time and producing higher quality RBJ parts.

References

- [1] The British Standards Institution, *BS EN ISO/ASTM 52900:2017 Additive manufacturing*, BSI Standards Ltd., 2017, pp. 1–30.
- [2] B. Redwood, *3D Hubs Knowl. Base*, 2017.
- [3] I. Gibson, D. W. Rosen and B. Stucker, *Additive Manufacturing Technologies*, 2010, p. 459.
- [4] S. Morales-Planas, J. Minguella-Canela, J. Lluma-Fuentes, J. A. Travieso-Rodriguez and A. A. García-Granada, *Materials (Basel)*, 2018, **11**, 1–11.
- [5] H. Liu, W. Li, C. Liu, J. Tan, H. Wang, B. Hai, H. Cai, H. J. Leng, Z. J. Liu and C. L. Song, *Biofabrication*, 2016, **8**, year.
- [6] A. Cornille, R. Auvergne, O. Figovsky, B. Boutevin and S. Caillol, *Eur. Polym. J.*, 2017, **87**, 535–552.
- [7] C. J. Tuck, B. Begines Ruiz, Y. He, R. D. Wildman and R. J. Hague, *Reactive Additive Manufacturing*, 2018.
- [8] F. Khuluza, F. K. Chiumia, H. M. Nyirongo, C. Kateka, R. A. Hosea and W. Mkwate, *Front. Public Heal.*, 2023, **11**, 1–10.
- [9] B. Crichton, *J. R. Soc. Med.*, 2004, **97**, 328–329.
- [10] R. Elmqvist and S. Bromma, *Measuring Instrument of the Recording Type*, 1951.
- [11] H. P. Le, *J. Imaging Sci. Technol.*, 1998, **42**, 49–62.
- [12] C. H. Hertz, *Ink Jet Record*, 1968.
- [13] C. H. Hertz, *Liquid Jet Recorder*, 1972.

-
- [14] C. H. Hertz, *Method And Apparatus for High Resolution Inkjet Printing*, 1986.
- [15] J. S. Kelly and B. S. Lindblom, *Scientific Examination of Questioned Documents*, Taylor & Francis Group, 2nd edn., 2006, p. 204.
- [16] S. D. Hoath, in *S. D. Hoath*, John Wiley & Sons, Ltd, 2016, pp. 1–12.
- [17] R. Houben, *Ph.D. thesis*, Universiteit Twente, 2012.
- [18] N. Reis, C. Ainsley and B. Derby, *J. Appl. Phys.*, 2005, **97**, 8–14.
- [19] I. M. Hutchings and G. D. Martin, *Inkjet Technology for Digital Fabrication*, 2012, pp. 1–372.
- [20] J. L. Fernandez, *Ph.D. thesis*, University of Nottingham, 2018.
- [21] FujiFilm Dimatix Inc., *Jettable Fluid Formulation Guidelines*, 2013.
- [22] R. N. Wenzel, *Ind. Eng. Chem.*, 1936, **28**, 988–994.
- [23] J. E. Fromm, *IBM J. Res. Dev.*, 1984, **28**, 322–333.
- [24] N. Reis and B. Derby, *Solid Free. Addit. Fabr.*, San Francisco, CA, USA, 2000, pp. 117–122.
- [25] B. Derby, *Engineering*, 2015, **1**, 113–123.
- [26] D. Jang, D. Kim and J. Moon, *Langmuir*, 2009, **25**, 2629–2635.
- [27] N. D. Parab, J. E. Barnes, C. Zhao, R. W. Cunningham, K. Fezzaa, A. D. Rollett and T. Sun, *Sci. Rep.*, 2019, **9**, year.
- [28] J. Li, F. Rossignol and J. Macdonald, *Lab Chip*, 2015, **15**, 2538–2558.
- [29] The British Standards Institution, *BS EN ISO 17296-2: Standard on Additive Manufacturing (AM) Technologies*, 17561-2:2016, 2016.
- [30] S. J. Park, H. G. Ju, S. J. Park, S. Hong, Y. Son and I. H. Ahn, *Mater. Des.*, 2023, **231**, 112045.
- [31] Y. Bai and C. B. Williams, *Rapid Prototyp. J.*, 2015, **21**, 177–185.

-
- [32] A. Yegyan Kumar, Y. Bai, A. Eklund and C. B. Williams, *Addit. Manuf.*, 2018, **24**, 115–124.
- [33] Q. B. Nguyen, D. N. Luu, S. M. Nai, Z. Zhu, Z. Chen and J. Wei, *Arch. Civ. Mech. Eng.*, 2018, **18**, 948–955.
- [34] S. Berretta, O. Ghita and K. E. Evans, *Eur. Polym. J.*, 2014, **59**, 218–229.
- [35] S. Beitz, R. Uerlich, T. Bokelmann, A. Diener, T. Vietor and A. Kwade, *Materials (Basel)*., 2019, **12**, year.
- [36] Y. Bai, G. Wagner and C. B. Williams, *J. Manuf. Sci. Eng. Trans. ASME*, 2017, **139**, year.
- [37] J. Clayton, D. Millington-Smith and B. Armstrong, *Jom*, 2015, **67**, 544–548.
- [38] D. Drummer, M. Drexler and F. Kühnlein, *Phys. Procedia*, 2012, **39**, 500–508.
- [39] S. O. Onuh and K. K. Hon, *Int. J. Mach. Tools Manuf.*, 1998, **38**, 329–342.
- [40] A. Townsend, N. Senin, L. Blunt, R. K. Leach and J. S. Taylor, *Precis. Eng.*, 2016, **46**, 34–47.
- [41] H. Miyanaji, K. M. Rahman, M. Da and C. B. Williams, *Addit. Manuf.*, 2020, **36**, year.
- [42] A. P. Clares, Y. Gao, R. Stebbins, A. C. Van Duin and G. Manogharan, *Mater. Sci. Addit. Manuf.*, 2022, **1**, 20.
- [43] A. Ellis, C. J. Noble and N. Hopkinson, *Addit. Manuf.*, 2014, **1**, 48–51.
- [44] R. K. Mcgeary, *J. Am. Ceram. Soc.*, 1961, **44**, 513–522.
- [45] J. P. Kruth, P. Mercelis, J. Van Vaerenbergh, L. Froyen and M. Rombouts, *Rapid Prototyp. J.*, 2005, **11**, 26–36.
- [46] N. Hopkinson and P. Erasenthiran, *Method and Apparatus for Combining Particulate Material*, 2013.
- [47] D. Chauhan, *Ph.D. thesis*, Georgia State University, 2018.
- [48] H. R. Thomas, N. Hopkinson and P. Erasenthiran, 2006, 682–691.

-
- [49] N. Hopkinson and P. Erasenthiran, Solid Free. Fabr. Symp. Proc., Austin, Texas, 2004, pp. 312–320.
- [50] HP Development Company, *HP Multi Jet Fusion technology*, 2018.
- [51] K. A. Emamjomeh, AliPrasad, M. A. Novick and E. M. Fung, 2015, **1**, 7.
- [52] H. J. O'Connor, A. N. Dickson and D. P. Dowling, *Addit. Manuf.*, 2018, **22**, 381–387.
- [53] HP Development Company, *The HP Multi Jet Fusion voxel*, 2017.
- [54] I. Rishmawi, M. Salarian and M. Vlasea, *Addit. Manuf.*, 2018, **24**, 508–520.
- [55] M. Ziaee and N. B. Crane, *Addit. Manuf.*, 2019, **28**, 781–801.
- [56] Y. Bai and C. B. Williams, *Solid Free. Fabr. 2017 Proc. 28th Annu. Int. Solid Free. Fabr. Symp. - An Addit. Manuf. Conf. SFF 2017*, 2020, 249–260.
- [57] D. Oropeza and A. J. Hart, *Addit. Manuf.*, 2021, **48**, 102448.
- [58] K. M. Rahman, A. Wei, H. Miyanaji and C. B. Williams, *Addit. Manuf.*, 2023, **62**, 103377.
- [59] L. O. Grant, C. F. Higgs and Z. C. Cordero, *J. Eur. Ceram. Soc.*, 2023, **43**, 2601–2613.
- [60] K. Zhao, Z. Su, Z. Ye, W. Cao, J. Pang, X. Wang, Z. Wang, X. Xu and J. Zhu, *J. Mater. Res. Technol.*, 2023, **27**, 5449–5469.
- [61] A. Kumar, Y. Bai, A. Eklund and C. B. Williams, *Procedia Manuf.*, 2017, **10**, 935–944.
- [62] Z. Qiao, Z. Wang, C. Zhang, S. Yuan, Y. Zhu and J. Wang, *AIChE J.*, 2012, **59**, 215–228.
- [63] R. K. Holman, M. J. Cima, S. A. Uhland and E. Sachs, *J. Colloid Interface Sci.*, 2002, **249**, 432–440.
- [64] J. Zhang, B. J. Allardyce, R. Rajkhowa, X. Wang and X. Liu, *Addit. Manuf.*, 2021, **38**, 101820.

-
- [65] S. Riechmann, O. Wunnicke and A. Kwade, *Materials (Basel)*., 2021, **14**, 1–15.
- [66] M. Vaezi and C. K. Chua, *Int. J. Adv. Manuf. Technol.*, 2011, **53**, 275–284.
- [67] N. B. Crane, *Addit. Manuf.*, 2020, **33**, 101127.
- [68] S. Bafaluy Ojea, J. Torrents-Barrena, M. T. Pérez-Prado, R. Muñoz Moreno and F. Sket, *J. Mater. Res. Technol.*, 2023, **23**, 3974–3986.
- [69] H. Miyanaji, S. Zhang and L. Yang, *Int. J. Mach. Tools Manuf.*, 2018, **124**, 1–11.
- [70] H. Miyanaji, M. Orth, J. M. Akbar and L. Yang, *Front. Mech. Eng.*, 2018, **13**, 504–512.
- [71] S. Mirzababaei and S. Pasebani, *J. Manuf. Mater. Process.*, 2019, **3**, 8–12.
- [72] R. Shanthar, K. Chen and C. Abeykoon, *Adv. Eng. Mater.*, 2023, **25**, 2300375.
- [73] S. Ziegelmeier, F. Wöllecke, C. J. Tuck, R. D. Goodridge and R. J. Hague, *J. Mater. Res.*, 2014, **29**, 1841–1851.
- [74] S. Vock, B. Klöden, A. Kirchner, T. Weißgärber and B. Kieback, *Prog. Addit. Manuf.*, 2019, **4**, 383–397.
- [75] S. Dadbakhsh, L. Verbelen, O. Verkinderen, D. Strobbe, P. Van Puyvelde and J. P. Kruth, *Eur. Polym. J.*, 2017, **92**, 250–262.
- [76] N. V. Gama, A. Ferreira and A. Barros-Timmons, *Materials (Basel)*., 2018, **11**, year.
- [77] F. M. De Souza, P. K. Kahol and R. K. Gupta, *ACS Symp. Ser.*, 2021, **1380**, 1–24.
- [78] A. Das and P. Mahanwar, *Adv. Ind. Eng. Polym. Res.*, 2020, **3**, 93–101.
- [79] N. Mahajan and P. Gupta, *RSC Adv.*, 2015, **5**, 41839–41854.
- [80] H. W. Engels, H. G. Pirkel, R. Albers, R. W. Albach, J. Krause, A. Hoffmann, H. Casselmann and J. Dormish, *Angew. Chemie - Int. Ed.*, 2013, **52**, 9422–9441.
- [81] The Business Research Company, *Polyurethane Global Market Report 2020*, 2020.

-
- [82] T. B. R. Company, *Polyurethane Global Market Report 2024*, 2024.
- [83] R. Gogoi, M. Alam and R. Khandal, *Int. J. Basic Appl. Sci.*, 2014, **3**, 118–123.
- [84] A. D. Jenkins, R. F. Stepto, P. Kratochvíl and U. W. Suter, *Pure Appl. Chem.*, 1996, **68**, 2287–2311.
- [85] C. E. Oppon, *Ph.D. thesis*, University of Northumbria, 2016.
- [86] A. Delavarde, G. Savin, P. Derkenne, M. Boursier, R. Morales-Cerrada, B. Nottelet, J. Pinaud and S. Caillol, *Prog. Polym. Sci.*, 2024, **151**, year.
- [87] C. Defeyt, J. Langenbacher and R. Rivenc, *Herit. Sci.*, 2017, **5**, 1–11.
- [88] D. K. Chattopadhyay and K. V. Raju, *Prog. Polym. Sci.*, 2007, **32**, 352–418.
- [89] K.-C. Hung, C.-S. Tseng and S.-H. Hsu, in *Adv. Polyurethane Biomater.*, ed. S. L. Cooper and J. Guan, Woodhead Publishing, 2016, ch. 5, pp. 149–170.
- [90] D. E. Heath and S. L. Cooper, *Biomater. Sci. An Introd. to Mater. Third Ed.*, 2013, 79–82.
- [91] T. Lister and J. Renshaw, *Understanding Chemistry for Advanced Level*, Stanley Thornes Ltd, 3rd edn., 2000, pp. 237–238.
- [92] K. Ligier, K. Olejniczak and J. Napiórkowski, *Polym. Test.*, 2021, **100**, 107247.
- [93] W. J. Xu, J. J. Wang, S. Y. Zhang, J. Sun, C. X. Qin and L. X. Dai, *RSC Adv.*, 2018, **8**, 20701–20711.
- [94] S. Wang, Y. Yuan, P. Tan, H. Zhu and K. Luo, *Constr. Build. Mater.*, 2020, **265**, 120725.
- [95] Y. Yanping, *Mater. Sci. Mater. Rev.*, 2018, **1**, 1–8.
- [96] A. Yadav, F. M. De Souza, T. Dawsey and R. K. Gupta, *Ind. Eng. Chem. Res.*, 2022, **61**, 15046–15065.
- [97] J. O. Akindoyo, M. D. Beg, S. Ghazali, M. R. Islam, N. Jeyaratnam and A. R. Yuvaraj, *RSC Adv.*, 2016, **6**, 114453–114482.

-
- [98] G. Guerrero-Vacas, J. Gómez-Castillo and O. Rodríguez-Alabanda, *Rapid Prototyp. J.*, 2024, **30**, 32–49.
- [99] J. Raasch, M. Ivey, D. Aldrich, D. S. Nobes and C. Ayranci, *Addit. Manuf.*, 2015, **8**, 132–141.
- [100] P. Szarlej, I. Carayon, P. Gnatowski, M. Glinka, M. Mroczyńska, A. Brillowska-Dabrowska and J. Kucińska-Lipka, *Materials (Basel)*, 2021, **14**, year.
- [101] S. Rossi, M. Fedel, S. Petrolli and F. Deflorian, *J. Coatings Technol. Res.*, 2016, **13**, 427–437.
- [102] A. Mehra, *Green and Bio Polyols Industry worth \$6.9 billion by 2027*, 2021, <https://www.researchandmarkets.com/reports/5302588/green-and-bio-polyols-global-market-trajectory>.
- [103] J. Patel, M. L. Chaudhary and R. K. Gupta, *Bio-Based Polym. Farm to Ind. Vol. 2 Curr. Trends Appl. Part 1 - Green Gold Harnessing Used Veg. Oil Sustain. Polyurethane Prod.*, 2024, **2**, 1–19.
- [104] O. Vandenplas, A. Cartier, J. Lesage, Y. Cloutier, G. Perreault, L. C. Grammer, M. A. Shaughnessy and J. L. Malo, *J. Allergy Clin. Immunol.*, 1993, **91**, 850–861.
- [105] C. Carré, Y. Ecochard, S. Caillol and L. Avérous, *ChemSusChem*, 2019, **12**, 3410–3430.
- [106] J. J. Warner, P. Wang, W. M. Mellor, H. H. Hwang, J. H. Park, S. H. Pyo and S. Chen, *Polym. Chem.*, 2019, **10**, 4665–4674.
- [107] O. Kreye, H. Mutlu and M. A. Meier, *Green Chem.*, 2013, **15**, 1431–1455.
- [108] J. Sternberg and S. Pilla, *Green Chem.*, 2020, **22**, 6922–6935.
- [109] R. H. Bean and T. E. Long, *Polym. Int.*, 2024, **73**, 5–8.
- [110] M. Srivastava, S. Rathee, V. Patel, A. Kumar and P. G. Koppad, *J. Mater. Res. Technol.*, 2022, **21**, 2612–2641.
- [111] V. Marco, G. Massimo and G. Manuela, *Prog. Addit. Manuf.*, 2024.
- [112] A. Jayswal and S. Adanur, *J. Thermoplast. Compos. Mater.*, 2023, **36**, 1450–1471.

-
- [113] M. Alvarez Gómez, D. Moreno Nieto, D. Moreno Sánchez, A. Sanz de León and S. Molina Rubio, *Polymers (Basel)*, 2023, **15**, year.
- [114] F. Fenollosa-Artes, L. Jorand, A. Tejo-Otero, P. Lustig-Gainza, G. Romero-Sabat, S. Medel and R. Uceda, *Proc. Inst. Mech. Eng. Part B J. Eng. Manuf.*, 2023, **237**, 1128–1135.
- [115] C. Ge, L. Priyadarshini, D. Cormier, L. Pan and J. Tuber, *Packag. Technol. Sci.*, 2018, **31**, 361–368.
- [116] P. C. Caracciolo, N. J. Lores and G. A. Abraham, *Polyurethane-based structures obtained by additive manufacturing technologies*, Elsevier Inc., 2019, pp. 235–258.
- [117] P. Kröber, J. T. Delaney, J. Perelaer and U. S. Schubert, *J. Mater. Chem.*, 2009, **19**, 5234–5238.
- [118] C. Sturgess, C. J. Tuck, I. A. Ashcroft and R. D. Wildman, *J. Mater. Chem. C*, 2017, **5**, 9733–9745.
- [119] C. Sturgess, *Ph.D. thesis*, University of Nottingham, 2018.
- [120] M. Müller, Q. U. Huynh, E. Uhlmann and M. H. Wagner, *Prod. Eng.*, 2014, **8**, 25–32.
- [121] M. Zawadzki, K. Zawada, S. Kowalczyk, A. Plichta, J. Jaczewski and T. Zabielski, *RSC Adv.*, 2022, **12**, 3406–3415.
- [122] T. Colton and N. B. Crane, *Addit. Manuf.*, 2021, **37**, 101711.
- [123] H. Chen, Q. Nie and H. Fang, *Phys. Fluids*, 2020, **32**, 102003.
- [124] M. Denesuk, G. L. Smith, B. J. Zelinski, N. J. Kreidl and D. R. Uhlmann, *J. Colloid Interface Sci.*, 1993, **158**, 114–120.
- [125] A. Depalo and A. C. Santomaso, *Colloids Surfaces A Physicochem. Eng. Asp.*, 2013, **436**, 371–379.
- [126] Sigma-Aldrich Company, *1,4-Butanediol - Safety Data Sheet*, 2019.
- [127] Sigma-Aldrich Company, *Hexamethylene diisocyanate for Synthesis - Safety Data Sheet*, 2005.

-
- [128] Sigma-Aldrich Company, *Poly(hexamethylene diisocyanate) - Safety Data Sheet*.
- [129] Sigma-Aldrich Company, *Poly(hexamethylene diisocyanate) - Product Specification Sheet*.
- [130] Sigma-Aldrich Company, *Paraffin oil - Certificate of Analysis (Lot STBJ4943)*, 2019.
- [131] Sigma-Aldrich Company, *Paraffin oil - Safety Data Sheet*, 2020.
- [132] E. Delebecq, J.-p. Pascault, B. Boutevin and F. Ganachaud, 2013.
- [133] L. Bengtström, M. Salden and A. A. Stec, *Fire Sci. Rev.*, 2016, **5**, year.
- [134] N. Mahmood, A. U. Khan, M. Sohail Khan, Z. Ali, A. U. Haq and A. Wutzler, *J. Appl. Polym. Sci.*, 2011, **122**, 1012–1018.
- [135] D. Guhl, *Polyurethanes High Perform. Coatings, Eur. Coatings Conf. 5*, 2008, 119–137.
- [136] M. Hui, L. Yu-Cun, C. Tao, H. Tuo-Ping, G. Jia-Hu, Y. Yan-Wu, Y. Jun-Ming, W. Jian-Hua, Q. Ning and Z. Liang, *E-Polymers*, 2017, **17**, 89–94.
- [137] Fujifilm, *Fujifilm Prod.*, 2017, 2017.
- [138] O. Oktavianty, Y. Ishii, S. Haruyama, T. Kyoutani, Z. Darmawan and S. E. Swara, *IOP Conf. Ser. Mater. Sci. Eng.*, 2021, **1034**, 012091.
- [139] D. Oropeza and A. J. Hart, *Int. J. Adv. Manuf. Technol.*, 2021, **114**, 3459–3473.
- [140] Freeman Technology Ltd., *W7013 Stability & Variable Flow Rate Method*, 2007.
- [141] A. Strondl, O. Lyckfeldt, H. Brodin and U. Ackelid, *JOM*, 2015, **67**, 549–554.
- [142] A. B. Spierings, M. Voegtlin, T. Bauer and K. Wegener, *Prog. Addit. Manuf.*, 2016, **1**, 9–20.
- [143] Malvern Panalytical, *Mastersizer 3000 - Smarter Particle Sizing*, 2019.
- [144] P. Wang, D. Auhl, E. Uhlmann, G. Gerlitzky and M. H. Wagner, *Appl. Rheol.*, 2019, **29**, 162–172.

-
- [145] D. Sarkar, J. C. Yang, A. Sen Gupta and S. T. Lopina, *J. Biomed. Mater. Res. - Part A*, 2009, **90**, 263–271.
- [146] D. I. Lim, H. S. Park, J. H. Park, J. C. Knowles and M. S. Gong, *J. Bioact. Compat. Polym.*, 2013, **28**, 274–288.
- [147] L. Jiao, H. Xiao, Q. Wang and J. Sun, *Polym. Degrad. Stab.*, 2013, **98**, 2687–2696.
- [148] M. Ravey and E. M. Pearce, *J. Appl. Polym. Sci.*, 1997, **63**, 47–74.
- [149] Y. Kanbur and U. Tayfun, *J. Thermoplast. Compos. Mater.*, 2018, **31**, 1661–1675.
- [150] P. J. Smith and A. Morrin, in *P. J. Smith and A. Morrin*, 2017, pp. 1–11.
- [151] S. Schliske, C. Rosenauer, T. Rödlmeier, K. Giringer, J. J. Michels, K. Kremer, U. Lemmer, S. Morsbach, K. C. Daoulas and G. Hernandez-Sosa, *Adv. Mater. Technol.*, 2021, **6**, year.
- [152] C. Gao, Y. Zhang, S. Mia, T. Xing and G. Chen, *Colloids Surfaces A Physicochem. Eng. Asp.*, 2021, **609**, 125676.
- [153] S. D. Hoath, S. Jung and I. M. Hutchings, *Phys. Fluids*, 2013, **25**, 21701.
- [154] H. Y. Jun, S. J. Kim and C. H. Choi, *Nanomaterials*, 2021, **11**, year.
- [155] K. Sztymela, M. Bienia, F. Rossignol, S. Mailley, S. Ziesche, J. Varghese and M. Cerbelaud, *Fabrication of modern lithium ion batteries by 3D inkjet printing: opportunities and challenges*, 2022.
- [156] A. Franck, *Understanding Rheology of Structured Fluids*, 2016.
- [157] N. Y. Akhanova, E. S. Negim, Y. Yerlanuly, D. G. Batryshev, M. M. Eissa, D. Y. Schur, T. S. Ramazanov, K. M. Al Azzam, M. M. Muratov and M. T. Gabdullin, *Heliyon*, 2024, **10**, e33282.
- [158] E. Triwulandari, W. Fatriasari, A. H. Iswanto, M. Septiyanti, E. F. Umam and M. Ghozali, *J. Mater. Res. Technol.*, 2022, **19**, 2204–2214.
- [159] C. Yanen, M. Y. Solmaz, E. Aydoğmuş and H. Arslanoğlu, *Mater. Chem. Phys.*, 2024, **312**, year.

-
- [160] K. M. Seeni Meera, R. Murali Sankar, J. Paul, S. N. Jaisankar and A. B. Mandal, *Phys. Chem. Chem. Phys.*, 2014, **16**, 9276–9288.
- [161] K. Badri, W. Sien, M. Shahrom, L. Hao, N. Baderuliksian and N. Norzali, *Solid State Sci. Technol.*, 2010, **18**, 1–8.
- [162] A. M. Hezma, I. S. Elashmawi, A. Rajeh and M. Kamal, *Phys. B Condens. Matter*, 2016, **495**, 4–10.
- [163] S. Hong, N. young Park, S. Ju, A. Lee, Y. Shin, J. S. Kim, M. K. Um, J. W. Yi, H. G. Chae and T. Park, *Polym. Test.*, 2023, **124**, 108086.
- [164] J. Long, A. Nand and S. Ray, *Materials (Basel)*., 2021, **14**, 1–29.
- [165] L. Jiang, Z. Ren, W. Zhao, W. Liu, H. Liu and C. Zhu, *R. Soc. Open Sci.*, 2018, **5**, year.
- [166] H. Chen and Y. F. Zhao, *Rapid Prototyp. J.*, 2016, **22**, 527–538.
- [167] H. Wang, Q. S. Wang, J. J. He, Z. L. Mao and J. H. Sun, *Procedia Eng.*, 2013, **52**, 377–385.
- [168] I. Basak, G. Nowicki, B. Ruttens, D. Desta, J. Prooth, M. Jose, S. Nagels, H. G. Boyen, J. D’haen, M. Buntinx and W. Deferme, *Polymers (Basel)*., 2020, **12**, 1–14.
- [169] A. Bastola, Y. He, J. Im, G. Rivers, F. Wang, R. Worsley, J. S. Austin, O. Nelson-Dummett, R. D. Wildman, R. Hague, C. J. Tuck and L. Turyanska, *Mater. Today Electron.*, 2023, **6**, 100058.
- [170] S. Seipel, J. Yu and V. A. Nierstrasz, *Sci. Rep.*, 2020, **10**, 1–10.
- [171] Z. Hussain, Z. Kiaee, M. Nazarzadeh, C. Reichel, S. Tepner, T. Tuladhar, M. Jahn and R. Keding, *Micromachines*, 2023, **14**, 80.
- [172] H. Dong, W. W. Carr and J. F. Morris, *Phys. Fluids*, 2006, **18**, year.
- [173] H. Sadeghian, Y. Hojjat, M. Ghodsi and M. R. Sheykhholeslami, *Int. J. Adv. Manuf. Technol.*, 2014, **70**, 1091–1099.

-
- [174] A. Olszewski, P. Kosmela, A. Piasecki, W. Żukowska, M. Szczepański, P. Wojtasz, M. Barczewski, R. Barczewski and A. Hejna, *Polymers (Basel)*, 2022, **14**, year.
- [175] S. Ziegelmeier, F. Wöllecke, C. Tuck, R. Goodridge and R. Hague, 24th Int. SFF Symp., 2013, pp. 354–367.
- [176] L. Markusson, *Ph.D. thesis*, Luleå University of Technology, 2017.
- [177] Freeman Technology Ltd., *Measuring and understanding the flow properties of powders with the FT4 Powder Rheometer*, 2016.
- [178] E. M. Littringer, R. Paus, A. Mescher, H. Schroettner, P. Walzel and N. A. Urbanetz, *Powder Technol.*, 2013, **239**, 162–174.
- [179] G. Egger, P. E. Gygax, R. Glardon and N. P. Karapatis, *10th Solid Free. Fabr. Symp.*, 1999, 255–263.
- [180] E. Cazares-Cortes, M. Nerantzaki, J. Fresnais, C. Wilhelm, N. Griffete and C. Ménager, *Nanomaterials*, 2018, **8**, year.
- [181] J. W. Roberts, C. J. Sutcliffe, P. L. Green and K. Black, 2019.
- [182] Y. Wang and Y. F. Zhao, *Procedia Manuf.*, 2017, **10**, 779–790.
- [183] M. J. Cima and E. M. Sachs, *Solid Free. Fabr. Symp.*, 1991, 187–194.
- [184] S. Lamnini, H. Elsayed, Y. Lakhdar, F. Baino, F. Smeacetto and E. Bernardo, *Heliyon*, 2022, **8**, e10651.
- [185] U. Scheithauer, T. Slawik, E. Schwarzer, H. J. Richter, T. Moritz and A. Michaelis, *J. Ceram. Sci. Technol.*, 2015, **6**, 125–132.
- [186] K. Rane and M. Strano, *Adv. Manuf.*, 2019, **7**, 155–173.
- [187] S. Holland, T. Foster, W. MacNaughtan and C. Tuck, *J. Food Eng.*, 2017, **220**, 12–19.
- [188] S. M. Gaytan, M. A. Cadena, H. Karim, D. Delfin, Y. Lin, D. Espalin, E. MacDonald and R. B. Wicker, *Ceram. Int.*, 2015, **41**, 6610–6619.
- [189] S. Holland, C. Tuck and T. Foster, *Carbohydr. Polym.*, 2018, **200**, 229–238.

-
- [190] C. Schmutzler, A. Zimmermann and M. F. Zaeh, *Procedia CIRP*, 2016, **41**, 1017–1022.
- [191] H. Miyanaji, 2018, 20.
- [192] A. Hu, Y. Huang, Z. Chen, Y. Yang, Y. Xu and T. Wang, *Adv. Theory Simulations*, 2023, **6**, 1–15.
- [193] A. J. D’Ovidio, B. Knarr, A. J. Blanchard, G. W. Bennett, W. Leiva, B. Duan and J. M. Zuniga, *Polymers (Basel)*., 2024, **16**, 626.
- [194] F. M. De Souza, P. K. Kahol and R. K. Gupta, *ACS Symp. Ser.*, 2021, **1380**, 1–24.
- [195] J. Bernardini, D. Licursi, I. Anguillesi, P. Cinelli, M.-B. Coltelli, C. Antonetti, A. Maria, R. Galletti and A. Lazzeri, *BioResources*, 2017, **12**, 3630–3655.
- [196] Y. Bai and C. B. Williams, *Nanotechnology*, 2018, **29**, year.